PSFC-RR-00-6 **DOE/ET-54512-337**

Study of Molybdenum Sources and Screening in the Alcator C-Mod Tokamak

D. Pappas

June 2000

Plasma Science and Fusion Center
Massachusetts Institute of Technology
Cambridge, MA 02139 USA

This work was supported by the U.S. Department of Energy, Cooperative Grant No. DE-FC02-99ER54512.

Study of Molybdenum Sources and Screening in the Alcator C-Mod Tokamak

by

Dimitrios Pappas

Ptychio, Physics, University of Thessaloniki, Greece, 1990

Submitted to the Department of Nuclear Engineering
in partial fulfillment of the requirements for the degree of

Doctor of Philosophy

at the

MASSACHUSETTS INSTITUTE OF TECHNOLOGY

September 2000

Signature of Author _____
Department of Nuclear Engineering
May 26, 2000

Certified by _____
Dr. Bruce Lipschultz
Senior Research Scientist
Thesis Supervisor

Certified by _____
Ian H. Hutchinson
Professor of Nuclear Engineering
Thesis Reader

Accepted by _____
Sow-Hsin Chen
Professor of Nuclear Engineering
Chairman, Department Committee on Graduate Studies

Study of Molybdenum Sources and Screening in the Alcator C-Mod Tokamak

by

Dimitrios Pappas

Submitted to the Department of Nuclear Engineering
on May 26, 2000 in Partial Fulfillment of the
Requirements for the Degree of
Doctor of Philosophy

ABSTRACT

In this thesis a study of molybdenum sources and screening in Alcator C-Mod is presented. This work contributes in characterizing the performance of molybdenum, a high Z material, as a tokamak first wall surface.

Understanding the molybdenum production mechanism is crucial if one wants to minimize it. A simple physical sputtering model has been developed that calculates the molybdenum source at the divertor, providing satisfactory agreement with the spectroscopic results. The effect of deuterons, boron ions, and redeposited molybdenum incident on the target is included in the calculation which shows that the boron ions dominate the sputtering. It is also found that the probability of molybdenum being "promptly" redeposited (within a gyration after having been sputtered) can be as high as 80%. High probability of redeposition is favorable because it reduces the net erosion. Specifically, it has been found that although the molybdenum gross erosion peaks close to the separatrix, the net erosion peaks further away in the target plate.

Three surfaces have been identified spectroscopically in C-Mod to be significant sources of molybdenum: the inner wall, the outer divertor and the antenna protection tiles. The inner wall is the only important source during limited plasma operation, while, in diverted discharges, the molybdenum generated there is very well screened by the plasma. In RF-heated diverted plasmas, it is believed that the antenna protection tiles are the source of most of the molybdenum that ends up in the core. The outer divertor can not be excluded as a contributor to the core molybdenum density but there are indications that it is often not the dominant source during RF heating. This result is significant since it is expected that the divertor target in the next generation fusion devices will be made primarily with a high-Z material.

The study of boronization as a surface conditioning method which reduces the molybdenum source rates and core concentration has shown a varying effectiveness dependent on first wall surface location. The beneficial effects of boronization disappear rather fast for the outer divertor, last longer for the inner wall, with the antennas and

plasma core benefiting the most.

Thesis Supervisor: Dr. Bruce Lipschultz
Senior Research Scientist, Plasma Science and Fusion Center

Thesis Reader: Prof. Ian H. Hutchinson
Professor, Department of Nuclear Engineering

Acknowledgments

I would like to thank here all the people that helped me, directly or indirectly, to complete this thesis. I will do my best to acknowledge as many as I can.

I would like to thank my supervisor Dr. Bruce Lipschultz for his advice and guidance over the years and for helping me improve the quality of this thesis. Many thanks to Prof. Ian Hutchinson not only for reviewing my thesis but also for his continuous support all these years and for his constructive comments during the Nuclear Engineering seminars.

I am grateful to Drs. John Goetz, Brian LaBombard, Garry McCracken, Rudolf Neu, Spencer Pitcher, John Rice, Peter Stangeby, and Jim Terry for fruitful discussions and for patiently answering my questions. Special thanks to John Goetz, John Rice, and Jim Terry for, additionally, making the C-Mod control room a fun place for me to work.

I wish to thank Dr. Kevin Wenzel for his assistance during my first years at MIT and for his friendship. I am grateful to both Prof. Elias Gyftopoulos and Dr. Manos Chaniotakis for offering their advice and help whenever I needed it. I would like to additionally thank Manos Chaniotakis for his friendship.

With this opportunity I would like to thank all of my Professors during my undergraduate years in Greece and, especially, Profs. L. Vlahos, D. Papadopoulos, J. H. Seiradakis, and A. Nicolaidis for making it easier for me to come to MIT. I am especially grateful to Prof. Loukas Vlahos for getting me interested in Plasma Physics and for offering his advice even during my graduate years.

I would like to thank collectively all the members of the PSFC community who assisted me in any way all these years and especially those who considered me a friend.

I would like to thank my fellow graduate students, especially Chris Boswell, Antonio Bruno, Sanjay Gangadhara, Jim Gilmore, George Haldeman, Damien Hicks, Imad Jureidini, Chi Kang Lee, Yijun Lin, Dan Lo, Alexander Mazurenko, Thomas Sunn Pedersen, Jim Reardon, Khash Shadman, and Maxim Umansky for their friendship. I am especially grateful to all my friends in Greece who kept in touch with me during all these years and made my life at MIT much happier.

Most importantly, my loving thanks go to all my family members, and especially to my parents and my wife, Glykeria, for their continuous support, love, and patience. My

gratitude to my wife for having gone through it all with me and to my young daughter, Evaggelia, who made me smile even during moments of frustration.

Table of Contents

List of Figures

List of Tables

Chapter 1

Introduction

1.1 Plasma-Wall Interaction

Plasma at the edge of the vessel in which it is contained, can interact with the surrounding surfaces through a variety of processes. The type of the interaction and its severity depend on a combination of a number of plasma parameters and wall surface properties. This "plasma-wall" interaction is unavoidable even in the case of magnetically confined plasmas, due to diffusion of energetic particles across the magnetic field. The result of this interaction can be the release of wall material ("impurities") into the plasma, which can potentially lead to either one, or all, of the following three significant problems:

a) impurity radiation, which can lead to plasma cooling, confinement degradation and possibly even to plasma termination,
b) dilution of the working fuel (typically hydrogen isotopes), which will make the attainability of ignition (self-sustained steady burn) in the next generation fusion devices extremely difficult, and
c) short lifetime of vessel components.

It is therefore extremely important for the scientific community to understand and control this interaction. Experimentally, two major approaches have been pursued in the various fusion devices, and in particular in tokamaks, which currently represent the most

promising concept in achieving ignition. In both approaches the main contact area between the plasma and wall is just a small fraction of the total vessel area. There is however a conceptual difference. When a "limiter" is used, the last closed flux surface is defined by physical contact with a part of the wall. On the other hand, in the "divertor" concept, external magnetic fields are used to divert magnetic flux lines away from the main plasma, therefore guiding escaping ions onto material targets that are spatially removed from the plasma core. The two configurations are shown in Fig. 1-1. While the limiter approach makes more efficient use of the magnetic volume, it is now widely accepted that any future magnetic reactor device will use the divertor concept. Its main advantages over the limiter are based on its remoteness from the core plasma, which implies that it is harder for impurities produced at the divertor target to enter the confined plasma. It is also believed that ultimately an appropriately designed divertor will be able to handle the enormous heat flux densities that are expected to be present in fusion reactors. A recent review of experimental divertor physics can be found in Ref. [1].

There are a number of impurity source generation mechanisms, a thorough review of which is given by McCracken [2]. The most important are "sputtering", "evaporation", and "arcing" [3]. Sputtering, which will be described in detail in Chapter 5, is a momentum transfer process in which atoms from a surface of a solid are removed as a result of impact by ions or atoms. In evaporation, surface erosion occurs as a result of a surface material having a high vapor pressure due to high surface temperature. Finally, a unipolar arc can be produced between the plasma and the wall. The required potential for the formation of the arc, is produced by the plasma "sheath". The sheath is a narrow non-neutral region, of the order of a few Debye lengths, formed in front of the surface as a consequence of the electron thermal velocity being larger than that of the ions [4,5]. The sheath formation aggravates also the problem of sputtering, since plasma ions are accelerated to the target by the sheath's electric field.

An important aspect of the plasma-wall interactions problem is the choice of the first wall materials. Apart from having to satisfy a number of thermodynamic and mechanical properties, the plasma facing materials should be optimized to minimize impurity production, neutron activation, and hydrogen isotope retention. Of course the final choice has to be a compromise of the above criteria. Two classes of materials are used in

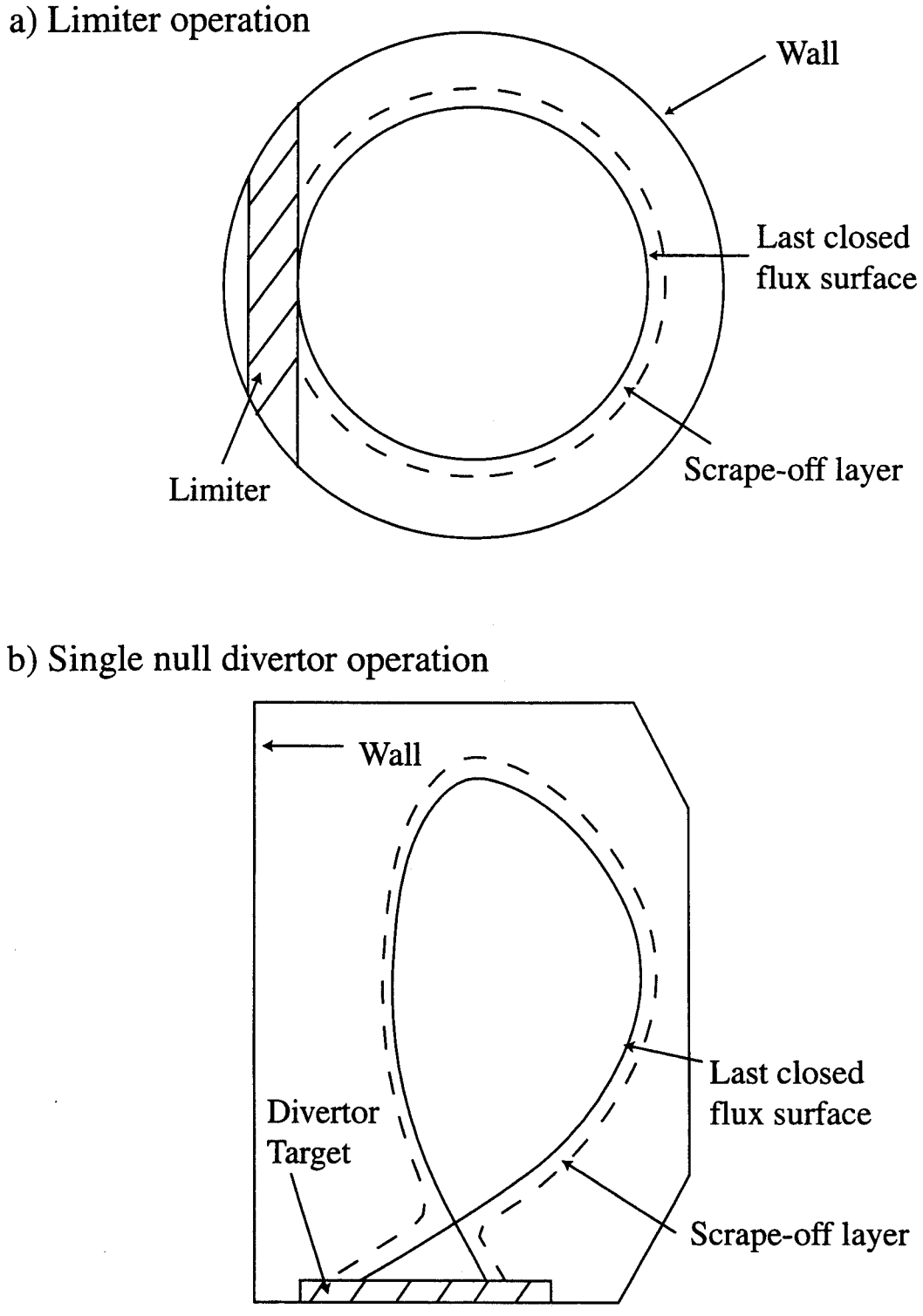

Fig. 1-1: Schematic poloidal diagram of a tokamak a) with a limiter and b) with a divertor [3]. The toroidal field is normal to the page.

present-day tokamaks. In terms of impurity generation, low-Z materials, such as beryllium and carbon, have the advantage of being fully stripped of electrons in the core, thus minimizing radiation losses. The majority of tokamaks use these materials in an attempt to minimize such power losses. On the other hand, the use of a high-Z material, such as molybdenum or tungsten, leads to a reduction of the source generation owing to their low sputtering yields compared to low-Z materials. High-Z materials have typically fewer problems with radiation damage and tritium retention as well. However, the transport of such high-Z impurities from the plasma interaction surface into the main plasma needs to be minimized, since only low concentrations of these highly efficient radiators can be tolerated in the core.

Finally, much effort has been put into developing methods for "conditioning" the plasma facing materials [3]. These methods aim at minimizing both the adsorption of impurities and hydrogen isotopes, other than the plasma species, in the walls and the sputtering of high-Z impurities. They include baking of the vessel, typically to 200-350° C, using a variety of plasma discharges to remove adsorbed gases from the wall, and covering the wall with layers of low-Z materials such as boron and carbon, known as "boronization" and "carbonization".

~~Alcator C-Mod, as is true for almost~~ all tokamaks currently operating, has devoted a large part of its physics program to plasma-surface interactions and more generally to plasma edge research. The interested reader can find a comprehensive review of the subject in Refs. [3, 6, 7].

1.2 Alcator C-Mod Tokamak

Alcator C-Mod, located at the Plasma Science and Fusion Center at MIT, is a compact, high magnetic field, diverted tokamak [8]. It is the third in a series of compact, high-field tokamaks built at MIT, following Alcator A (1974-1981) and Alcator C (1978-1986). Its predecessors, being traditional in design, operated with circular cross-section limited plasmas. In contrast, Alcator C-Mod can operate with highly elongated single or double null diverted plasmas.

The major parameters of Alcator C-Mod are listed in Table 1-1. The working fuel is

typically deuterium gas, although helium plasmas have also been run. All the magnets are made of copper. To reduce resistive heating the magnets are cooled down to liquid nitrogen temperatures. This permits higher current densities in the magnet and hence the generation of stronger magnetic fields. In a standard plasma discharge the magnetic field is 5.4 T, although C-Mod has operated occasionally with a magnetic field as high as 7.9 T. The strong magnetic field, combined with the compact design, allows the production of plasmas with high densities. As in all tokamaks, the plasma current, which is necessary for equilibrium, is also a source of plasma heating through the resistance to the current caused by electron-ion collisions. However, since the resistivity of the plasma drops as the temperature increases, auxiliary heating power is supplied in the form of ion cyclotron range-of frequency (ICRF) waves. Until the beginning of the 1999 run campaign the maximum RF power launched into the plasma was a total of 3.5 MW introduced via two antennas located at the D and E horizontal ports (two out of the ten horizontal access ports used for various plasma diagnostics). Since then, another antenna has been added in J port that is designed to introduce up to an extra 4 MW of RF power into the plasma. Although this represents a significant extension of capabilities for C-Mod, it brings up the question of what effect such high auxiliary powers will have on impurity source rates.

Parameter	Achieved	Designed
Major Radius (m)	---	0.67
Minor Radius (m)	---	0.21
Toroidal B-Field (m)	8.0	9.0
Plasma Current (MA)	1.5	3.0
Elongation	1.8	1.8
RF Power (MW)	5.	8.0
Core Electron Temperature (keV)	5.	---
Core Electron Density (10^{21} m^{-3})	1.5	---

Table 1-1: Major machine parameters of Alcator C-Mod. The achieved parameters (by November 1999) are compared with the design values.

A poloidal cross-section of the vessel is shown in Fig. 1-2. There is an "open" divertor at the top and a "closed" one at the bottom of the machine. Under typical conditions the plasma is diverted towards the lower target plate, as illustrated in the figure. The separatrix defines two different magnetic topologies: a region of closed magnetic field lines inside it and one of open magnetic field lines outside it that are intended to guide ions that escape the core plasma to the divertor target plates. In the following, unless mentioned otherwise, the term "divertor" will be a reference to the lower divertor. Whenever required by the experiments, plasma configurations are also produced in which the inner wall acts as a limiter. Actually, during the first 200 to 300 ms of every discharge, the plasma is always limited at the inner wall, as the plasma current ramps up to the requested value.

Alcator C-Mod has another prominent feature. All of the plasma facing surfaces, covering the stainless steel vessel walls near the plasma, consist of molybdenum (Z=42) tiles. It is the only tokamak of this size and performance that has experimented with high Z tiles at this level of coverage. The molybdenum wall combined with the high magnetic field and plasma density represents a unique environment for the study of the plasma interaction with a high-Z material and its effects to the plasma performance. Even more so because the divertor densities and target heat fluxes obtained in Alcator C-Mod are comparable to those expected in the next generation fusion reactors.

1.3 Thesis Goals

Since most of the present-day tokamaks do not use high-Z materials as plasma-facing components, there is a lack of an adequate experimental database on their effect on edge conditions and plasma performance and their ability to structurally withstand the rather harsh plasma environment encountered in tokamaks. This lack of information becomes even more critical when it has been widely accepted by the plasma physics community that the divertor target in the next generation fusion reactors should be constructed with a high-Z material, due to their fewer problems with radiation damage and lower tritium retention and sputtering yields compared to low-Z materials. Specifically, in the design of the plasma-facing components of the International Thermonuclear Experimental Reactor

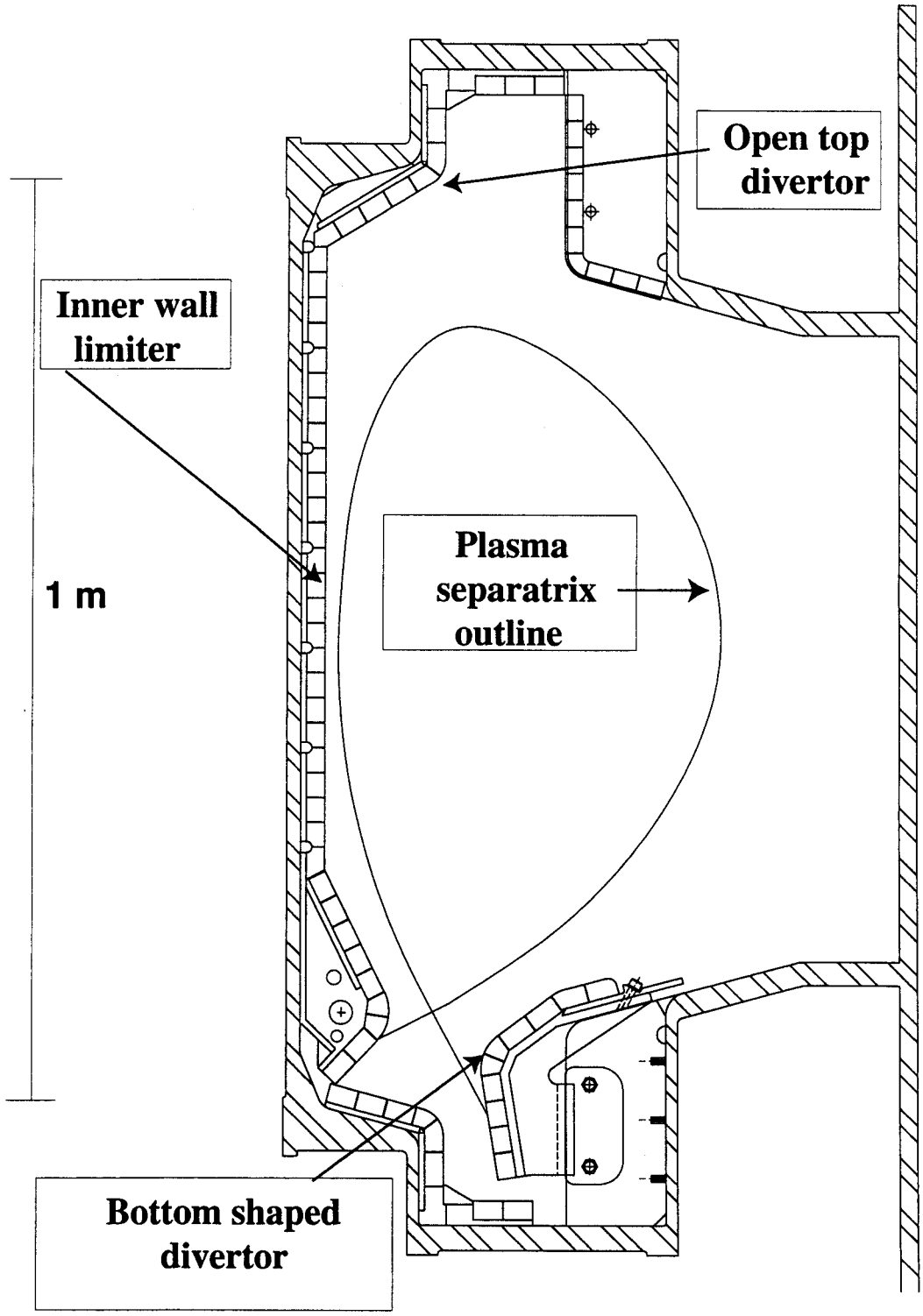

Fig. 1-2: Poloidal view of the Alcator C-Mod vacuum vessel. Plasma can be diverted towards the top open divertor, towards the bottom shaped divertor, or limited on the inner wall.

(ITER), which is envisioned to be the next major step in the world's tokamak fusion program, tungsten was chosen as the main divertor target material[1] [9]. Hence, Alcator C-Mod, with its molybdenum walls, presents an opportunity to evaluate a high-Z material under reactor relevant conditions, as is the case at least in the C-Mod divertor. It should be noted that molybdenum itself is not a reactor candidate material because, unlike tungsten, is susceptible to long term activation. However, molybdenum can be considered as prototypical of tungsten as far as erosion and deuterium retention are concerned.

This thesis is devoted to spectroscopic study and identification of all important molybdenum sources in Alcator C-Mod and of the plasma parameters that enhance molybdenum production and subsequently of conditions under which production is minimum. It also aims to understand the molybdenum generation mechanisms and investigate the effectiveness of the plasma screening of produced molybdenum from the core plasma. Differences in source rates and screening between diverted and limited discharges are also investigated.

In Chapter 2 the visible spectroscopy system, which is the basis of the molybdenum source measurements, is described, together with some of the C-Mod diagnostic systems that are relevant to the thesis. The spectroscopic method used for the determination of impurity sources is presented.

Chapter 3 reports the experimental findings on molybdenum source rates from various Alcator C-Mod surfaces. The dependence of source levels on plasma parameters and on RF power as well as correlations with core molybdenum levels are investigated. The relative contribution of the various molybdenum sources to the plasma core molybdenum content is discussed. The mechanisms believed to contribute the most to the molybdenum generation are described.

Chapter 4 discusses the effectiveness of boronization as a surface conditioning method which reduces the molybdenum source rates and core concentration. Differences in the rate of removal of the boron layer from the various surfaces are inferred from

---

[1] CFC will also be used in the ITER divertor mainly due to its capability to handle very high thermal loads. The majority of the first-wall will be clad with beryllium, primarily due to its low-Z atomic number, its good oxygen gettering properties, and its ability to protect underlying first-wall structures from off-normal thermal loads [9].

measurements in the molybdenum source rates.

In Chapter 5 measured molybdenum source rates from the outer divertor are compared to rates calculated from a standard physical sputtering model utilizing divertor Langmuir probe data. The model is described in detail and it is used to obtain information on the type of plasma discharges that contribute the most to the divertor erosion. Net erosion measurements, made during the 1995-1996 run campaign with a set of appropriately modified molybdenum tiles, are compared with a campaign-integrated net erosion prediction, based on the model.

Finally, in Chapter 6 the major findings of this thesis are summarized and measures that could reduce the observed molybdenum source rates are discussed.

Chapter 2

Experiment and Plasma Diagnostics

There are many diagnostics used to observe tokamak plasmas and they vary according to the nature of the quantity being diagnosed. In general, all diagnostics fall into three major categories of measuring either radiation, or electromagnetic fields, or particles. The diagnosis of molybdenum is realized via measurements of radiation. However, correct interpretation of the data requires the use of a number of other diagnostic systems. In this chapter, an extensive presentation of the visible spectroscopy system, used for the acquisition of the majority of the data presented in this thesis, is followed by a brief presentation of all other principal C-Mod diagnostics of interest, and a description of the spectroscopic technique used for the determination of impurity sources.

2.1 Visible Spectrometer

2.1.1 The instrument

Most of the deuterium and impurity emission in the plasma edge and scrape-off layer (SOL) occurs in the visible region of the spectrum. It is therefore important to have spectroscopic diagnostics capable of monitoring and quantifying this emission. In Alcator C-Mod, a multiple-spatial-input, absolutely calibrated spectrometer is used to monitor the wavelength region from about 250 nm to 1200 nm. This device, referred to as the Chromex spectrometer, after the company supplying the basic instrument, is used as the baseline diagnostic for the characterization of impurities in the edge. This is the

instrument used for the measurement of the molybdenum source levels that are presented in this thesis.

The Chromex spectrometer, of the asymmetrical Czerny-Turner configuration [10], has a focal length of 250 mm. One of three available diffraction gratings is used, depending on the wavelength resolution, or equivalently on the spectral band width, desired. The basic characteristics of the three gratings (600 mm^{-1}, 1200 mm^{-1}, 1800 mm^{-1}) are shown in Table 2-1 [11, 12]. All molybdenum data have been obtained with the 1200 mm^{-1} grating. The system has a straight entrance slit with a height of 9.8 mm and a width adjustable from 10 μm to 2 mm. Light from 16 optical fibers (14 until the summer of 1997) is focused onto the entrance slit and then imaged through the system onto a CCD at the exit plane. The system has a nominal *f* number of "*f* /4.0". The *f* number for circular entrance apertures is defined as the ratio of the focal length to the diameter of the aperture. For an *f* /4.0 system this ratio is 4.0 and it corresponds to a $\tan^{-1}(0.125) = 7.13^{\circ}$ acceptance angle. This definition is extended to geometries like the one found in the Chromex spectrometer. The *f* number is then defined as [10]

$$f = (\pi F^2 / 4A)^{1/2} \tag{2-1}$$

where, for the specific case, F is the focal length and A the area of the square grating. The knowledge of the *f* number is important for the design of the collection optics. The angle of acceptance is the practical variable of interest. The spectrometer's light transmission as a function of the angle has been measured for Chromex [13] and the result is shown in Fig. 2-1. The FWHM of the curve gives an acceptance angle of $\sim \pm 7^{\circ}$ which is what is expected for an *f* /4.0 system.

The CCD is an 1152x1242-pixel thermo-electrically cooled array operating in a frame

Grating (mm^{-1})	Blaze wavelength (nm)	Band width (nm)	Unbinned Resolution (nm)
600	500	141.0	0.27
1200	330	72.8	0.13
1800	250	45.5	0.08

Table 2-1: Blaze wavelength, spectral band width, and nominal resolution at 546 nm for the three gratings using a 20 μm slit width [11, 12].

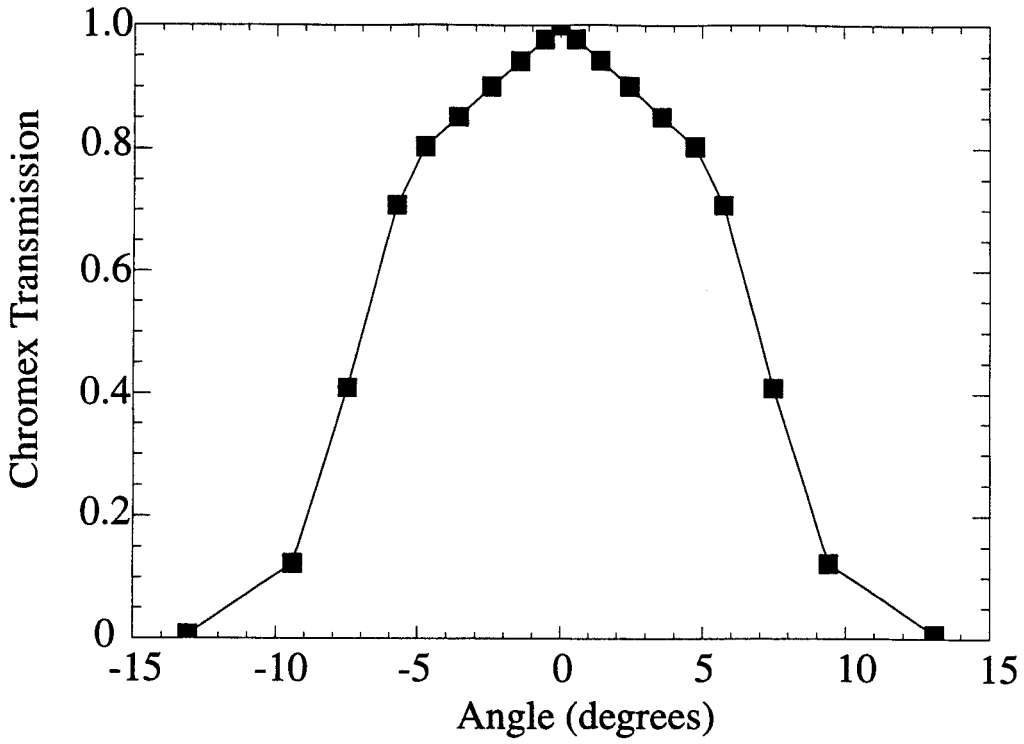

Fig. 2-1: Spectrometer's light transmission as a function of the angle from the normal to the entrance slit [13].

transfer mode with a 16 bit/430 kHz ADC. Cooling of the CCD to -32 degrees centigrade reduces the thermally induced charge to approximately 0.2 % of the dynamic range, for the standard data acquisition settings (56 ms exposure time). Under the frame transfer mode only the top half frame (576x1242) of the detector is illuminated and the data are subsequently shifted to the lower frame to be read out and digitized while illumination of the top frame continues. Of these pixels, the 1242 pixels row dimension is parallel to the spectrally resolving dimension of the instrument. The 576 pixels column direction is hardware-accumulated into 16 channels-bins corresponding to the 16 input fibers viewing various plasma edge locations, thus providing spatial resolution. The binning configuration was chosen based on the notion of minimization of the interchannel cross-talk without considerable reduction on the signal level. With the same logic in mind, 4 pixels in between bins were discarded. The above selections came as a result of illuminating all 16 fibers simultaneously with a continuous source. The result, together with the selected bin configuration, is shown in Fig. 2-2. (In the original 14-input fiber

configuration all bins were comprised of 41 rows while the two last rows were discarded). The solid line between bins in Fig. 2-2 represents the 4 pixels wide zone that is not processed. In Fig. 2-3 a close-up of the region between two of the bins (4 and 5) is shown. The signal in the discarded region is at or below the 0.5 % level compared to the peak signal in the adjacent bins. Further investigation of the effect using more of the dynamic range of the spectrometer and actual data during plasma operation, in which one of the bins was not connected intentionally to any of the optical fibers, have shown the interchannel cross-talk in our measurements to be at the 0.5 % level. For the molybdenum data acquisition, the cross-talk level was typically comparable with the thermally induced background and therefore did not constitute a significant source of error. The spectrometer's time resolution, which is mainly limited by the data readout time [10,12], was 45 ms with the 14-input fiber system and increased to 56 ms with the 16-input fiber configuration.

The spectrometer is physically located in the Alcator C-Mod cell, next to where the tokamak is. It is therefore inaccessible during plasma operation. However, it is continuously monitored and controlled with a computer located in the Alcator C-Mod control room. The system has been fully automated in a way that the spectrometer can be run unattended as long as a grating, a central Chromex wavelength, and a slit width have been chosen. Changes in the above three parameters can be made easily in between shots, and hence all the operational regimes of the spectrometer are accessible at any time.

2.1.2 System Calibration

Wavelength calibration

The absolute wavelength calibration of the system was described analytically by Lumma [12] and only its basic features will be reproduced here. The extent of the spectral region in which each of the three gratings is operational depends on the resolution of each one of them. The 600 mm^{-1} grating, with the lowest resolution, was calibrated from approximately 250 nm up to 1310 nm. The other two were also calibrated down to 250 nm but up to different wavelengths: the 1200 mm^{-1} grating up to 1090 nm while the 1800 mm^{-1} up to the H_α line at 656 nm. For the calibration, low-pressure mercury and hydrogen lamps were used. For the long wavelength calibration of both the 600 mm^{-1} and

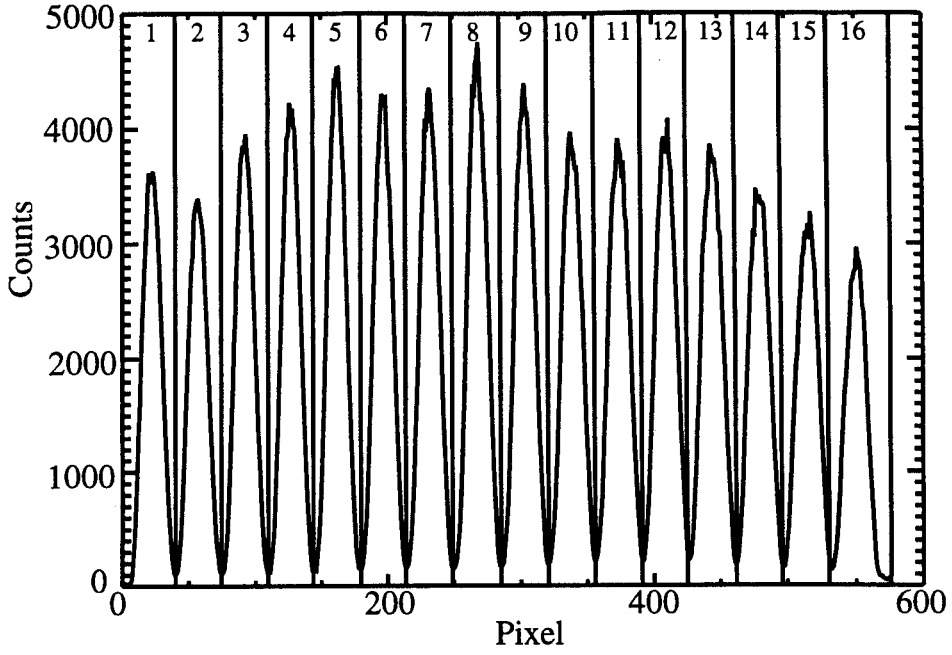

Fig. 2-2: Binning of the 576 CCD pixels in the spectrometer's spatially resolving dimension. The solid line between bins represents the 4 pixels wide zone that is not processed.

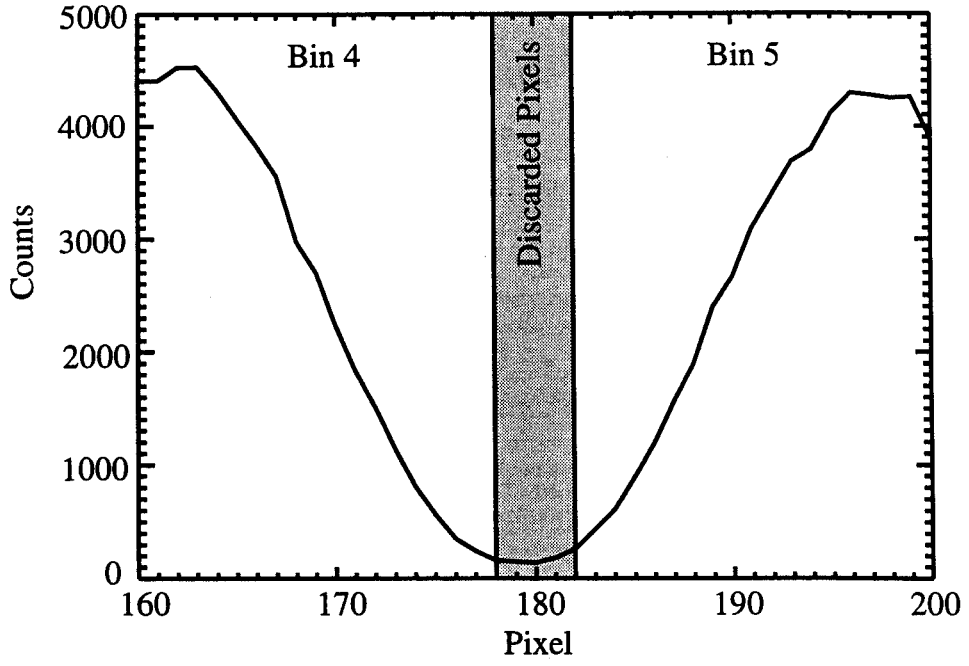

Fig. 2-3: A close-up of the CCD region between two of the bins (4 and 5). During plasma operation, any signal measured in the shaded region is discarded.

1200 mm^{-1} gratings, second and third diffraction orders of known lines were utilized.

The calibration was performed at one of the central CCD bins with the assumption that the calibration is independent of bins. It basically involves two steps for each of the gratings. In the first step, the actual spectral wavelength mapped onto the detector center was determined, for a given setting of the spectrometer center wavelength. This was accomplished by placing the peaks of known spectral lines from the calibration lamps at the center of the CCD and recording the corresponding spectrometer settings. In the second step, the dispersion (nm/pixel) of the different gratings was measured at the center of the detector as a function of wavelength. The combination of the information obtained from the two steps produces a mapping between detector pixels and spectral wavelengths for a given spectrometer center wavelength setting.

Intensity calibration

A 150-Watt light source (made by Labsphere, Inc, model URS-600) which emits continuous radiation, through a circular opening, has been used for the intensity calibration of the spectrometer and the associated collecting optics. The source has a spatially uniform output radiance. Its spectral radiance is known between 300 nm and 2400 nm (Fig. 2-4) which practically covers all the wavelength range of interest for the Chromex spectrometer. For a given grating, the calibration of the spectrometer is performed at specific Chromex setting of central wavelengths. To increase the accuracy of the calibration measurements it is important to use the whole dynamic range of the system. This in return requires that each of the 16 input fibers be calibrated separately since otherwise there would be significant errors due to interchannel cross-talk. For each of the fibers, or equivalently for each of the CCD bins, a measurement is taken with the lamp switched on and one with the lamp turned off, in order to subtract the dark current rate. The above procedure leads to a calculation of the inverse spectral sensitivity as a function of wavelength for each of the 16 bins. This is given as the ratio of the spectral radiance ($mW/cm^2/\mu m/sterad$) of the continuum light source to the measured count rate. Fig. 2-5 shows the inverse sensitivity for bin 8 as a function of pixel (or equivalently wavelength), for the 1200 mm^{-1} grating and a central wavelength of 405 nm, which are the typical spectrometer settings when molybdenum emissions are monitored (see Section

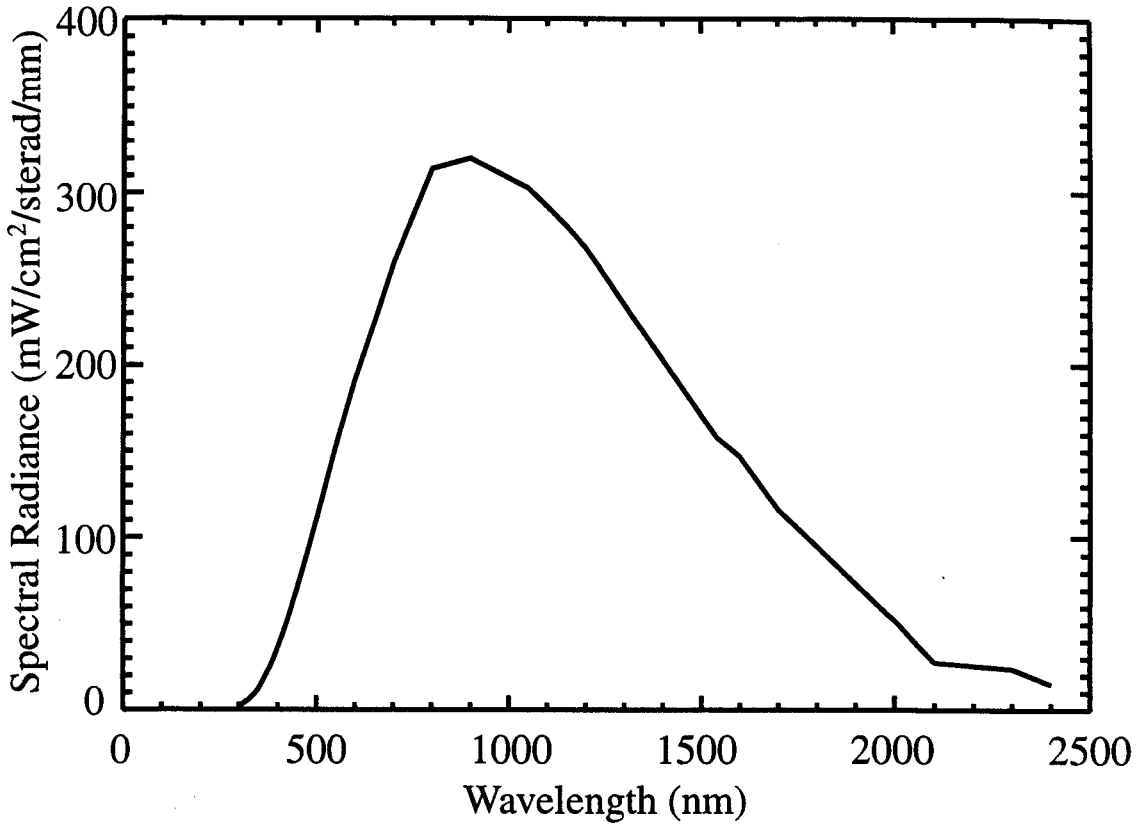

Fig. 2-4: Spectral radiance of the lamp used for the absolute intensity calibrations.

2-3). A 20 μm slit was used for these experiments. The shape of the inverse sensitivity curve is not constant as a function of Chromex wavelength setting and from the one grating to the other, which is why a separate calibration is used whenever the spectrometer is used in a different spectral region. In Fig. 2-6 the inverse sensitivity data from the same calibration are now plotted as a function of bin for the central pixel. It can be seen that the spectrometer's sensitivity is, in general, higher at the center of the CCD and decreases towards the edges.

Only first order diffraction was included in the calibration. Higher order diffraction would, at most, increase the value of the inverse sensitivity by a few percent in certain wavelength regions [12]. However, around 400 nm, where the molybdenum lines of interest are observed (see Section 2-3), there is no such concern since the lamp radiance decreases fast below 300 nm.

The intensity calibration is not necessarily performed with the same entrance slit as the

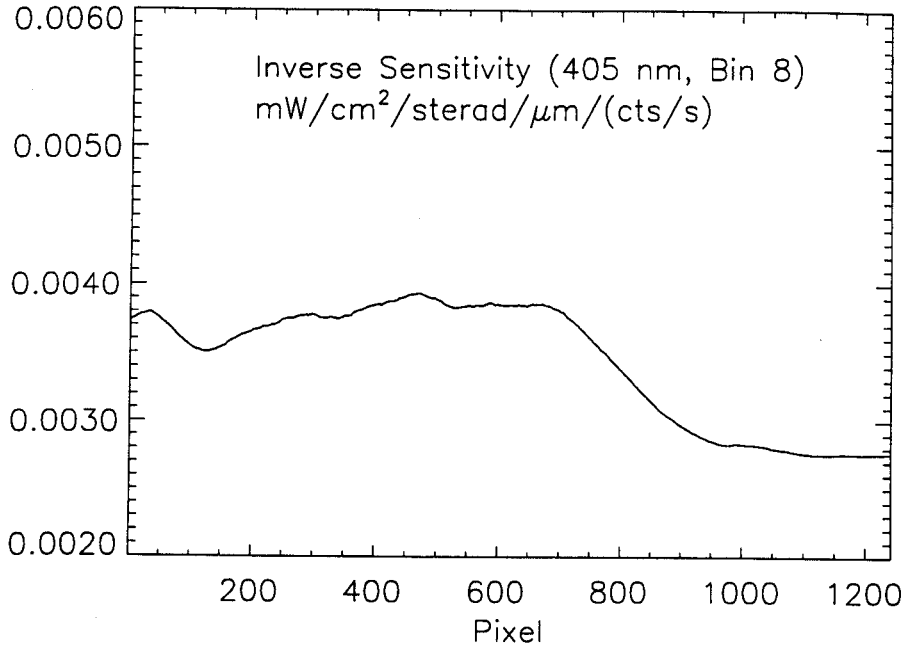

Fig. 2-5: Inverse sensitivity for bin 8 as a function of pixel. The data were taken with the 1200 mm^{-1} grating, at 405 nm, and with a 20 μm entrance slit. The wavelength corresponding to pixels 1 and 1242 is 369.5 nm and 439.7 nm respectively.

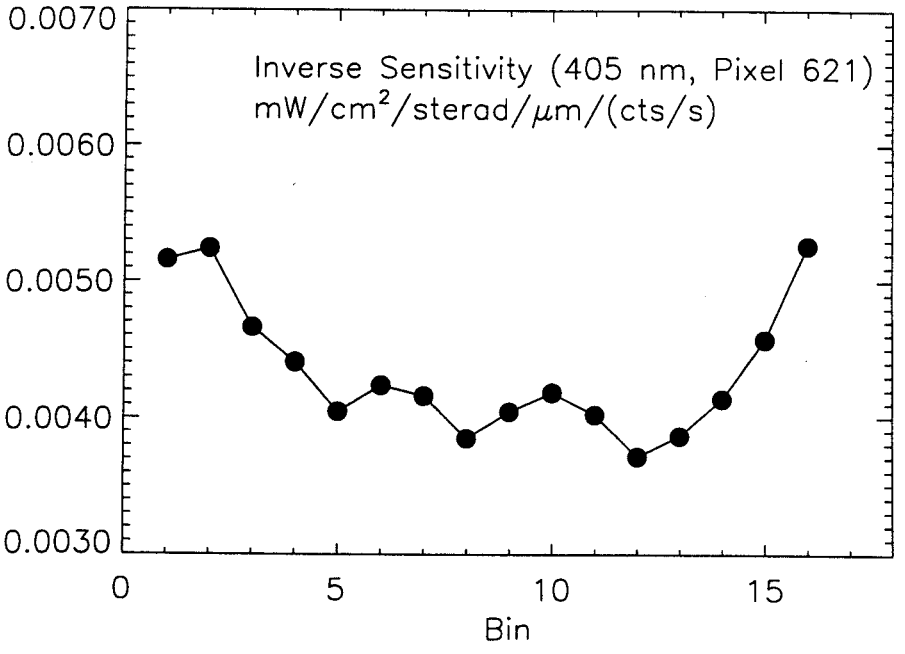

Fig. 2-6: Inverse sensitivity as a function of bin at 405 nm, with a 20 μm entrance slit, and the 1200 mm^{-1} grating.

one used during data acquisition experiments. This is prompted by the frequent need to increase the count rate without simultaneously increasing the dark current, as would be the case if the exposure time during calibration would increase too much. This effect has to be calculated since the slit width is also occasionally varied even in between shots, depending on the strength of the signal of interest (typical slit width values during molybdenum data acquisition range from 20 μm to 80 μm). For this reason, the system's response to changes in the slit width was investigated. The result for bin 8 and pixel 621 for a central wavelength of 405 nm and the 1200 mm^{-1} grating is shown in Figs. 2-7 and 2-8. In Fig. 2-7, the intensity normalized to the signal for the 20 μm slit is plotted versus the slit width for slit widths up to 500 μm. Figure 2-8 shows a subset of these data for slit widths in the range 10 to 25 μm. As seen in the two figures the signal is linear with the slit width from 10 μm up to about 100 μm. Above about 300 μm, further opening of the slit has no effect on the measured signal due to the fact that the slit opening is larger than the fiber diameter (400 μm). Below 10 μm, the signal is practically zero. For most of the slit widths, for which the data are plotted in Figs. 2-7 and 2-8, only the intensity at the central region (bin 8 and pixel 621) of the CCD was measured. However, for the 12 and 20 μm slits, the intensity was measured at every pixel on the CCD. Taking the ratio of the two signals for all pixels, normalized by their ratio for bin 8 and pixel 621, it allowed calculating the slit effect as a function of the location on the CCD.

To complete the intensity calibration, the same lamp is used to measure the light transmission of the collection optics (lenses and periscopes), and of the relay fibers used to connect certain views with the spectrometer, at the Chromex central wavelengths of interest.

After data acquisition, the information on the optics transmission is used to determine the inverse sensitivity for that optical system by dividing the inverse sensitivity of the input fiber by the transmission of the periscope η_{per}, the transmission of the relay fiber η_{rel}, and the slit factor η_{slit} (intensity normalized to the signal for the 20 μm slit, see Fig. 2-7):

$$\text{Inv. Sensitivity (system)} = \text{Inv. Sensitivity (input fiber)} / \eta_{per} / \eta_{rel} / \eta_{slit} \qquad (2.1)$$

The signal intensity is extracted by simply multiplying the inverse sensitivity of the

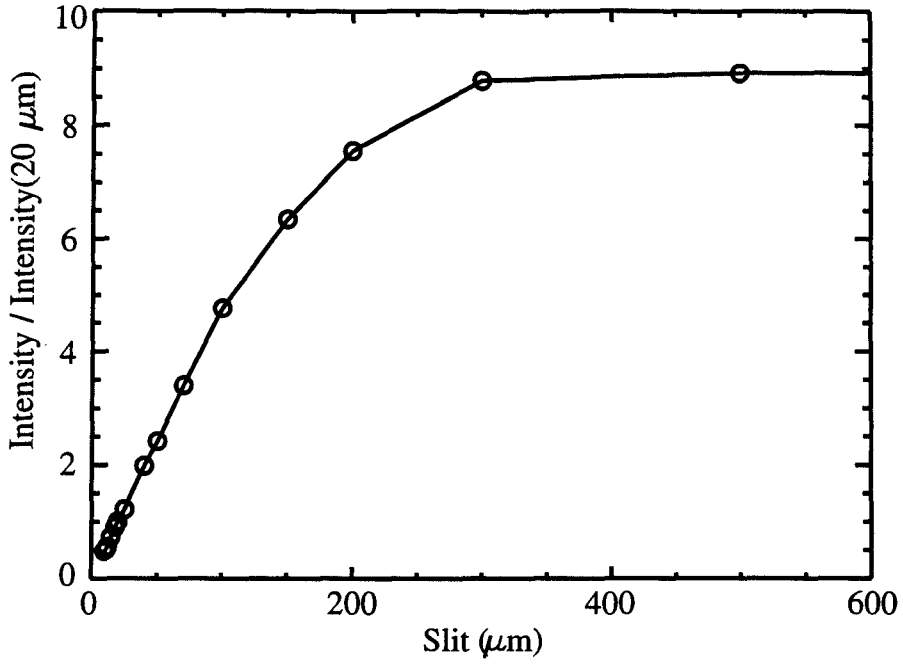

Fig. 2-7: Effect of entrance slit on signal intensity. The signal is normalized to the intensity for the 20 μm slit. The data were obtained with the 1200 mm^{-1} grating at 405 nm for bin 8 and pixel 621.

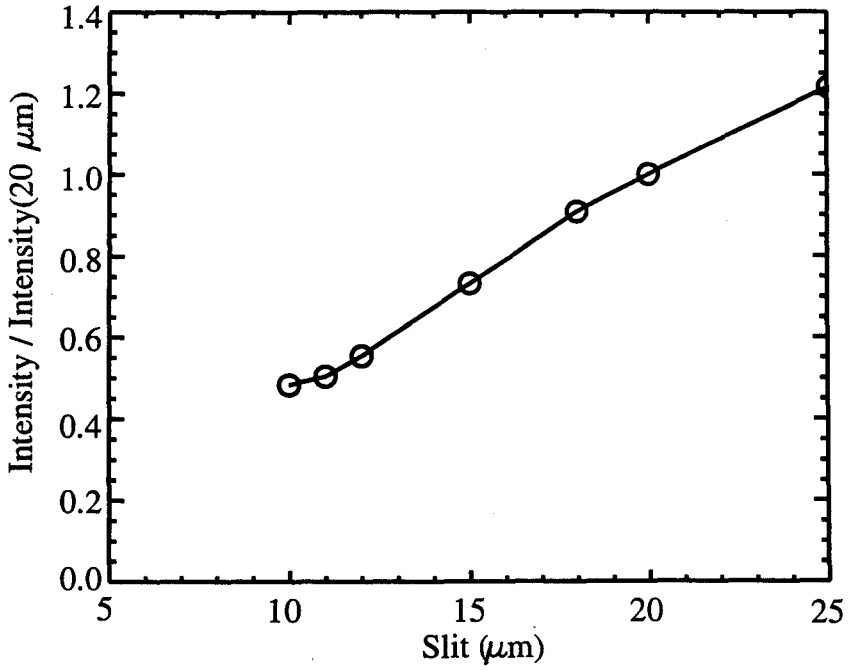

Fig. 2-8: Normalized intensities versus slit width for slits 10 to 25 μm wide. The data are a subset of the data shown in Fig. 2-7.

system with the measured count rate. The spectrometer's central wavelength is chosen to be the same as the one chosen during the intensity calibration. Data collection starts at about 100 ms before the beginning of the plasma discharge, thus providing information on the thermal background, which is subtracted before applying the intensity calibration information.

2.1.3 Available spectroscopic views

A number of collection optics systems are available which enables coverage of most of the surfaces expected to produce measurable amounts of molybdenum. Surfaces systematically monitored include the outer divertor, the inner wall, and, during the 1999 run campaign, the antenna protection tiles. Other available views covered the inner divertor, the antennas, and the outer limiters. Figure 2-9 shows a poloidal cross-section of the tokamak with sketches of all the major views, with the exception of the ones monitoring the antenna protection tiles which are sketched in Fig. 2-10. To have exact knowledge of where the radiation is originating from, the spatial coverage of all fiber views is calibrated by manned entry into the vacuum vessel. The fibers are back-illuminated and the location of the projected spot is recorded. This procedure is repeated before every experimental campaign to ensure proper alignment of the optics.

2.1.4 Detector shielding

During plasma discharges a considerable amount of neutrons is produced. These neutrons interact with the surrounding structure producing a number of highly energetic gamma rays (typically up to 10 MeV). Both neutrons and gamma rays, upon reaching the CCD can interact with it, depositing a considerable amount of energy, and thus producing a charge that will be read from the system just like any other charge produced from real data. This noise appears in the form of spikes in the spectra that can be generally distinguished from real spectral lines. The spikes are thinner than real lines and typically do not appear at the same detector position for two consecutive frames. The noise results from the random form of interaction of neutrons and gamma rays with the detector. However, it was observed that whenever the plasma neutron rate reached values 10^{13} s^{-1} or higher, the number of spikes present in the spectra increased so much that they

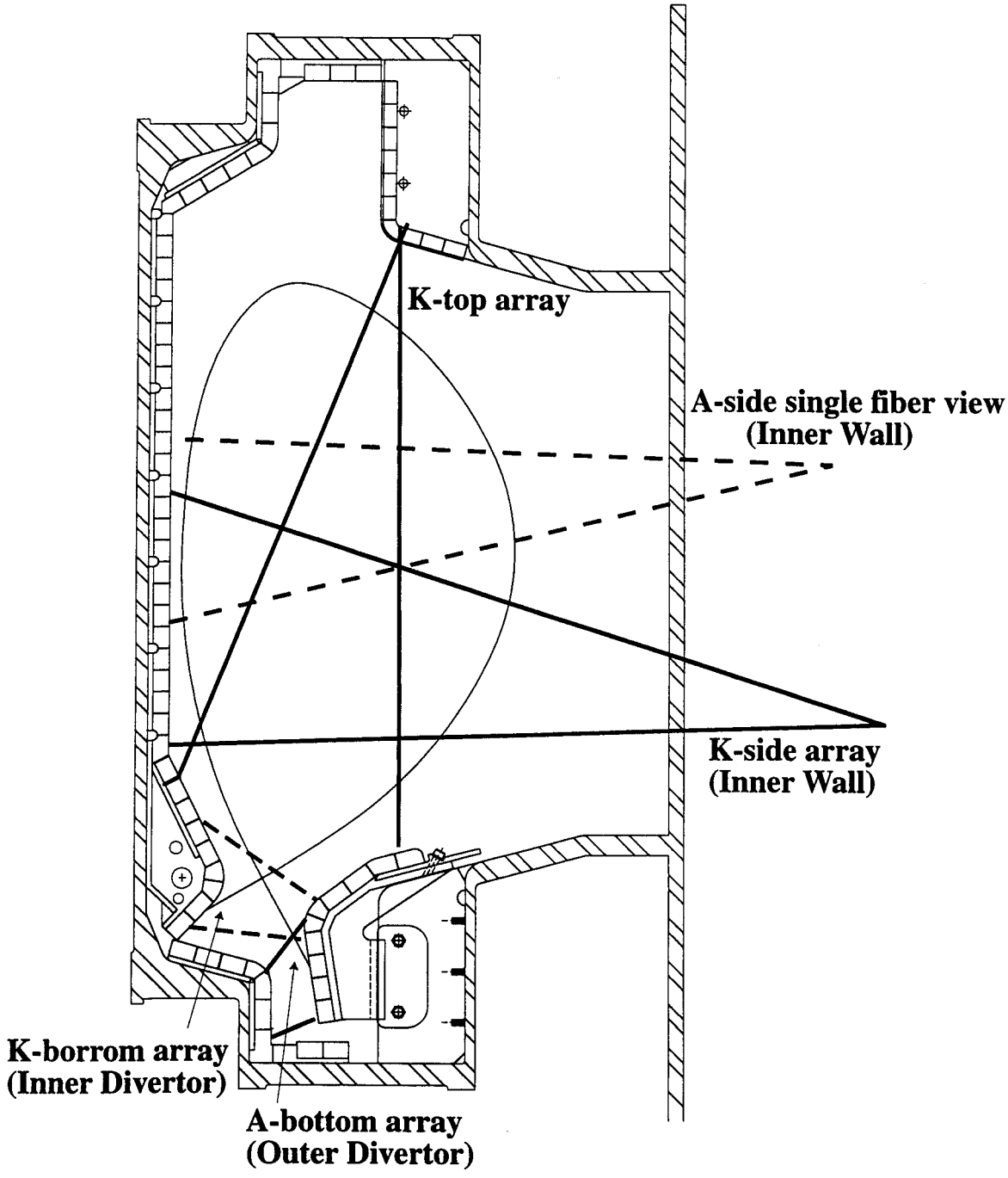

Fig. 2-9: Poloidal cross-section of the tokamak with sketches of all the major views, with the exception of the ones monitoring the antenna protection tiles.

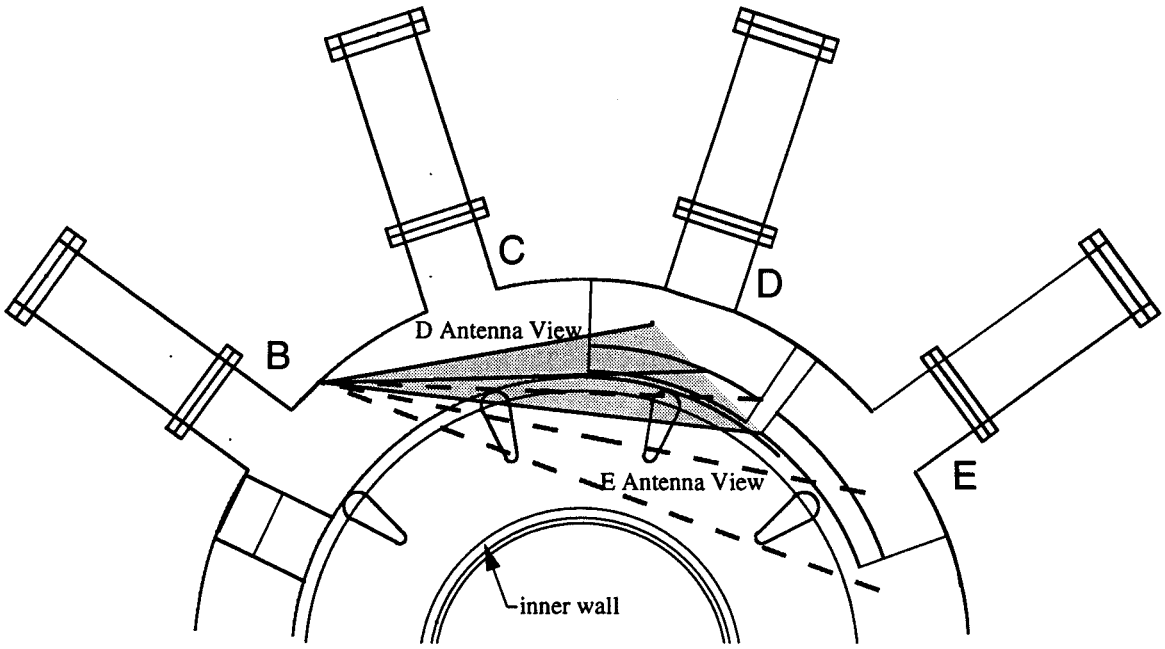

Fig. 2-10: Top view of Alcator C-Mod showing sketches of the D-port antenna view (shaded) and the E-port antenna view (dashed lines).

represented a significant source of error and made correct interpretation of the data extremely difficult. The problem is portrayed in Fig. 2-11 which shows two spectra, of the same spectral region, one taken during low neutron rate and one during high neutron rate.

This situation necessitated the use of shielding material around the CCD that would minimize the interaction of the detector with neutrons and gamma rays. This is in general not a simple problem, especially due to the complicated nature of the interaction of neutrons with matter. A combination of a low Z and a high Z material has to be used since the former are effective against neutrons and the latter against photons. For this reason, the detector was placed inside a rectangular housing, open from the one end, made with blocks of lead borated polyethylene (lead 80 % by mass, boron 1 %). The choice of the specific shielding material was a combination of availability and material properties. Lead, with its high Z atomic number, is always the first choice for shielding against gamma rays. Polyethylene and boron are very effective in slowing down energetic neutrons. Boron has the additional advantage of having a very high (n,α)[1] neutron absorption cross-section but at the same time is an emitter of a 0.48 MeV gamma ray which could possibly contribute to the problem. In principle, one could use a combination of ^{6}Li-enriched lithium doped polyethylene and lead, instead of borated material, due to the absence of any capture gamma rays in the n-^{6}Li interactions.

The "box" enclosing the spectrometer is 16" wide, 14" high, 20" long, and 4" thick. The CCD is placed towards the closed end of the housing to minimize interaction with neutrons and photons. The decision to leave the other side open was taken after observing that stopping the flow of air resulted in an increase in the CCD temperature. The dimensions of the housing were decided after running a number of cases with the Monte Carlo Neutron Photon transport code (MCNP) [14], taking into account the constraints imposed by the size of the spectrometer. The MCNP input file with the Alcator C-Mod geometry was provided by Fiore [15]. For each case 10^5 particle histories were run to ensure that the uncertainty in the results was low. Figures 2-12 and 2-13 give the MCNP-calculated neutron and photon fluxes per starting neutron respectively, with and without shielding, at the location of the CCD and as a function of the corresponding particles'

[1] $^{10}B + n \rightarrow {}^7Li + \alpha + \gamma\,(0.48\ MeV)$

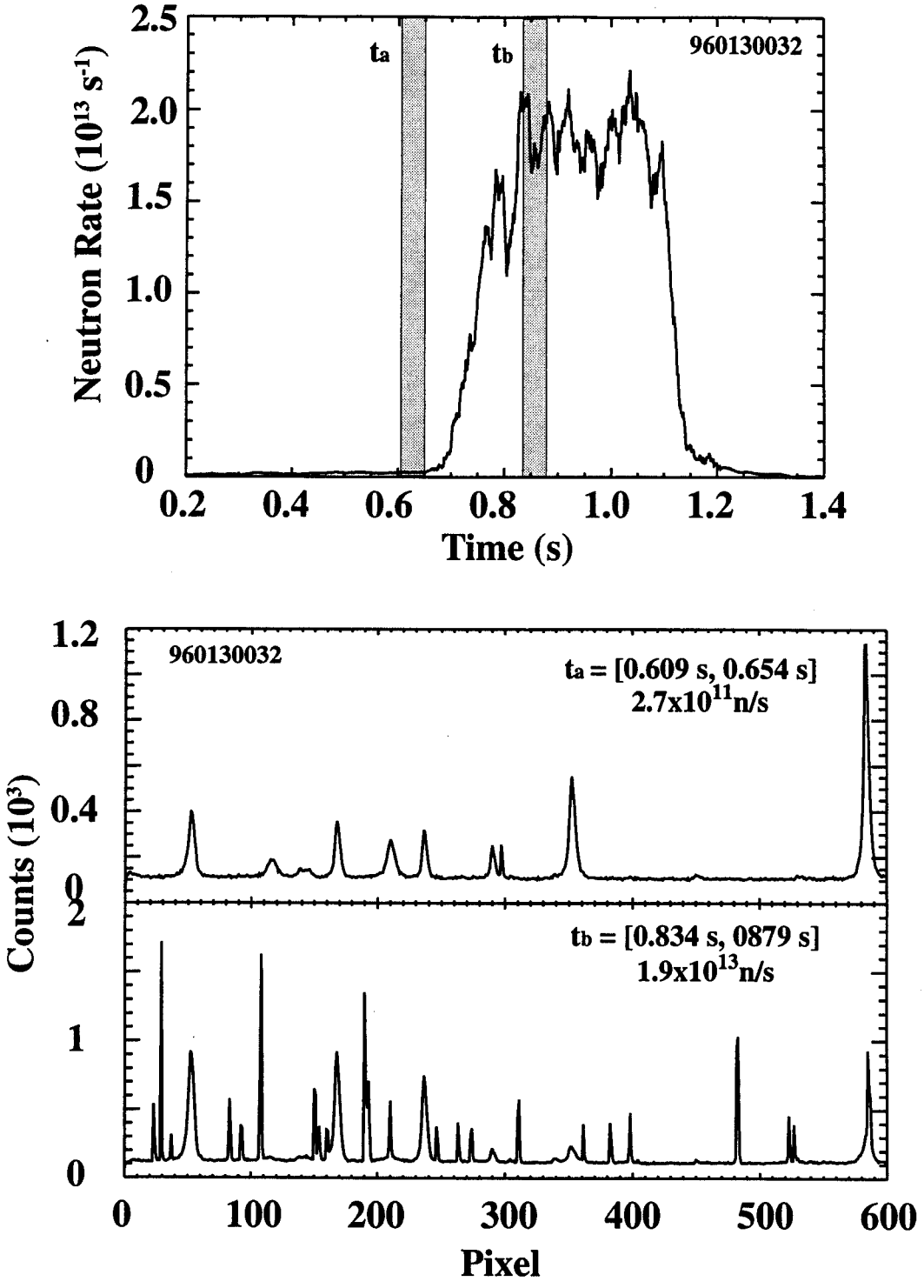

Fig. 2-11: Fusion neutron rate for plasma discharge 960130032 (top panel). Typical spectra, of the same spectral region, taken with the Chromex spectrometer (bottom panel) during the time slices indicated in the neutron rate time history. There is only one spike (around pixel 300) when the neutron rate is low but a significant number of them appear during the high neutron rate period.

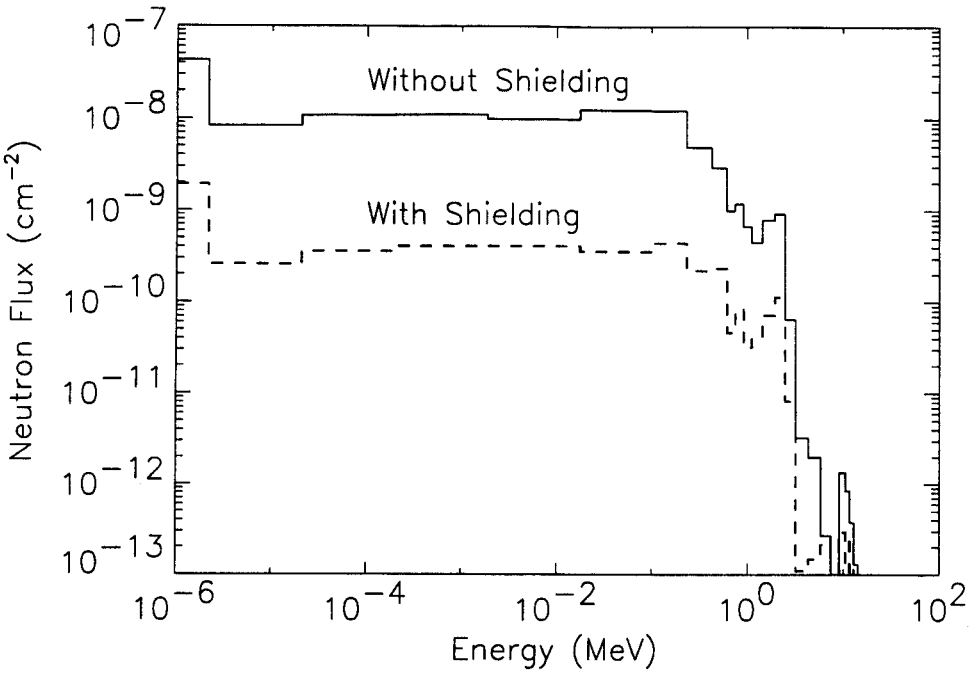

Fig. 2-12: Neutron flux per starting neutron at the CCD, with and without shielding, as calculated by the MCNP.

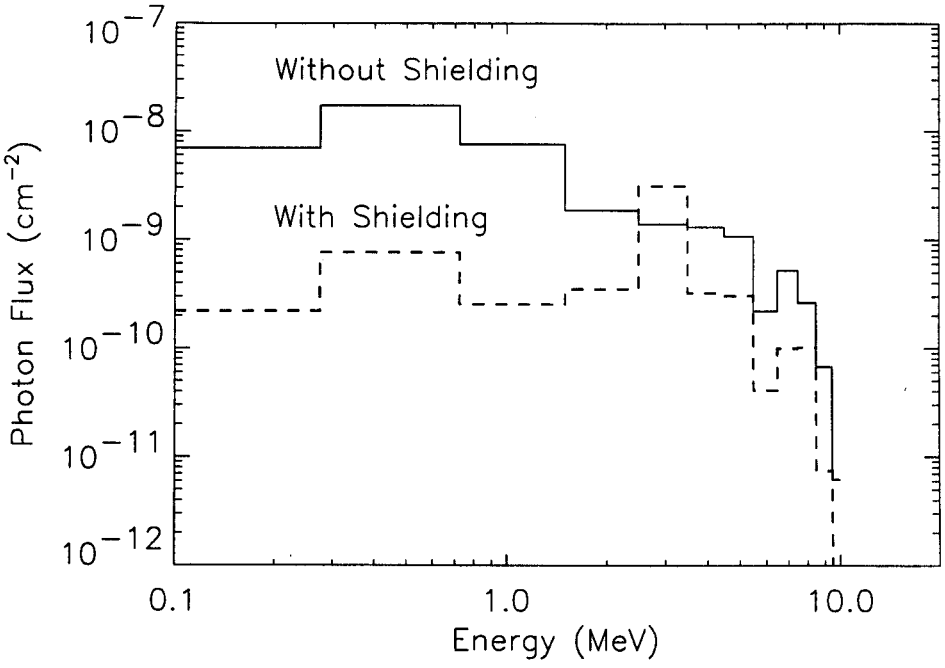

Fig 2-13: Photon flux per starting neutron at the CCD, with and without shielding, as calculated by MCNP.

energy. For neutrons, the total flux per starting neutron decreased from 1.2 x 10^{-7} cm^{-2} to 5. x 10^{-9} cm^{-2} or, if a 10^{13} s^{-1} fusion neutron rate is assumed, from 1.2 x 10^{6} cm^{-2} s^{-1} to 5. x 10^{4} cm^{-2} s^{-1}. The decrease in the photon flux per starting neutron was smaller: from 3.8 x 10^{-8} cm^{-2} to 5.6 x 10^{-9} cm^{-2}. Thus the MCNP code predicted a reduction in the neutron and photon fluxes of 24 and 6.8 respectively. However, the addition of shielding was found to reduce the total (i.e. for all bins) number of spikes by a factor of two or three, in discharges with comparable neutron rates (1.7 x 10^{13} s^{-1}). The smaller than expected reduction in the number of spikes should be mainly attributed to the differences in the shielding structure between the model and the experiment. In the model the housing was assumed to be uniform. In reality a hole in the shielding was necessary for a cable to connect the CCD with the spectrometer's controller. Smaller openings in the structure resulting from the not perfect alignment of bricks could also contribute to the difference between the two results. Overall, and despite its smaller than initially estimated effectiveness, the presence of the shielding facilitates considerably the analysis of data.

2.2 Plasma Diagnostics

In this section, all C-Mod diagnostics that are important in the analysis of the data presented in this thesis will be briefly described. Diagnostics that are not used will not be included in the presentation even if they are measuring the same physical properties as the systems described.

2.2.1 Electron Temperature and Density Core and Edge Diagnostics

The electron temperature and density measurements at the inner and outer divertor region are performed with a set of domed Langmuir probes [16] that are embedded in the tiles (see Fig 5-3 for the outer divertor array). The n_e and T_e profiles along the outer target, that are necessary, for the spectroscopic determination of the molybdenum sources (see section 2.3) as well as for the modeling of the outer divertor molybdenum sources (see Chapter 5) are obtained from these probes.

A two-color heterodyne interferometer [17] is the basic system for providing electron density profile measurements in the C-Mod main plasma. It consists of a CO_2 (10.6 μm)

laser diagnostic beam and HeNe (0.643 μm) laser vibration-compensation beam. It uses a number of diagnostic chords running vertically through the plasma. Each of the chords provides a line integrated electron density. These measurements are inverted to obtain electron density profiles and the volume-averaged core plasma density.

An electron cyclotron emission diagnostic is used for the electron temperature profiles [18]. Such a system measures the intensity of blackbody emission at various frequencies and uses the known variation of the toroidal magnetic field with major radius in the tokamak to localize the emission in the radial dimension.

2.2.2 Plasma Core Molybdenum Diagnostics

X-ray Spectrometer

A crystal five-radial-chord, independently spatially scanable, high resolution x-ray spectrometer array (Hirex) is used in Alcator C-Mod for observing line emissions in the 2.8-4.1 Å region of the spectrum [19]. Each of the spectrometers consists of a quartz crystal and a position-sensitive proportional counter detector. Spectra are typically collected every 50 ms during a discharge. One of the five spectrometers is always allocated, among other things, to the observation of a neon-like molybdenum (Mo^{+32}) line at 3.74 Å. The absolute calibration of the spectrometers is based on nominal value information of crystal reflectivity, spectrometer geometry, detector sensitivity, and Be window transmission. In addition to these spectrometers there is a tangentially viewing x-ray spectrometer (Hirex Jr.) with a 20 ms time resolution which also monitors systematically the 3.74 Å molybdenum line. This instrument is not independently calibrated, and for the purpose of calculating the core molybdenum concentration it was cross-calibrated [20] to the second of the radially viewing spectrometers, taking into account the difference in the observation line of sight. To calculate the core molybdenum density from the measured molybdenum brightness, information on the electron density and temperature profiles is employed.

Multi-Layer Mirror Polychromator

The core impurity content of molybdenum could also be measured, at least until the beginning of 1998, using a photometrically calibrated (± 20 %) multi-layer mirror

(MLM) based, XUV polychromator [21]. This low resolution system, also known as the Moly Monitor, had a fixed radial chord through the center of the plasma and was configured to simultaneously measure, with approximately 1-2 ms time resolution, specific emissions of the molybdenum spectrum in the 30 to 40 Å, 60 to 85 Å and 110 to 140 Å wavelength regions. Specifically, for the measurement of the molybdenum concentrations in the plasma, a 127.8 Å sodium-like molybdenum line (Mo^{+31}) was used, with the underlying assumption of no other strong lines present in the bandpass of the MLM instrument [21, 22]. The validity of the assumption becomes questionable at high plasma density operation ($\overline{n_e} \geq 1.8 \times 10^{20}$ m^{-3}). This is due to the typically low concentration of molybdenum in the plasma at such densities which means that the signal from other lines becomes comparable to the signal from the molybdenum line of interest [22].

2.3 Spectroscopic Determination of Impurity Sources

Spectroscopic determination of impurity influx from tokamak surfaces has been widely used to determine C influx [23,24]. The study of high-Z materials with this method is somewhat limited. Two examples can be found in Refs. [25] and [26].

The spectroscopic determination of the molybdenum source rates was made possible by monitoring a neutral molybdenum line at 386.4 nm through the available collection optics. This line is a member of a MoI triplet (λ = 379.8, 386.4, 390.2 nm), the brightest molybdenum lines observable in the operating range of the visible spectrometer. These three lines correspond to transitions to the ground state of the molybdenum atom. In Table 2-2 the experimentally observed Landé factor, the spontaneous transition probability A_{km}, and the quantum numbers for the total orbital angular momentum L, total spin S, and total angular momentum J are given for the upper level of each of the transitions [27,28].

A typical spectrum of the MoI triplet spectral region, observed through the outer divertor periscope (see Figs 2-9 and 3-17), is shown in Fig. 2-14. It is evident that the simultaneous appearance of the three lines facilitates the indisputable identification of the

Wavelength (nm)	G	$A_{km}(10^6\ s^{-1})$	L	S	J
379.8	1.736	68.97	1	3	4
386.4	1.892	62.37	1	3	3
390.2	2.299	61.65	1	3	2

Table 2-2: Landé factor g, spontaneous transition probability A_{km}, and quantum numbers for the total orbital angular momentum L, total spin S, and total angular momentum J for the MoI triplet (λ = 379.8, 386.4, 390.2 nm).

molybdenum line of interest even in cases where the molybdenum emission is not very strong. The selection of the 386.4 nm line, among the three in the triplet, was made because it had the minimum spectral interference from other lines, deuterium or impurity, in the region. Specifically, the 379.8 nm molybdenum line overlaps with the 379.7 nm deuterium Balmer ($9 \rightarrow 2$) line. Using it requires estimating the contribution, on the measured signal, of the 379.7 nm deuterium line, based on the measured intensities of other deuterium Balmer lines (see Fig. 2-14) and their known relative intensities. The error in the measured molybdenum source rate would have obviously been larger if the 379.8 nm line was used. On the other hand, the 390.2 nm line is less intense than the 386.4 nm line (the ratio of relative intensities is approximately 5 to 7), and the measurements would have also included greater degrees of uncertainty. It should be noted that since the lines of interest are actually at the ultraviolet, quartz windows and fibers were used to minimize the transmission losses.

The neutral molybdenum particle influx, Γ, can be derived from the measured intensity I of the MoI line, using the relation (see Appendix A) [25, 29]:

$$\Gamma = 4\pi I\,(S/XB), \tag{2.2}$$

where (S/XB) is the number of molybdenum ionizations per emitted photon. S is the ionization rate, X is the excitation rate, and B the branching ratio, which is defined as the ratio of the Einstein coefficient A_{km}, describing the probability for the spontaneous transition of an electron from an upper energy level k to a lower energy level m, to the sum of the Einstein coefficients $\sum_m A_{km}$ for all transitions originating from the same

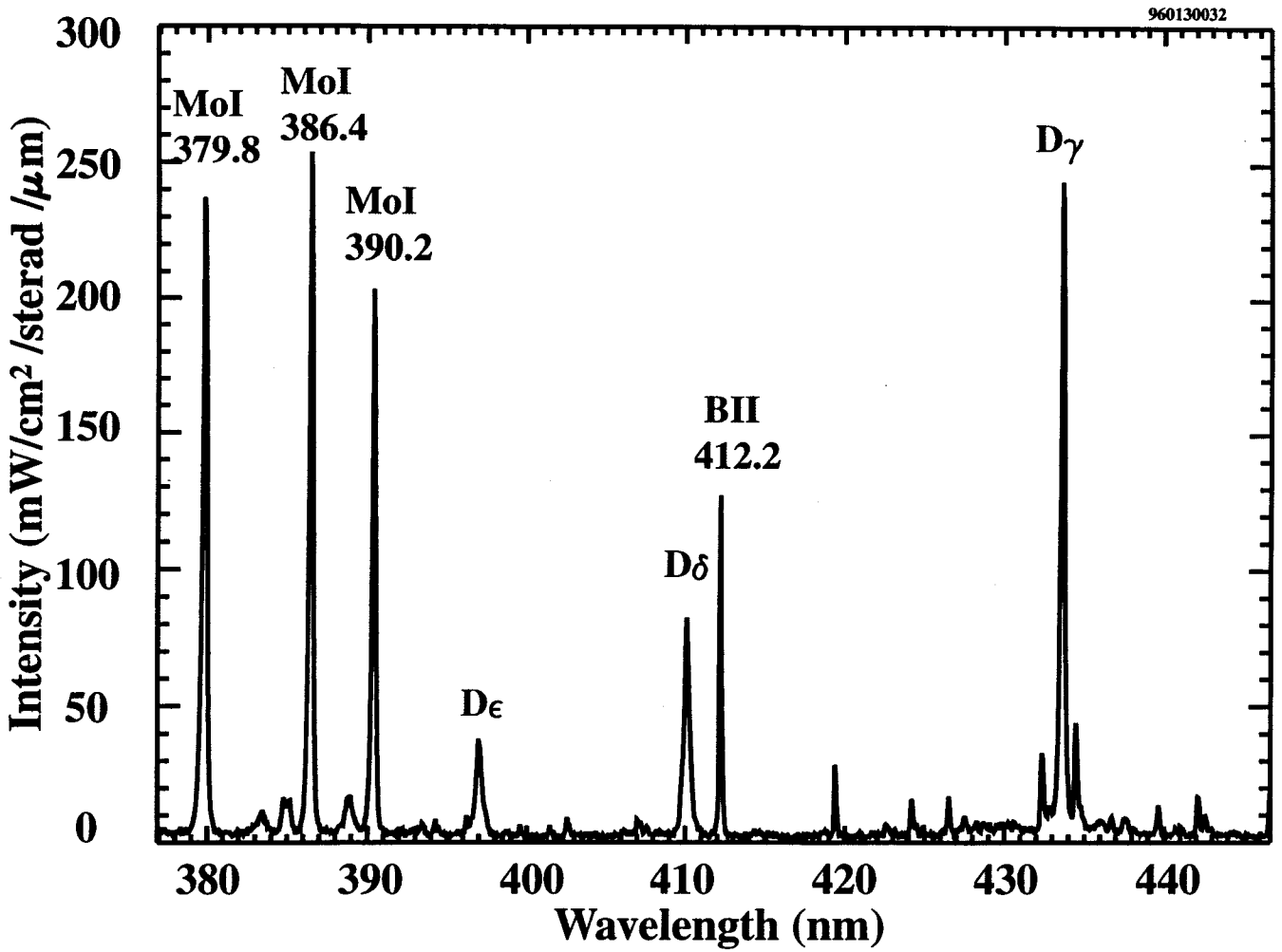

Fig 2-14: Typical spectrum taken from a divertor view. The MoI triplet lines are clearly observed. Simultaneous observation of other lines (e.g. deuterium Balmer series, BII) is possible.

upper state. In Eq. 2.2 the intensity I is in units of photons per unit time, unit area, and unit solid angle. In Fig. 2-14 the measured signal is in units of power per unit area, unit solid angle, and unit wavelength. The intensity, I, is obtained by integrating the signal below the line of interest and by multiplying with the inverse of the photon energy $1/E_\nu = \lambda/(h\,c)$, where λ is the photon wavelength and h and c the Planck and speed of light constants respectively. Eventually, the molybdenum source rate from the various surfaces is calculated by multiplying the molybdenum influx, Γ, with the appropriate area, as will be described in more detail in Chapter 3.

Equation 2.2 is valid as long as a) recombination of ions within the plasma is negligible and b) all impurity atoms are ionized within the field of view [24, 25]. The first condition is typically satisfied in the Alcator C-Mod (and all tokamaks) since the temperatures observed in the plasma boundary are sufficiently high that impurities entering from the various surfaces are rapidly ionized through several ionization stages (T_e > ionization potential I, I = 7.1 eV for neutral molybdenum). Of course, at high plasma densities ($\overline{n_e} \geq 1.7\times10^{20}\ m^{-3}$ for 800 kA Alcator C-Mod ohmic plasmas [16]) a distinctive edge plasma regime is observed in divertor tokamaks (''detachment''[2]), which is characterized by electron temperatures lower than 5 eV and where recombination starts becoming very important. Equation 2.2 may not be valid under these conditions but as it will be shown in Chapter 5 this is of no consequence since the energy acquired by various projectiles in such a cold plasma is small and typically below the threshold for molybdenum sputtering. On the other hand, the second condition for the validity of Eq. 2.2 is realized by monitoring emissions almost perpendicularly to the various surfaces and with the viewing area being larger than the neutral molybdenum ionization length which for typical C-Mod divertor conditions is smaller than 1 mm.

Appropriate *S/XB* data as a function of the plasma electron temperature and density are available for the MoI triplet from the Atomic Data and Analysis Structure (ADAS) database [30]. These data are presented in Table 2-3. The *S/XB* values are given for a single ''384.5 nm line'', which corresponds to the ''379.8, 386.4, 390.2 nm''

[2] In detachment both pressure and temperature at the target plate are significantly reduced from their values observed upstream along magnetic field lines.

S/XB for Mo $z^7P^0 \rightarrow a^7S$ (3845.7 nm)

Electron Temperature (eV) \ Electron Density (m^{-3})	$1x10^{18}$	$1x10^{19}$	$1x10^{20}$	$5x10^{20}$	$1x10^{21}$	$2x10^{21}$	$5x10^{21}$
1	0.00741	0.00788	0.012	0.0268	0.044	0.0786	0.186
2	0.0743	0.0779	0.109	0.232	0.383	0.692	1.64
5	0.335	0.349	0.475	1.03	1.73	3.17	7.51
10	0.604	0.628	0.859	1.90	3.24	5.95	14.1
20	0.872	0.905	1.24	2.74	4.67	8.57	20.3
50	1.19	1.23	1.64	3.53	5.93	10.8	25.4
100	1.39	1.43	1.87	3.80	6.31	11.1	26.4

Table 2-3: Molybdenum ionizations per emitted photon (*S/XB*) for the "384.5 nm line", which corresponds to the "379.8, 386.4, 390.2 nm" molybdenum line triplet (from Table 4 (a) of Ref. [30]).

molybdenum line triplet. To obtain the ionizations per emitted photon for each of the three lines of the triplet, the values of Table 2-3 must be multiplied by (see Appendix B of Ref. [30]):

$$\frac{(2S+1)(2L+1)}{2J+1}$$

where L, S, and J are the quantum numbers for the total orbital angular momentum, total spin, and total angular momentum respectively for the upper level of each of the transitions. For all three transitions (see Table 2-2) L = 1 and S = 3 while J is 4 for the 379.8 nm line, 3 for the 386.4 nm line, and 2 for the 390.2 nm line respectively. Hence, the multiplying factor is 21/7 for the 386.4 nm MoI line, 21/9 for the 379.8 nm line and 21/5 for the 390.2 nm line. Figures 2-15 and 2-16 show the calculated number of ionizations per emitted 386.4 nm photon as a function of the electron temperature and density. The *S/XB* is very sensitive to changes of the temperature in the 1 eV to 20 eV range for all electron densities but is practically constant for temperatures above the 45 eV point. As also seen in the figures the higher the temperature the more sensitive *S/XB*

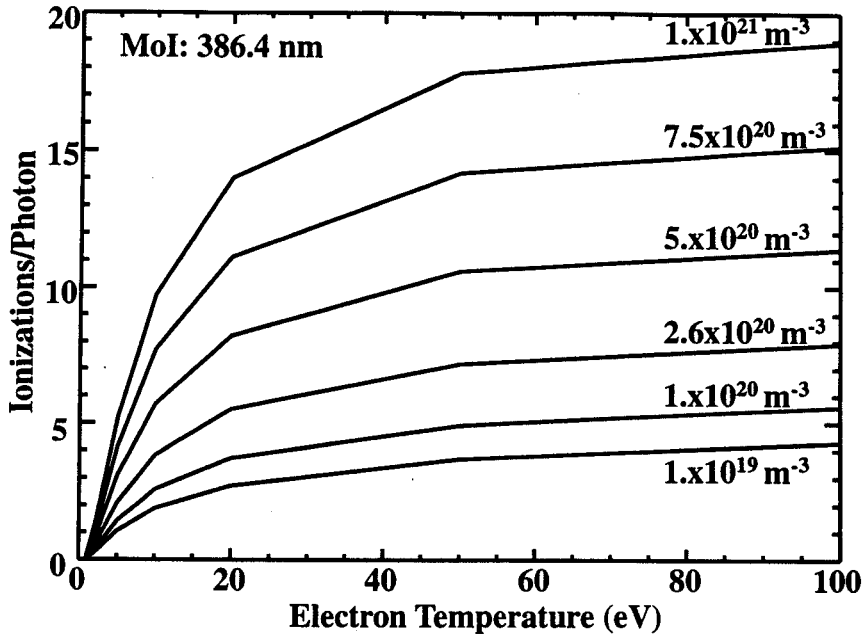

Fig. 2-15: Molybdenum ionizations per 386.4 nm emitted photon (*S/XB*) as a function of the electron temperature for a number of electron densities. Calculated using the data of Table 2-3 that have been multiplied by 3.

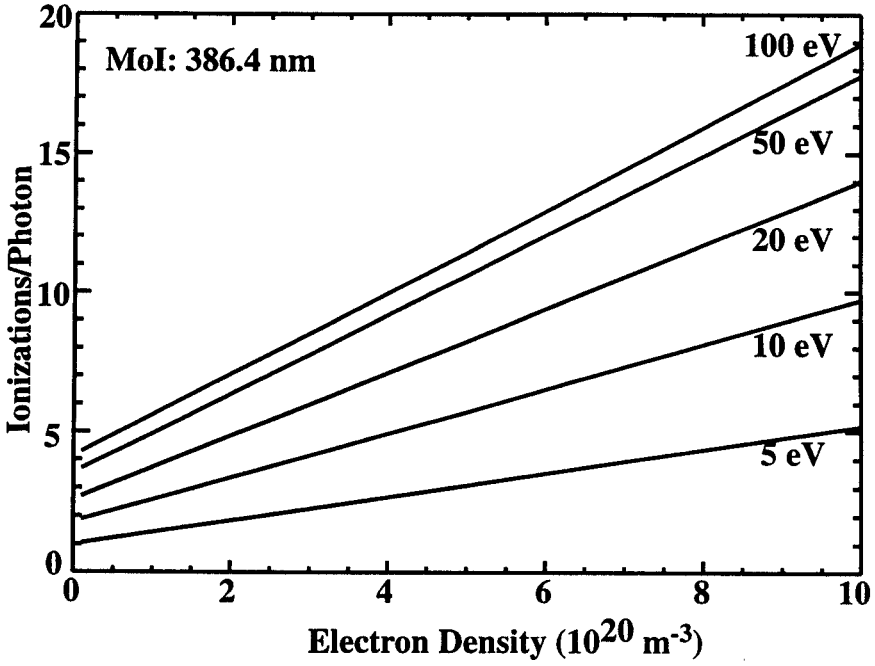

Fig. 2-16: Molybdenum ionizations per 386.4 nm emitted photon (*S/XB*) as a function of the electron density for a number of electron temperatures. Calculated using the data of Table 2-3 that have been multiplied by 3.

is to changes in the density.

It is clear from the figures that accurate calculation of the source levels requires the knowledge of both the electron temperature and density at the point where the emission originated. Recalling that the measurements are line-integrated values, it should be noted that it is inherently assumed that since we are dealing with neutral molybdenum radiation and that the molybdenum ionization length is small, the emissions originate close to the observed surface. As it has already been mentioned, for the outer divertor source measurements, the local electron temperature and density, as a function of time, are obtained from the set of Langmuir probes embedded in the outer divertor target. Similar information was available for the inner divertor as well but this surface does not typically produce measurable levels of molybdenum radiation. For the other views there has not been in general available information on the plasma parameters in the neighborhood of the surface monitored and one constant *S/XB* value was assumed based on typical local plasma conditions estimated from fast scanning probe data.

2.4 Calculation of Boron Flux to the Divertor Target

In Chapter 5, a model that calculates the molybdenum emission at the outer divertor target is described. As will be shown, sputtering of molybdenum with boron ions impacting on the divertor surface plays a crucial role in the model. It is therefore necessary to be able to estimate the boron flux to the target at the same time we measure the molybdenum emissions emanating from it, since it is these emissions that we are trying to match with the model. As seen in Fig. 2-14, a pretty intense boron line at 412.2 nm is included in the spectral region monitored with the spectrometer during observation of the molybdenum emissions. This line, from singly ionized boron ions, can be used in estimating the boron flux to the target. Actually, what can be directly calculated from this line is the boron influx from the target in the same way the molybdenum lines are used in calculating the molybdenum influx: using Eq. 2.2. With the boron influx available, one can then, using certain assumptions, estimate the boron flux to the target.

Using Eq. 2.2 for the calculation of the boron influx requires knowledge of the *S/XB* for the 412.2 nm line. This information was not directly available to us. However, the

S/XB for 703.3 nm B line

Electron Density (m^{-3}) \ Electron Temperature (eV)	1	2	5	10	15	20	30	50	100	150
$1x10^{19}$	0.00138	0.0295	0.379	1.24	2.16	3.11	5.19	10.3	28.0	49.5
2x1019	0.00264	0.0513	0.597	1.84	3,13	4.44	7.25	14.0	36.8	49.5
$5x10^{19}$	0.00751	0.130	1.29	3.67	6.04	8.39	13.3	25.0	61.9	104.0
$2x10^{20}$	0.0477	0.694	5.13	12.9	20.1	27.1	41.7	75.3	176.0	285.0

Table 2-4: Ionizations per emitted photon (*S/XB*) for the 703.3 nm B line [31].

S/XB values were available for another boron line, at 703.3 nm, from the ADAS database (see Table 2-4) [31]. Of course, this line can not be monitored simultaneously with the molybdenum lines of interest, since it is in a completely different spectral region. So it can not be used for real time calculation of the boron influx in the shots of interest. It allows us, though, to estimate the *S/XB* for the 412.2 nm line from the corresponding information for the 703.3 nm line. This was done by measuring the intensities of the two lines during shots with, as much as possible, identical conditions through the divertor chords. The use of the divertor chords is necessary not only for checking the similarity in the local temperature and density conditions with the Langmuir probes but also for knowing what these conditions are, since the *S/XB* values depend on both. If the conditions are indeed similar, then the boron influx is the same in the two shots. Hence, using Eq. 2.2, we can obtain the S/XB for the 412.2 nm line from

$$(S/XB)_{412.2} = (S/XB)_{703.3}\frac{I_{703.3}}{I_{412.2}} \qquad (2.3)$$

The above procedure was followed for a number of shots and the S/XB values for the 412.2 nm line were estimated from Eq. 2.3. In Fig. 2-17 the intensities of the two lines for one of the divertor chords (# 12) are plotted as a function of time for two shots characterized by similar electron temperature and density divertor conditions until about 0.8 s. The density and temperature shown in the figure are from the probe that corresponds to the divertor view used. The intensity of the 412.2 nm line has been

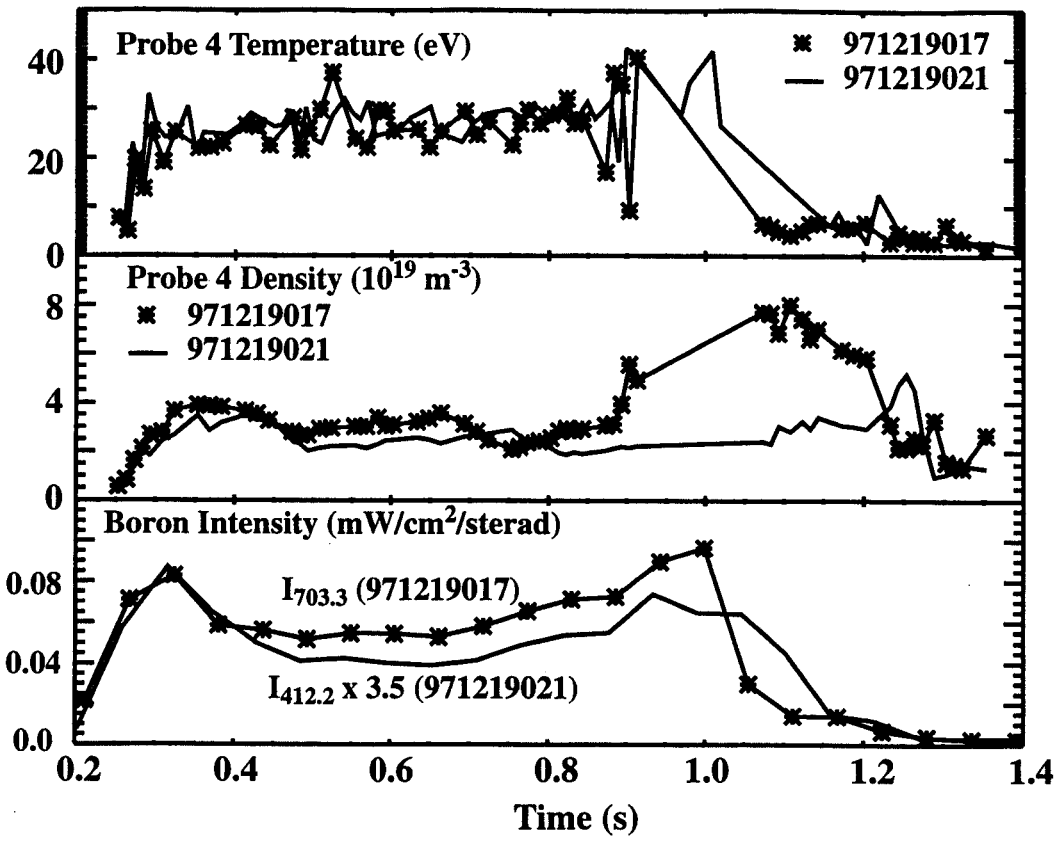

Fig. 2-17: Comparison of the intensities of the boron 412.2 nm and 703.3 nm lines for similar electron temperature and density conditions. The intensity of the 412.2 nm line has been multiplied by 3.5.

multiplied by 3.5. As seen in the figure, the ratio of the two lines remains approximately constant during the shot. This implies that, to first order, the *S/XB*'s for the two lines have similar temperature and density dependence. Considering the uncertainties in the measurements and in the *S/XB* data for the 703.3 nm line, as well as the fact that the two shots are not exactly identical, the simple solution was chosen to assume that for all temperatures and densities the ratio of the *S/XB*'s is a constant value. Based on data similar to the ones shown in Fig. 5-17, it was assumed that

$$(S/XB)_{412.2} = 3.5 * (S/XB)_{703.3}. \qquad (2.4)$$

With the *S/XB* values for the 412.2 nm line available, we can now calculate the boron influx simultaneously with the molybdenum influx. However, as mentioned, what we are after is the boron flux to the target. To get that, we make the assumption that the boron flux to the target is equal to the boron influx for all locations at the outer divertor. This, of

course, is only a convenient assumption since boron ions can in principle return at other points on the target or even diffuse away. An important parameter is the boron ionization length. For T_e = 20 eV and $n_e = 1. \times 10^{20}$ m^{-3}, it is ~ 1.5 mm. This means that boron particles are ionized pretty close to the surface and it is probable that they return in the vicinity of the point that originated from. In any case uncertainties of the order of two would be expected from the above procedure.

Chapter 3

Molybdenum Sources in Alcator C-Mod

There are a number of surfaces in Alcator C-Mod which are significant sources of molybdenum. The strength of each source, and hence their relative strength, can vary significantly during a shot, depending on the plasma phase (limited vs. diverted, ohmic vs. RF, L-mode vs. H-mode[1]) and on the plasma parameters. This chapter includes all the experimental results regarding the molybdenum sources, and their dependence on plasma conditions, in Alcator C-Mod. The processes believed to be responsible for the molybdenum generation in each of the surfaces are also discussed. Whenever possible, the core molybdenum density levels will be compared to the sources with ultimate goal to identify the relative contribution of the various molybdenum sources to the plasma core molybdenum content.

3.1 Inner Wall

As it has already been mentioned in Chapter 1, the inner wall is used as a plasma limiter

[1] L-mode (for low) and H-mode (for high) are two characteristic types of confinement modes in tokamak plasmas with heating additional to ohmic [3]. L-mode is the lowest confinement regime observed. The H-modes are confinement regimes characterized by improved energy confinement with respect to the L-mode. In Alcator C-Mod two main types of H-modes are observed: the ELM-free H-mode in which the impurity particle confinement time is practically infinite, which leads to impurity accumulation in the core, and the EDA H-mode, characterized by enhanced D_α radiation, in which the impurity particle confinement time increases only by a small factor without any adverse effects on the energy confinement [32, 33].

at the beginning of every plasma discharge. Less frequently, inner-wall limited plasma configurations, that last for the whole shot, are produced, typically as part of experiments that compare limited to diverted plasmas. This direct interaction of the core plasma with the wall results in significant neutral molybdenum radiation from the inner wall. When the plasma is diverted, the molybdenum source is substantially smaller, frequently dropping below the spectrometer's detection limit.

The inner wall is continuously monitored with a single wide-angle view that covers a significant fraction of it around the plasma midplane, where most of the interaction with the wall is expected to occur. A fiber array is also available for monitoring the inner wall. This system is not used in a regular basis, since that would require allocating many of the spectrometer's fibers to the observation of the inner wall, which, as mentioned, is not a strong source of molybdenum during diverted plasma configurations. However, it is occasionally used to obtain the profile of the molybdenum emissions. Hence, unless stated otherwise, the inner wall data presented in this thesis were obtained with the single fiber system. Figure 3-1 shows a poloidal cross-section of an Alcator C-Mod tokamak diverted plasma together with the single and multiple fiber array views mentioned above. It should be noted that the two viewing systems are not in the same toroidal location. The specific views are from the 1999 Alcator C-Mod campaign. In prior campaigns the monitored area was slightly different.

The inner wall molybdenum source rate, Φ_W, is calculated from the single-fiber measured influx, Γ (Eq 2.2), under the assumption that the emissions from the inner wall are toroidally symmetric:

$$\Phi_W = 2\,\pi\,R_W\,Z_W\,\Gamma = 8\,\pi^2\,R_W\,Z_W\,I\,(S/XB). \qquad (3.1)$$

In the above expression the intensity I is in units of photons per unit time, unit area, and unit solid angle, $R_W = 0.44$ m is the major radius at the inner wall and $Z_W \approx 0.219$ m is the length viewed in the vertical direction by the single fiber. The above value for Z_W, which is for the 1999 run campaign, is calculated after taking into account that the spectrometer has an f number of "f/4.0" and hence its acceptance angle (~7°) is smaller than the fiber's (~12.8°), which has an f number of "f/2.2" (see Fig. 3-1). Since there is no diagnostic providing information on the electron density and temperature at the inner wall, a constant *S/XB* factor was used, independently of plasma phase and conditions,

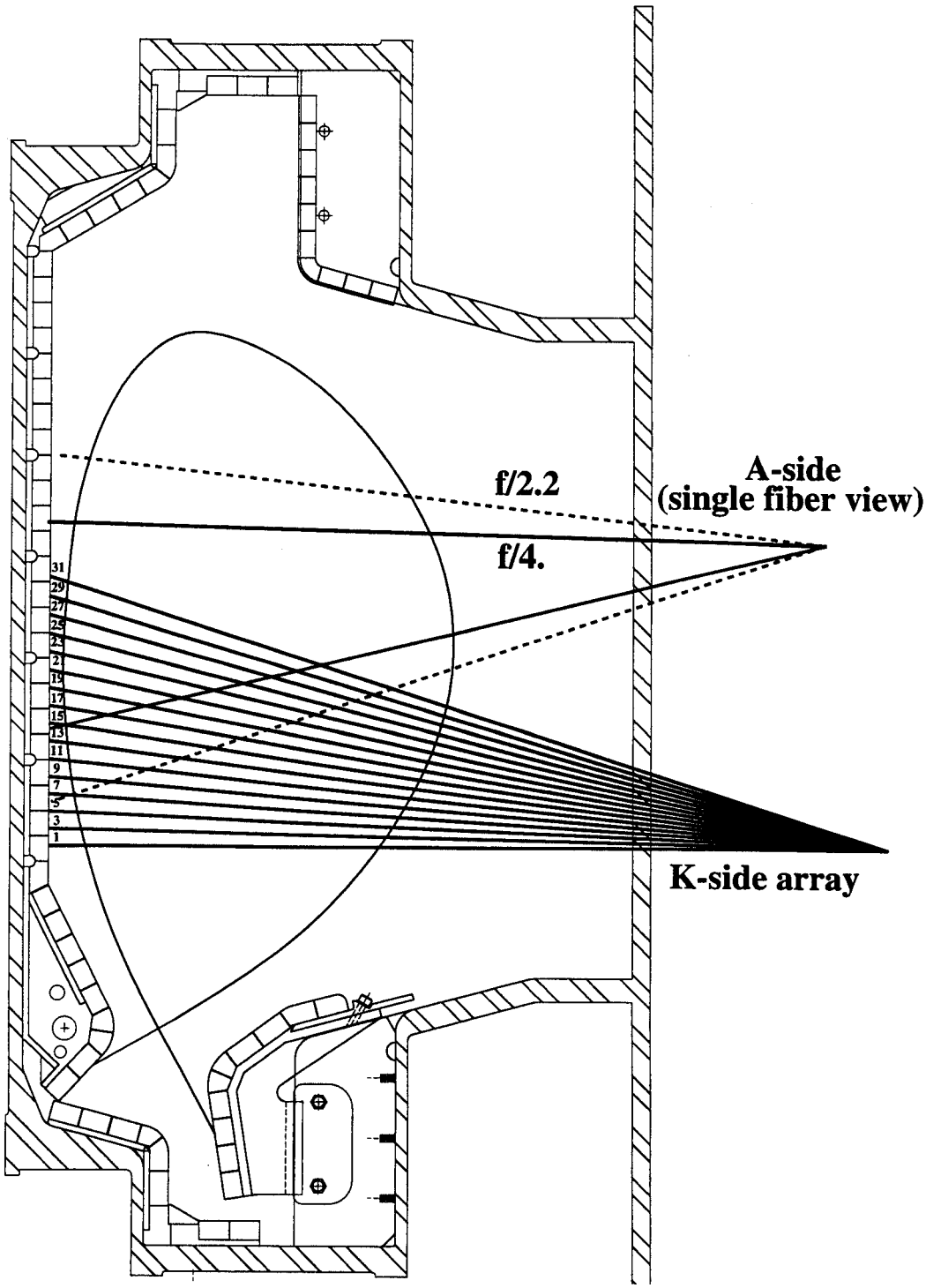

Fig. 3-1: Poloidal cross-section of the C-Mod vessel with the two views monitoring the inner wall. For the single-fiber view the area monitored is calculated based on the spectrometer's *f* number (*f* /4.0) rather than the fiber's (*f* /2.2).

assuming a value of $5.x10^{19}$ m^{-3} for the density and a value of 25 eV for the temperature. For these parameters, the number of ionizations per 386.4-nm photon is ~ 3.41 (see section 2.3). Of course taking *S/XB* to be constant increases the uncertainty in the molybdenum source rate. In practice, however, the error is generally not very big due to the relatively small variation of the *S/XB* factor with electron density and temperature, in the parameter range of interest. For example using a density of $2.\times10^{19}$ m^{-3} and a temperature of 15 eV gives an *S/XB* of 2.46, which is only ~38 % smaller than the value used for the calculation of the molybdenum source rate and within the experimental uncertainties of the measurement.

Figures 3-2 and 3-3 show the time history of the inner wall molybdenum source rate for two representative plasma discharges, with no auxiliary RF heating. In Fig. 3-2 the plasma is diverted at t = 0.27 s while in Fig. 3-3 it stays limited for the entire shot. There is a clear difference between the two types of discharges in terms of the inner wall molybdenum source behavior. In both shots the molybdenum influx is pretty high initially, when the plasma is limited at the inner wall. However, in the case of the diverted plasma discharge, the molybdenum production drops sharply right after the plasma is diverted, signifying a reduction in the interaction between the plasma and the inner wall. On the contrary, the source stays high for the whole duration of the limited plasma shot. Of course, as shown in the two figures, there are additional differences between the two shots, in particular in plasma parameters such as the plasma current and the volume averaged electron density, that will be shown to influence the molybdenum influx levels. However, the main effect on the molybdenum source can still be attributed to the different type of plasmas in the two shots. The source rate is always much smaller when the plasma is diverted independently of the plasma conditions. For plasmas that stay limited for the whole shot, the molybdenum source rate is typically high early during the plasma current ramp-up phase but its level during the steady state portion depends strongly on other parameters. In the example shown in Fig. 3-3 the pretty high molybdenum level is a consequence of the very low electron density which implies a rather hot edge that favors increased physical sputtering. In both figures, the core molybdenum brightness is also plotted. There is a clear correlation between the inner wall molybdenum source rate and the corresponding core molybdenum signal whenever the

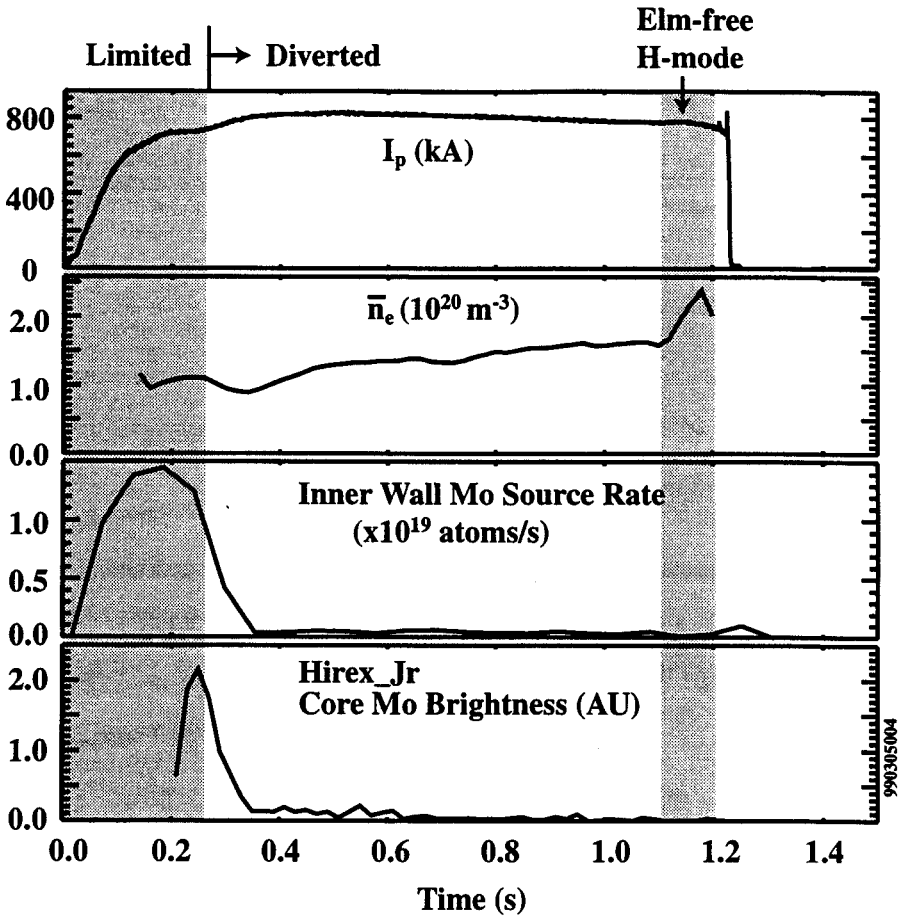

Fig. 3-2: Typical time history of the inner wall molybdenum source rate for a diverted plasma discharge with no auxiliary RF heating. The plasma current, volume averaged electron density, and core molybdenum brightness traces are also shown.

plasma is limited. The initial time lag between the two signals in Fig 3-2 is attributed to the fact that the Hirex spectrometer monitors a neon-like (Mo^{+32}) molybdenum line. The excitation of a closed shell electron is not easy and the specific line is not observed before the plasma heats up to 1.5 to 2.0 keV. On the contrary the Moly Monitor (see Fig. 3-3) observes emissions from a sodium-like (Mo^{+31}) molybdenum line, which is excited at much lower temperatures, and any time lag between the two signals is mainly due to impurity transport from the point of generation to the core plasma. This correlation during the limited phase is consistently observed and will again be evident from other data presented in the rest of this thesis. With the absence of any other sources of molybdenum, such as is the case for the two ohmic-heated limited plasmas presented in

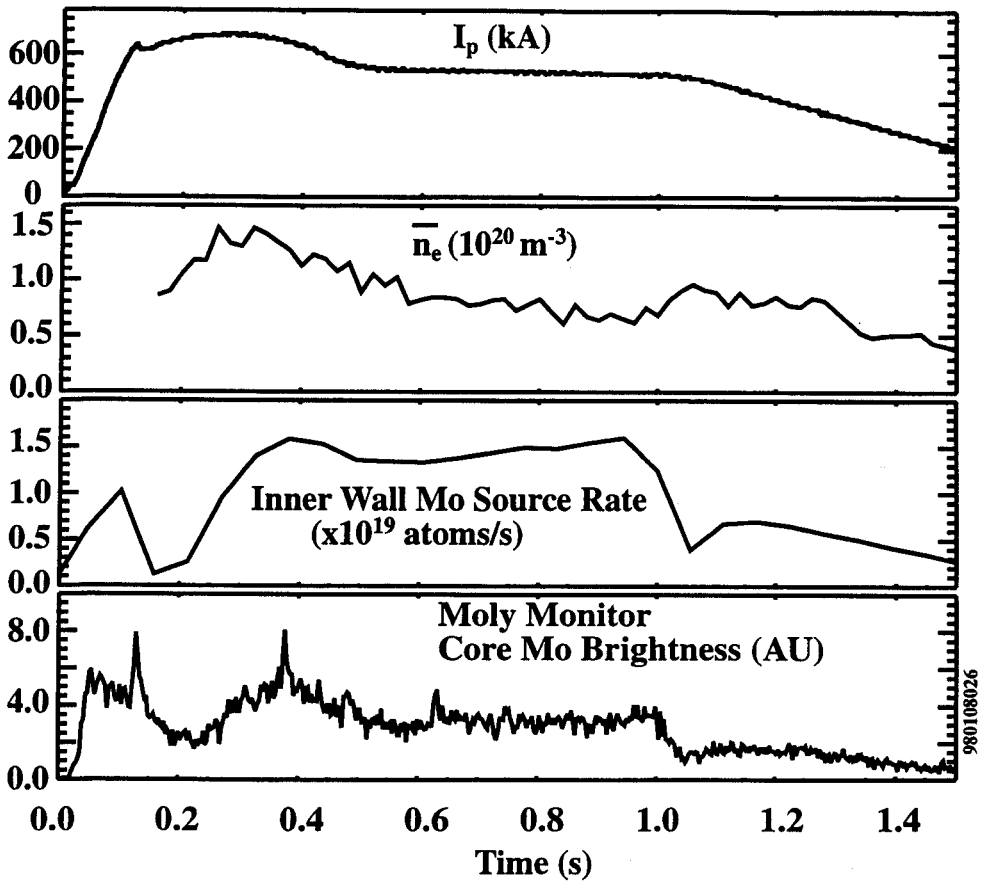

Fig 3-3: Typical time history of the inner wall molybdenum source rate for an inner-wall limited plasma discharge with no auxiliary RF heating. The plasma current, the volume averaged electron density, and the core molybdenum brightness traces (from the Moly Monitor) are also shown.

Figs. 3-2 and 3-3, the implication is that the inner wall is the main source of the molybdenum that ends up in the core during the inner wall limited phase of discharges. This was somewhat expected since many molybdenum neutrals coming from the inner wall are emitted directly inside the last closed flux surface and they do not have to cross the scrape-off-layer as other neutrals originating from other surfaces have.

3.1.1 Effect of Plasma Current

As it was already mentioned, the toroidal plasma current is a source of resistive plasma heating. Hence, for high plasma current values there is more power available to the plasma. It is of interest, therefore, to investigate if there is any correlation between the

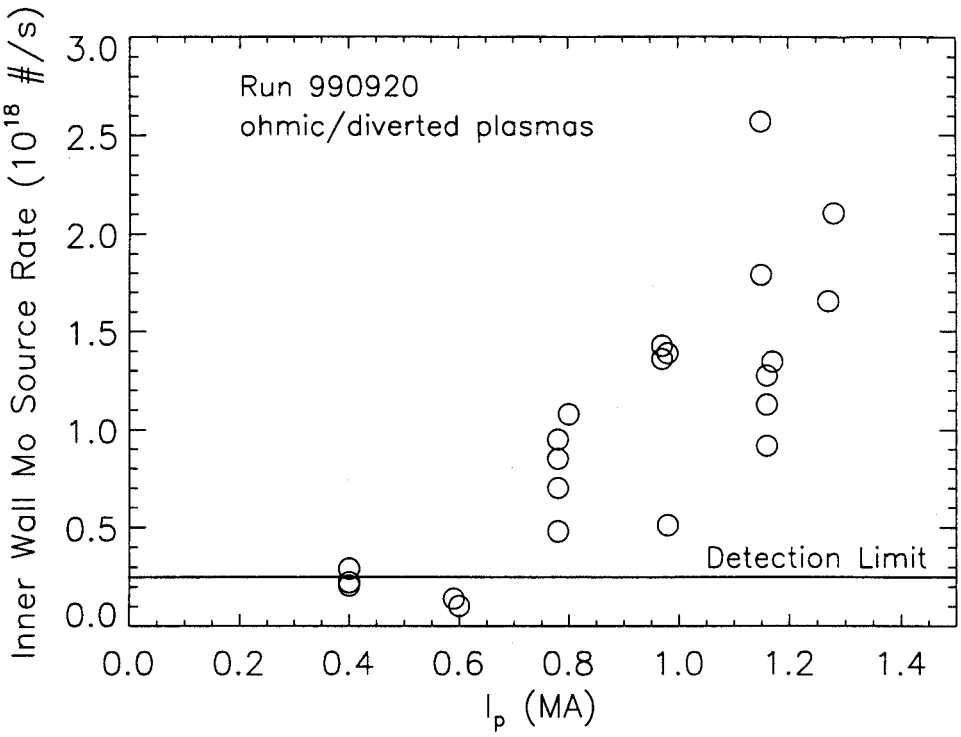

Fig 3-4: Effect of the plasma current on the inner wall molybdenum source rate during the ohmic phase of diverted plasmas.

plasma current level and molybdenum emissions at the various surfaces. Figure 3-4 shows the effect of plasma current on the inner wall molybdenum source rate during the ohmic phase of diverted plasma discharges. Although there is significant spread in the data at each plasma current value, the overall trend is that the source rate increases with increasing current. Part of the spread may be attributed to variations in the electron density which ranged from 1.4 to 1.8×10^{20} m^{-3}. The core molybdenum density is, in general, very low during the ohmic phase of discharges and the associated uncertainties very big and were not plotted. A similar plot has not been generated for limited discharges due to lack of available data.

3.1.2 Effect of Electron Density

The electron density is frequently varied in Alcator C-Mod not only from day to day but also from shot to shot during dedicated runs that intend to investigate its effect on various

experimental findings. During one such experiment a number of 500 kA, ohmic, inner-wall limited plasmas were generated. Actually in some of these shots, the electron density was also varying during the shot. An example of a single shot is given in Fig. 3-3. To investigate the effect of the density on the molybdenum source from the inner wall, averages of the electron density and source rate were taken during the portion of the discharge that the plasma current remained constant to 500 kA (typically between 0.6 s and 1.0 s). The result is shown in Fig. 3-5. It is clear that increase of the electron density results in a decrease of the emissions from the inner wall. This was the "anticipated" result since high average electron density means that the edge is also denser and at the same time cooler, which results in a reduction of physical sputtering. No inner wall molybdenum source data from a dedicated density scan for diverted discharges are available. As already mentioned, frequently during the diverted phase of discharges the wall source rate is close or below the spectrometer's detection limit which makes the

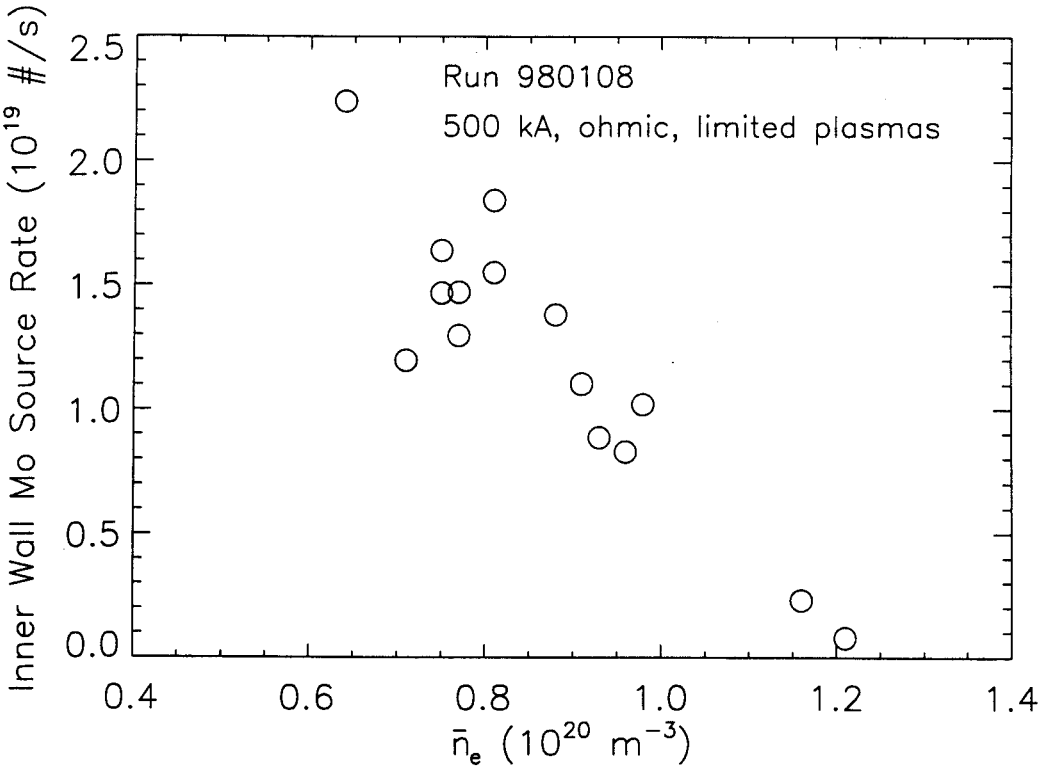

Fig. 3-5: Effect of electron density on the inner wall molybdenum source rate during the ohmic phase of inner-wall limited plasma discharges. A representative shot is shown in Fig. 3-3.

investigation of the effect of certain parameters hard.

3.1.3 Effect of RF Power

The effect of the RF power on the inner wall molybdenum source is different for limited and diverted discharges. The RF power does not seem to have a strong effect on the magnitude of the molybdenum emissions during diverted plasma operation at least for intermediate density, $\overline{n_e} \approx (1.5-2.0)\times 10^{20}$ m^{-3}, L-mode plasmas. This is illustrated in Figs. 3-6 and 3-7. Figure 3-6 shows the time histories of the electron density, the RF power, the molybdenum source and the core molybdenum density for an L-mode, 1 MA diverted plasma. The molybdenum source is monotonically decreasing and does not

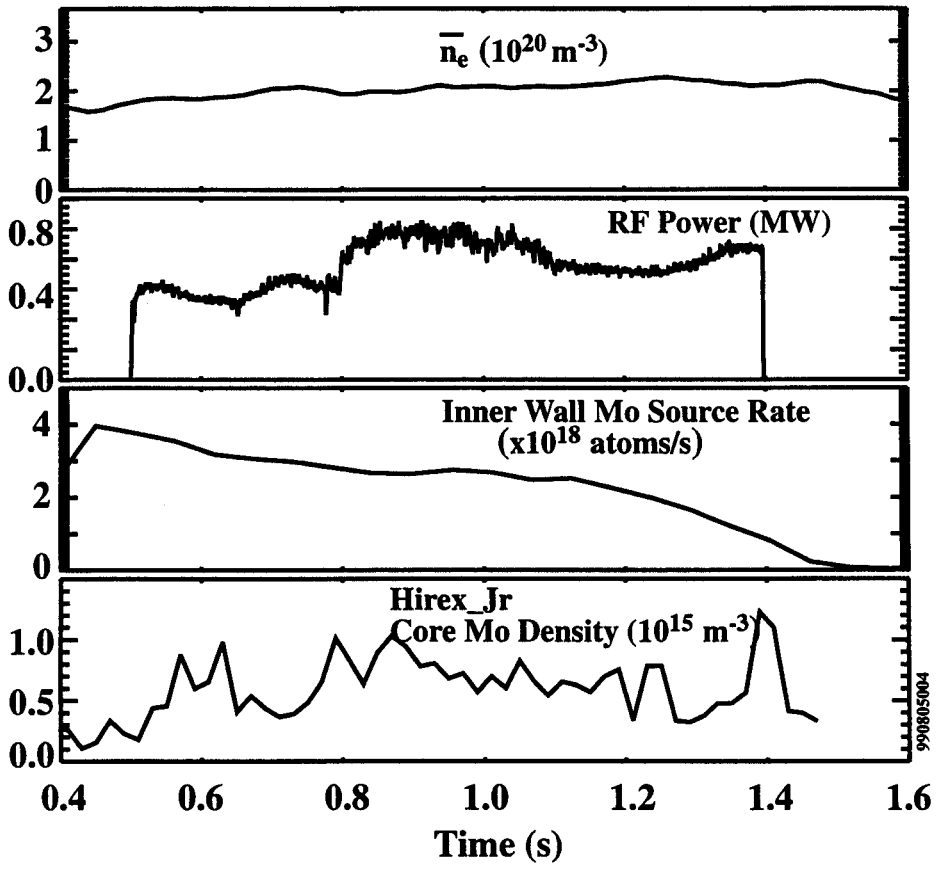

Fig. 3-6: Time histories of electron density, RF power, inner wall molybdenum source rate and core molybdenum density for a 1MA, L-mode diverted plasma. The RF power has no observable effect on the molybdenum emissions.

follow the launched RF power, which is changing in discrete steps and has its maximum value during the second step. In addition, the electron density increases only slightly during the shot and can not be assumed to mask any hypothetical strong dependence of the molybdenum emissions on the RF power. By taking time averages of the RF power and the molybdenum source rate during each of the RF power steps for a number of discharges, with similar characteristics to the one shown in Fig. 3-6 and from the same run day (990805), the dependence of the source level on the rf power was investigated more thoroughly. The result is shown in Fig 3-7. The small increase of the molybdenum source for RF powers greater than 0.8 MW is believed to be primarily coincidental and not due to a direct effect of the RF power to the molybdenum source. The reason is that for any given shot the findings were similar to the ones observed in Fig. 3-6: the RF steps

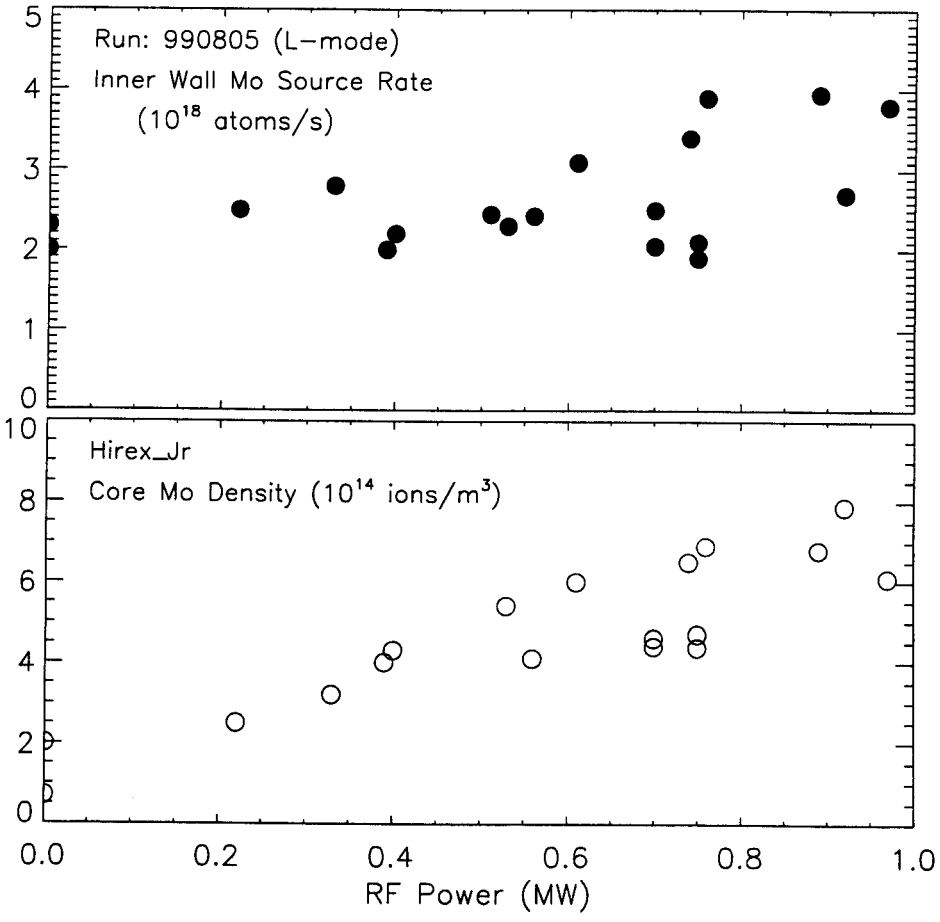

Fig. 3-7: Inner wall molybdenum source rate and core molybdenum density versus RF power for 1MA, L-mode diverted plasmas.

had no observable effect on the molybdenum source. The apparent slight correlation between source and RF power is attributed to the fact that in many of the other shots the bigger RF step was changed to be at the beginning of the RF pulse, and thus coincided with the stronger molybdenum emissions. On the contrary, the core molybdenum density shows a clear correlation with the RF power level implying that most of the molybdenum ions in the core have originated from a surface other than the inner wall. This result is very important if we consider that the inner wall was the largest source observed during these experiments. (The source levels from the two other significant emitters of molybdenum, the outer divertor and the antenna protection tiles, will be presented, for the same set of shots, in Figs. 3-22 and 3-34). This is a clear indication of very good screening of molybdenum at the inner wall which can be attributed to strong sinks on the inside.

In inner wall limited L-mode plasmas the situation is distinctively different, as illustrated in Fig. 3-8. During the RF pulse the molybdenum source rate more than doubles comparing to the ohmic value. Similar behavior has also been observed during reversed shear experiments where ICRF waves are launched into the plasma during the initial limited phase of the plasma. Once again, as for other limited discharges, the core molybdenum signal correlates with the molybdenum source level. The direct effect of the RF power on the molybdenum source rate for inner-wall limited plasmas can be attributed to the direct interaction between the hot plasma core and the inner wall.

3.1.4 Effect of Transport

As it has already been mentioned, the molybdenum source levels at the inner wall depend on the type of the H-mode confinement. Figures 3-9 and 3-10 give two examples of how two different types of H modes affect the wall source. The data depicted in Fig. 3-9 show the effect of ELM-free H-modes while the data in Fig. 3-10 the effect of EDA H-modes. The data in both figures are from diverted discharges. In Fig. 3-9 the time histories of the D_α signal, the RF power injected into the plasma, the inner wall molybdenum source rate, and the core molybdenum density are plotted. The plasma transitions into a series of ELM-free H-modes starting at around 0.95 s as indicated by the sudden reduction in D_α signal level. For the time resolution of the Chromex spectrometer (56 ms), the first three

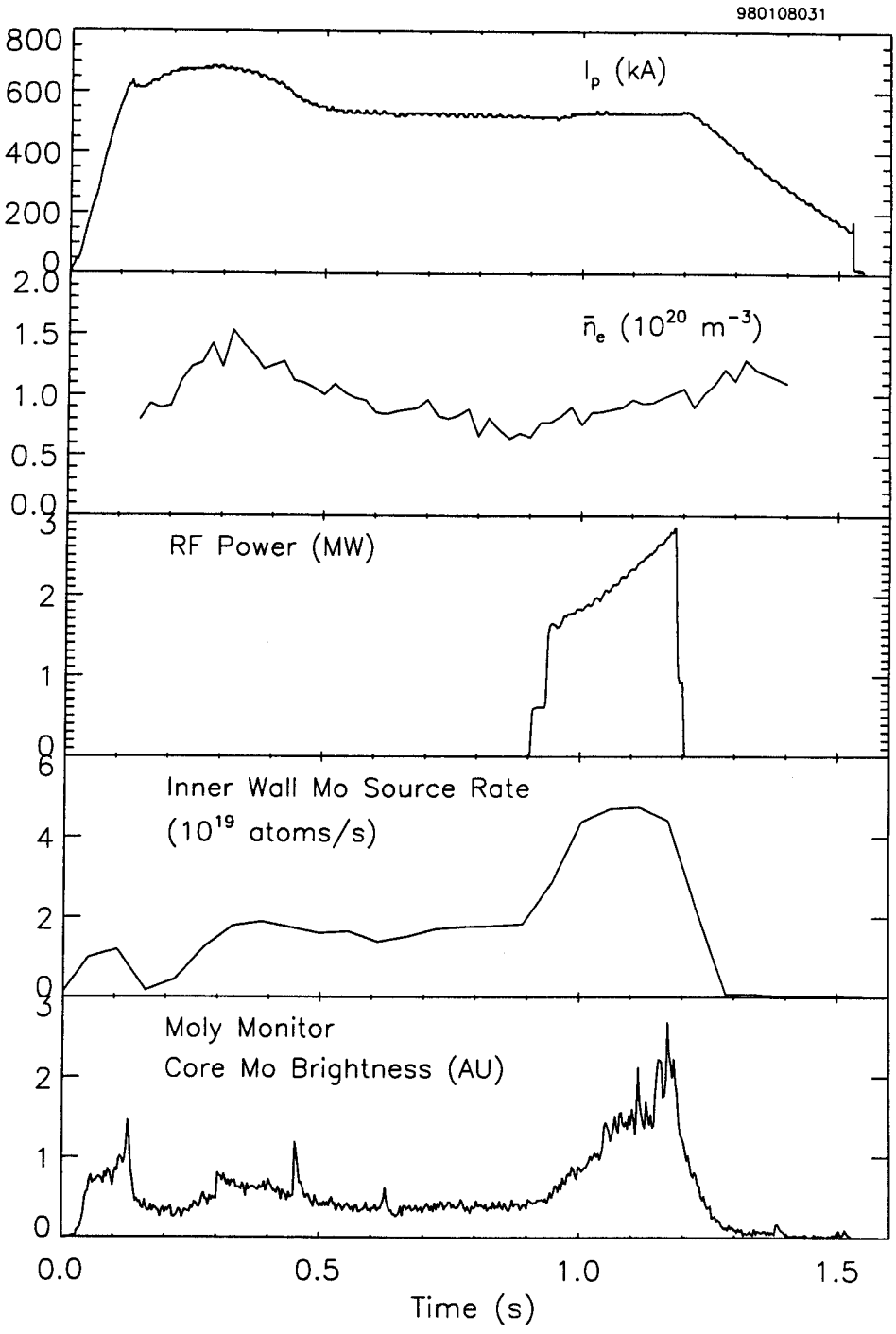

Fig. 3-8: Time histories of plasma parameters, the inner wall molybdenum source rate, and the core molybdenum brightness for an inner-wall limited discharge.

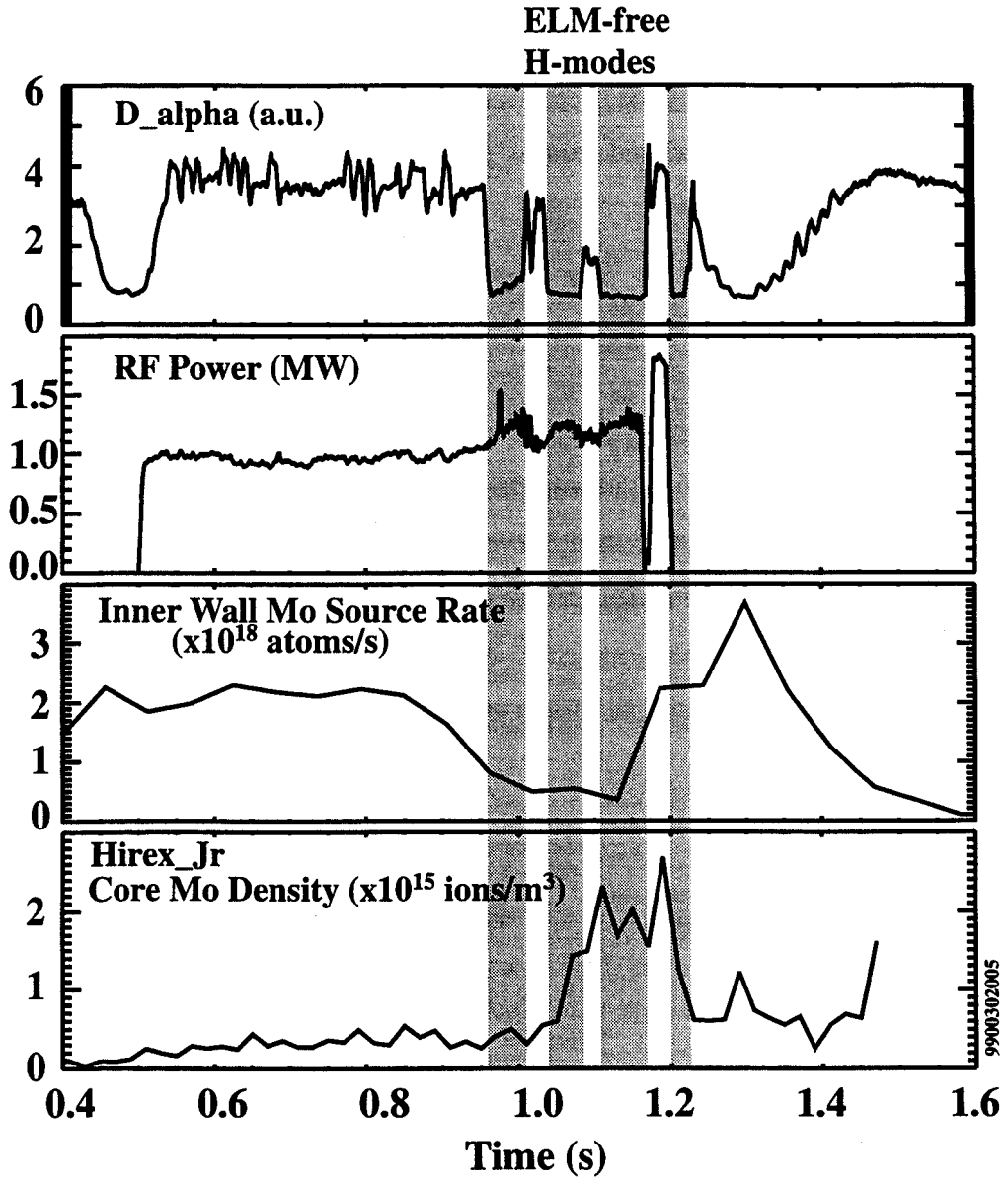

Fig. 3-9: Effect of ELM-free H-mode on the inner wall molybdenum source rate. The time histories of the D_α signal, the RF power, the inner wall molybdenum source rate, and the core molybdenum density are plotted.

H-modes can be considered as a single ELM-free H-mode. The molybdenum source rate drops sharply when the plasma goes into the series of ELM-free H-modes. This decrease can be thought of as a consequence of the shrinking of the scrape-off-layer width which accompanies the transition from L-mode to H-mode. The result is a reduction in the interaction of the plasma with the walls that surround it. In contrast to what happens with the molybdenum source rate, the molybdenum core density increases rapidly during the

ELM-free phase due to the almost infinite particle confinement time that characterizes this regime. This anti-correlation between the molybdenum wall source rate and the core density is another indication that the inner wall is not the main source of the molybdenum that ends up in the core in diverted plasma discharges, in contrast to what happens in inner-wall limited plasmas.

In the shot analyzed in Fig. 3-10, the plasma transitions into an EDA H-mode just after 0.8 s. It is evident that during the EDA H-mode, unlike what was observed during ELM-free H-modes, the wall source rate reaches levels that are distinctly higher than the ones measured during the L-mode phase. The initial drop in the source rate just after the L-H transition correlates with the small delay in the establishment of the EDA H-mode as seen by the temporary decrease in the D_α signal level. Hence, it is possible that this decrease in the emissions can be attributed to the same causes that are responsible for the reduction of the molybdenum source level during ELM-free H-modes. With the physics of the EDA H-modes not yet fully understood, the reason for the increase of the wall molybdenum

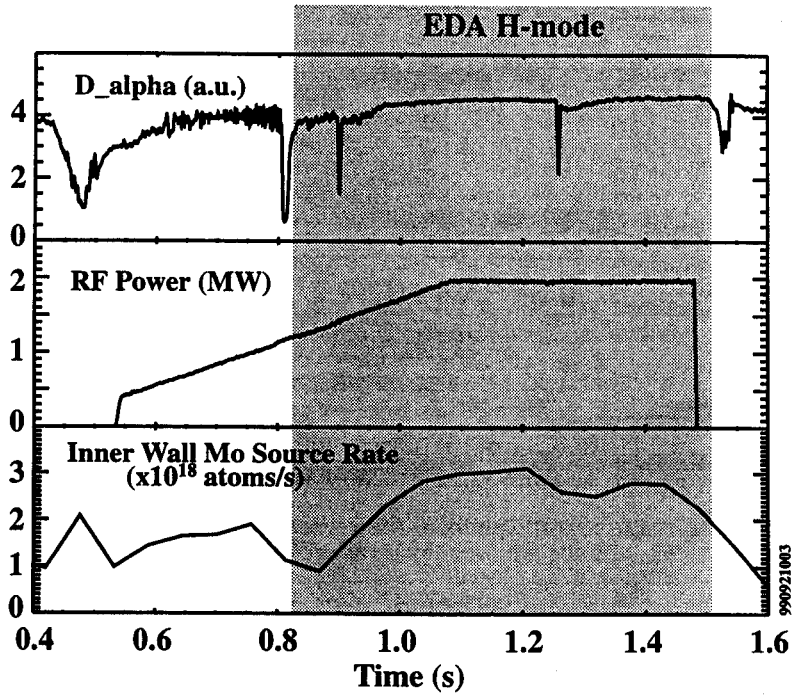

Fig. 3-10: Effect of EDA H-mode on the inner wall molybdenum source rate. The time histories of the D_α signal, the RF power, and the inner wall molybdenum source rate are plotted.

emissions during this phase stays uncertain. However, it should be mentioned that the molybdenum source increase is consistent with the increased recycling that is implied by the enhanced D_α signal.

3.1.5 Effect of the Inner Gap

The inner, or "left", gap is defined as the smallest distance between the inner wall cylinder and the plasma last closed flux surface. By definition, the inner gap is zero for an inner-wall limited plasma. For diverted plasmas it is of the order of 1 cm. It is frequently varied between shots depending on the requirements on plasma geometry and performance. Just as a transition from limited to diverted plasmas results in a reduction in the molybdenum source rate, it was expected that an increase in the inner gap would result in a decrease in the molybdenum emissions from the inner wall since a wider scrape-off-layer leads to colder temperatures at the wall. To verify the above prediction, shots 022 through 025 from the 991021 run were dedicated to monitoring the effect of varying inner gap. In each of these shots a stairstep inner gap scan was performed. An example is given in Fig. 3-11 which shows the three left gap steps and the corresponding effect on the inner wall molybdenum source. For the specific plasma discharge (991021024), all other parameters (plasma current, plasma density, confinement type) that could influence the inner wall molybdenum source level did not change during the period that the gap was changing. The plasma current was kept to 800 kA and the volume averaged electron density, which is also shown in the figure, to ~ 1.5 x 10^{20} m^{-3}. The constant electron density also indicates, indirectly, that the plasma did not go into an H-mode, despite putting 0.8 MW of RF power into the plasma from the E antenna from t = 0.6 s to 1.5 s. The results presented in Fig. 3-11 show, as expected, a reduction in the inner wall molybdenum source rate with increasing inner gap. Once again it is shown that, for a diverted plasma, the core molybdenum density does not follow the changes in the inner wall molybdenum emission levels.

All four shots in the survey were 800 kA plasma discharges but only in the one shown in Fig. 3-11 the plasma stayed in L-mode throughout the shot. The cause for this difference was that higher RF power was used in the other shots. One of them

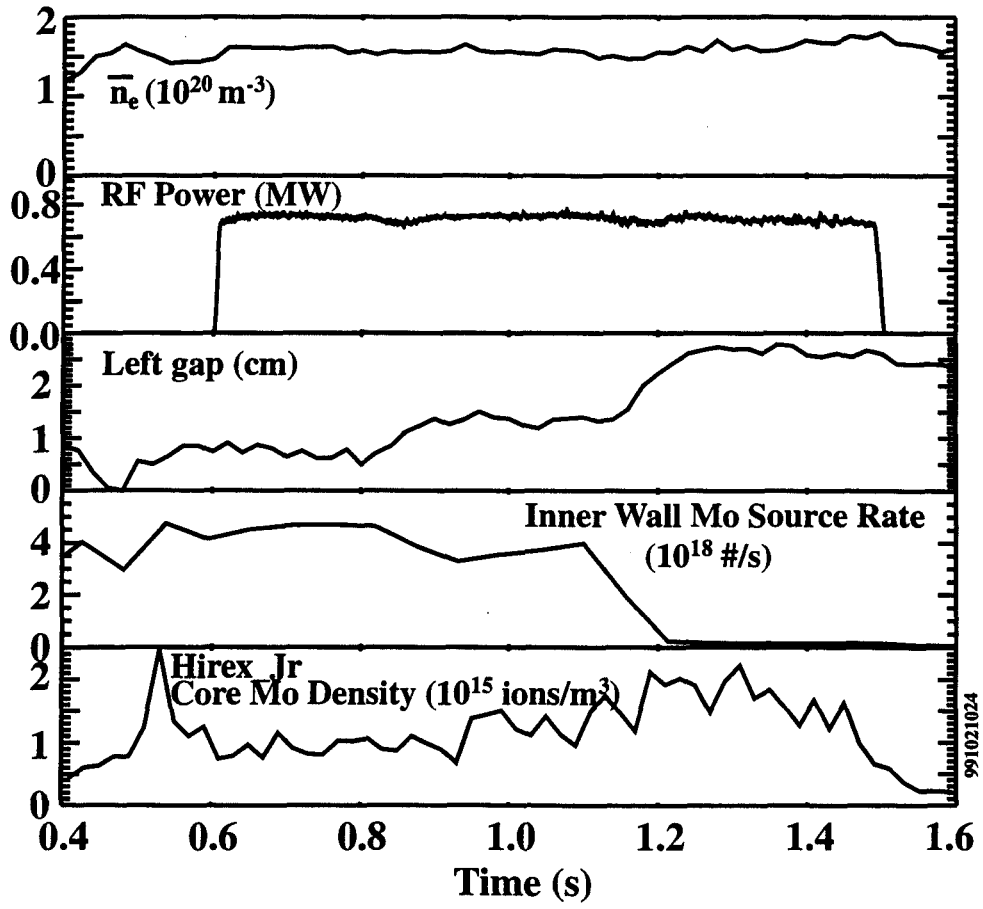

Fig. 3-11: Effect of stairstep left (inner) gap scan on the inner wall molybdenum source rate for an L-mode, medium density, Alcator C-Mod discharge. The RF power (0.8 MW) is on from 0.6 s to 1.5 s.

(991021025) went into a sequence of alternating L-modes and ELM-free H-modes for all three gap steps, simply due to the high RF power input (2.3 MW). In the two others an H-mode was obtained with constant RF power (0.9 MW in 991021022, 1.3 MW in 991021023) only for the larger inner gap, revealing a dependence of the confinement mode on the inner gap. Since the confinement mode has been shown to affect the inner wall molybdenum source level, only the L-mode data points were used in this analysis. These points all had $\bar{n}_e \approx 1.5\times10^{20}$ m^{-3}. The difference in the input RF power was not a problem, as long as the plasma stayed in L-mode, since it has been shown that for L-mode diverted plasmas the RF power level does not have a strong effect on the inner wall molybdenum emissions. The outer gap also varied unintentionally in some of the shots

but it is not expected to have any effect on the inner wall molybdenum emissions. Figure 3-12 shows the effect of the inner gap scan on the inner wall molybdenum source rate for L-mode confinement. A strong dependence of the molybdenum source level on the inner gap is demonstrated with the molybdenum emissions decreasing with increasing left gap.

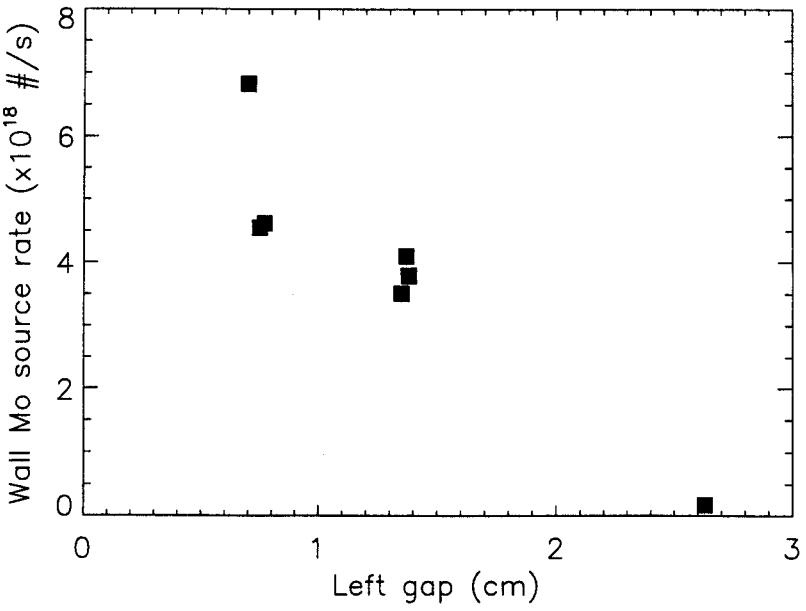

Fig. 3-12: Inner wall molybdenum source rate versus left (inner) gap for L-mode confinement. $I_p = 800$ kA, $\overline{n_e} \approx 1.5\times10^{20}$ m^{-3}.

3.1.6 Molybdenum Emissions in Helium Plasmas

The overwhelming majority of the Alcator C-Mod plasmas use deuterium as their fuel. However, occasionally helium plasmas are generated to investigate the differences between the two types of plasmas. As far as the molybdenum generation at the various surfaces is concerned, helium plasmas have been found to be significantly worse than deuterium plasmas. The situation for the inner wall is illustrated in Fig. 3-13 for an L-mode, diverted plasma. The molybdenum source rate during the initial limited phase of the discharge is actually similar to what it is observed for deuterium plasmas. (Note that the second peak in the molybdenum source rate around 0.38 s is a result of the plasma becoming again briefly limited as indicated by the inner gap going to zero.) However, during the diverted phase of the discharge, the molybdenum source levels are a factor of

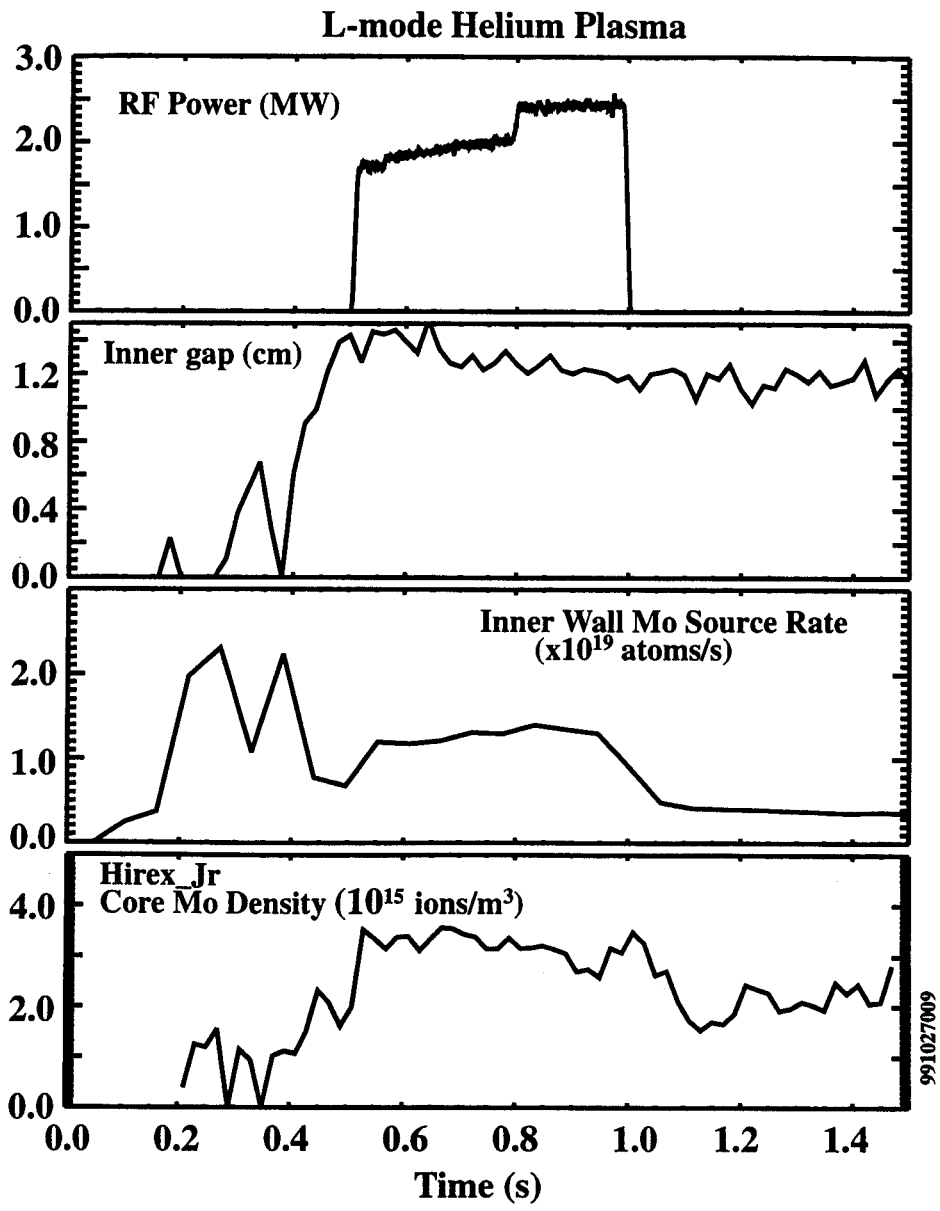

Fig. 3-13: Effect of helium plasmas on molybdenum emissions from the inner wall. The time histories of the RF power, inner gap, inner wall molybdenum source rate, and core molybdenum density are given. The molybdenum source rate during the diverted phase is a factor of 3 higher than typical values observed for deuterium plasmas.

3 higher than the typical values measured with deuterium plasmas. Note that there seems to be a strong correlation between the molybdenum source and the RF power level for L-mode Helium plasmas, unlike what it has been seen for deuterium plasmas in section 3.1.3. It should be mentioned though that, with deuterium fuel, the plasma would have

already transitioned to some type of H-mode if 2 MW of auxiliary heating had been used and hence the conditions for the two L-mode plasmas are not identical. The core molybdenum density is also higher than usual but it does not correlate with the wall emissions. The reason for the increased molybdenum generation at the inner wall can be attributed to the considerably higher molybdenum sputtering yield for helium projectiles. (For a given target, the sputtering increases with the atomic mass of the incident projectile. For more details on physical sputtering see Chapter 5.)

3.1.7 Inner Wall Molybdenum Emission Profiles

Up until now, only data from the single-fiber viewing system monitoring the inner wall have been presented. However, inner wall molybdenum emission profiles have also been obtained using the available fiber array (see Fig. 3-1) for a variety of conditions. This fiber array monitors most of the lower half of the inner wall extending up to about nine centimeters above the midplane. The profiles shown will not be from separate discharges but from a single one that starts with the plasma being limited at the inner wall, as it is always the case, then gets diverted and later transitions into an EDA H-mode. Three profiles will be given, one for each of the phases mentioned: the limited, the diverted ohmic phase, and the EDA H-mode phase. The times histories of the basic plasma parameters for the discharge analyzed are shown in Fig. 3-14. The inner wall molybdenum source rate, as obtained from the single fiber system, is also shown. It has all the basic characteristics already described in the previous sections. During the EDA H-mode, the source level, although not evident from the figure, increases from its prior level. The profiles analyzed were for the time slices denoted on the figure as "t_1", "t_2", and "t_3". The three inner wall molybdenum intensity profiles are presented in Fig. 3-15. It should be mentioned that signal levels lower than ~0.001 mW/cm^2/st are below the spectrometer's detection limit for the specific viewing system and should not be considered for further analysis. The signals are plotted versus the distance of the imaged location from the Alcator C-Mod midplane. There is a distinct difference between the profile obtained during the limited phase ($t = t_1$) and the other two. The profile for the former exhibits two maxima of unequal magnitude. The position of the maxima is asymmetric with respect to the C-Mod midplane. The bigger of the two maxima is about

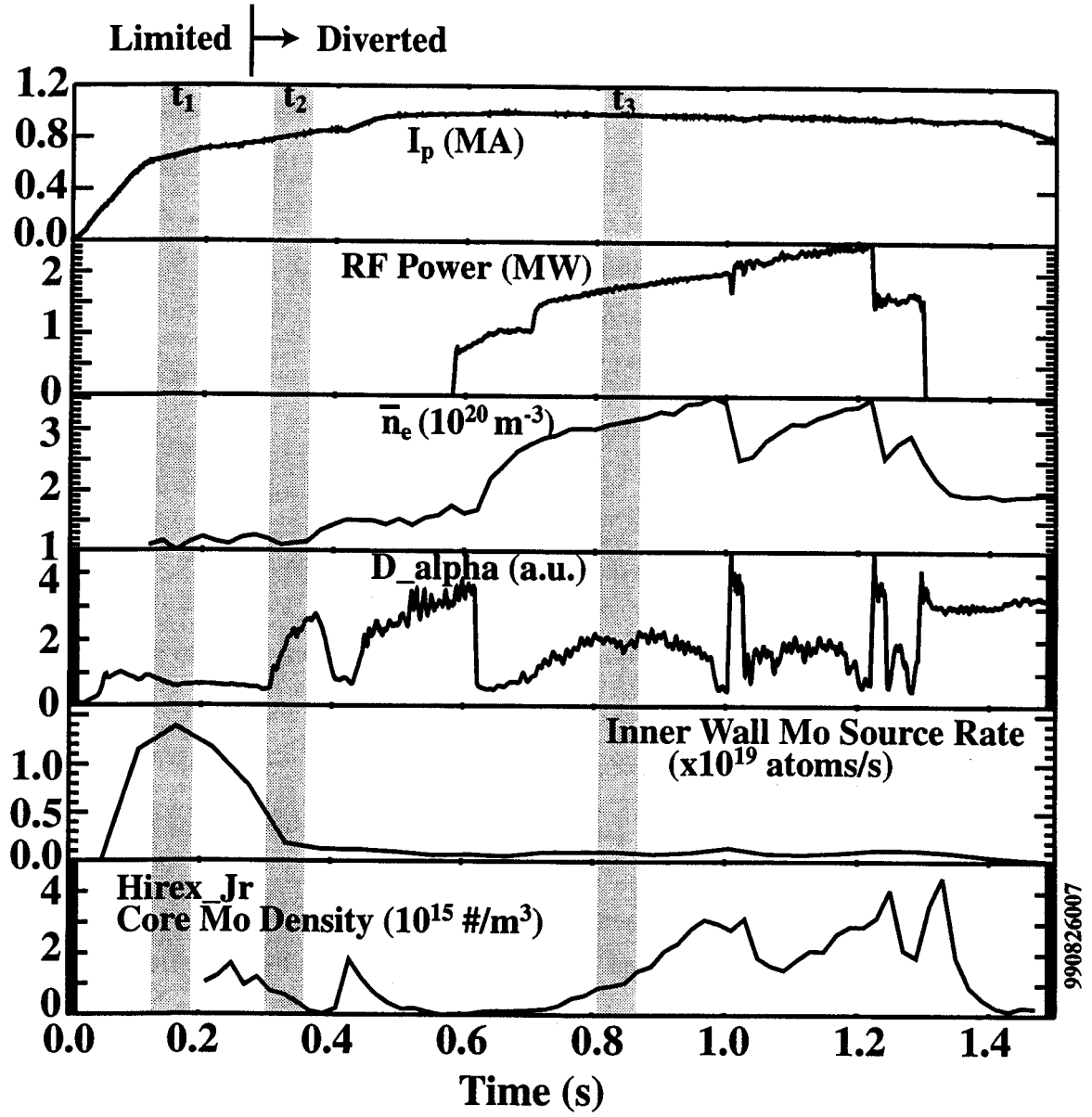

Fig. 3-14: Time histories of the basic plasma parameters and of the inner wall molybdenum source rate for the shot for which the inner wall molybdenum emission profiles are presented in Fig. 3-15. The time slices "t_1", "t_2", and "t_3" indicate the periods for which the profiles are given.

4.5 cm above the midplane while the other is about 3 cm below it. They are actually even more asymmetric with respect to the plasma midplane which is typically one or two cm below the C-Mod midplane. The array's spatial resolution, which is ~2 cm, can not account for the asymmetry. As the plasma gets diverted ($t = t_2$), the smaller of the two

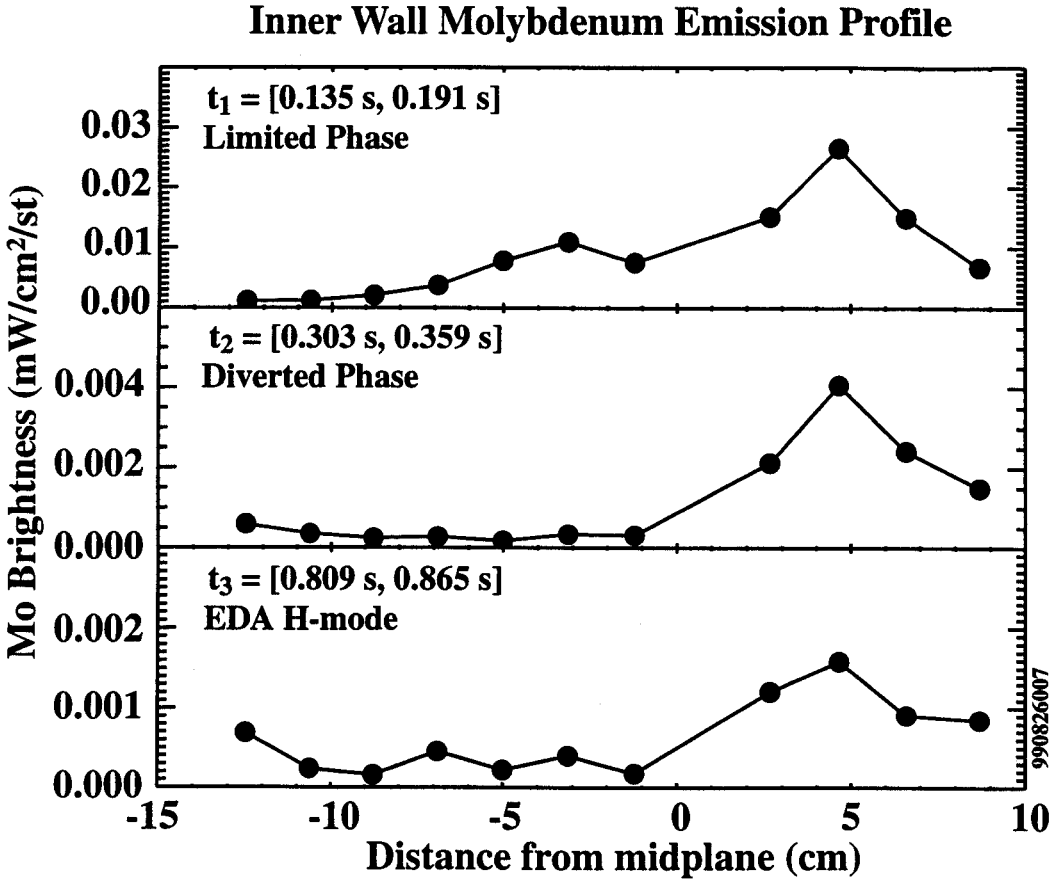

Fig. 3-15: Inner wall molybdenum emission profiles for three different plasma phases: limited, diverted ohmic, and EDA H-mode. The molybdenum brightness is plotted versus the distance from the Alcator C-Mod midplane. Signals levels smaller than ~0.001 mW/cm^2/st are below the spectrometer's detection limit.

maxima disappears and the intensity of the signal for all views drops by a factor of ~ 8 and higher. The specific time period was chosen because the signal actually drops even further later in the ohmic phase, becoming practically undetectable. During this period, the extent of the source is very small and localized around the peak. When the plasma goes into an EDA H-mode ($t = t_3$), the emission levels increase again just above the detection limit for a few of the views around the peak. It is interesting that the location of the single peak for the two last profiles coincides with the location of the bigger of the two peaks for the limited phase. It is possible that the emission profile is still the same in all phases but it can not be distinguished after the plasma gets diverted since the signal in the vicinity of the smaller maximum drops below the system's detection limit. The

existence of two maxima can be attributed to the intersection points of the magnetic flux surfaces with the wall. Finally, it should be noted that no profiles were obtained for any ELM-free H-modes because the signal, in agreement with what it was found for the single fiber system, drops below the detectable level for all views.

3.1.8 Mechanism

As it has already been mentioned, many of the data presented are consistent with physical sputtering being the dominant mechanism responsible for the molybdenum generation at the inner wall. Unfortunately, the inner wall is not a well-diagnosed surface but we have no indication that some other mechanism, such as evaporation, could play a role there. As far as the type of particles causing physical sputtering, there are two possibilities: charge-exchange neutrals from the main plasma or escaping ions. However, the flux of charge-exchange neutrals out of a helium plasma is much lower than for a hydrogenic plasma which contradicts the results presented in section 3.1.6. Hence, ion physical sputtering is the only process that can explain the bulk of the results obtained by monitoring the inner wall.

3.2 The Inner and Outer Divertor Plates

By design, the divertor plates are the regions which are expected to handle most of the power efflux from the main plasma. Therefore, they are the main areas of concern for all tokamaks, regarding intrinsic impurity generation and erosion. However there are differences between the inner and the outer divertor. In Alcator C-Mod, as observed in many tokamaks, there is a strong dependence of divertor plasma parameters, especially an in/out asymmetry, on the ion B $\times\nabla$ B-drift direction [34]. When the toroidal field vector is directed clockwise, as seen from the top, the ions drift downwards. In Alcator C-Mod this is the ''normal'' operating mode. Under these conditions the inner divertor is much colder than the outer divertor. Actually, the inner divertor is typically detached, which as already mentioned implies that the electron temperature T_e is below 5 eV. At such low electron temperatures, the energy, $E_i = (2 + 3\ Z_i + M_i/M_D)\ T_e$ (see Eq. 5.27), of a

deuteron (D) or an impurity ion, with mass M_i and charge Z_i, hitting the target plate is typically below the threshold for physical sputtering of molybdenum, despite the ion's acceleration inside the sheath. As a result, the inner divertor is not a source of significant molybdenum emissions. (The light paths for the inner divertor view are shown in Fig 3-16.) On the contrary the outer divertor has been consistently one of the bigger, if not the biggest, sources of molybdenum observed and much effort has been put in monitoring it, understanding it, and deriving scalings with the various plasma parameters.

The geometry of the outer divertor view can be seen in Fig. 3-17. It should be noted that the exact positions for the imaged spots may change slightly from campaign to campaign. The light paths of these fibers end at divertor plate positions where the domed Langmuir probes 1 through 7, used to obtain local electron temperature and density as a function of time, are situated. If a view that falls in between probes is used, then the data from the adjacent probes are interpolated. Typically 5 or 6 fibers of the Chromex fibers are dedicated to monitoring the outer divertor target. For each one of the fibers used, the molybdenum influx is again calculated from the measured intensity using Eq. 2.2. The total molybdenum source rate is then obtained by integrating, poloidally and toroidally, the molybdenum influxes over the divertor surface. This is done with the assumption of toroidal symmetry, which is actually already employed when the data from Langmuir probes, located in a port different than the outer divertor view, are used.

Figure 3-18 shows the molybdenum source rate for an 800 kA ohmic discharge (see also Fig. 3-2 for the corresponding inner wall data). The striking feature is that although the source levels are pretty high, which will become more evident when compared to data presented in the following sections, they do not seem to correlate at all with the core molybdenum density, as shown by the Hirex Jr. signal. This result is an indication that at least in the ohmic phase the divertor is particularly effective in screening impurities originating at its targets. In any case, as shown by the core molybdenum signal, in ohmic diverted plasmas the amount of molybdenum in the core is very small and is not a source of concern for tokamak operation.

In the following, the effect of various plasma parameters on the divertor source rate will be investigated. Obviously, all data will be from the diverted phase of discharges since during the limited phase, or for limited discharges, there is practically no plasma in

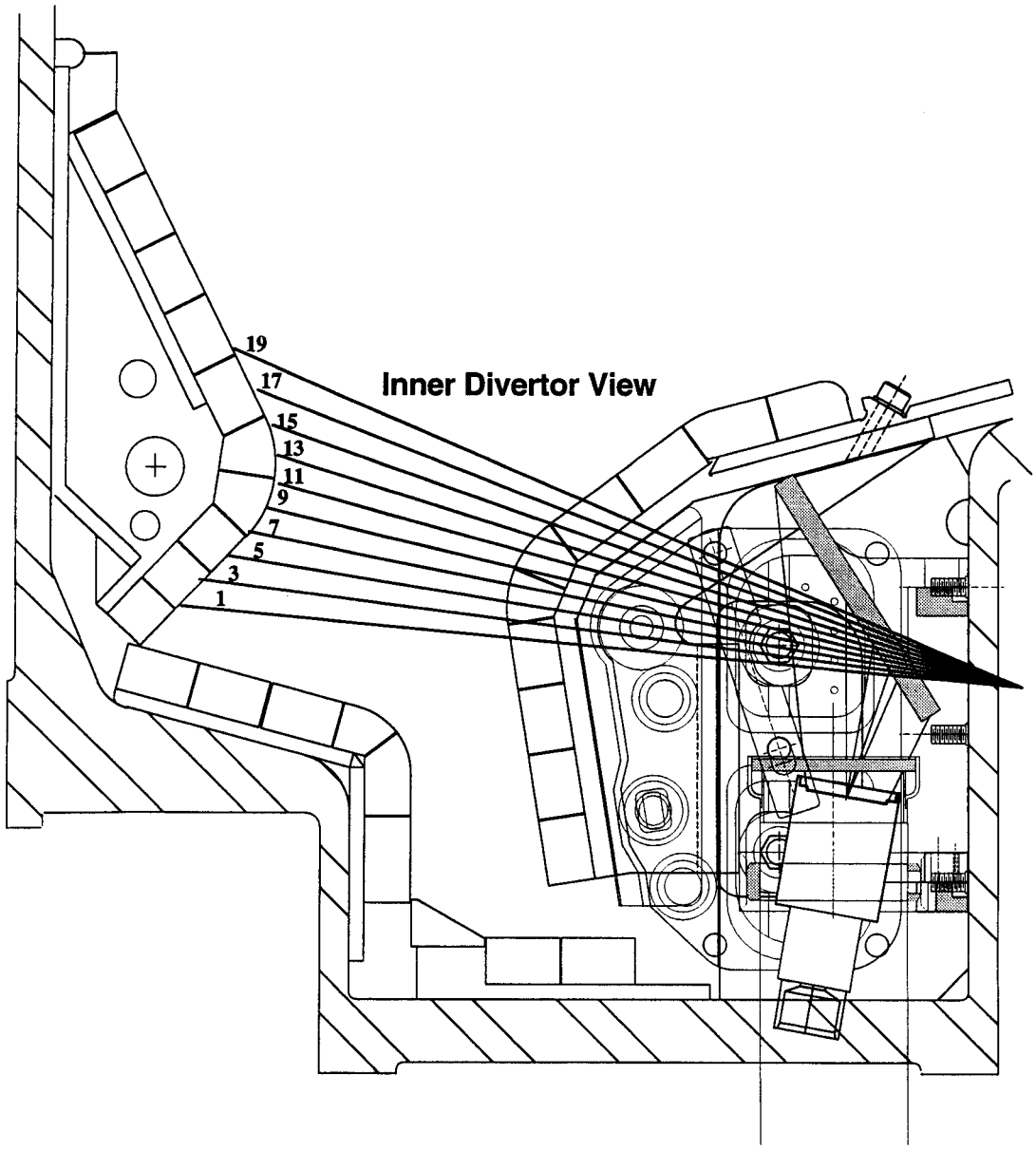

Fig. 3-16: The inner divertor view. The inner divertor is monitored through an opening in the outer divertor.

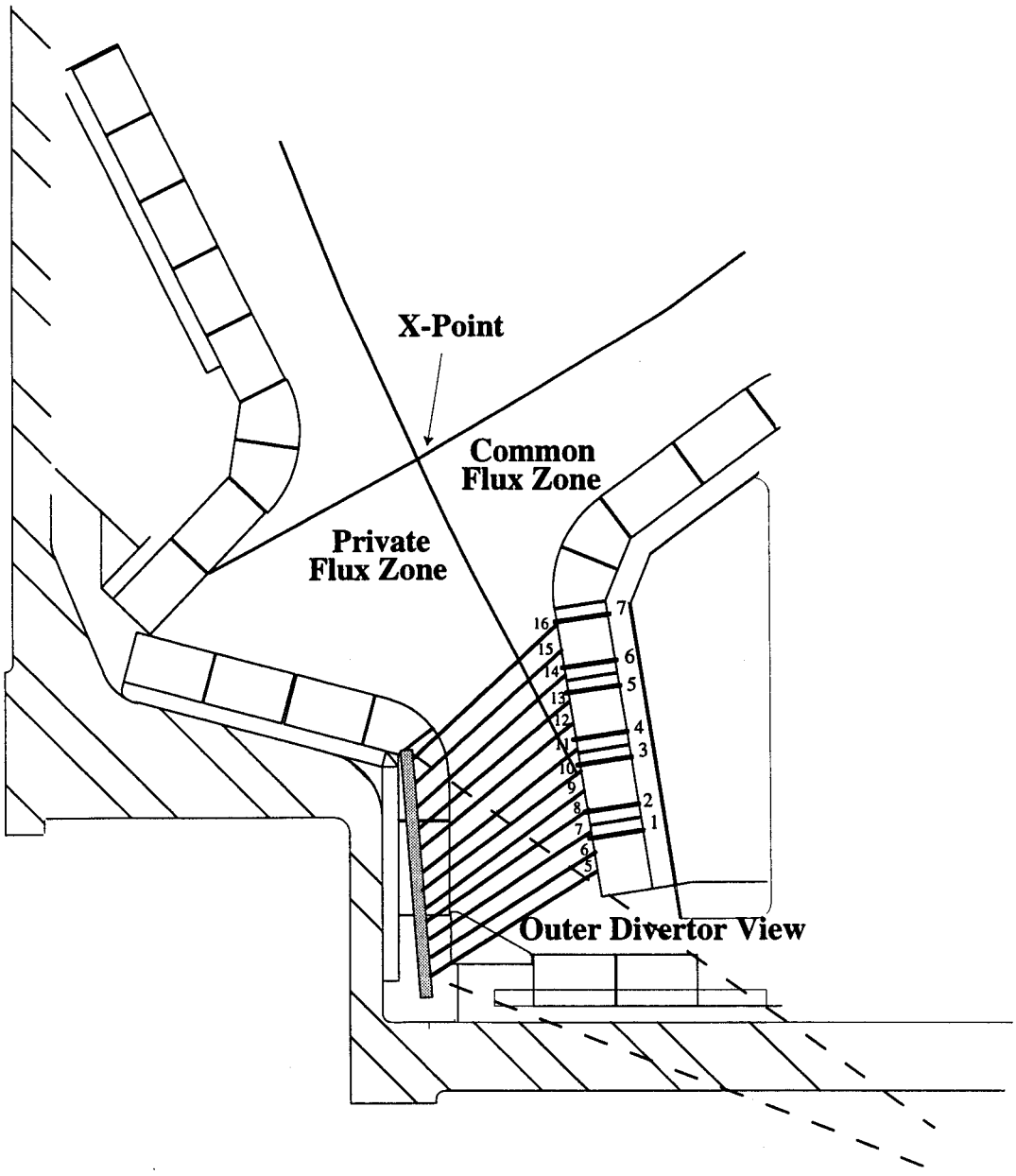

Fig. 3-17: The outer divertor view. The 7 Langmuir probes on the vertical target are also shown.

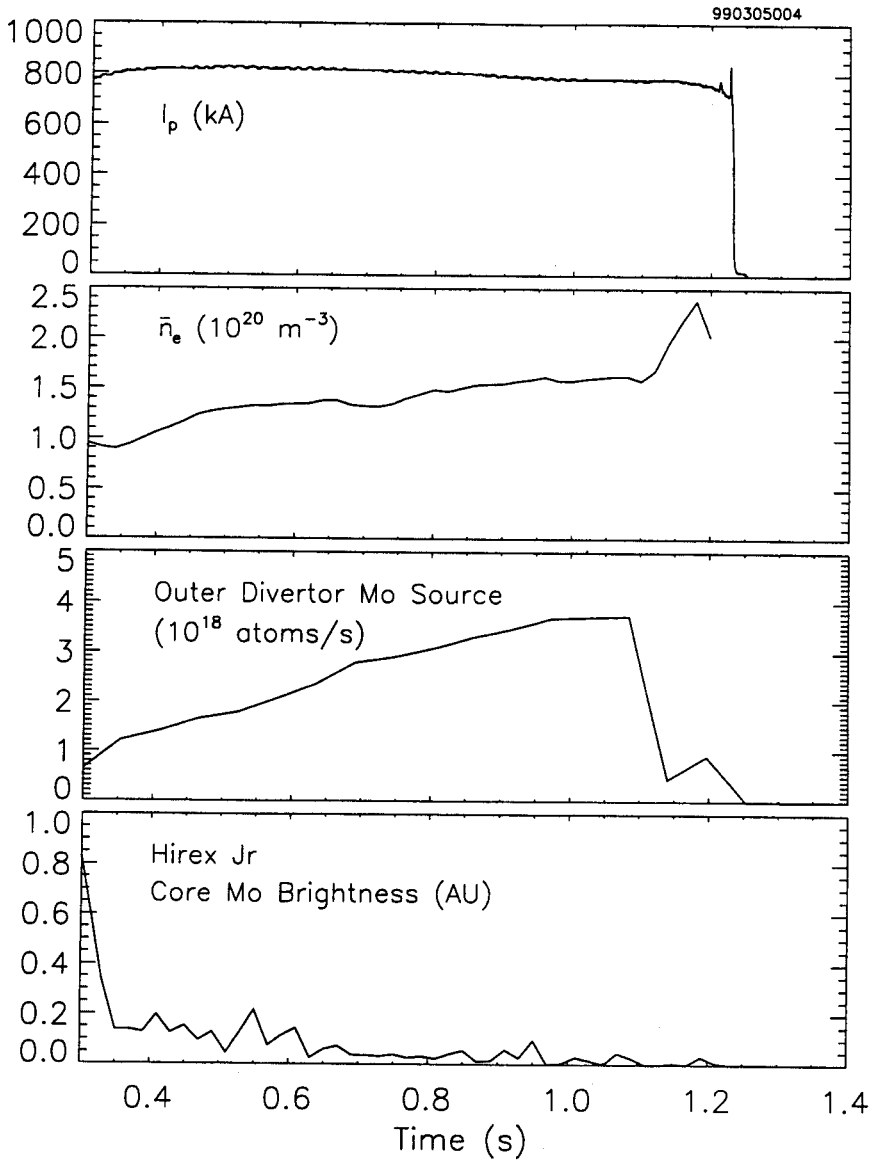

Fig. 3-18: Time history of the outer divertor molybdenum source rate for an ohmic discharge. The plasma current, volume averaged electron density, and core molybdenum brightness traces are also shown. The molybdenum brightness units are the same as the ones used in Fig. 3-2.

the divertor region and the source is zero.

3.2.1 Effect of Plasma Current

Figure 3-19 shows the effect of plasma current on the outer divertor molybdenum source

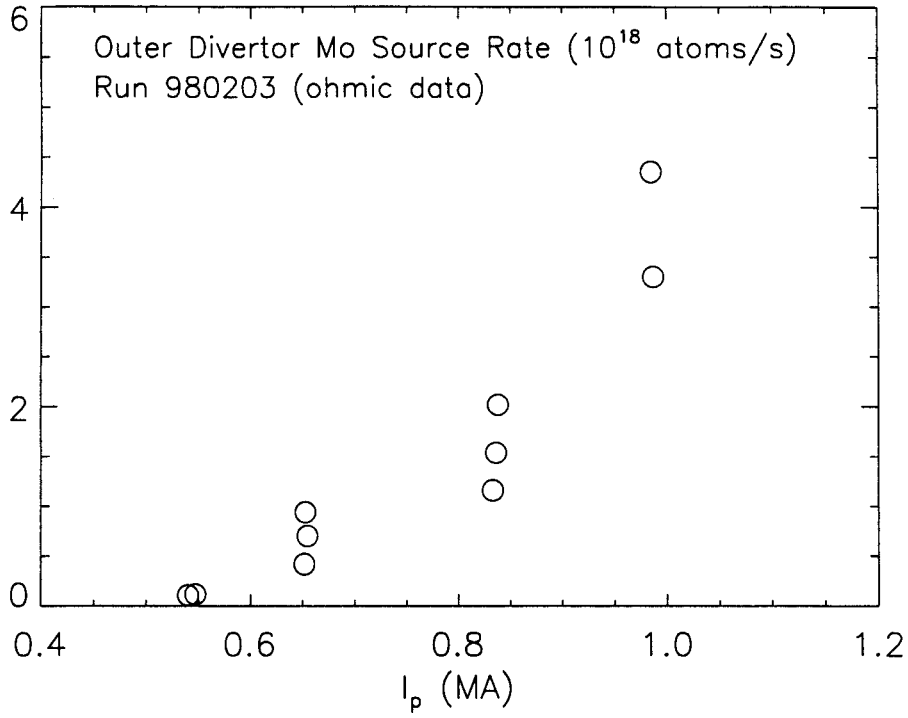

Fig. 3-19: Effect of the plasma current on the outer divertor molybdenum source rate during the ohmic phase of plasmas. The electron density ranges from 1.25 to 1.35×10^{20} m^{-3}.

rate during the ohmic phase of diverted plasma discharges. The data are from a single run with the volume averaged electron density varying only slightly: from 1.25 to 1.35×10^{20} m^{-3}. Similarly to what has already been observed with the inner wall emissions, the outer divertor source rate increases with increasing plasma current, a result that was anticipated since for high plasma currents there is more power available to flow in the scrape-off-layer.

3.2.2 Effect of Electron Density

The electron density levels affect strongly the molybdenum emissions at the outer divertor. Overall, high volume averaged densities imply higher local divertor densities. There are models predicting this relation, which actually depends on the edge plasma regime. (Note that for Alcator C-Mod, LaBombard [16] has identified three distinctive edge plasma regimes: a) ''sheath-limited'' for densities below 1×10^{20} m^{-3} for ~800 kA

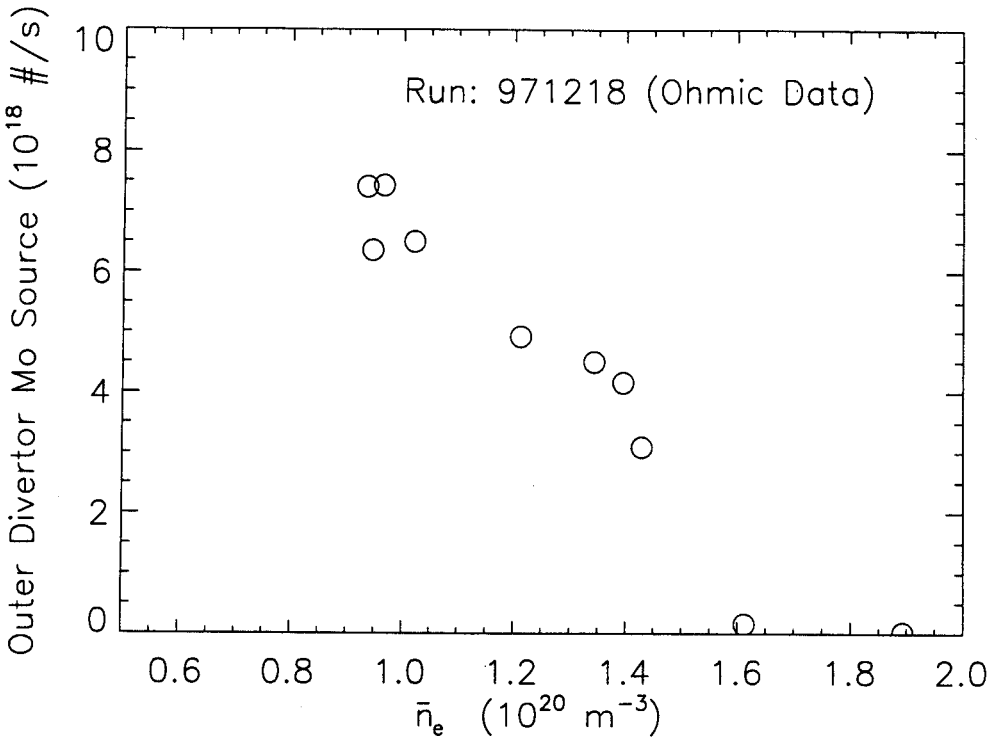

Fig. 3-20: Effect of electron density on the outer divertor molybdenum source rate during the ohmic phase of plasma discharges. The plasma current was 800 kA.

ohmic plasmas, b) ''high-recycling'' for moderate plasma densities 1.5×10^{20} m^{-3} and, c) ''detached'' which as previously mentioned occurs for densities greater than 1.7×10^{20} m^{-3} for ~800 kA ohmic discharges.) Figure 3-20 shows that the molybdenum source rate decreases with increasing density. Although higher densities could correspond, depending on the ion speed or in other words the temperature, to higher fluxes at the target, they also lead to lower edge temperatures which means less energetic projectiles. The latter effect dominates, resulting in reduced physical sputtering and reduced emission.

3.2.3 Effect of RF Power

The outer divertor emissions have been found to depend on the RF power level. An example is shown in Fig. 3-21 where the appropriately scaled molybdenum source rate follows very closely the step change in the RF power level. The data are from a 1 MA, L-mode plasma discharge. The molybdenum core density is also given for the same shot

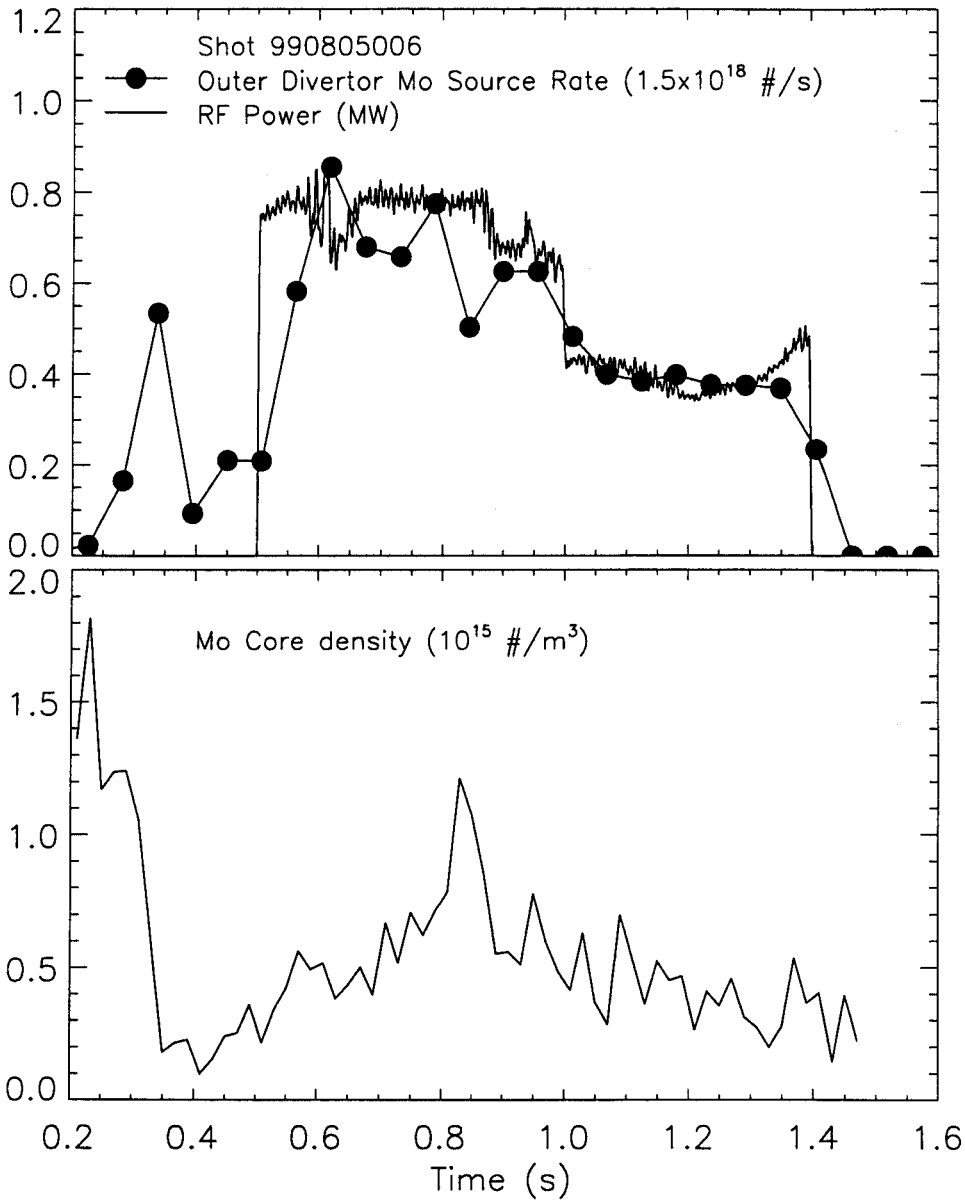

Fig. 3-21: Time histories of RF power, outer divertor molybdenum source rate (top panel) and core molybdenum density (lower panel) for a 1MA, L-mode plasma.

and it also correlates with the RF power. This shot is one of a series of shots, with similar characteristics, which had the RF power changing in discrete steps (see also Fig. 3-6 and Fig. 3-32). As for the inner wall data, averages of the RF power, the molybdenum source rate, and the core molybdenum density were taken during each of the RF power steps. The results are plotted in Fig. 3-22. Unlike what was found for the inner wall, the molybdenum source correlates with the RF power level and hence with the molybdenum

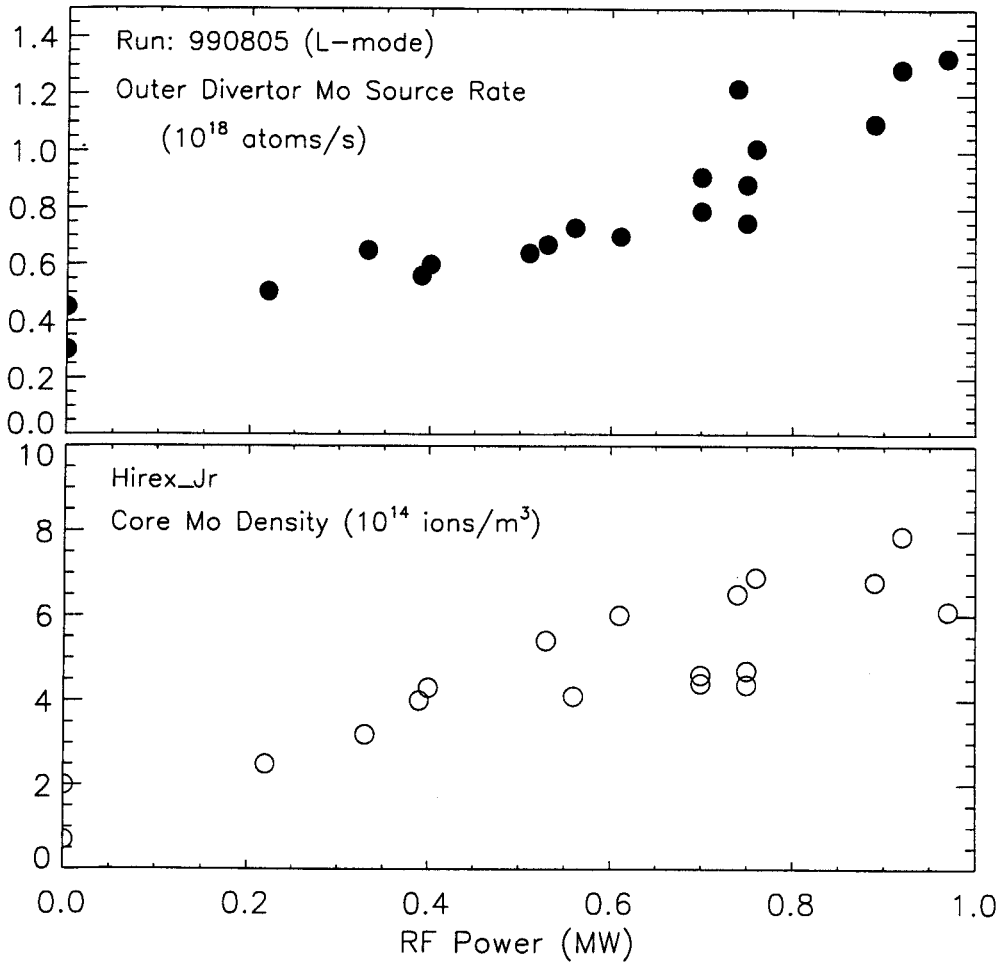

Fig. 3-22: Outer divertor molybdenum source rate and core molybdenum density versus RF power for 1MA, L-mode plasmas.

core density. However, this does not necessarily mean that the outer divertor is the source of the molybdenum that ends up in the core since not all molybdenum sources are investigated here. On the contrary, in the remainder of this thesis, other cases will be shown that indicate that most of the molybdenum that originates from the outer divertor is well screened by the plasma and does not end up in the core. In addition, recalling the ohmic data presented in Fig. 3-18, where the divertor molybdenum source rate reached values close to $4. \times 10^{18}$ atoms/s without any observable effect in the core molybdenum levels, it is difficult to believe that, during L-mode discharges, lower divertor molybdenum levels would dominate the core molybdenum density.

3.2.4 Effect of Transport

As found for the inner wall, the type of plasma confinement has an effect on the molybdenum emission levels from the outer divertor. Specifically, it is observed that when the plasma transitions into an ELM-free H-mode, the emissions drop sharply. This is illustrated in Fig. 3-23, for the same shot that was used in the investigation of the effect of the ELM-free H-modes to the inner wall data. This effect is again attributed to the

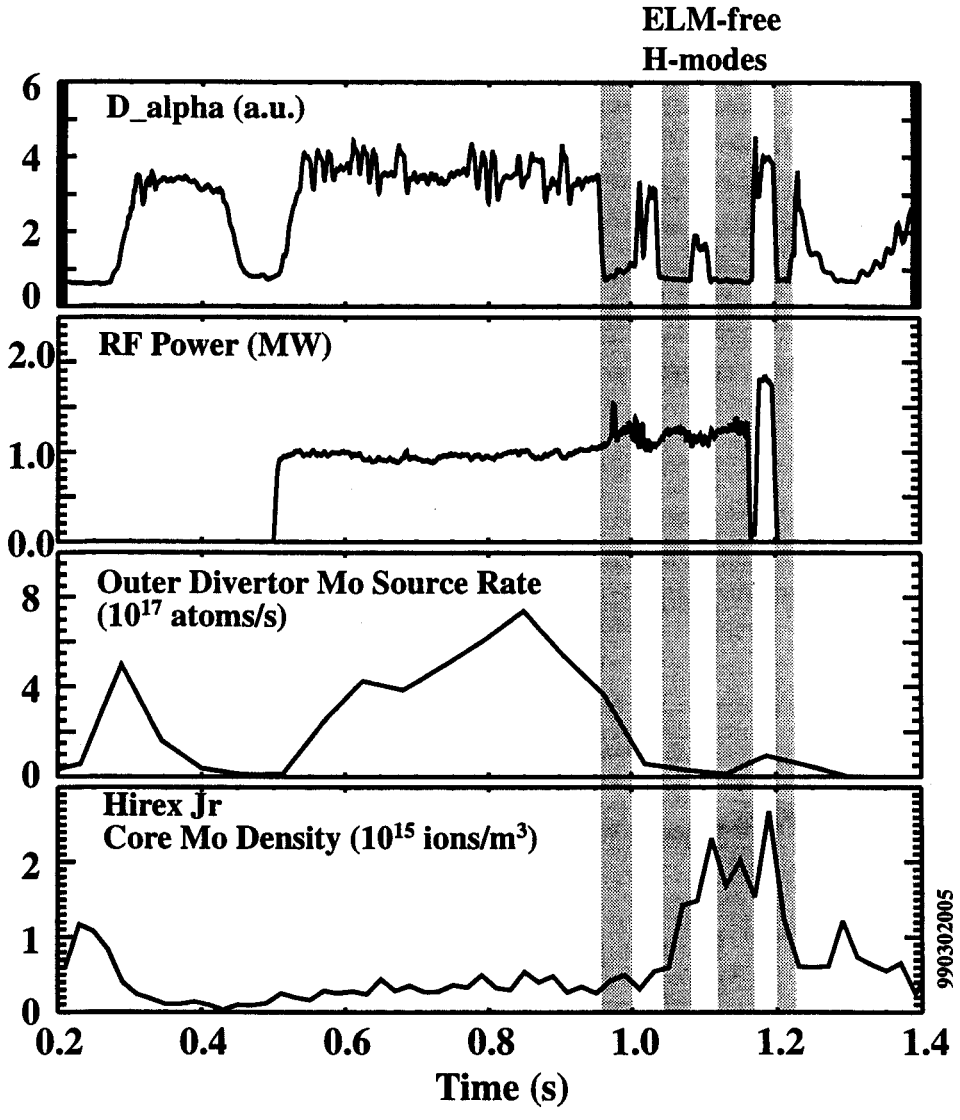

Fig. 3-23: Effect of ELM-free H-mode to the outer divertor molybdenum source rate. The time histories of the D_α signal, the RF power, the divertor molybdenum source rate, and the core molybdenum density are plotted.

reduction of the scrape-off-layer width that is observed during ELM-free H-modes. Comparing the molybdenum source and core data, we should mention that there is an anti-correlation between them, which is an important indication that the divertor plate is not the origin of the molybdenum found in the core, although if the core impurity confinement time is infinite no other source would be needed.

In Fig. 3-24 the effect of the EDA H-mode is investigated. It is hard to identify if the EDA H-mode has any effect on the source rate or the source rate level simply increases

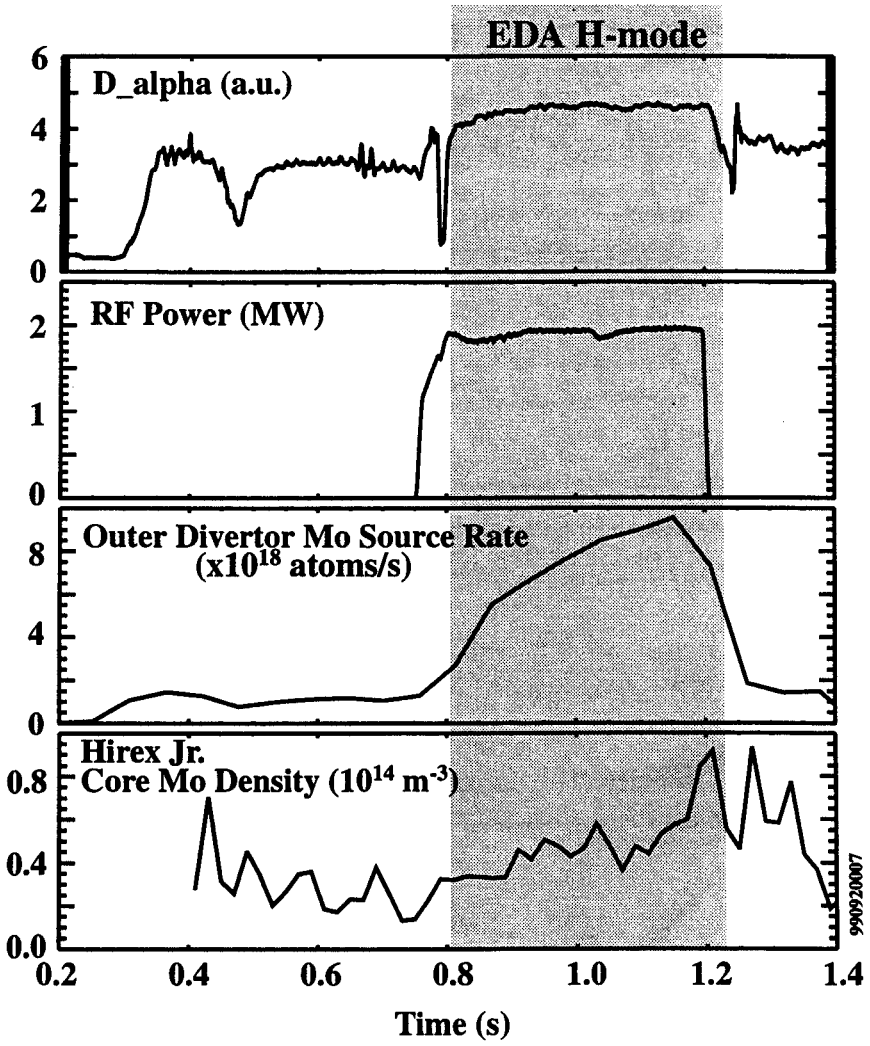

Fig. 3-24: Effect of EDA H-mode to the outer divertor molybdenum source rate. The time histories of the D_α signal, the RF power, the divertor molybdenum source rate, and the core molybdenum density are plotted.

due to the RF power launched into the plasma. However, if the source rate level during the EDA H-mode ($\sim 8 \times 10^{18}$ atoms/s) is compared to rates measured during typical L-mode shots, it looks as if the RF power alone can not explain the observed emissions. Of course, one should be careful when comparing source rates from two different run days because changes in the surface conditions could have an effect on the molybdenum emissions. To be conclusive, data from a dedicated experiment are needed that will investigate if the EDA H-modes play any role at all in the divertor molybdenum emissions or the observed increase in the source is due to the RF power only.

3.2.5 Molybdenum Emissions in Helium Plasmas

We have seen that for helium plasmas, the molybdenum emissions from the inner wall increase by about a factor of 3 compared to the typical levels measured during deuterium plasmas. The observed enhancement is even higher for the case of the outer divertor. Figure 3-25 compares the molybdenum source rate at the outer divertor for a deuterium and a helium plasma. Similar RF power levels (~ 2.5 MW) are launched into the plasma, as seen in the top panel. The plasma with the deuterium fuel transitions into an EDA H-mode for the period that the RF is on while the helium plasma stays in L-mode. We observe that in L-mode helium plasmas the measured molybdenum source rate is 10 times higher the one measured in EDA H-mode deuterium plasmas (in the figure the molybdenum source for the deuterium plasma has been multiplied by a factor of 10 for all times). As previously mentioned, the increased molybdenum emissions for helium plasmas can be explained by the higher sputtering yield when molybdenum is bombarded by helium ions compared to when it is bombarded by deuterons. As far as the effect on the core is concerned, the molybdenum density is only three times higher for the helium plasma (bottom panel), much lower than the corresponding increase in the outer divertor source rate. However, it is not straightforward to compare L-mode and EDA H-mode plasmas. Not only because they are characterized by different impurity confinement times, being a few times larger in EDA H-modes, but, in addition, because other parameters, such as the density, may play a role. With increasing electron density (as is the case in EDA's), the penetration of impurities in the plasma becomes harder, possibly

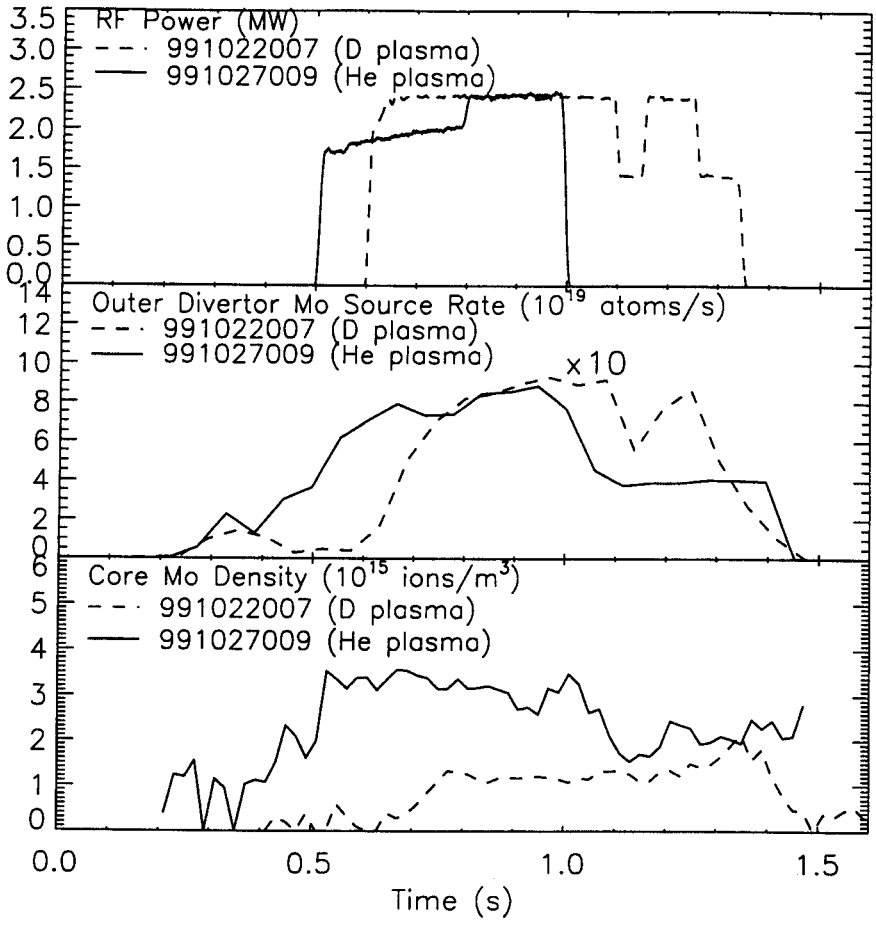

Fig. 3-25: Effect of helium plasmas on molybdenum emissions from the outer divertor. The divertor molybdenum source rate is plotted (middle panel) for two discharges, one with helium fuel and one with deuterium fuel. The curve for the deuterium plasma is multiplied by a factor of 10. The RF power level is comparable for both shots (top panel). The core molybdenum density is drawn at the bottom panel. The deuterium discharge goes into an EDA H-mode when the RF turns on while the helium plasma stays in L-mode.

because they are ionized further outside in the scrape-off-layer.

3.2.6 Outer Divertor Molybdenum Emission Profiles

As already mentioned, the outer divertor source rate is calculated by integrating the molybdenum influxes measured with the 5 or 6 fibers that are typically allocated for monitoring the vertical outer divertor target. Thus, there is almost always information on the molybdenum emission profile. This information is valuable since it shows which

parts of the divertor, and under which conditions, are more affected by the interaction with the plasma.

Figure 3.26 shows the time histories of the RF power, the D_α signal, the molybdenum influx for views 10, 12, 14, 15, and 16 (See Fig. 3-17), and the molybdenum source rate for a discharge that after about 0.87 s essentially transitions into an ELM-free H-mode. In terms of the molybdenum source rate, this shot has all the typical characteristics that have already been presented: When the RF turns on, and during the L-mode, the emissions are higher compared to the ohmic phase. When the transition to the ELM-free H-mode occurs, the molybdenum source rate drops. However, the molybdenum influx does not show the same time behavior at all locations along the target. It should be noted, though, that one should be careful to account for movements of the separatrix with respect to the target. As the "strike point", the intersection of the separatrix with the divertor target, moves, the conditions on the location monitored by the spectrometer chords can change as a result of this movement and not due to a possible simultaneous change in the plasma phase. This is because a point on the target may move, for example, from the "private-flux-zone", the cold plasma region bounded by the divertor targets and the plasma separatrix below the X-point, to the "common-flux-zone", the region outside the separatrix, excluding the private-flux-zone, which is characterized by higher temperatures and fluxes (see Fig. 3.17). Figure 3-27 shows three emission profiles, one for each of the time slices that are indicated in Fig. 3.26 as "t_1", "t_2", and "t_3" and correspond to the ohmic, the L-mode, and the ELMF-free H-mode respectively. The profiles are plotted as a function of the distance of the location imaged on the target from the point monitored with view # 8. This was chosen arbitrarily and hence the relative distance along the target is what is important. The approximate location of the separatrix for all profiles is also drawn. It should be noted that there are uncertainties both in the actual positions monitored and the location of the separatrix but they do not change the main results obtained. It is observed that in the ohmic and L-mode phases the influx peaks away from the plasma separatrix. In the ohmic phase the profile is rather flat in the region of the strongest activity while for the L-mode the emissions are stronger as we move higher on the plate. Actually, there are other discharges in which the profile during the L-mode is more flat, looking closer to what we observe for the ohmic phase. However, the profile is

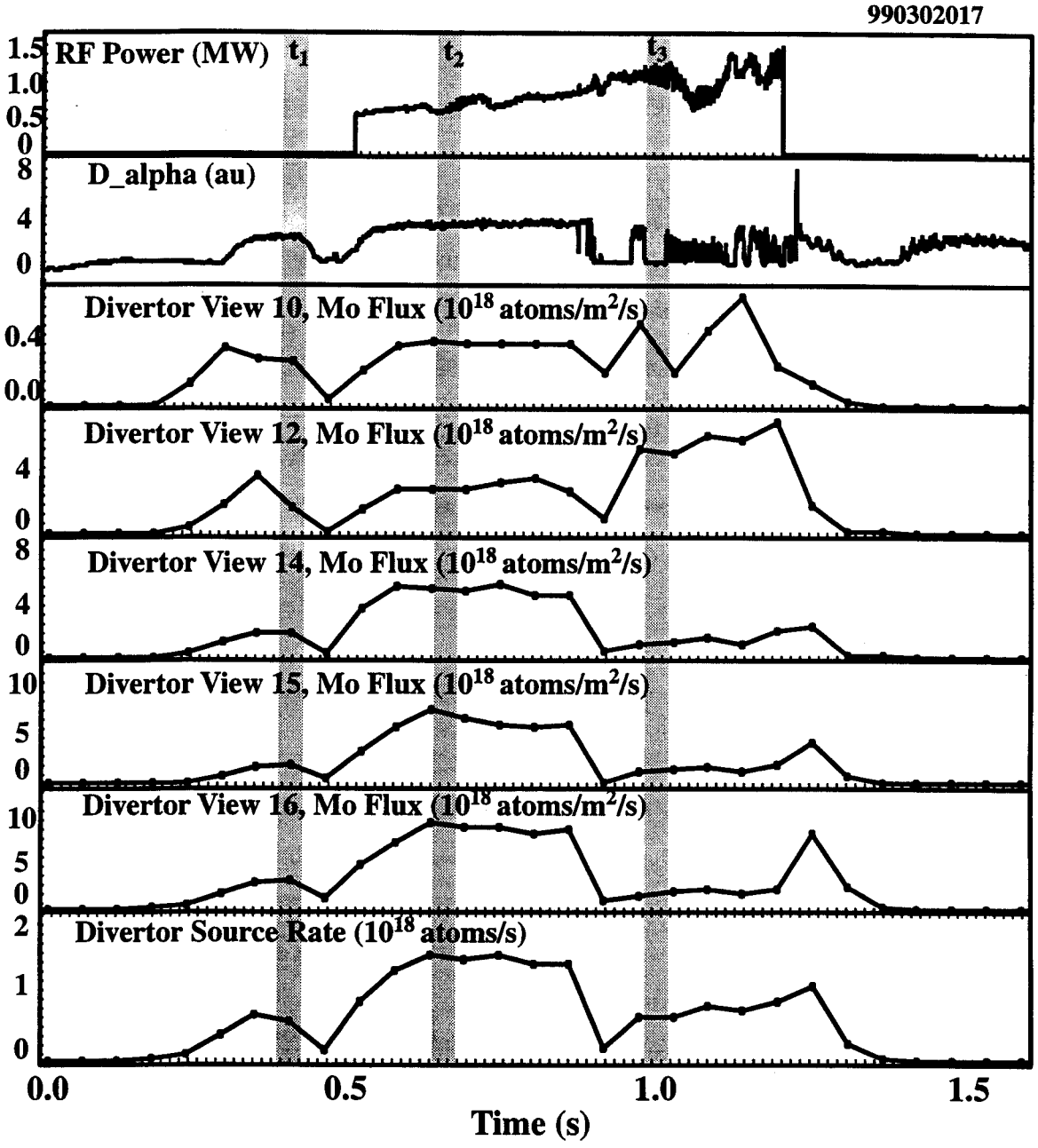

Fig. 3-26: Time histories of the RF power, the D_α signal, the molybdenum influx for views 10, 12, 14, 15,16, (see Fig. 3-17) and the molybdenum source rate for the discharge that the outer divertor emission profiles are shown in Fig. 3-27. Times "t_1", "t_2", and "t_3" indicate the periods for which the profiles are given.

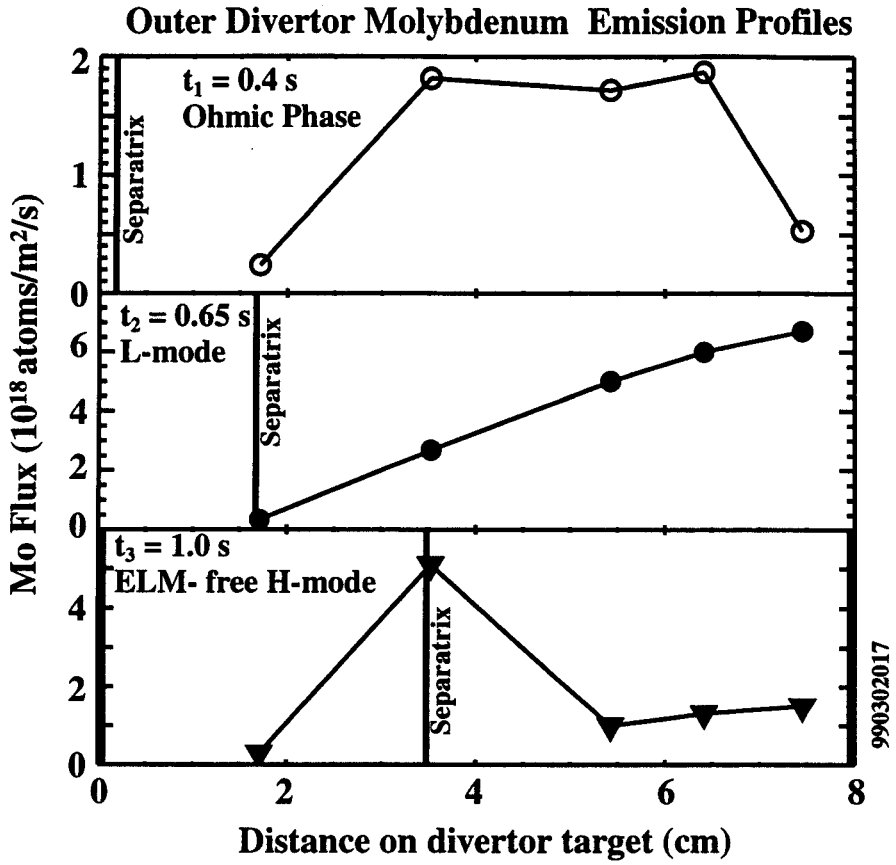

Fig. 3-27: Outer divertor molybdenum influx as a function of the location on the divertor target for ohmic, L-mode, and ELM-free H-mode conditions. The data were taken with views (from left to right) 10, 12, 14, 15, and 16. The location monitored with view # 8 was arbitrarily taken as the reference point from which the distance on the target is measured. The approximate location of the separatrix is also shown.

distinctly different during the ELM-free H-mode. The molybdenum emissions now peak around the separatrix. The emissions have also decreased in all locations with the exception of the area around the separatrix where they have increased compared to the L-mode values. This change in the emission profile is consistent with the reduction in the scrape-off-layer width that is observed in ELM-free H-modes.

An example of an outer divertor molybdenum emission profile during an EDA H-mode is given in Figs. 3-28 and 3-29. Views 10, 12, 14, and 16 were used for these data. In Fig. 3-28 the time histories of the RF power, the D_α signal, the molybdenum influxes, and the molybdenum source rate are given. The plasma goes into an EDA H-mode after 0.65 s.

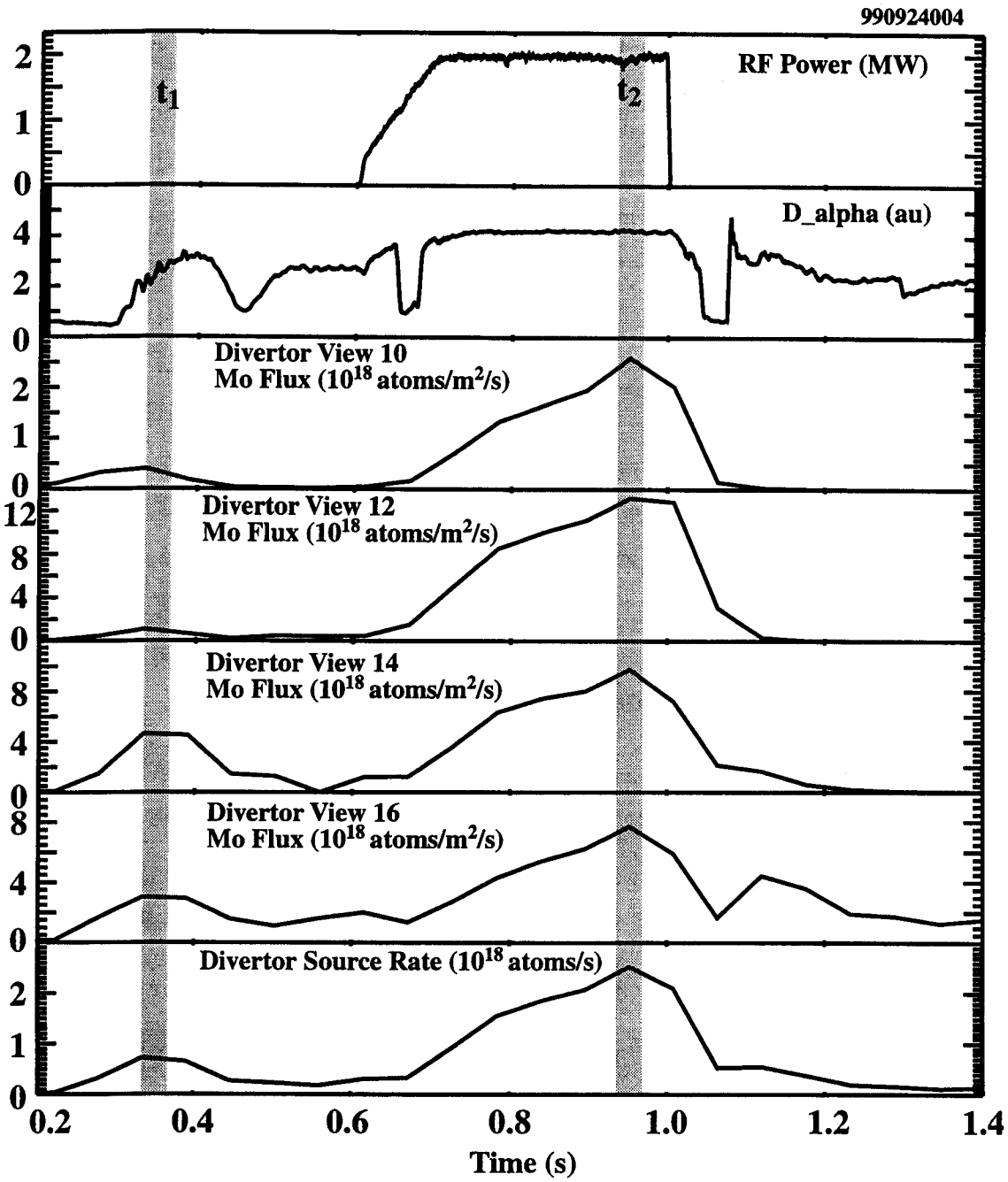

Fig. 3-28: Time histories of the RF power, the Dα signal, the molybdenum influx for views 10, 12, 14, 16, and the molybdenum source rate for the discharge that the outer divertor emission profiles are shown in Fig. 3-29. Times "t_1" and "t_2" indicate the periods for which the profiles are given.

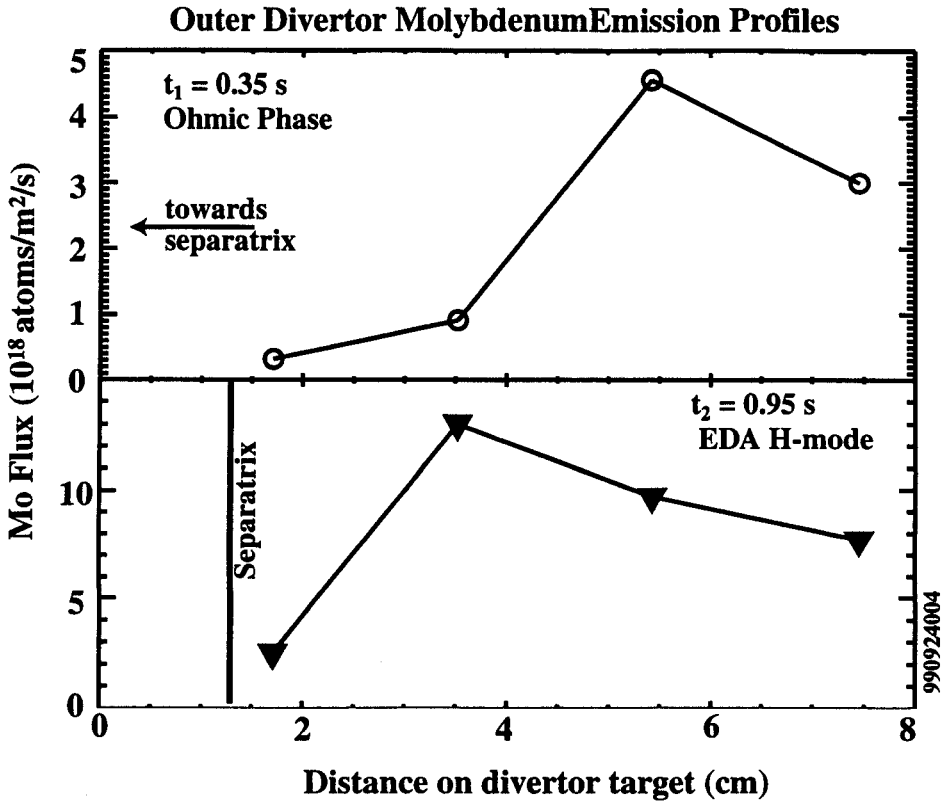

Fig. 3-29: Outer divertor molybdenum influx as a function of the location on the divertor target for ohmic and EDA H-mode conditions. The data were taken with views 10, 12, 14, and 16.

The transition leads to an increase of the molybdenum signal in all spectroscopic channels, and hence in the molybdenum source rate, in agreement to what has already been discussed in section 3.2.4. Two profiles are shown in Fig. 3-29. One during the ohmic phase ($t = t_1 = 0.35$ s) and one during the EDA H-mode ($t = t_2 = 0.95$ s). The molybdenum emissions for the ohmic phase peak again away from the separatrix. During the EDA H-mode, the emissions peak closer to the separatrix but still clearly in the common-flux-zone, unlike the ELM-free H-modes where they were found to be stronger at the vicinity of the strike point.

3.2.7 Mechanism

The measured outer divertor molybdenum emissions are generally consistent with expectations, assuming that physical sputtering is the dominant molybdenum generation

mechanism. In addition, the Langmuir probe data also indicate that the molybdenum emission patterns, such as those shown in the previous section, are related to the profiles of the electron temperature and the ion flux to the target. For this reason, and due to its importance, this subject is investigated extensively in Chapter 5 where a simple sputtering model is developed that successfully calculates the outer divertor molybdenum influx.

3.3 The Antenna Protection Tiles

During the first years of this study, the outer divertor and the inner wall were the only surfaces that had been identified as significant emitters of molybdenum. However, the lack of consistent correlation between molybdenum sources and core molybdenum concentration in diverted plasmas meant that not all sources of molybdenum had been identified. For this reason a number of spectroscopic views were allocated to monitor the emission levels from various candidate surfaces, including the three C-Mod (outer) limiters and the (then) two ICRF antennas. All these views were aimed towards the machine midplane. However, none of the above surfaces ended up being strong sources of molybdenum nor correlated with core molybdenum density levels. Emissions from the limiters were occasionally observed but there was no systematic correlation with core molybdenum levels. On the other hand, no molybdenum at all was found to be emanating from the vicinity of the antennas at the midplane. Then, during the 1998 run period, a fast CCD camera [35] monitoring the antennas revealed hot regions (glowing) at, and injections originating from, the top of the D-port antenna. During the vacuum vent that followed the 1998 campaign, significant erosion, that had characteristics of both arcing and melting, was found along the top "protection" tiles of both (D & E) antennas. These tiles, which surround the C-Mod antennas, are intended to minimize the interaction of the plasma with the antennas. It should be noted that the antenna protection tiles are 5 mm further away from the plasma than the outer limiters which were not an important molybdenum source. (A picture of the D and E-port antennas, together with the protection tiles, is given in Fig. 3-30.) As a result of the findings mentioned above, the antenna midplane spectroscopic views were reoriented prior to the 1999 run campaign to

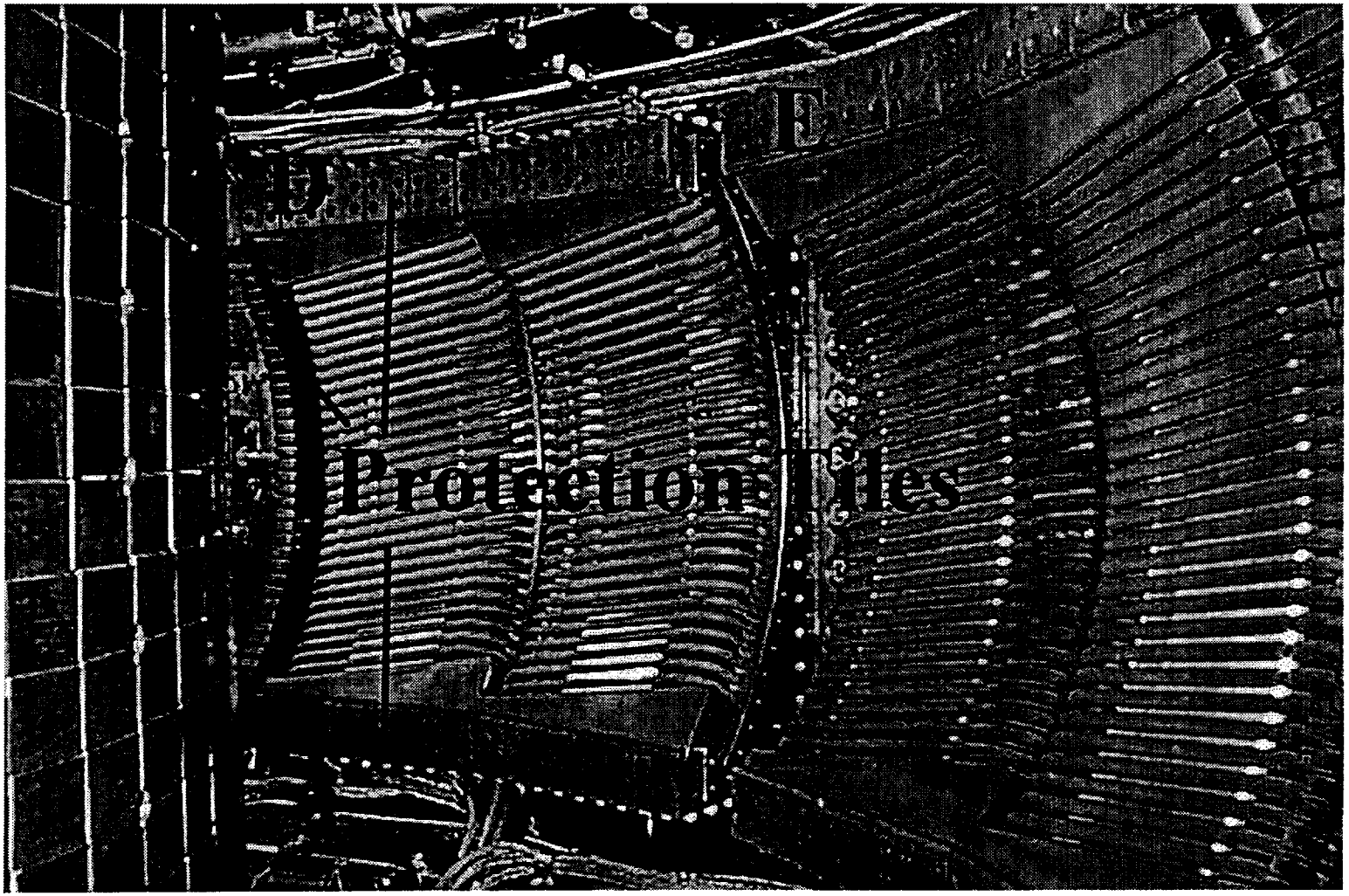

Fig. 3-30: A photograph of the D and E-port Antennas. The protection tiles around the D-port antenna are noted. Our spectroscopic views are directed towards the top protection tiles for both antennas.

monitor the D and E-port antenna tops. The results obtained during the 1999 campaign verified that the top protection tiles constitute important sources of molybdenum during ICRF heating. The most important findings regarding these sources will be presented in the following sections. Due to the fact that the specific spectroscopic views became available only recently, scalings of the sources with parameters such as density, plasma current and right gap have not been investigated. The reason is that, as it will be shown, the antenna molybdenum source rate depends strongly on the RF power level and proper investigation of the above parameters required dedicated experiments. However, for the right gap, there are indications from the available data that it does not affect the antenna emission levels but it still needs further investigation. It should be noted that from now on any reference to antenna emissions will actually refer to emissions from the antenna top protection tiles and not the antennas themselves.

The molybdenum source rate from the top protection tiles of each of the two (D and E) antennas is calculated from the single fiber measured influx, Γ (Eq 2.2):

$$\Phi_{Ant} = \pi R_{Ant}^2 \Gamma = 4\pi^2 R_{Ant}^2 I (S/XB). \quad (3.2)$$

In the above expression, R_{Ant} is the radius of the area viewed by the fiber, which is calculated using the spectrometer's *f*-number ("*f* /4.0") rather than the fiber's ("*f* /2.2"), as was also done for the single fiber system that monitors the inner wall. This distance is $R_{D,Ant}$ = 12.34 cm for the D antenna view and $R_{E,Ant}$ = 17.34 cm for the E antenna view. A constant value (= 3.26) was used for the ***S/XB***, independently of plasma phase and conditions. It was calculated for "typical local" plasma parameters (T_e = 30 eV, n_e = $2x10^{19}$ m^{-3}), based on fast scanning probe data.

3.3.1 Effect of RF Power

The effect of the RF power on molybdenum source rates from the antenna protection tiles was studied not only during routine antenna operation but also in dedicated experiments in which the RF power level was supplied in steps during a shot. This was important because changes in surface conditions from a run day to another, mainly due to boronization (see Chapter 4), could mask out possible correlations.

Figures 3-31 and 3-32 give two examples of the time history of the E antenna

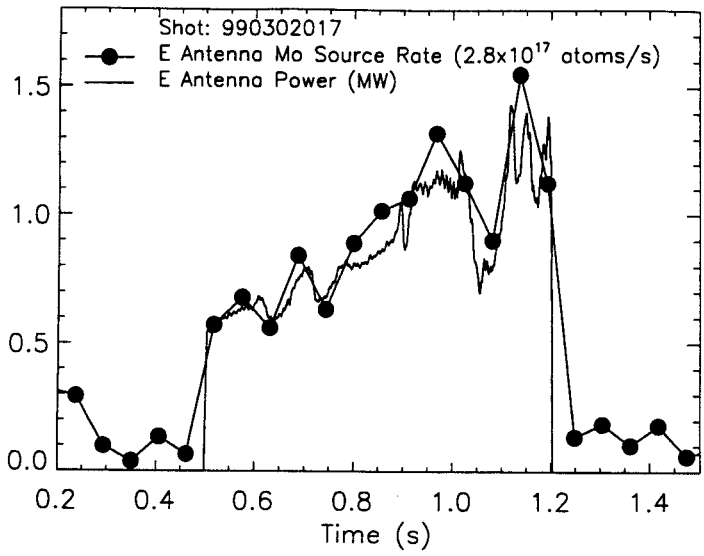

Fig. 3-31: Time history of the E antenna molybdenum source rate for a discharge in which the E antenna power is ramped from 0.6 to 1.4 MW and no other antenna is on. The plasma goes into elm-free H-mode at 0.87s.

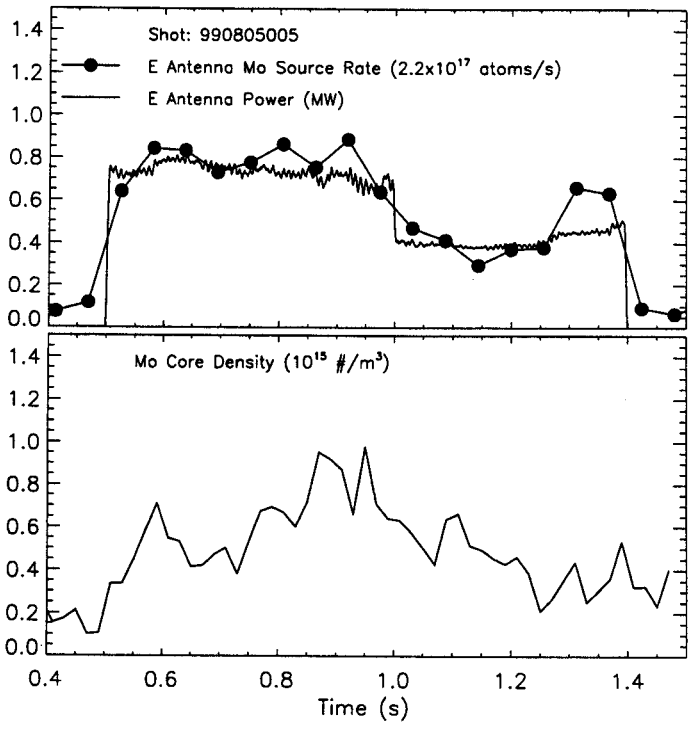

Fig. 3-32: Time history of the E antenna molybdenum source rate for a discharge in which the E antenna power is stepped down from 0.75 to 0.4 MW and no other antenna is on. The core molybdenum density is also plotted. The plasma stays in L-mode for the whole shot.

molybdenum source rate for shots that the E antenna RF power was changing in a controlled way and no other antenna was energized. In Fig. 3-31 the plasma goes into an elm-free H-mode around 0.87 s, a transition which does not seem to affect the source rate. As will be shown in section 3.3.2 after analyzing data from a number of shots, the confinement mode has no effect on the antenna molybdenum source rate, in contrast to what is observed for the outer divertor and inner wall source rates. In Fig. 3-32 the plasma stays in L-mode for the duration of the shot. As can be seen from both figures the molybdenum source rate is clearly correlating with the RF power level. It also correlates pretty well with the core molybdenum density as shown in Fig. 3-32. However, the effect of the RF power on the E antenna molybdenum source is not as strong when it is the D antenna that supplies the power to the plasma. This is evident from Fig. 3-33 which shows the E antenna molybdenum source rate (second panel from the top) for shots 991021016 and 991021017. These discharges had comparable plasma parameters, with the density being slightly higher in the former. Their basic difference was that only E antenna was turned on in the 991021016 while only D was on in 991021017. The RF pulse was, for all practical purposes, identical in the two shots. In both cases the power was ramped from 0.75 MW to 1.5 MW between 0.6 and 1.5 s. Both plasmas transitioned into ELM-free like H-modes. The transition occurred at 1.0 s in the 991021016 shot and a bit earlier (0.95 s) in the 991021017 shot. The measured source rate from E antenna is not only significantly smaller when the D antenna is supplying the RF power but it is also independent of the RF power level. The latter observation can not be generalized since there are discharges where the E antenna source rate seems to follow the D antenna RF power. However, in general the correlations of the E antenna molybdenum source rate with the RF power level are weaker when the RF power is provided by the D antenna only. Similar conclusions can be drawn for the molybdenum emission from the D antenna. . Once again the source observed is higher when the RF power is supplied by the antenna in question (D), rather than the other antenna (E). This is also illustrated in Fig. 3-33 (third panel from the top). Similarly to what has already observed with the E-port antenna, the D antenna source rate seems to follow, although not as strongly, the RF power only when the D antenna is on. There is, however, a significant difference from the findings for the E antenna. The measured D antenna source rate is typically two to three

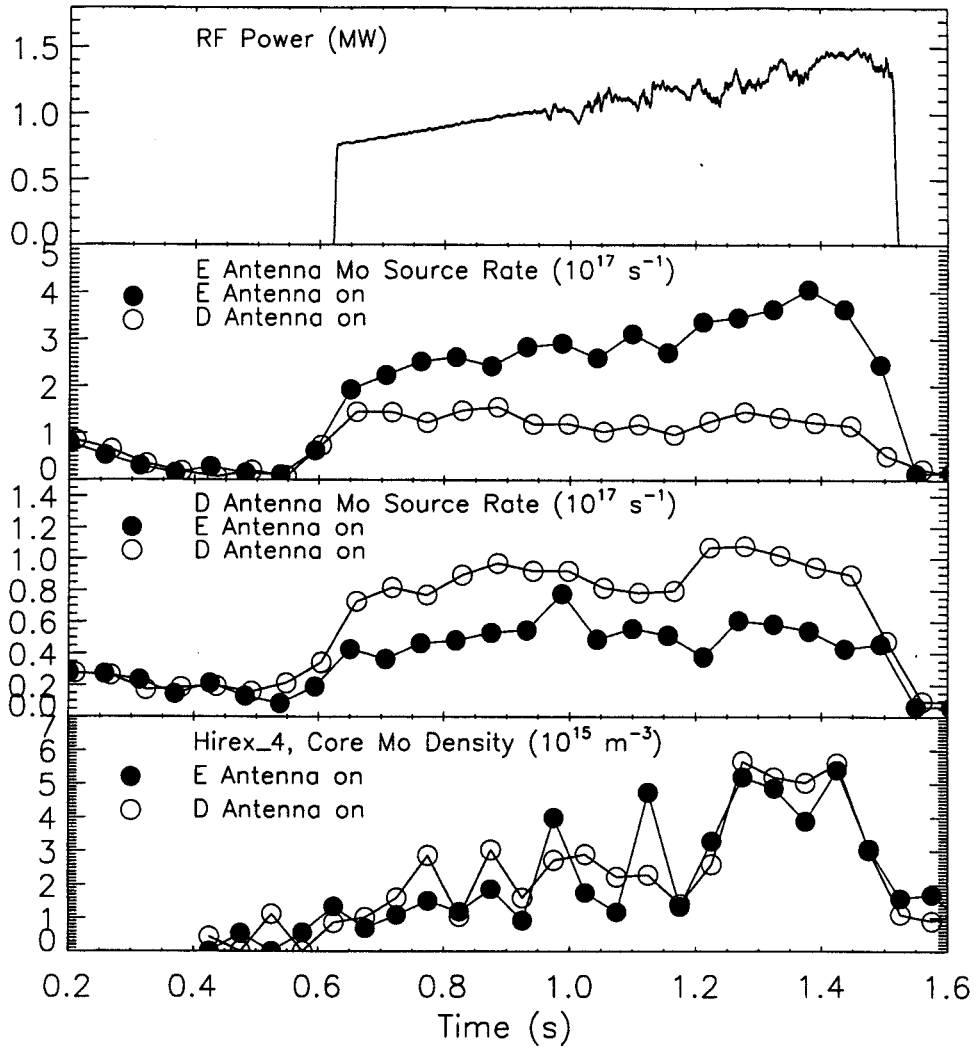

Fig. 3-33: Comparison of the E antenna (second panel from top) and D antenna (third panel) molybdenum source rate for two plasma discharges (991021016 and 991021017) with similar characteristics, in which two different antennas (E and D respectively) were used to provide the same RF pulse. In the figure, the RF pulse from D antenna (discharge 991021017) is shown, but it was for all practical purposes identical to the E antenna RF pulse. The core molybdenum is also plotted for the two discharges.

times lower than the corresponding one from the E antenna for similar RF power pulses. This difference is too big to be attributed in possible intensity calibration uncertainties. For this reason our focus was placed mainly in obtaining correlations with the E antenna source rates, and specifically with the E antenna on, as will be evident in the following sections.

The above results imply that the correlations between sources and RF power can be mainly attributed to a local effect, rather than to a global effect through the heating of the plasma, since the key parameter is not the total RF power introduced to the plasma but which antenna is used to provide it. Of course the heating of the plasma may also partially contribute to the observed molybdenum emissions since some molybdenum is always generated independently of which antenna is used.

In Fig. 3-33 the core molybdenum density was also plotted which is shown to correlate with the RF power and the antenna molybdenum emissions. However, it is interesting that the core molybdenum density levels are equivalent in the two shots. If the antennas are the main source of the molybdenum that ends up in the core during the RF period, one would expect the core molybdenum density to be higher during the 991021016 discharge since the total molybdenum source rate for the two antennas is higher during this shot. Of course, the above statement should be true only if we are monitoring all the antenna sources. It is possible that there are other sources in the antennas that we do not pick up with our fibers. Part of the discrepancy can also be attributed to the difference between the electron densities in the two shots, since impurities are better screened from the main plasma with increasing density. The volume averaged electron density was $\overline{n_e} \approx 1.73 \times 10^{20}$ m^{-3} during the L-mode phase of the 991021016 discharge and $\overline{n_e} \approx 1.5 \times 10^{20}$ m^{-3} during the same period of the 991021017 plasma. Hence, the effect of the density goes in the right direction but it is uncertain that the relatively small density difference between the two shots can explain by itself the observations of Fig. 3-33.

To get a better understanding on how the antenna source rates scale with the applied RF power, the 990805 Alcator C-Mod run was devoted in monitoring the antennas for a number of similar 1 MA plasma discharges, with small variation in density, in which the E antenna was supplying the RF power in discrete steps. Examples of discharges from that run are shown in Figs. 3-6, 3-21, and 3-32. The D antenna was only briefly used in two of the shots and did not supply more than 0.2 MW of power. Two of the shots were ohmic which practically give the spectrometer's detection limit for the antenna views. These experiments were performed long after a boronization, to ensure that the surfaces had relatively little amounts of boron covering them, which would make measured source rate levels smaller and corresponding uncertainties bigger. In addition none of the

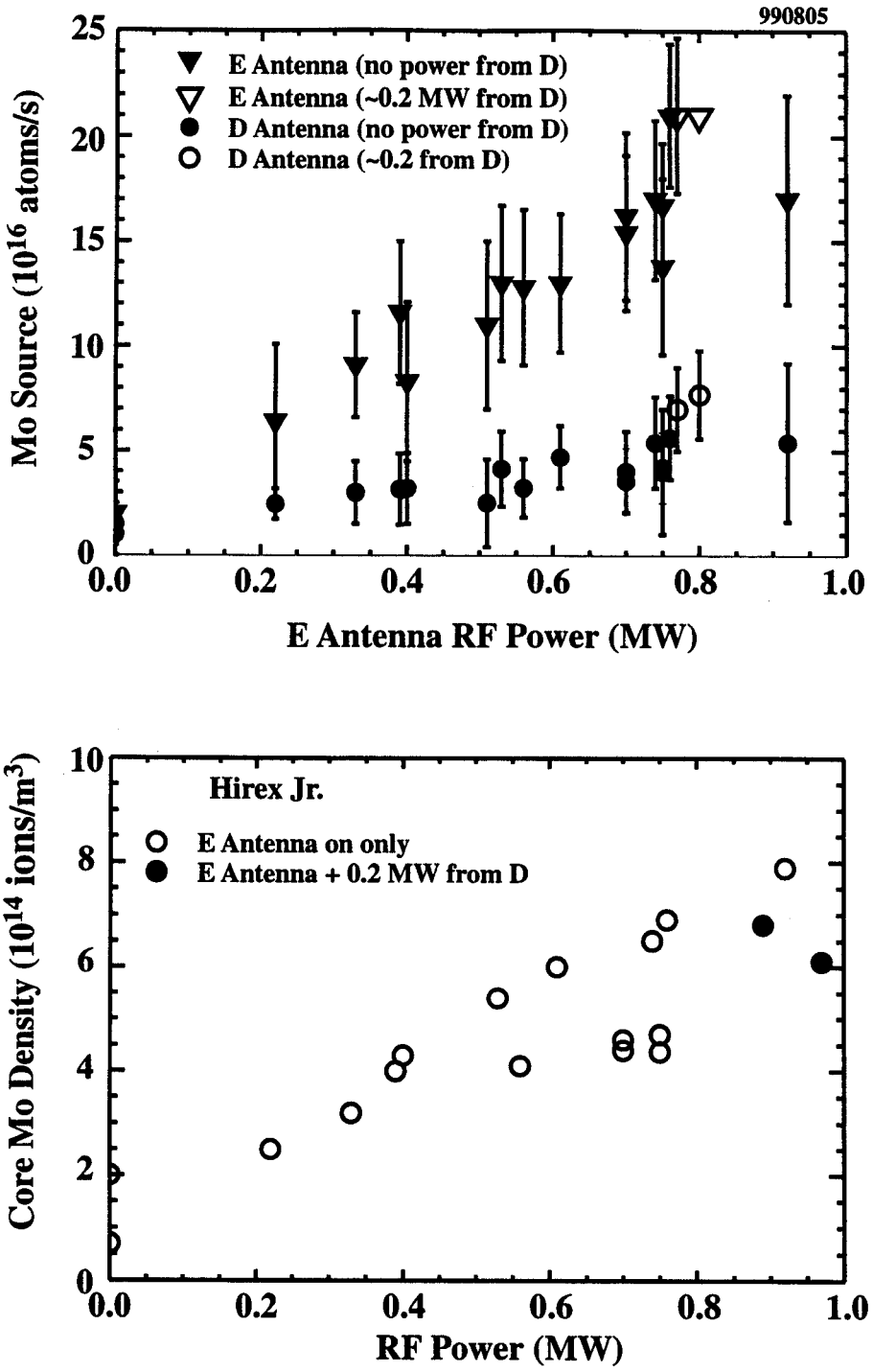

Fig. 3-34: Molybdenum source rates from the two antennas as a function of the applied E antenna RF power (top panel). The closed symbols are for plasmas that no power from D was introduced while the open symbols for the two shots that approximately 0.2 MW of power were launched with the D antenna. In the bottom panel the core molybdenum density is given as a function of the total RF power.

plasmas went into an H-mode since the power supplied by the antenna was always below the L-H threshold. Figure 3-34 plots (top panel) time averaged values of the D and E antenna molybdenum source rates as a function of the E antenna RF power. The error bars are due to the uncertainty in the spectroscopic measurement of the molybdenum signal only, and do not include uncertainties in the temperature and density which are used for the calculation of the S/XB. There is clearly a linear relation between the E antenna RF power and the corresponding source rate. The D antenna emissions seem also to increase slightly with the E antenna power but the change in the signal is almost comparable to the error bars. The open symbols for both antennas give the emissions for the two shots that some power from the D antenna was introduced as well, which justifies why these points have higher values than other points with comparable E antenna RF powers. Finally, in the bottom panel of Fig. 3-34 the core molybdenum density for the same shots is plotted. The only difference is that it is plotted as a function of the total RF power, which as already mentioned implies that the D antenna power, which is not higher than 0.2 MW, was added for the shots that the specific antenna was used. It is seen in the figure that the molybdenum core density correlates with the antenna molybdenum emissions. Recall that the same set of data were used to investigate correlations of the wall and divertor molybdenum sources with the RF power and molybdenum core density (see Figs. 3-7 and 3-22) and that correlation was found only for the divertor. However, we have seen other indications that the outer divertor is not the main source of the molybdenum ions that end up in the core. This leaves the antennas as the major candidate that could explain the measured core molybdenum levels, at least in terms of the sources that have been identified.

3.3.2 Effect of Transport

Unlike what was found for the inner wall and outer divertor molybdenum emissions, the type of plasma confinement does not seem to have any effect on the molybdenum generated at the antennas. An example for a specific shot was already given in Fig. 3-31, where the source follows the changes in the RF power level, without being affected by the fact that the plasma transitions from an L-mode to and ELM-free H-mode. Recall that the source rate from the other sources investigated drops sharply upon the transition to

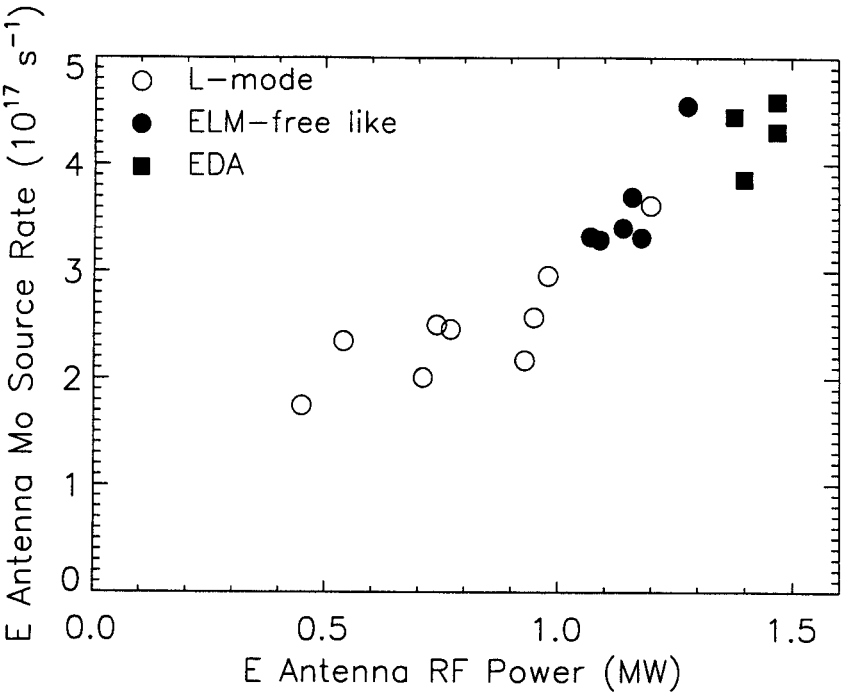

Fig. 3-35: Effect of the confinement mode on the E antenna molybdenum source rate. The data are from the 990302 and 990420 runs.

the ELM-free H-mode. By taking time averages of the RF power and the molybdenum source rate from the E-port antenna for various confinement phases, and for shots that the D antenna was not used, Fig. 3-35 was generated. There, it is shown that the scaling of the source with the RF power level is the same independently if the plasma is in L, EDA, or ELM-free H-mode.

3.3.3 Mechanism

In the past, many ICRF heating experiments have been plagued by large metallic impurity influxes, originating from the antenna Faraday shield [e.g. 36, 37]. It has been explained theoretically [38] and also shown experimentally [39] that these effects are due to inductive coupling between the antenna straps and the Faraday shield. This interaction results in the generation of sheaths of order of the applied voltage (RF sheath rectification) and consequently to increased physical sputtering since plasma ions are accelerated to very high energies. It has been also shown that, among other things, the RF

sheath rectification process can be minimized by proper alignment of the Faraday screen elements with the magnetic field at the plasma boundary and by lowering the plasma density at the Faraday screen surface by using side protection tiles (as done in Alcator C-Mod). These considerations have been taken into account in the design of the C-Mod ICRF antennas and indeed no appreciable emissions have been monitored emanating from the Faraday screens themselves. In contrast, as it was reported in the previous sections, emissions have been observed from the protection tiles and especially the ones on the top. However, similar results have been observed in other experiments. Specifically on Phaedrus [40] it has been shown that inductive coupling is possible also between the antenna and side limiters which leads to the formation of large sheaths on field lines in the scrape-off-layer outside the antenna. We believe that this mechanism is likely responsible or the impurity generation from the C-Mod antenna protection tiles. This belief is backed by the measurements made by LaBombard [41] who has found, using a fast scanning probe, that the potential in the plasma edge was affected by the presence of RF. Specifically, his probe measurements were made on field lines connected to the J-port antenna and showed an increase of the floating potential on those field lines when the RF was turned on. Actually, the increase was even higher when the optimum (for core heating) phasing between the current straps was not used. There are no direct measurements in C-Mod on what the effect of the D and E-port antennas on the plasma potential is. It is possible that the same effect may be true for these antennas as well. Hence, our working hypothesis is that the molybdenum generation from the protection tiles can be attributed to an RF sheath rectification process which causes the acceleration of plasma ions to high energies and leads to increased sputtering. This hypothesis is consistent with the observation that the correlations between molybdenum sources and RF power could only be explained by a local effect, as was shown in section 3.3.1. It is also consistent with the fact that the molybdenum source rate from the antennas seems to be independent of the confinement mode and outer gap since it is not easy to explain how a change in these parameters would have no effect at all in the source rate, unless the mechanism would not "care" for the details of the edge plasma profiles.

3.4 Conclusions

Using visible spectroscopy, we have identified three surfaces in Alcator C-Mod that are significant sources of molybdenum, with their strength depending on the plasma conditions: the inner wall around the midplane, the outer divertor, and the antenna protection tiles. The outer limiters, which are 5 mm closer to the plasma than the antenna protection tiles, and the inner divertor target are not important molybdenum sources.

The inner wall has been identified as the only important source during limited plasma operation. Wall emissions correlate strongly with the core molybdenum density for all cases studied. However, the inner wall does not contribute significantly to the core molybdenum content in diverted plasmas, despite frequently being the strongest source observed. This implies a very good screening of the molybdenum by the plasma at the inside of the tokamak.

In ohmic operation, the core molybdenum levels are very low and do not constitute a concern for tokamak operation. It was found that during this phase the divertor is particularly effective in screening impurities originating at its targets.

The antenna source seems to be a very important source, if not the most important, during RF operation, showing good correlation with core molybdenum density. However, we can not exclude the outer divertor as also being an important source during RF operation, although there are a number of available indications that would support the idea that it is often not the dominant. In support of the above, in Chapter 4 it will be shown that the beneficial effects of boronization wear out relatively fast for the outer divertor while they are felt for a longer period in the core.

Our observations regarding the screening of molybdenum are consistent with screening results obtained in Alcator C-Mod for another non-recycling impurity, namely nitrogen [42]. Specifically, it was observed that screening depended strongly on the poloidal position of injection, with the penetration being easiest when impurities were injected from the outer midplane and hardest when the gas was injected from the inner wall and the divertor.

Physical sputtering seems to be the dominant mechanism responsible for the production of molybdenum at the various surfaces. For the outer divertor, the subject will

be discussed in detail in Chapter 5. For the case of the protection tiles, the sputtering is believed to be enhanced by an RF sheath rectification effect.

In light of the above findings, it should be noted that using a material such as molybdenum for the antenna protection tiles is not advisable. Firstly, because the tiles are located in a region of the tokamak where the screening of impurities is poor; and secondly, because molybdenum being a metal is susceptible to the RF sheath rectification effect. A change of the molybdenum antenna protection tiles with an insulating material, such as boron nitride, is under consideration in Alcator C-Mod. The discussion on the suitability of using a high-Z material at the divertor target is referred to Chapter 5.

Chapter 4

Effect of Boronization on Molybdenum Sources and Core Density

Alcator C-Mod uses a number of surface-conditioning methods aiming at reducing the influx, through sputtering and desorption, of impurities from the walls and controlling the hydrogen isotopes content in them. Baking (heating to greater than 130 degrees Celsius) of the vacuum vessel is performed once at the beginning of every experimental campaign, or whenever the vessel is exposed to atmosphere and re-evacuated, and results in thermal removal of wall adsorbed impurities. Electron cyclotron discharge cleaning (ECDC) is carried out typically prior to the first plasma discharge at the beginning of every C-Mod run day, or even in between plasma discharges if deemed necessary, and employs particle bombardment for surface cleaning. In ECDC, microwaves of fixed frequency (2.45 GHz) at the electron cyclotron resonance are used to excite a low temperature discharge. To achieve cleaning of all surfaces, the resonant magnetic field (0.085 T) is swept from the inner to the outer wall. The ECDC working gas is typically deuterium or helium with pressures on the order of 5×10^{-5} torr. The choice of gas depends on the type of plasma discharges that are scheduled during a particular run day since using ECDC results not only in cleaning of the various surfaces of impurities but also in loading of the walls with the gas used. It should be noted that, in terms of molybdenum sources, it has been observed that using ECDC leads to a temporary reduction (for a shot or two) of the molybdenum emissions from the various surfaces. Finally, boronization is a conditioning technique that is used in Alcator C-Mod aiming mainly at minimizing the release of high-

Z impurities, and more specifically of molybdenum which is the material of the first wall surfaces. However, the advantages of boronization do not simply stem from covering the walls with a low-Z film, that even upon getting into the plasma would not radiate significant amounts of energy. Boron acts also as a getter and thin boron films pump both oxygen and hydrogen while boronized surfaces have a low affinity for water vapor [3]. In this chapter the boronization technique is briefly described and its effectiveness in reducing the molybdenum source levels and core density is investigated.

4.1 Boronization in Alcator C-Mod

During boronization a boron layer is deposited onto the molybdenum plasma facing components. The procedure being employed is similar to the normal ECDC, using a helium-diborane (10% B_2D_6, 90% He) mixture as the working gas instead of helium or deuterium. The ECDC discharge is used to dissociate the helium-diborane gas. The toroidal field is again swept to move the resonance layer across the chamber. Unlike the usual ECDC procedure, the discharge is pulsed at a 50% duty cycle to allow the diborane gas to fill the chamber more uniformly before dissociating. The gas system was properly modified to provide complete toroidal coverage by injecting the gas through a continuous toroidal tube with holes spaced approximately 1 cm. The toroidally continuous "showerhead" plus the pulsing of the machine both maximize toroidal uniformity. Some level of non-uniformity of course is inevitable. Specifically, the presence of the toroidal field was found to lead to preferential coating of protruding surfaces such as the RF antennas, secondary outboard limiters, and re-entrant mirrors [43]. The boronization is typically applied for 8 to 16 hours. Typical deposition rates (averaged over the surface of the machine) are about 10 nm/ hour.

The first boronization in Alcator C-Mod was carried out in January of 1996 and was found to have a number of beneficial effects for plasma performance [43]. The core molybdenum density decreased by at least a factor of ten, and carbon, which had been the dominant low-Z impurity prior to boronization with a concentration of ~ 0.5 %, was reduced by about a factor of three. After boronization, boron and carbon levels were about equal. Oxygen levels were also reduced by about an order of magnitude, becoming

negligible, while core radiation was reduced by up to a factor of three. Boronization also allowed access to wider operating conditions. This is in general expected since boronization allows higher densities to be obtained without excessive radiation, as a result of the decreased impurity concentrations. Of course the reduced core radiation means that more power is available to flow in the edge, thus challenging the power handling capabilities of the divertor.

Since January 1996, the boronization of the vacuum vessel is repeated whenever the experimental results show the beneficial effects of boronization to be completely diminished (e.g. when high molybdenum core densities are measured or when the EDA H-mode regime can not be accessed). This typically occurs every few weeks, assuming continuous plasma operation. During the first run period utilizing boronization, there were a limited number of spectroscopic views that could monitor changes in the molybdenum generation from various plasma facing components. The most complete viewing coverage of the wall surfaces was available during the 1999 run campaign. For this reason data from this campaign will be used in the remainder of this chapter to investigate how boronization affects molybdenum production around the tokamak. With this in mind the effect of boronization on core molybdenum density is also revisited.

4.2 Effect on Molybdenum Source Rates and Core Density

The study of the boronization effects on molybdenum source levels and core density is based on the data obtained during three consecutive Alcator C-Mod runs in the beginning of March 1999. The boronization of the vessel was performed at the evening of March 2nd. It was estimated that, on average, 98 nm of boron were deposited on the walls [44]. The resonance was taken out to R=1.03 m (recall that C-Mod's major radius is 0.67 m while the plasma minor radius is 0.21m). Measurements from the run day prior to boronization (990302) are compared to the data from the two runs (990303-990304) immediately after. Data from 990305, the third day following boronization, were not used because only ohmic plasmas were generated during that day and hence the plasma conditions were completely different than the conditions in the other 3 days. The

comparison is made for both the limited phase of the plasma discharge and the diverted phase during ICRF injection. The surfaces monitored for molybdenum sources included all significant molybdenum emitters: the D and E-port antennas, the inner wall, and the outer divertor. The J-port antenna was not yet operational during these runs. By monitoring the molybdenum impurity source rates at the various surfaces and the corresponding molybdenum density in the core, it is in principle possible to draw conclusions on the relative contribution of the sources in the observed molybdenum core content. Finally, it is important to emphasize that it is expected that the time it takes for the molybdenum levels to return to values measured prior to a boronization depends on two very important parameters: the boronizing conditions, such as the thickness of boron layer deposited and spatial extent of resonance sweep; and the type of plasma discharges that are run, which can both differ a lot from boronization to boronization. Hence any numbers in this chapter that depend on the parameters mentioned above should not be considered a priori right for all other boronizations.

Figure 4-1 shows the short-term effect of boronization on the neutral molybdenum line intensity from a view of the divertor. Both spectra are taken under similar conditions. For both shots the plasma current was 800 kA, 1.4 MW of RF power was launched from the E-port antenna, and the plasma was in an EDA H-mode. The situation portrayed in Fig. 4-1 is typical. Immediately after boronization (shot 990303005 was the second successful plasma attempt during the 990303 run) the neutral molybdenum intensity is for all views below the spectrometer's detection limit. However, gradually, and as the film of boron starts to diminish in thickness, the molybdenum intensity starts to increase and it eventually reaches the pre-boronization levels.

During the limited phase of the plasma discharges the only significant molybdenum source, as was already discussed in section 3.1, is the inner wall, which acts as the plasma limiter. Figure 4-2 shows the effect of boronization on the wall source rate and core molybdenum density for the limited phase. The core molybdenum data were obtained with the Hirex x-ray spectrometer, as was all core molybdenum data presented in this chapter. As observed in the figure, both the molybdenum source and the core density decrease by a factor of 10 or more immediately after boronization. It takes about 35 discharges after boronization for the two signals to approach the pre-boronization levels.

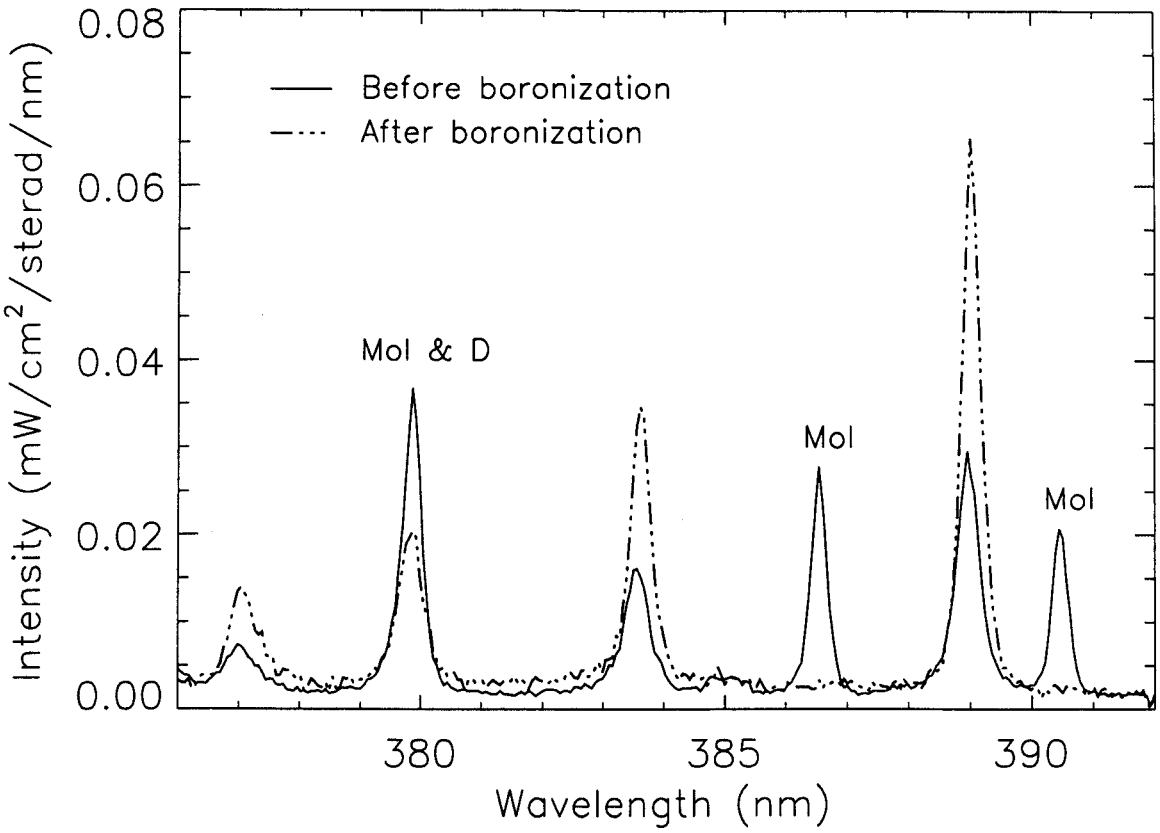

Fig. 4-1: Typical spectra, taken with a divertor view before (shot 990302013) and after (shot 990303005) boronization, of the spectral region where the three MoI lines are observed. The 379.8 nm molybdenum line overlaps with the 379.7 nm deuterium Balmer line and can not be used for comparisons. All other strong lines in the spectrum belong also to the deuterium Balmer series.

Overall, there is a very good correlation between the two signals, which gives additional confidence that the inner wall is the source of the molybdenum reaching the core during the limited phase of the discharges.

The effectiveness of boronization for RF-heated, diverted plasma discharges is presented in Figures 4-3 through 4-5. The impact on the E-port antenna molybdenum source and to the core molybdenum density is shown in Fig. 4-3, on the outer divertor and inner wall source rates in Fig. 4-4 and on the D-port antenna source in Fig 4-5. For all these discharges only the E-port antenna was supplying RF power to the plasma. The data selected are during EDA H-modes only. This was necessary since not only, as has already been mentioned in Chapter 3, some of the molybdenum source rates depend on plasma confinement, but also because proper comparison with core molybdenum

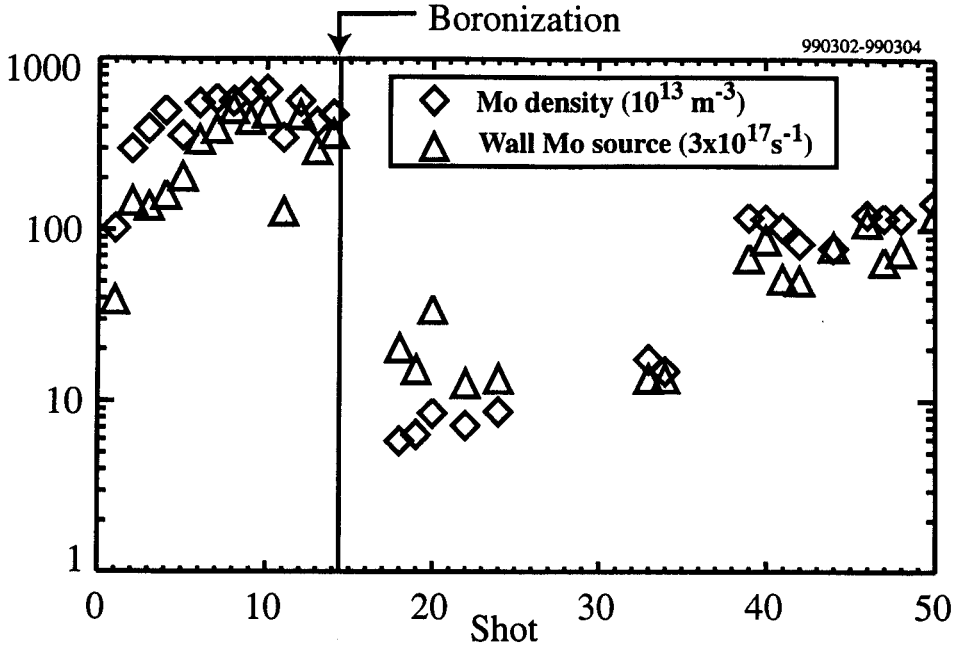

Fig. 4-2: Effect of boronization on inner wall molybdenum source and corresponding core density for the limited phase of discharges.

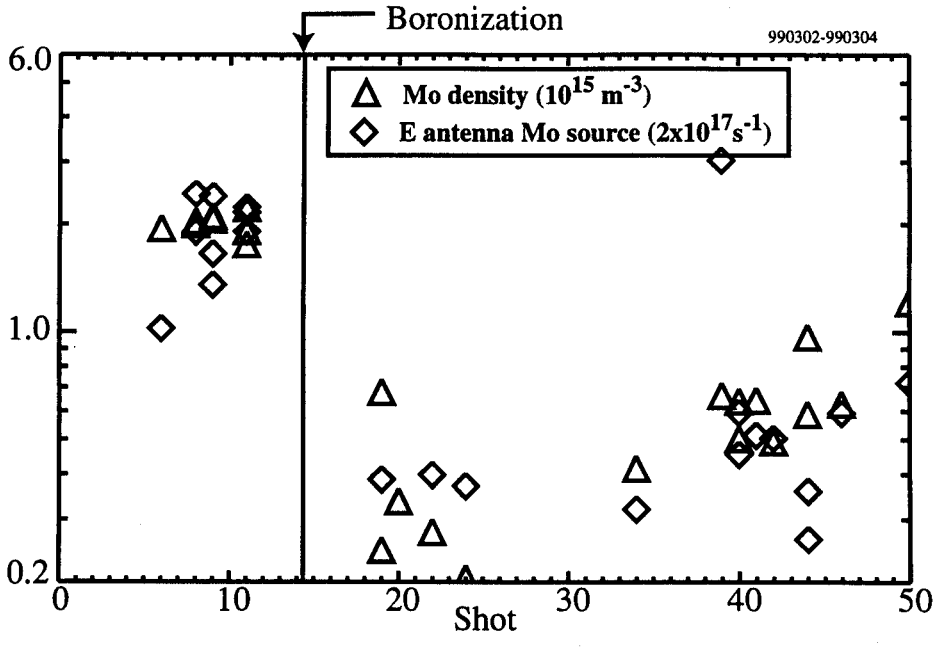

Fig. 4-3: Effect of boronization on the E-port antenna molybdenum source and core density for diverted, RF-heated plasmas using the E-port antenna.

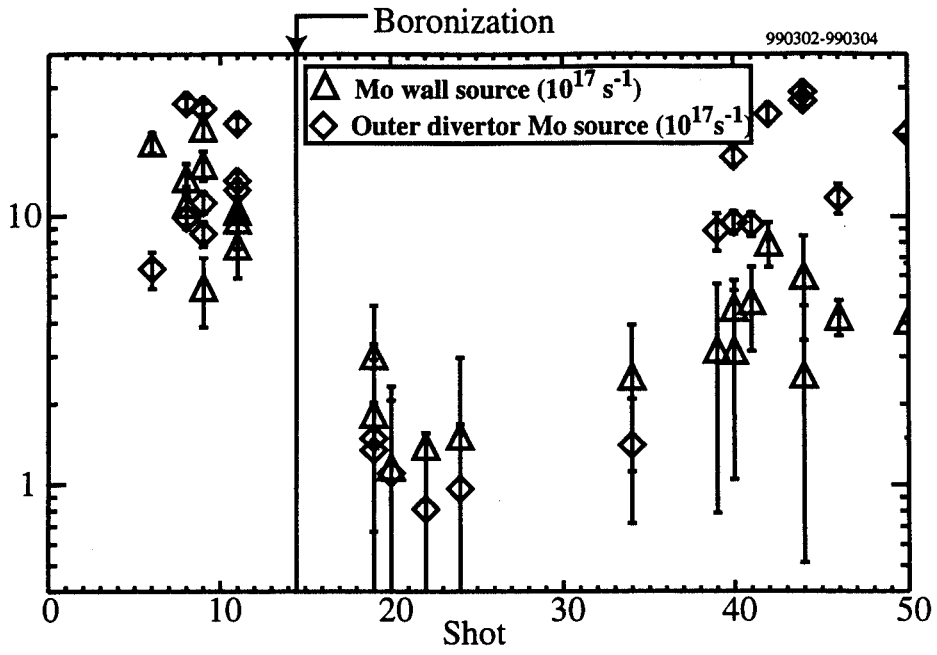

Fig. 4-4: Changes, resulting from boronization, in the outer divertor and inner wall sources for the diverted, RF-heated phase of plasma discharges.

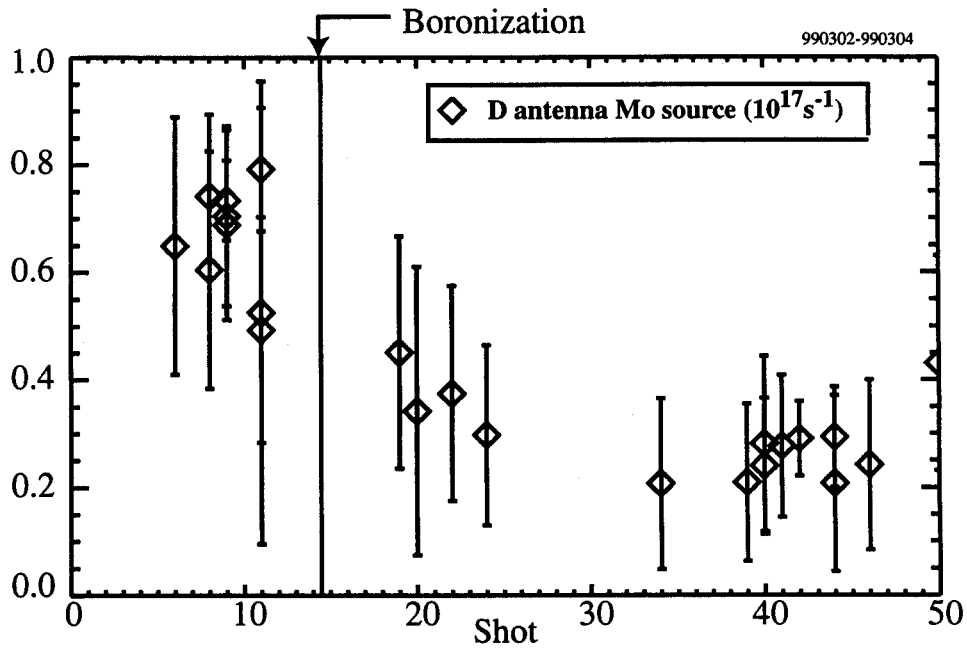

Fig. 4-5: Effect of boronization on the D-port antenna molybdenum source, generated during RF heating with the E-port antenna only.

densities requires quasi-stationary plasma conditions, as is the case for EDA H-modes. Multiple points were used from shots, in which more than one EDA H-modes were obtained. The data show significant correlation between the E-port molybdenum source and the core molybdenum density (Fig. 4-3). Both signals decrease by a factor of 4 or 5 after boronization and their rate of increase is similar. By the end of the second day, or 35 shots after boronization, their levels are still below the pre-boronization values. On the contrary, the outer divertor "behaves" unboronized as early as 20 shots after covering the walls with boron (Fig. 4-4). The inner wall source also approaches pre-boronization values, but with a considerably slower rate than the outer divertor. However the uncertainty in the wall source measurements in the diverted phase is pretty high as seen by the error bars in Fig. 4-4. This is simply due to the typically low emissions from the inner wall during the diverted phase. Finally, Fig. 4-5 shows the effect of the boronization to be longer lasting for the D-port antenna. This is, however, explained by the non-use of the D-port antenna during these experiments combined with the predominantly local nature of the mechanism that causes the sputtering from the antennas, as has been noted in Chapter 3. The latter also explains the small drop in the source rates right after boronization. Since only the E-port antenna was used in all these experiments the source from D antenna was pretty small even before boronizing.

The study of the impact of boronization on the molybdenum source levels has shown a varying effectiveness for the various surfaces. The boronization effects disappear rather fast for the outer divertor, somewhat expected since it handles most of the power that flows in the scrape-off-layer. This is in agreement with measurements made by Wampler [45], as part of the molybdenum erosion measurements in Alcator C-Mod (see Chapter 5), that revealed that the outer strike point region was the only area around the vessel with negligible boron coverage at the end of the 1995-1996 experimental campaign. The effects last longer for the inner wall, with the antennas benefiting the most, supporting earlier findings that showed preferential coating of protruding surfaces. In principle, the above information could be used to change the procedure of boronization in a way that more boron is deposited on surfaces that loose it faster. Finally, the correlation of the E-port antenna source with the core molybdenum density and the faster rate, compared to the core molybdenum density, with which the outer divertor and inner wall molybdenum

signals reach pre-boronization levels imply that most of the molybdenum found in the plasma core originates from the E-port antenna protection tiles. The above results are complementary to the findings of Chapter 3. There, it was shown that the antenna emissions correlate with the core molybdenum density. The same was true for the outer divertor source during RF operation, with the exception during ELM-free H-modes. With the boronization results, it becomes evident that the contribution of the outer divertor molybdenum source to the core molybdenum density is small even during EDA H-modes, for which it was shown that the divertor emissions are typically the highest. Recalling that in Chapter 3 it was demonstrated that the inner wall source rate does not typically correlate with the core molybdenum levels, during the diverted phase of discharges, the results described here reinforce the notion that the antenna protection tiles are the surfaces of most interest, regarding molybdenum penetration to the main plasma.

Chapter 5

Outer Divertor Source Model

If we are to minimize the level of intrinsic impurities in the confined plasma, it is important to understand the processes that are responsible for their production at the various surfaces. Special care should be given to the divertor target. Even if the produced impurities are effectively screened from the plasma core, there are concerns, for the next generation long-pulse fusion devices, that significant erosion could occur at the divertor targets, as a result of the extremely high power that are expected to handle.

In Chapter 3 it was mentioned that comparing the outer divertor molybdenum emissions with the corresponding Langmuir probe data gave indications that sputtering is the mechanism responsible for the divertor molybdenum generation. The goal in this chapter is to develop a simple physical sputtering model, based on the probe data, that can provide satisfactory agreement with the measured outer divertor molybdenum source rates in Alcator C-Mod. The model is used to identify the type of plasma discharges that cause most of the sputtering. It is also used to calculate the 1995-1996 campaign-integrated gross and net erosion. The latter is compared to actual net erosion measurements obtained with specially modified molybdenum tiles. In the beginning of the chapter the important characteristics of the physical sputtering process, which is the basis of the outer divertor source model, are described.

5.1 Physical Sputtering

When an energetic particle, ion or atom, is incident on a solid surface it will penetrate the target unless it is previously backscattered (reflected) from surface atoms [7]. The

projectiles will lose energy and momentum due to collisions with the electrons and atoms of the solid. If any of the lattice atoms that were set in motion by the projectile receive sufficient energy to exceed the surface binding energy, E_S, they will be emitted or "sputtered", as long as they were moving in the right "direction". Thus the sputtering yield Y, which is defined as the number of emitted surface atoms per incident particle, will decrease with increasing surface binding energy and increase with increasing energy transfer from the projectile to the target atom. From the above description it is implied that there exists a threshold energy, E_{th}, for the incident projectile below which sputtering does not occur.

Using the conservation of momentum and energy, the energy transfer in an elastic collision between two nuclei is given by [7]

$$E = E_0 \frac{4 M_1 M_2}{(M_1+M_2)^2} \cos^2\varphi \equiv E_0 \gamma \cos^2\varphi \qquad (5.1)$$

where E_0 is the projectile energy, M_1 and M_2 are the masses of the incident and target atoms respectively, and φ is the angle between the direction of the projectile before the collision and the direction of the recoil atom in the center of mass frame. In Eq. 5.1, γ is the maximum energy transfer factor, $\gamma = 4 M_1 M_2 /(M_1 + M_2)^2$. For a head-on collision ($\varphi = 0$), the energy necessary to transfer E_S to the target atom is, from Eq. 5.1, E_S/γ. This should be considered as a lower limit for the threshold energy. This expression was modified by Bohdansky [46] who suggested that, for light particles incident on a heavy target, the threshold energy could be approximated by

$$E_{th} = \frac{E_S}{\gamma(1-\gamma)} \quad \text{for} \quad \frac{M_1}{M_2} < 0.2 \qquad (5.2)$$

where the (1- γ) factor takes into account the reflection process which is important for light ions. The surface binding energy, E_S, can be approximated by the thermal sublimation energy. For molybdenum the thermal sublimation energy is 6.9 eV [2].

The most widely used formula for the physical sputtering yield, in the case of normal incidence ($\alpha = 0$) on a surface, was given by Bohdansky [47, 48]:

$$Y(E_o, \alpha = 0) = Q\ S_n(E_o/E_{TF})\ g(E_o/E_{th}). \qquad (5.3)$$

Q is the "yield factor", in units of atoms per ion, which although it can be calculated from

analytical theory it is typically used as a fitting parameter, for best agreement with the experimental data. $S_n(E_o/E_{TF})$ is a nuclear stopping function, depending on the characteristic Thomas-Fermi energy

$$E_{TF}(eV) = 30.74 \frac{M_1 + M_2}{M_2} Z_1 Z_2 \left(Z_1^{2/3} + Z_2^{2/3}\right)^{1/2}, \tag{5.4}$$

where Z_1 and Z_2 are the atomic numbers of the projectile and the target atom respectively. Finally, $g(E_o/E_{th})$ is a threshold function calculated from

$$g(E_o/E_{th}) = (1-(E_{th}/E_o)^{2/3})\,(1-E_{th}/E_o)^2\,. \tag{5.5}$$

In the original Bohdansky formula, the nuclear stopping function $S_n(E_o/E_{TF})$ was based on an analytic fit to the Thomas-Fermi Potential [49, 50]:

$$S_n^{TF}(E/E_{TF}) = \frac{3.441\sqrt{E/E_{TF}}\,\ln(E/E_{TF}+2.718)}{1+6.335\sqrt{E/E_{TF}}+E/E_{TF}\,(6.882\sqrt{E/E_{TF}}-1.708)}. \tag{5.6}$$

However this function is too large for low values (< 0.01) of the reduced energy E_0/E_{TF}. In a revised version of the Bohdansky formula [51], S_n was calculated from an analytic fit to the Kr - C potential [52]:

$$S_n^{KrC}(E/E_{TF}) = \frac{0.5\ln(1+1.2288\,E/E_{TF})}{E/E_{TF}+0.1728\sqrt{E/E_{TF}}+0.008(E/E_{TF})^{0.1504}}. \tag{5.7}$$

The semi-empirical Bohdansky formula (Eq. 5.3) describes the sputtering yield for all projectile-target combinations for a wide range of projectile energies. The parameters Q, E_{TF}, and E_{th} are tabulated for the most important materials involved in plasma-wall interaction in Ref. [48]. Q and E_{th} values are based on experimental results while E_{TF} is calculated from Eq. 5.4. Using the large number of fitting values obtained for Q and E_{th} from various experimental and sputtering yield data, Garćia-Rosales [51] derived analytic expressions for these two parameters. The scaling formula for Q, which is based on Sigmund's sputtering yield theory [53], is

$$Q\,E_S^{2/3} = 1.633\,Z_1^{2/3}\,Z_2^{2/3}\left(Z_1^{2/3}+Z_2^{2/3}\right)^{1/3}\frac{M_1^{5/6}\,M_2^{1/6}}{M_1+M_2}\,\frac{0.15+0.05\,M_2/M_1}{1+0.05\,(M_2/M_1)^{1.6}}. \tag{5.8}$$

The formula for E_{th} is an empirical scaling with the mass ratio:

$$\frac{E_{th}}{E_S} = b_1 \left(\frac{M_2}{M_1}\right)^{b_2} + b_3 \left(\frac{M_2}{M_1}\right)^{b_4} \quad \text{with} \quad b_1 = 7.0, b_2 = -0.54, b_3 = 0.15, b_4 = 1.12. \quad (5.9)$$

Both formulae are valid only for normal incidence and were derived using fit values of the parameters Q and E_{th} for the revised Bohdansky formula.

The sputtering yield predicted from Eq. 5.3 increases approximately linearly with the incident ion energy above E_{th}, reaches a maximum and then decreases at high energies. This decrease is due to the creation of the recoils very deeply in the solid that the chance of escape decreases. Figure 5-1 gives the sputtering yields, as calculated from the revised Bohdansky formula, versus the incident particle energy when molybdenum is bombarded with H, D, He, and C projectiles at normal incidence. The Mo self-sputtering yield for normal incidence is also plotted. It can be seen that molybdenum self-sputtering starts becoming critical for energies above 500 eV, where the yield is approaching unity. For a

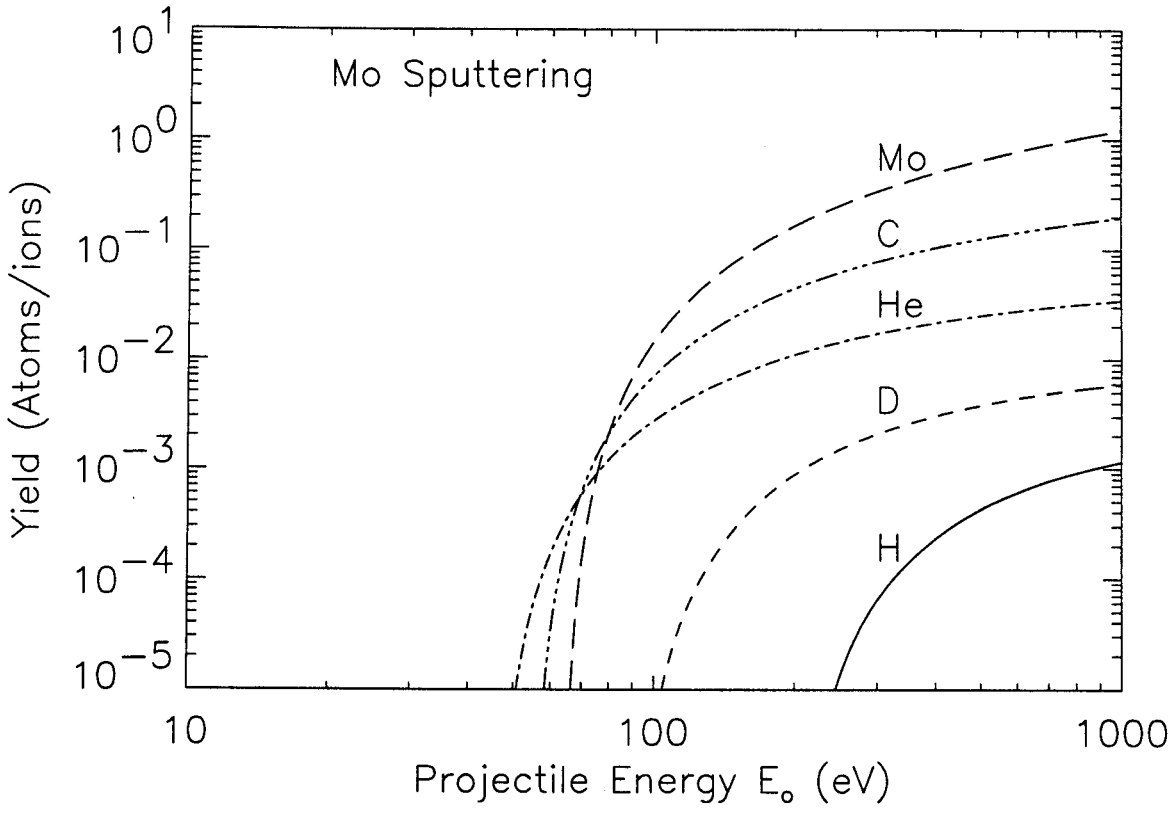

Fig. 5-1: Molybdenum sputtering yields versus projectile energy for bombardment with H, D, He, C, and Mo at normal incidence, using the revised Bohdansky formula. The parameters Q, E_{TF}, and E_{th} are obtained from Ref. [48].

molybdenum target, the maximum in the yields occurs in energies higher than 1000 eV for all projectiles, and is not shown in Fig. 5-1.

The sputtering yield increases with the angle of incidence, α (see Fig. 5-2), with respect to the result obtained for normal (α=0) incidence (Eq. 5.3) [7, 3, 48]. This is because more energy is dumped close to the surface [7]. However, at large angles the projectiles do not penetrate the solid and reflection becomes more probable than sputtering [7]. Therefore, the angular dependence of the yield will exhibit a maximum. The position of the maximum, as well as the shape of the yield vs. angle curve, depends greatly on the projectile-lattice atom combination and the energy of the incident particle [48, 7, 3]. For example, for light particles incident on heavy targets with energies below ~200 eV, which is the region of interest for many plasma surface interactions, the variation of the yield with incident angle is small while for other projectile-target combinations and energies the yield can increase by an order of magnitude [7, 48]. The knowledge of the dependence of the sputtering yields on the angle of incidence is of extreme importance for fusion experiments since the magnetic field lines cross many of the vessel surfaces at oblique angles. Specifically in the divertor, the angle between the field lines and the target is of the order of 1°. In practice, however, it is hard to calculate the distribution in angle of incidence of the projectiles. This is because the surface roughness, the acceleration in the plasma sheath, and the ion Larmor radius complicate the problem. The effect of the sheath is illustrated schematically in Fig. 5-2. Outside the sheath, which in the case of a surface at oblique angle to the magnetic field consists of a magnetic and an electrostatic part, the ions are confined by the magnetic field. Inside the sheath, even in the magnetic part, the electric field is strong enough that deflects ions from their motion along the magnetic field and pulls them towards the direction perpendicular to the plate [54]. The combined effect of the sheath, the ion Larmor radius, and the surface roughness is that gyrating particles that follow field lines with small inclination angles to the surfaces impact at angles that are closer to the normal [3]. Chodura [55] has calculated that, for light ions, the mean angle of incidence is $\alpha = 65^\circ$. As it will be discussed again later, this value will be used in our model.

The angular distribution of sputtered particles is typically a cosine distribution [48]. Their energy distribution is given, to first approximation, by [7, 48, 56]:

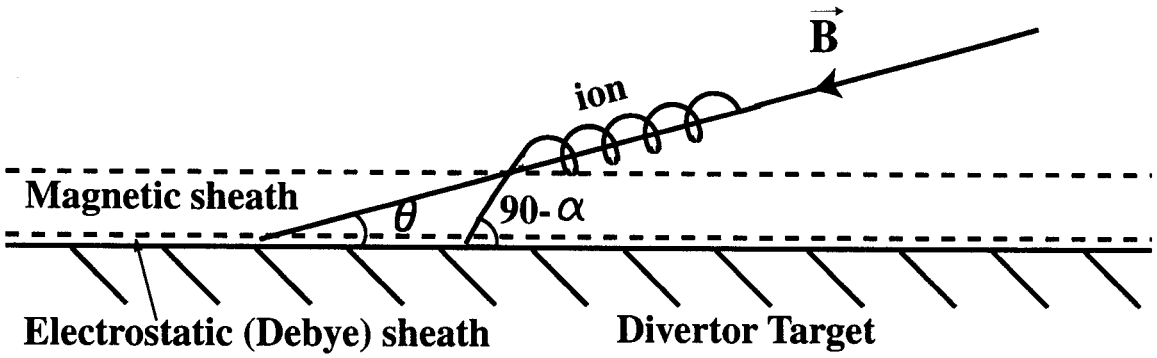

Fig. 5-2: Schematic view of an ion's trajectory in the proximity of the divertor region. The ions follow the magnetic field up to the beginning of the (magnetic) sheath. Inside the sheath, the electric field tends to pull the plasma flow closer to the direction of the normal to the target [55].

$$\frac{dY}{dE} \propto \frac{E}{(E+E_S)^3}. \tag{5.10}$$

This distribution is commonly referred to as the Thompson energy distribution. Equation (5.10) has a maximum at half the binding energy ($E = E_S/2$), which is typically a few eV. The energy distribution cannot extend beyond the maximum transferable energy. Generalizing the result of Eq. 5.2, the maximum energy that can be transferred to a target atom from a projectile of energy E_0 is given by $E_o\ \gamma\,(1-\gamma)$. The maximum energy, E_{max}, with which the atom can be emitted, will be reduced by the binding energy E_S:

$$E_{max} = E_o\ \gamma\,(1-\gamma) - E_S. \tag{5.11}$$

For example, in the case of deuterium ions incident on molybdenum with energy 150 eV, the maximum sputtered energy calculated from Eq. 5.11 is 4.1 eV.

For more detailed information on physical sputtering the interested reader is referred to Refs. [7], [48], [3] and references therein.

5.2 The Model

Source rate calculations have been routinely made, especially in tokamaks with low-Z plasma interaction surfaces. Two such examples are the study by Pitcher [57] for the

DITE graphite limiter and by Krieger [58] for the ASDEX Upgrade carbon divertor. Calculations involving high-Z plasma interaction surfaces are fewer. Examples are the studies by Lipschultz [59] and Philipps [60] of molybdenum sputtering from the Alcator C limiter and Textor test limiter respectively and by Naujoks [61], which modeled tungsten as divertor target material for fusion devices.

The important elements of the erosion/redeposition model used in this study are based on the work done by Naujoks et al. [61]. The model attributes the molybdenum sputtering to the combined action of deuterium, boron, and returning molybdenum ions impinging on the surface. The contribution from all other ions is assumed negligible. The assumption that boron is contributing to the divertor erosion is based on the observation that it is, as mentioned in Chapter 4, the main low-Z impurity following boronization of the Alcator C-Mod vessel. Molybdenum self-sputtering is attributed to locally produced molybdenum atoms, as will be described analytically. The model described here is a slightly modified version of the model initially presented in Ref. [62]. While the basic principles are still the same, a number of improvements have been made that are described in Appendix B.

Figure 5-3 shows the outer divertor region with the domed Langmuir probes and the standard configuration for the spectroscopic views of the outer divertor. A typical plasma separatrix is also drawn. In this case, the strike point is between probes 3 and 4. That means that some of the probes (1 through 3 in the case drawn) are in the private-flux-zone. As it will be shown, there is less molybdenum sputtering in the part of the divertor target that is in the private-flux-zone, due to lower energy acquired by the projectiles incident on the surface and lower fluxes. In general, a variety of configurations can be run in Alcator C-Mod that could place the strike point at any position on the vertical plate: from as high as the divertor nose to lower than probe 1.

The influx of sputtered molybdenum at the Alcator C-Mod divertor surface can be computed at each probe location by utilizing the measured ion saturation current density J_s, the inclination angle, θ (see Fig. 5-2), of the field lines with respect to the divertor target surface from magnetic field reconstruction [63], and the local plasma characteristics (T_e, n_e). The ion saturation current density, J_s, provided by the domed Langmuir probes is the current density parallel to the magnetic field lines. To obtain the

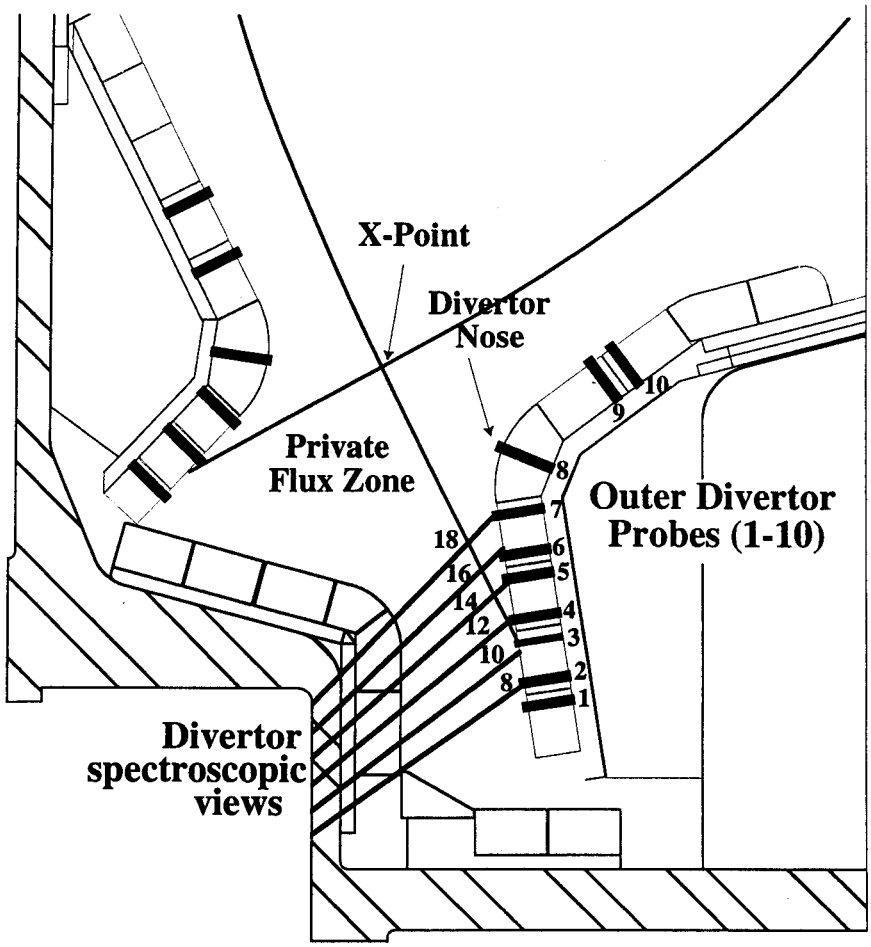

Fig. 5-3: Poloidal cross section of the divertor region. The divertor spectroscopic views use local electron temperature and density obtained with the divertor Langmuir probes. A typical plasma separatrix is also drawn.

current density normal to the surface, J_s has to be multiplied by the sine of the inclination angle. A typical value of this angle for the Alcator C-Mod outer divertor vertical target is 0.5-1 $^\circ$ while it is slightly larger (~2 $^\circ$) for the horizontal plate above the divertor nose. Ignoring, for the moment, molybdenum self-sputtering, the molybdenum influx caused by deuterium and boron ions at each probe location can be calculated from

$$\Gamma_0 = (\Gamma_D\, Y_D + \Gamma_B\, Y_B)\sin\theta \tag{5.12}$$

where Γ_D, Γ_B are the deuteron and boron fluxes entering the sheath and Y_D, Y_B the molybdenum sputtering yields due to deuterium and boron ions respectively. It should be noted that the ion fluxes entering the sheath stay constant, and hence they are equal to the ion flux at the probe.

The measured ion current density at the probe can be approximated with

$$J_s = \Gamma_D\, e + \Gamma_B\, Z_B\, e \tag{5.13}$$

where Z_B is the charge of the boron ions. If we define as β the ratio of boron to deuterium ion flux

$$\beta \equiv \frac{\Gamma_B}{\Gamma_D}, \tag{5.14}$$

we get for J_s

$$J_s = \Gamma_D\,(1+\beta\, Z_B)\, e. \tag{5.15}$$

The deuteron flux is then given by

$$\Gamma_D = \frac{J_s / e}{1+\beta\, Z_B}. \tag{5.16}$$

Combining now Eqs. 5.12, 5.14, and 5.16 gives for the molybdenum influx due to deuterium and boron ions

$$\Gamma_0 = \frac{(J_S / e)}{1+\beta\, Z_B}\sin\theta\,(Y_D + \beta\, Y_B). \tag{5.17}$$

Up to this point we have not taken into account the fact that a large fraction of the eroded molybdenum atoms, that are subsequently ionized, can be redeposited onto the plate, contributing even further to molybdenum sputtering. Actually, for shallow magnetic field line inclination, as is the case in Alcator C-Mod, a major fraction of the ions are redeposited within the first gyration, a process called "prompt redeposition". It

should be noted that although the redeposited ions may contribute in the molybdenum sputtering, this effect is ultimately beneficial since it leads to a reduction of the net erosion. This will be made clear in section 5.7. In this model only the promptly redeposited molybdenum ions are considered to contribute to molybdenum self-sputtering. This means that it is assumed that all ions that are not promptly redeposited are transported away from the immediate area. In reality, the majority of the non-promptly redeposited ions will be pushed back onto the surface owing to friction with the plasma flow. As will be explained in a following section in more detail, if we assume that all these ions return to the plate at the point of their emission, their contribution to the molybdenum sputtering will not typically exceed 10 to 15 % of the total calculated result. Hence, the error made by neglecting them is minimal. The crucial parameter is the ratio p of the ionization length $\lambda_{ion} = u_{at}/(S(T_e)\, n_e)$ to the gyroradius $\rho = m_{Mo} u_{ion}/(q_{Mo}\, B)$:

$$p \equiv \lambda_{ion}/\rho \approx q_{Mo}\, B/\, (m_{Mo}\, S(T_e)\, n_e)\,. \qquad (5.18)$$

B denotes the total local magnetic field, which is approximated by the local toroidal magnetic field, m_{Mo} and q_{Mo} the molybdenum mass and ion charge, u_{at} and u_{ion} the speed of the molybdenum neutral atom and ion respectively, and $S(T_e)$ the electron temperature dependent neutral molybdenum ionization rate which is obtained from the ADAS database [64] and plotted in Fig. 5-4. To obtain Eq. 5.18 it was implicitly assumed that $u_{at} = u_{ion}$, which should be correct to first order, at least for singly ionized ions (q_{Mo}= e).

The effect of prompt redeposition is illustrated for p = 1 in Fig. 5-5 [61]. The magnetic field, which is not shown, is directed out of the page, almost parallel to the target surface. It is assumed that all sputtered particles emitted from a point at the plate become ionized on a hemisphere of radius equal to the ionization length λ_{ion}. All the particles that are ionized in the right half-space will not be redeposited in contrast to all the particles that are ionized in the left half-space which will hit the target, giving in this case a probability of prompt redeposition equal to 50%. The probability of prompt redeposition can also be calculated in the general case that the parameter p has values other than unity. Assuming a $\cos\theta$ distribution of the sputtered particles, and ignoring the sheath effect and multiple ionizations, the fraction of promptly redeposited particles is given by [61, 65]

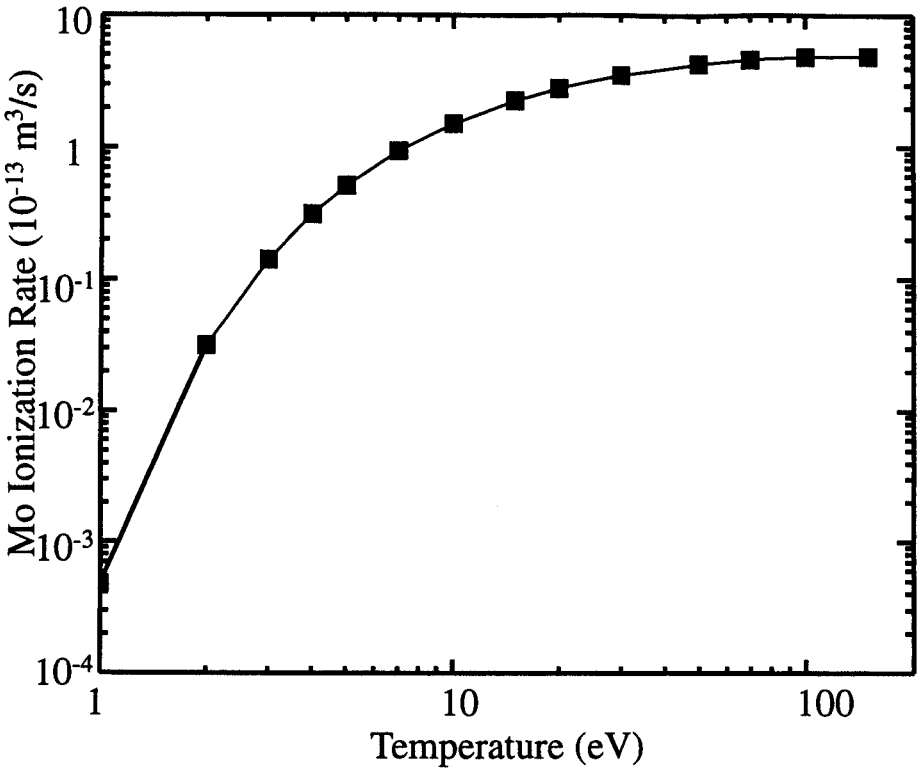

Fig. 5-4: Neutral molybdenum ionization rate as a function of temperature [64].

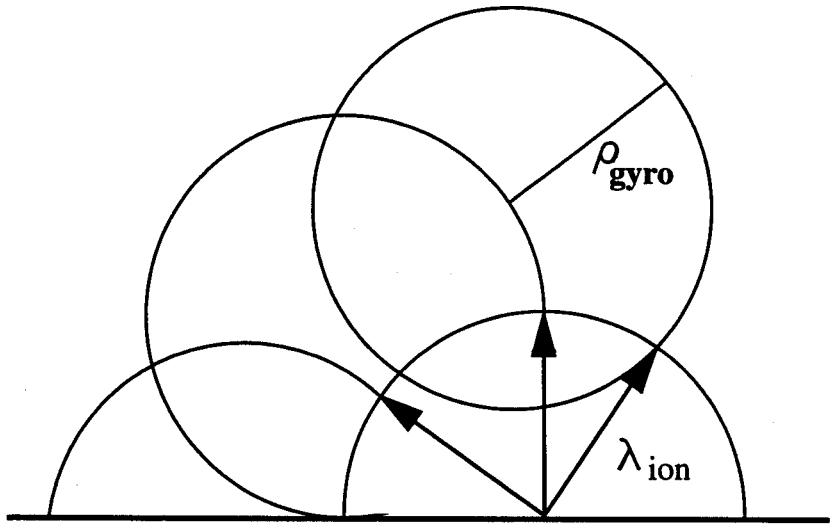

Fig. 5-5: The principle of prompt redeposition [61]. The magnetic field is directed towards the viewer, almost parallel to the plate.

$$P_{pr,0} = \frac{1}{2}[1 + sig(1-p)(1+\frac{4p^2}{(1-p^2)^2})^{-1/2}]. \quad (5.19)$$

This function is plotted in Fig. 5-6. The smaller the value of p the bigger the probability of prompt redeposition $P_{pr,0}$.

In a more complete description of the process, the effects of sheath electric field and multiple ionizations have to be included [61]. If a sputtered particle is ionized inside the sheath then it will be attracted by the plate, which results in an increased probability of prompt redeposition. At the same time, however, the dilution of electrons in the sheath, results in lower ionization probability (higher λ_{ion}) and hence (Eq. 5.18) a reduction in prompt redeposition. Finally, at high electron densities there is an increased probability for multiple ionizations, which implies that the ion gyroradius becomes smaller and the fraction of the promptly redeposited ions decreases. These effects have been considered in detail by Naujoks with the ERO code [66]. The probability of prompt redeposition is then approximated by the expression [67]:

$$P_{pr,ERO} = \frac{1}{2}[\exp(-2p) + \exp(-p/5)]. \quad (5.20)$$

This expression is also plotted in Fig. 5-6 and can be compared with the result from the simplified model. The ratio of this expression to the prediction of Eq. 5.19 is plotted in Fig. 5-7 for the range of the parameter p that is of interest in Alcator C-Mod. As it can be seen from the figure, for $0 < p < 1$, which characterizes the majority of the C-Mod divertor data, the two calculations give results that differ at most by 25%. In this region the simplified model seems to overestimate the fraction of the promptly redeposited ions while for $p > 1$ it underestimates it. For the C-Mod outer divertor model presented here, the probability of prompt redeposition was calculated based on Eq. 5.19. However, the possible error introduced by not using Eq. 5.20 is small when taking into account the uncertainties in many of the other parameters used.

For the conditions occurring in the Alcator C-Mod divertor, the probability of prompt redeposition can reach values close to unity (or somewhat smaller if Eq. 5.20 is used). Assuming an electron temperature of $T_e = 20$ eV, an electron density of $n_e = 5. \times 10^{19}$ m^{-3}, and a central toroidal magnetic field of 5.3 T, the parameter p for a singly charged molybdenum ion is 0.4 (from Eq. 5.18) while the corresponding probability of prompt

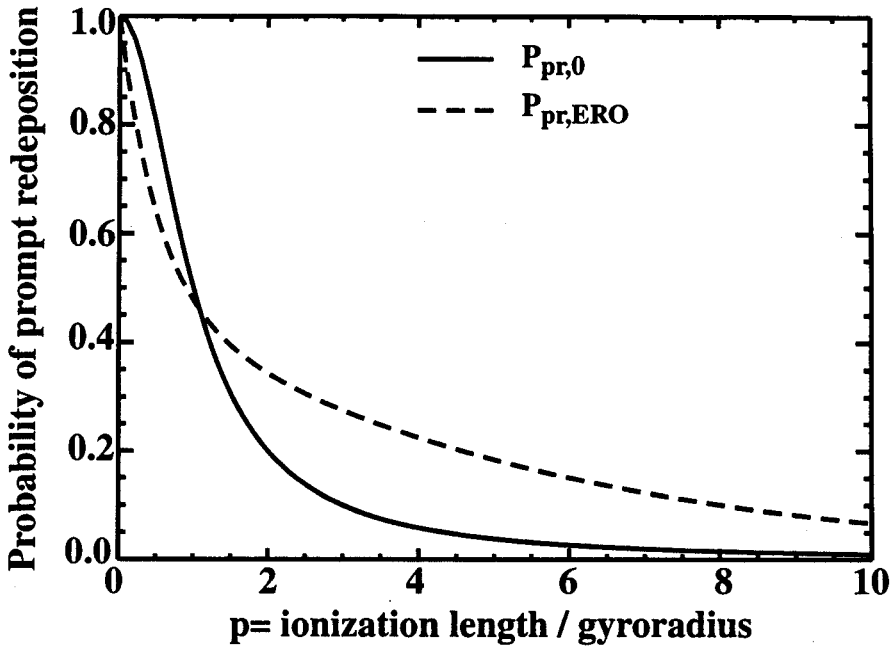

Fig. 5-6: Comparison of the probability of prompt redeposition calculated with the simplified model (Eq. 5.19) to the one obtained with the model utilizing the ERO code (Eq. 5.20).

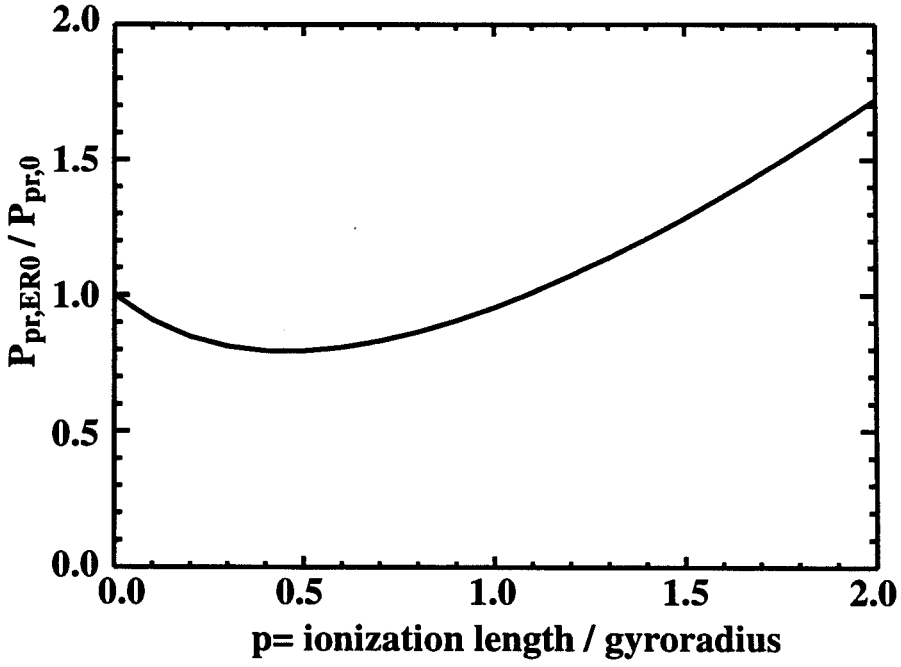

Fig. 5-7: Ratio of the probability of prompt redeposition calculated including all effects to the one obtained from the simplified model.

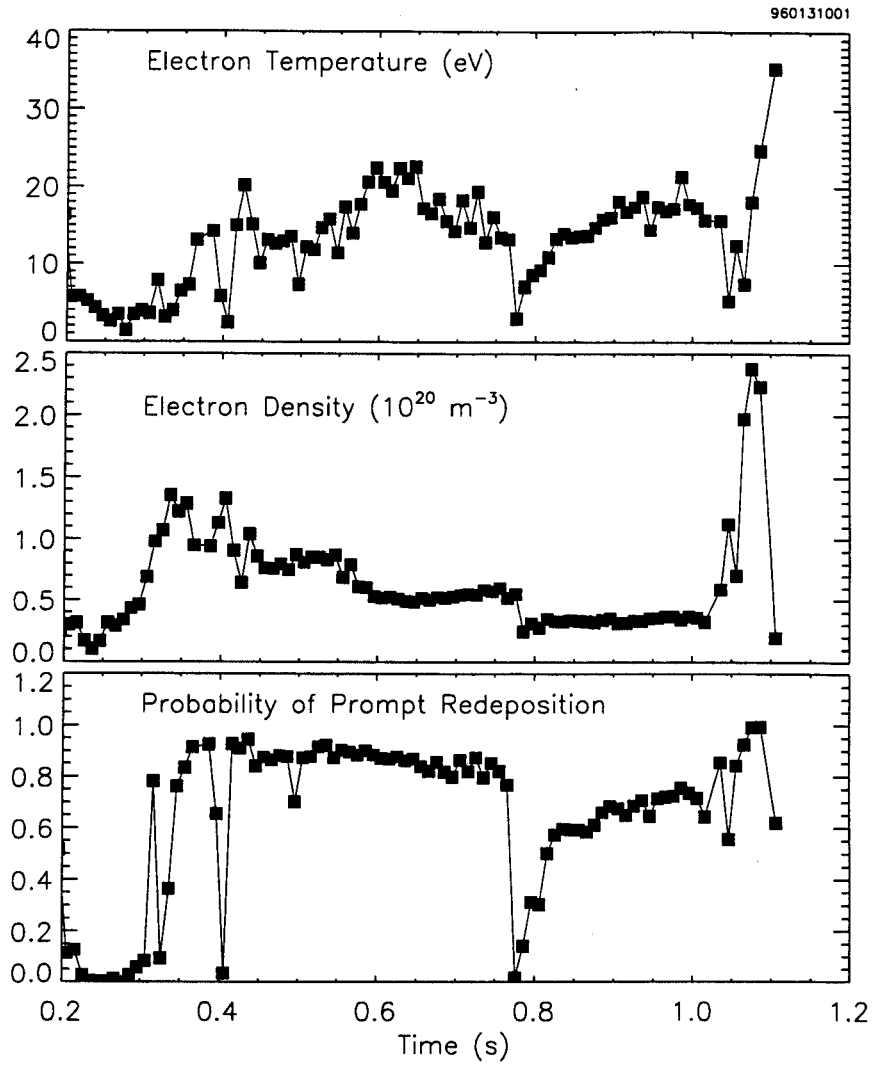

Fig. 5-8: Time histories of electron temperature, electron density, and probability of prompt redeposition, as calculated from Eq. 5-19 for a 5.3 T discharge and q_{Mo} = 1. The plasma electron temperature and density were measured with probe 4.

redeposition is $P_{pr,0}$ = 0.85 (from Eq. 5.19). Figure 5-8 shows the electron temperature and density values measured during a shot in the vicinity of probe 4 (see Fig. 5-3) and the corresponding probability of prompt redeposition as calculated from Eq. 5-19. As seen in the figure, the probability of prompt redeposition stays pretty high for the duration of the shot, except when the density or the temperature drop drastically.

The effect of redeposition on the molybdenum influx including self-sputtering can be calculated as follows:

$$\Gamma_{gross} = \Gamma_0 + \Gamma_0 \, P_{pr,0} \, Y_{Mo} + \Gamma_0 \, P_{pr,0} \, Y_{Mo} P_{pr,0} \, Y_{Mo} + \ldots$$

$$= \Gamma_0 \left(1 + P_{pr,0}\ Y_{Mo} + P_{pr,0}\ Y_{Mo} P_{pr,0}\ Y_{Mo} + \ldots\right)$$

$$= \Gamma_0 \sum_{j=0}^{\infty} \left(P_{pr,0}\ Y_{Mo}\right)^j$$

$$\Rightarrow \quad \Gamma_{gross} = \Gamma_0 \frac{1}{1 - P_{pr,0}\ Y_{Mo}}. \tag{5.21}$$

In the above expression, Γ_{gross} is the total molybdenum flux of the eroded particles, Γ_0 is the molybdenum influx due to the deuterium and boron ion sputtering that was calculated in Eq. 5.17, and Y_{Mo} is the molybdenum self-sputtering yield. The subscript in the total molybdenum influx denotes that this is actually the gross molybdenum influx, which should be distinguished from the net influx, since a fraction of the particles is redeposited. The calculated gross molybdenum influx is what will be compared with spectroscopic measurements since the emission is from neutral molybdenum which is excited during the ionization process. Substituting Γ_0, from Eq. 5.17, in Eq. 5.21 we obtain:

$$\Gamma_{gross} = \frac{(J_S / e)}{1 + \beta Z_B} \frac{Y_D + \beta\, Y_B}{1 - P_{pr,0}\ Y_{Mo}} \sin\theta \tag{5.22}$$

The flux of redeposited particles is simply $P_{pr,0}\ \Gamma_{gross}$

$$\Gamma_{redep} = \frac{(J_S / e)}{1 + \beta Z_B} \frac{(Y_D + \beta\, Y_B) P_{pr,0}}{1 - P_{pr,0}\ Y_{Mo}} \sin\theta. \tag{5.23}$$

Using Eq. 5.22 and 5.23 we can get the net influx

$$\Gamma_{net} = \Gamma_{gross} - \Gamma_{redep}$$

$$\Rightarrow \quad \Gamma_{net} = \Gamma_0 \frac{1 - P_{pr,0}}{1 - P_{pr,0}\ Y_{Mo}}$$

$$\Rightarrow \quad \Gamma_{net} = \frac{(J_S / e)}{1 + \beta Z_B} \left[\frac{(Y_D + \beta\, Y_B)\left(1 - P_{pr,0}\right)}{1 - P_{pr,0}\ Y_{Mo}}\right] \sin\theta. \tag{5.24}$$

Equation 5.24 will be the basis for calculating the outer divertor net molybdenum erosion, which in section 5.7 will be compared to actual net erosion molybdenum made during the 1995-1996 run campaign.

5.3 Model Assumptions

Several important assumptions have been made that are essential to this model. The calculation of yields is based on the (revised) single energy Bohdansky formula for normal incidence. However, in tokamaks the particle flux to the various surfaces has an energy and angular distribution. As an approximation, the bombardment will be described by a Maxwellian energy distribution at a fixed incidence angle. Firstly the appropriate yields for normal incidence will be calculated. At the end of the section appropriate adjustments will be made, wherever appropriate, for the angle effect.

The energy of the deuterons and boron ions at the target can be approximated by

$$E_i = 2\,T_i + Z_i \left| e\,V_S \right| + 0.5\,M_i\,c_S^2 \qquad (5.25)$$

The first term represents the average thermal energy per particle transported to a surface by a Maxwellian distribution of ions of temperature T_i (see Appendix C); the second term is the energy gain of an ion with charge Z_i when falling through the sheath potential V_S; and the third term the particle flow energy at the sheath edge, or equivalently the energy gain in the presheath. In the last term, M_i is the mass of the projectile and c_S is the common ion acoustic speed of all species, which for reasonably low impurity levels is practically equal to the acoustic speed of the majority background ions (= $\sqrt{(T_i+T_e)/M_D}$, with M_D being the deuteron mass). Here, we make use of the fact that the ions enter the sheath with their acoustic speed, as required by the sheath theory [6], and we additionally assume that the boron ions are well collisionally coupled to the deuterium ions, and thus are accelerated up to the deuterium acoustic speed as a result of friction with the plasma flow. This assumption should be valid for the high density conditions encountered in Alcator C-Mod. For simplicity, we have also used the isothermal approximation for the ion acoustic speed.

Returning to the second term of Eq. 5.25, it is shown by Chodura [54] that the potential drop in the sheath is independent of θ, the inclination angle of the field lines with respect to the target surface, as long as a small correction due to finite electron Larmor radius effects is neglected. What changes with θ is just the fraction of the total potential drop that occurs in the magnetic part of the sheath. The potential drop is most easily calculated

in the case of an electrostatic only sheath (θ=0) by the requirement that the total (ion + electron) current to the surface is zero. The result is given by [4]

$$eV_S = -\frac{T_e}{2}\ln\left[\frac{\left(1-\delta^2\right)M_i/M_e}{2\pi\left(1+T_i/T_e\right)}\right] \tag{5.26}$$

where δ is the total secondary electron emission coefficient due to ions and electrons and M_i, M_e the ion and electron masses respectively. If we take the ion temperature, T_i, equal to the electron temperature, T_e, and δ = 0, then Eq. 5.26 gives for deuterium plasmas: $eV_S \approx -2.8\,T_e$. As seen from Eq. 5.26, a nonzero secondary electron emission coefficient can reduce the potential drop significantly. However, secondary electron emission is suppressed for field lines incident at nearly glancing angles [7] and hence omitting δ should be a pretty good approximation for the Alcator C-Mod model. In practice it is customary to take $eV_S = -3\,T_e$. Equation 5.25 can now be rewritten as

$$E_i = 2\,T_i + 3\,Z_i T_e + 0.5\,M_i\frac{T_e+T_i}{M_D} = 2\,T_e + 3\,Z_i T_e + 0.5\,\frac{M_i}{M_D}2T_e$$

$$\Rightarrow \quad E_i = (2 + 3\,Z_i + M_i/M_D)\,T_e \tag{5.27}$$

The above result for the impact energy can be used in Bohdansky's formula to obtain the yield as a function of the temperature. This gives a satisfactory result except in the threshold region where the non-inclusion of the high energy tail of the Maxwellian distribution in the calculations, results in an underestimation of the sputtering yield. For this reason, the sputtering yields used here for deuterons and boron ions are convolutions of the single energy yield curve Y(E) for normal incidence, with a Maxwellian energy distribution f(E) shifted by the energy gained from the sheath potential, 3 Z_i T_e and in the presheath $(M_i/M_D)\,T_e$. With the unshifted Maxwellian energy distribution given by

$$f(E) = \frac{2}{T_i}\left(\frac{E}{\pi T_i}\right)^{1/2}\exp\left(-\frac{E}{T_i}\right) \tag{5.28}$$

the sputtering yield is obtained from the following equation, where $T_i = T_e$ was again assumed and $E_{Sheath} = 3ZiT_e + (M_i/M_D)T_e$ was used:

$$Y(T_e) = \int_{Max(E_{th},E_{Sheath})}^{\infty} Y(E)\left(\frac{E-E_{Sheath}}{\pi T_e}\right)^{1/2}\exp\left(-\frac{E-E_{Sheath}}{T_e}\right)\frac{2}{T_e}\,dE \tag{5.29}$$

In Fig. 5-9 the molybdenum yield for bombardment with a Maxwellian energy distribution of deuterium ions, accelerated in the sheath potential (Eq. 5.29), is compared to the monoenergetic yield (Eq. 5.3) for deuterons of energy 6 T_i = 6 T_e (see Eq. 5.27) As already mentioned, the two traces give similar result for all temperatures except in the region close to the threshold where the yield is underestimated in the monoenergetic case. For comparison, a third curve is included in the figure. It is the yield for an unshifted Maxwellian energy distribution of deuterons incident on molybdenum (Eq. 5.29 for E_{Sheath} = 3 Z_i T_e + (M_i / M_D) T_e = 0). The effect of the sheath is revealed when the two Maxwellian yields are compared.

The above description is valid only for deuterium and boron projectiles reaching the

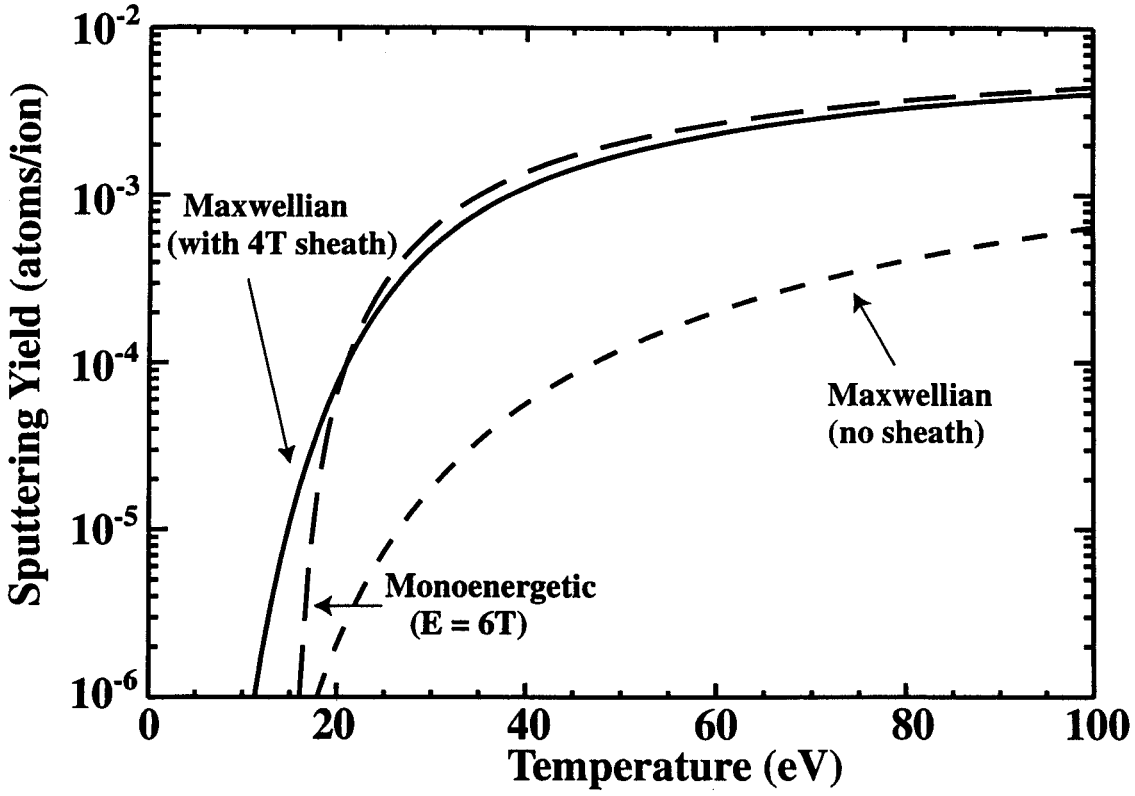

Fig. 5-9: Sputtering yield versus temperature for normal incidence of deuterium ions on molybdenum. Three curves are shown: for Maxwellian distribution of particles with and without sheath acceleration and for monoenergetic bombardment that includes sheath acceleration.

target. For the calculation of the molybdenum self-sputtering yield we need to have an estimate of the energy of the molybdenum ions returning to the divertor surface. Since only promptly redeposited molybdenum ions are considered, they do not have the time to reach thermal equilibrium. Hence the energy of the molybdenum ions will be the sum of the original energy of the sputtered atoms plus the energy gained in the sheath, which depends on where the molybdenum atoms are ionized with respect to the beginning of the sheath. In the current model, molybdenum is assumed, for simplicity, to be ionized just outside the sheath, gaining the full energy of 3 Z_{Mo} T_e on returning to the surface. As shown in Appendix D this is actually a pretty good approximation since the neutral molybdenum ionization length is comparable or larger than the deuterium ion gyroradius, which is the characteristic scale length of the magnetic part of the sheath [54]. (The electrostatic part of the sheath is much smaller, of the order of ten Debye lengths [54]). Since the threshold for molybdenum self-sputtering is 64 eV [48], the original energy of the sputtered molybdenum atoms, which is a few eV (see Section 5.1), can be neglected without introducing a significant error. Hence, for the calculation of the self-sputtering yield, the single energy Bohdansky formula for normal incidence is used with the assumption that all molybdenum ions have energy 3 Z_{Mo} T_e.

To complete the calculation of the energy gained inside the sheath by boron and molybdenum ions we need to have an idea of what their average charge state is. Boron ions are assumed to be helium-like (i.e. $Z_B = +3$). This choice is supported from previous calculations and experiments. Post et al. have calculated the average charge state as a function of the electron temperature for a number of elements [68]. The result is shown in Fig. 5-10. The average boron charge is 3 for temperatures in the range 5 to 30 eV. It should be noted that, under typical C-Mod conditions, electron temperature values do not exceed 50 or 60 eV outside the plasma separatrix. In addition, Matthews et al. have found, using plasma ion mass spectrometry on the DITE tokamak, that the fluxes of impurities such as carbon and oxygen are very similar in all charge states up to their helium-like states [69]. Even more importantly, Nachtrieb has recently measured in Alcator C-Mod, with the Omegatron ion mass spectrometer, significant levels of helium-like boron [70]. Specifically, in a rather cold region ($T_e < 10$ eV) of the scrape-off-layer, in the upper part of the tokamak, he estimated the helium-like boron flux to be about

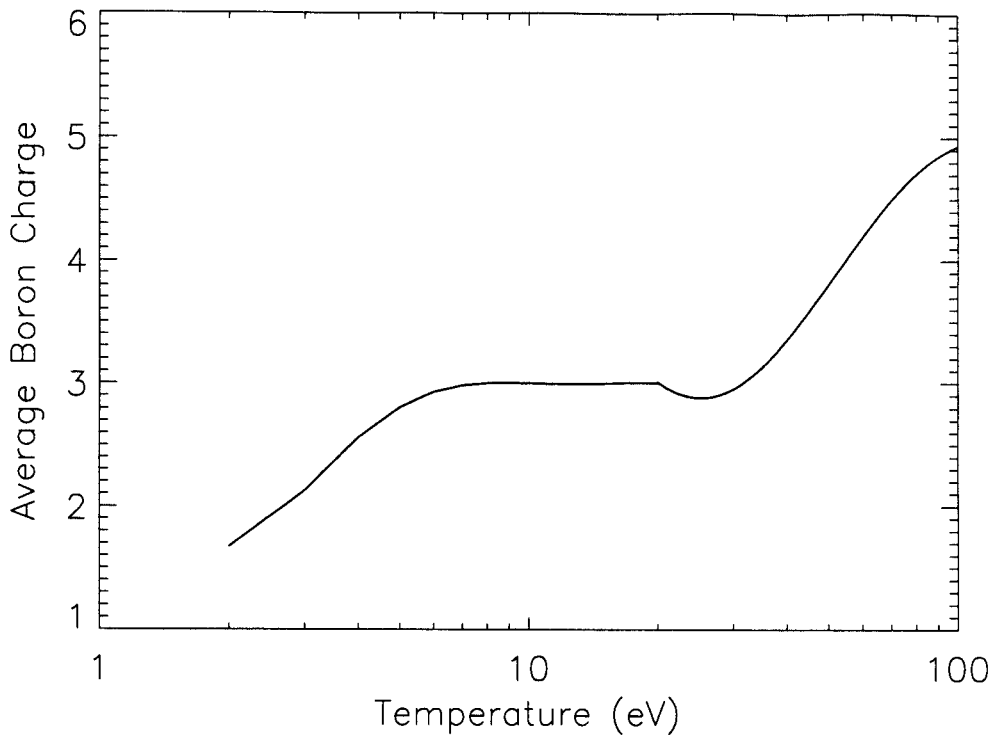

Fig. 5-10: Average charge state of boron as a function of the electron temperature as calculated in Ref. [68].

~ 2 % of the deuteron flux. For the promptly redeposited Mo ions an average charge Z_{Mo} = +1.5 is used. This is based on the fact that at high electron densities, such as is the case for Alcator C-Mod, particles can be ionized multiple times before completing their first orbit [61]. Although these additional ionizations will reduce the probability of prompt redeposition, some of the ions will make it back to the target. This assumption is further supported by a calculation, by Brooks and Ruzic, for tungsten in a D-T background plasma, in which an average charge of 2.1 is obtained for the redeposited ions [71]. It should be noted that the conditions assumed in their calculations, with the exception of the different background plasma, are pretty close to actual C-Mod experimental divertor conditions: the magnetic field was 5 T with an inclination angle $\theta = 3^\circ$, the electron density prior to the sheath $1. \times 10^{20}\ m^{-3}$, and the electron temperature 30 eV. With the above choices for the charge of boron and molybdenum ions, the typical energies with which the various projectiles arrive at the plate are (from Eq. 5.27): 6 T_e for deuterons, 16.4 T_e for boron ions, and 4.5 T_e for molybdenum ions.

Up to this point the yields for normal incidence have been calculated. However no adjustment has to be made to the molybdenum sputtering yields due to deuterium and boron ions despite the fact that their average angle of incidence is actually $\alpha = 65^{\circ}$ (see section 5.1). The reason is that for light ions incident on heavy targets, the sputtering yield for the energies of interest at $\alpha = 65^{\circ}$ is close to the yield at normal incidence [72]. Sputtering models have shown that different set of parameters characterize heavy ion sputtering of heavy targets. Brooks and Ruzic have found, in the same calculation that provided the average charge of redeposited tungsten, that sputtered tungsten ions tend to impact at near normal angles of incidence ($\alpha \approx 18^{\circ}$) [71]. Qualitatively, the difference in the angle of incidence between light and heavy projectiles can be explained as follows: Light ions, due to their relatively small mass, and hence gyroradius, are more strongly coupled to the magnetic field. On the other hand, heavy ions feel more strongly the effect of the accelerating electric field inside the sheath, which tends to pull them towards the normal to the surface (see Fig. 5-2). Since no data were available regarding the dependence on the angle of incidence of the Mo self-sputtering yield, the corresponding (for $\alpha \approx 18^{\circ}$) yield enhancement for tungsten self-sputtering as a function of the ion energy [7] was applied to the Mo self-sputtering. The tungsten data, which are calculated with the Monte Carlo program TRSPVMC [7], are shown in Fig. 5-11. The solid line, which is the fit to the tungsten data (shown with circles), gives the enhancement applied to the molybdenum self-sputtering yield for normal incidence as a function of the projectile energy.

As mentioned in the beginning of the chapter, the necessary parameters, Q, E_{th}, and E_{TF}, for the calculation of the yields are tabulated in Ref. [48] for the elements of interest with the exception of boron, for which Eqs. 5.8, 5.9, and 5.4 have been used. A summary of all the parameters used in the calculation of the molybdenum yields is given in Table 5-1. For the case of boron, the values used in the previous version of the model are also given in parenthesis for comparison. In Fig. 5-12, the sputtering yields of interest, as calculated based on the assumptions described in this section, are plotted as a function of the temperature. The top panel shows the yields for bombardment with deuterium and triply ionized boron ions and the bottom the self-sputtering yield for molybdenum ions redeposited at $\alpha = 18^{\circ}$. (The self-sputtering yield for $\alpha = 0^{\circ}$ is also shown for

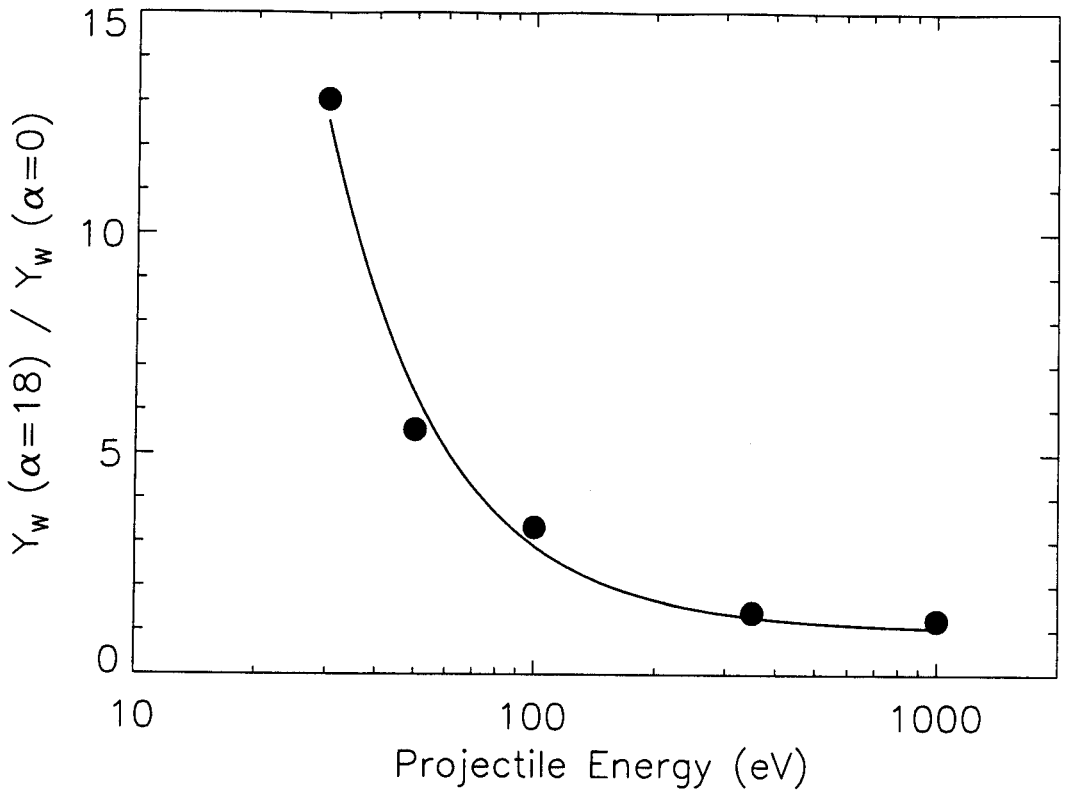

Fig. 5-11: Tungsten self-sputtering yield enhancement (with respect to the yield for normal incidence) as a function of energy for a projectile incident on the target at $\alpha = 18^\circ$ [7]. The fit (solid line) to the tungsten data was used to estimate the molybdenum self-sputtering yield for $\alpha = 18^\circ$.

Projectile	D	B	Mo
E_{th} (eV)	90	26.8 (52)	64
E_{TF} (eV)	4767	27825	533048
Q (atoms/ion)	0.023	1.28 (0.81)	18
Z	1	3	1.5
α	65°	65°	18°

Table 5-1: Parameters used in the model for the calculation of the molybdenum sputtering yield. E_{th}, E_{TF}, and Q for D and Mo are from Ref. [48]. In parenthesis the values used in the previous version of the model [62] if different from the ones used now.

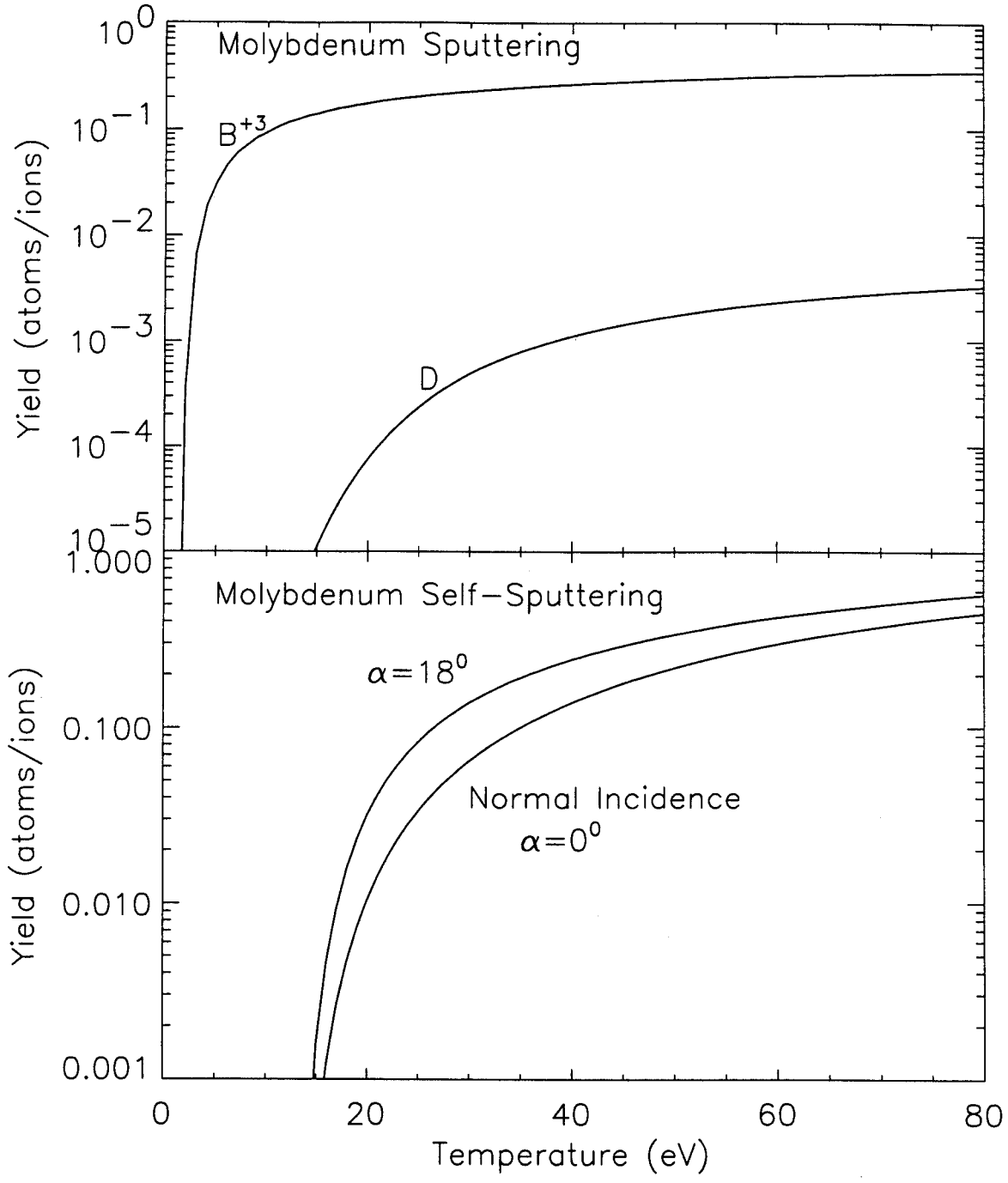

Fig. 5-12: Molybdenum sputtering yields as a function of the temperature for bombardment with deuterium and triply ionized boron projectiles having a Maxwellian energy distribution (top panel). The yields are calculated for normal incidence since $Y(\alpha = 65^{\circ}) \approx Y(\alpha = 0^{\circ})$. Also shown (bottom panel) the molybdenum self-sputtering yields used for the promptly redeposited projectiles of energy 4.5 T_e, incident at $\alpha = 18^{\circ}$. The self-sputtering yield for normal incidence ($\alpha = 0^{\circ}$) is given for comparison.

comparison). The sputtering yield due to deuterium ions is much lower than that due to the triply ionized boron ions. Hence, even at low boron concentrations, molybdenum sputtering by boron would be significant at all temperatures. It would actually dominate sputtering for temperatures $T_e \leq 20$ eV. Self-sputtering is also important for $T_e \geq 15$ eV. However, it does not become critical for any of the conditions that are typically encountered in the Alcator C-Mod divertor.

Finally, it has already been mentioned that the boron flux to the target is calculated from the spectroscopically measured brightness of the 412.2 nm BII line. This comprises the boron flux uncertainties discussed in Chapter 2: the lack of information on the real *S/XB* 's and the assumption that the boron flux to the target is equal to the boron influx as measured from the 412.2 nm line emission. The boron flux fraction is the ratio of the boron flux to the deuteron flux. The latter is approximated with $\Gamma_D = (J_S / e) \sin\theta$.

5.4 Comparison with Spectroscopy

There are seven probes located on the vertical face of the outer divertor. Six chordal spectroscopic views of this same surface were used during the experiments described here (see Fig. 5-3). The total Mo source rate, Φ, is obtained by integrating the Mo influxes over the divertor surface for both the model and the experiment. A comparison of the two results for an entire shot is shown in Fig. 5-13. Good agreement can be seen during the ohmic part of the shot. On the other hand, during the RF phase, the sputtering model predicts values 2-3 times higher for the molybdenum source. This trend is not repeatable. There are shots with better quantitative agreement during the ohmic phase while in others the match is better during the RF phase. However, for the majority of shots, the temporal behavior of both results is similar, signifying that the model incorporates most of appropriate physics. It should be noted that in the initial version of the model, where the boron fraction was kept constant during the shots, the calculated molybdenum source rate was consistently lower than the spectroscopically measured one during the RF phase. This implies that, at least in some shots, the non-variation of boron flux fraction with time was the reason for the discrepancy.

Similar results are also observed in individual chord and probe comparisons as seen by

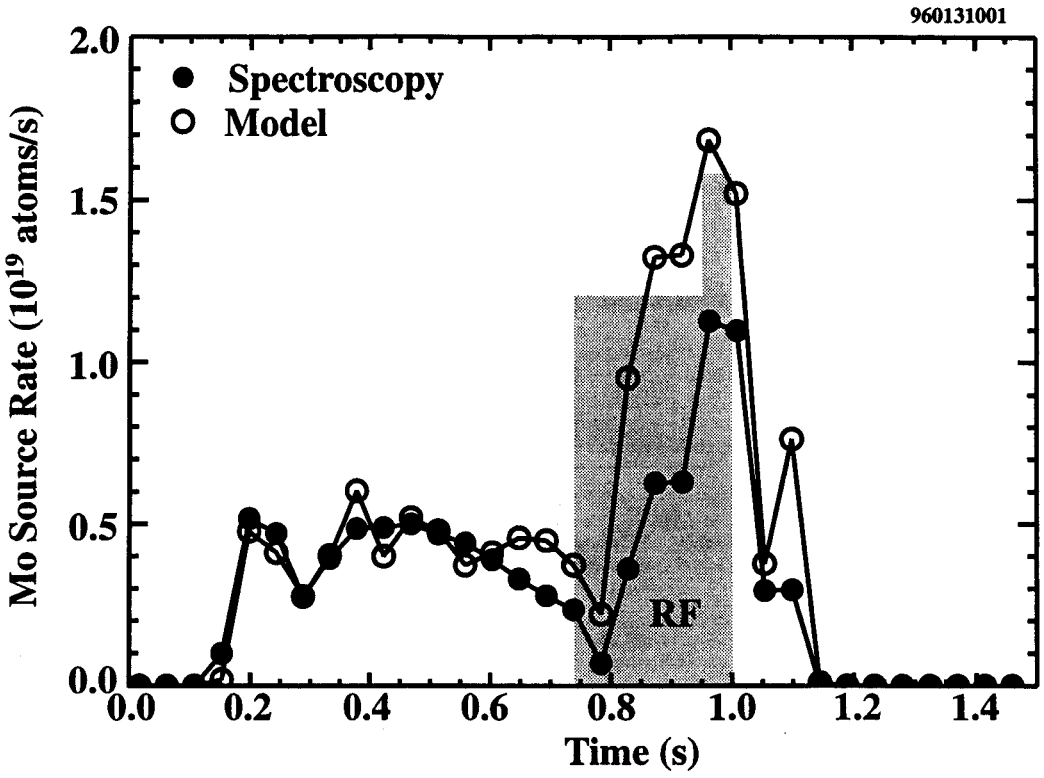

Fig. 5-13: Comparison of the calculated outer divertor source rate from spectroscopic data and the sputtering model. The RF power, which is also sketched, is increased from 1.2 to 1.6 MW at 0.95 s.

looking at Fig. 5-14. Figure 5-14 shows the molybdenum influxes measured with the spectrometer views # 8, # 10, # 12, # 14, # 16, and # 18 of Fig. 5-3 and the corresponding influxes calculated from probes # 2 through # 7 for the same case molybdenum shown in Fig. 5-13. (Recall from Fig. 5-3 that there is a one to one correspondence between these six views and probes, with view # 8 corresponding to probe # 2, view # 10 to probe # 3, etc). The agreement is fairly good for most of the probe-view pairs. There is, however, a significant discrepancy between the two results at the lower part of the outer divertor during the RF phase. The high molybdenum influx calculated from the # 2 probe data dominates the molybdenum source during this period and is the cause of the model overestimation of the source rate that was initially observed in Fig. 5-13. This increased calculated molybdenum influx at probe # 2 comes as a result of the combined high boron flux fraction and deuteron flux to the target during the RF phase in the vicinity of the specific probe, as shown in Fig. 5-15, and the increase in local temperature, as shown in

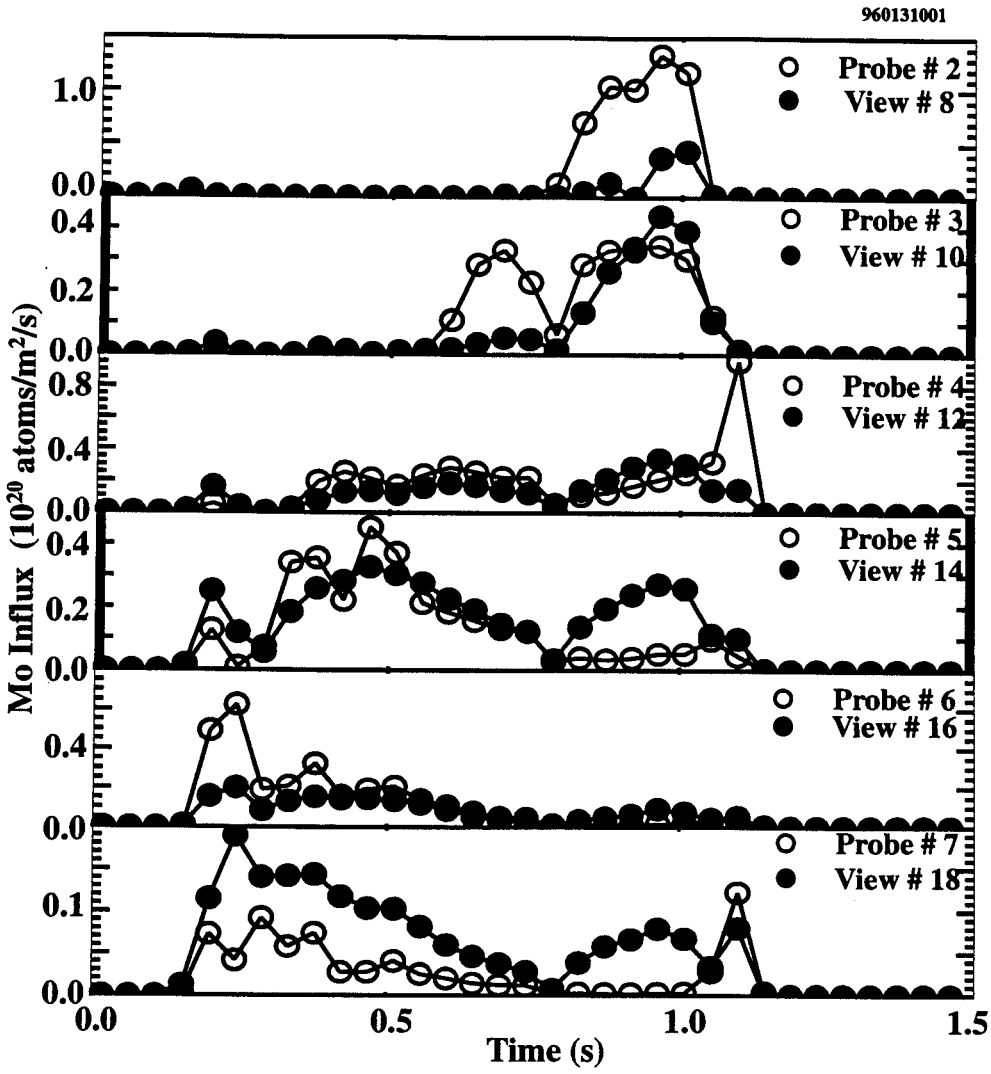

Fig. 5-14: Comparison of the spectroscopically measured molybdenum influx, for the six outer divertor chords used, to that calculated from the sputtering model for the corresponding probes.

Fig. 5-16. Specifically, Fig. 5-15, which gives the time history of the deuteron flux (left panel) and boron flux fraction (right panel) for all probes, shows that the deuteron flux and boron flux fraction measured during this period at the lower part of the divertor are the highest observed during the shot. The increase in the local temperature, which affects both the calculation of the yield and of the boron flux level through the *S/XB* 's, is also a combination of the turn-on of the RF power and the movement of the separatrix along the divertor target. The later "moves" probe # 2 from the private-flux-zone that it used to be during the ohmic phase to the common-flux-zone (see Fig. 5-3). In Fig. 5-16 this

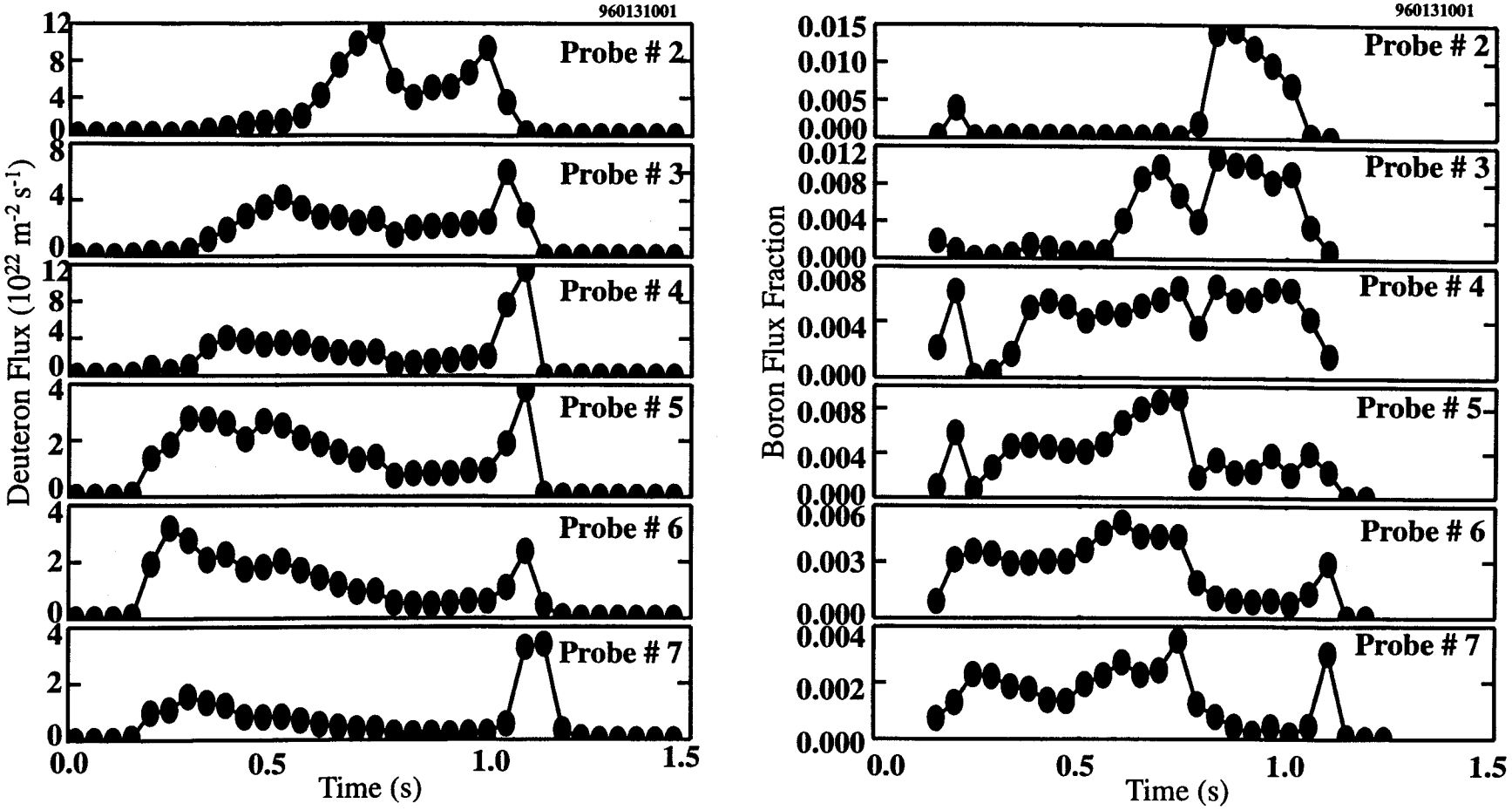

Fig. 5-15: Time history of the calculated deuteron flux (left panel) and boron flux fraction (right panel) in the vicinity of probes 2 through 7.

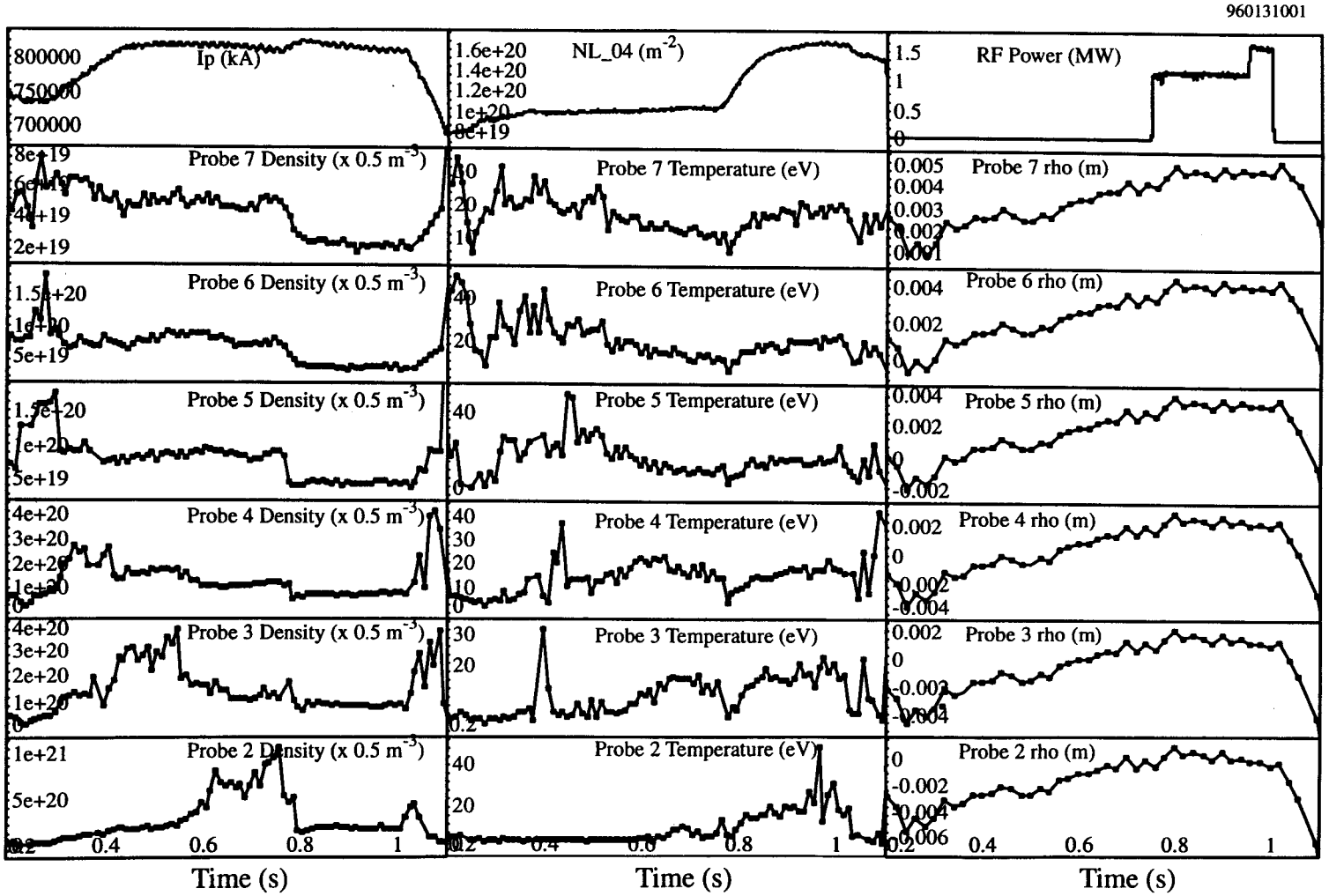

Fig. 5-16: Time history of electron plasma density and temperature in the vicinity of probes 2 through 7. The time history of the location of each probe with respect to the separatrix, the plasma current, the line integrated density, and the RF power is also given.

movement is denoted by the variable ρ (rho), which is defined as the distance from the plasma separatrix to a given flux surface, as measured in the midplane. It should be noted that positive values of ρ correspond to the common-flux-zone while negative values to the private-flux-zone for divertor measurements or core plasma for upstream measurements above the X-point. Although the above justify why the calculated molybdenum influx is high at the lower part of the divertor target during the RF phase, they do not explain the discrepancy with the result obtained from spectroscopy. Noting that the electron density has also a maximum at probe # 2 during the RF phase, one could possibly attribute part of the difference to greater errors in the calculation of the boron *S/XB* 's at high densities.

The results of such cases as Fig. 5-13 can also be integrated over an entire discharge. Figures 5-17 and 5-18 show a comparison between model and spectroscopy for a number of discharges from the 960130 run and from the 960213 and 960214 runs respectively. These discharges have widely varying conditions, including different plasma currents and volume averaged electron densities, but among them are included those with the highest measured molybdenum source rates during the 1995-1996 run period. In both figures, the molybdenum source rate averages during the ohmic phase of the shots are plotted in the top panel while the averages during the RF phase are plotted in the lower panel. The ohmic and RF averages are plotted as a function of the actual shot number. Before reaching any conclusions from these two graphs one should have the following things in mind:

Firstly, the vessel was boronized just prior to both the 960130 and the 960213 runs. The effect of the boronization is revealed in both figures. It is shown that the spectroscopically measured sources were lower than the calculated ones during the beginning of the first run day after the boronization. As mentioned in Chapter 4, at the beginning of a run day that immediately followed boronization of the chamber the molybdenum emissions from all locations observed were practically zero and gradually started to recover to their original levels as the day progressed. However, no corrections are made in the model with regards to boronization. The model calculates the sputtering assuming a 100 % molybdenum surface, based on the measured temperatures and densities, and hence it would predict higher molybdenum sputtering than measured, as

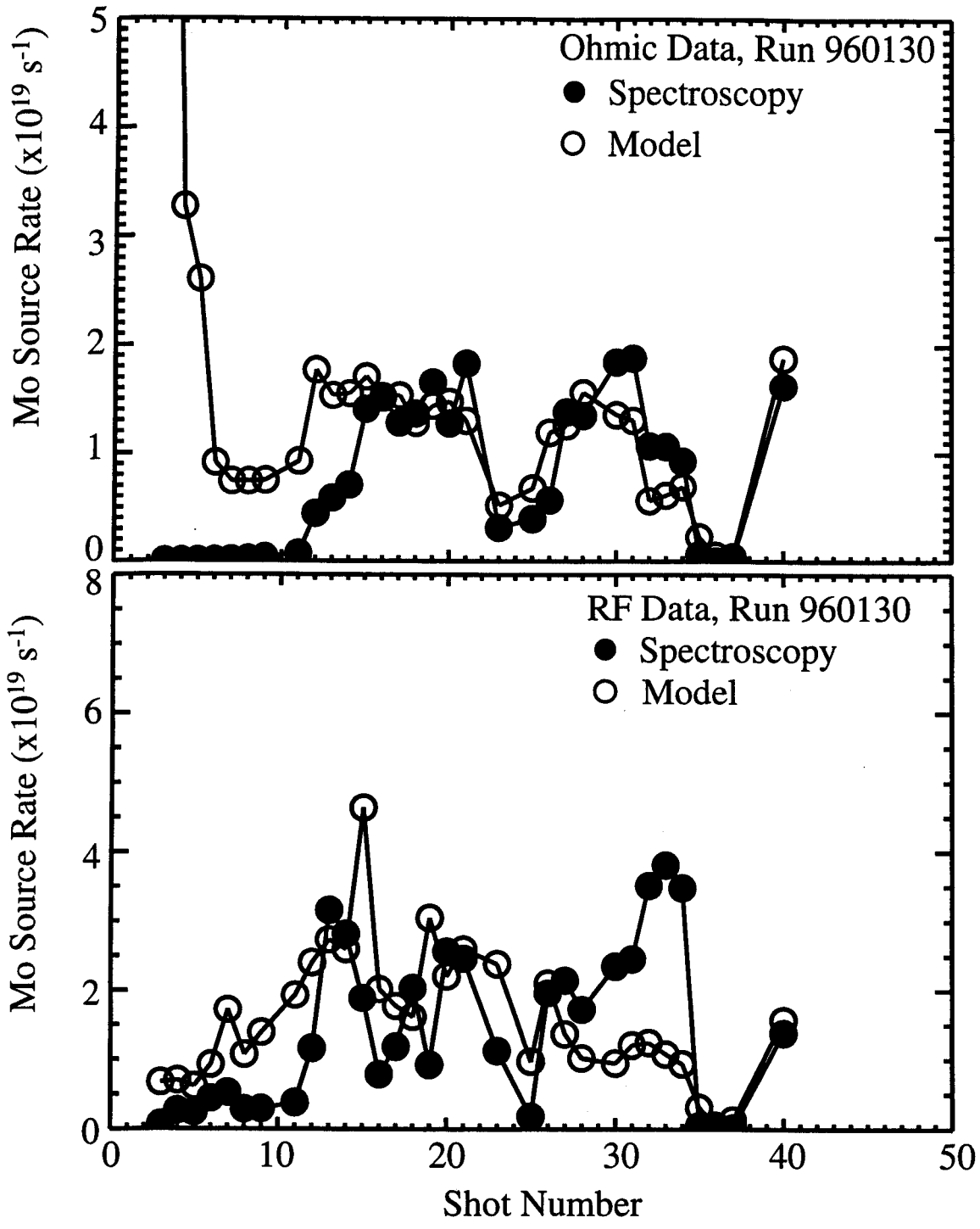

Fig. 5-17: Molybdenum source rates from spectroscopy and model for a number of shots from the 960130 run. Top panel: averages during the ohmic phase of each shot. Bottom panel: averages during the RF phase. The numbers for the shots are actual shot numbers.

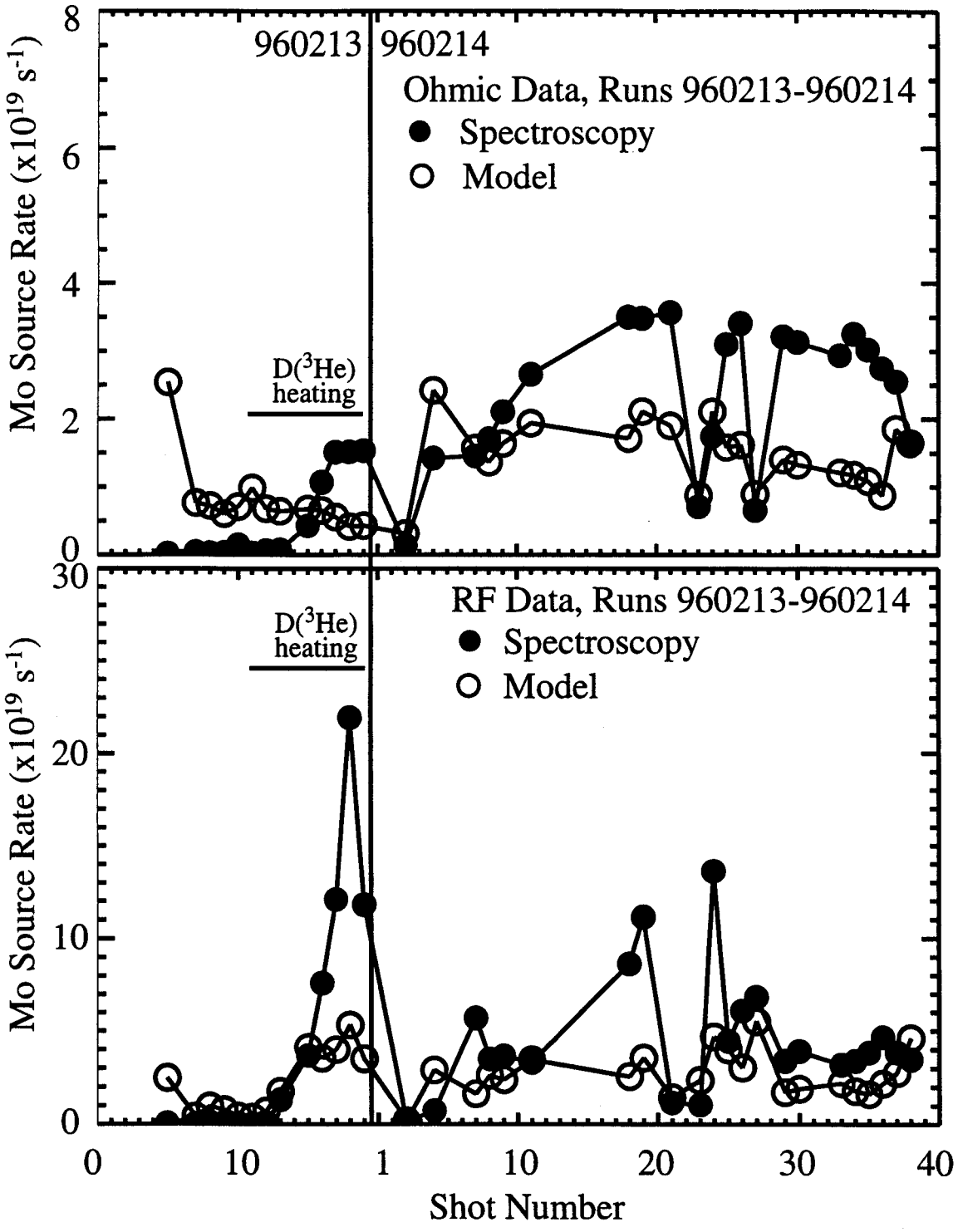

Fig. 5-18: Molybdenum source rates from spectroscopy and model for a number of shots from the 960213 and 960214 runs. Top panel: averages during the ohmic phase of each shot. Bottom panel: averages during the RF phase. The solid line defines the end of the 960213 run and the beginning of the 960214 run. The numbers for the shots are actual shot numbers.

long as the boronization is still effective. It could actually overestimate the sputtering even more since the probes typically overestimate the temperature immediately following boronization [73]. ECDC has a similar effect but it only lasts for a few shots. This explains the high molybdenum source rates that are predicted by the model in the first few shots of the 960214 run, especially in the ohmic phase (see Fig 5-18).

Secondly, if another impurity is introduced in the plasma at relatively high concentrations, it is expected that the spectroscopically measured molybdenum source rate will exceed the one predicted by the model since this other impurity, which is not accounted for in the model, is expected to contribute significantly to the molybdenum sputtering. This is obviously the case for the last 5-6 shots from the 960213 run (see Fig. 5-18) when ^{3}He was intentionally introduced in the plasma to be used in D(^{3}He) heating experiments.

Looking at the rest of the shots in Figs. 5-17 and 5-18, a noticeable difference exists. In Fig. 5-17 there is a satisfactory quantitative agreement between the two results in the ohmic phase but not during the RF phase while in the Fig. 5-18 the situation reverses with the agreement being good only during the RF phase. Of course, there is already some arbitrariness in the actual boron flux fraction and hence the absolute numbers are of less importance. What is important is that the model and spectroscopy show similar trends for the majority of shots examined.

Finally, it is of interest to know what the typical levels for the boron flux fraction that are used in the model are. In the previous version of the model, where the boron flux fraction was kept constant, the values needed for a good match between spectroscopy and model during the ohmic phase were 1.9 % for most of the runs, including 960130, and 4.8 % for the runs on the week that included the 960213 and 960214 runs. Figure 5-19 gives average values of the boron flux fraction used in the model at each probe location, for the ohmic and the RF phase of plasmas from the 960130 run (left panel) and 960213-960214 runs (right panel). As seen in Fig 5-19 there is a variation of the boron fraction with the probe location. The maximum is typically in probes # 3 though # 5 which is also the typical position of the outer strike point. During the 960130 run, the boron flux fraction used, does not exceed in most cases the 1 % value while in the 960213-960214 runs it reaches values 2 % or higher especially during the RF period. Hence, the measurements

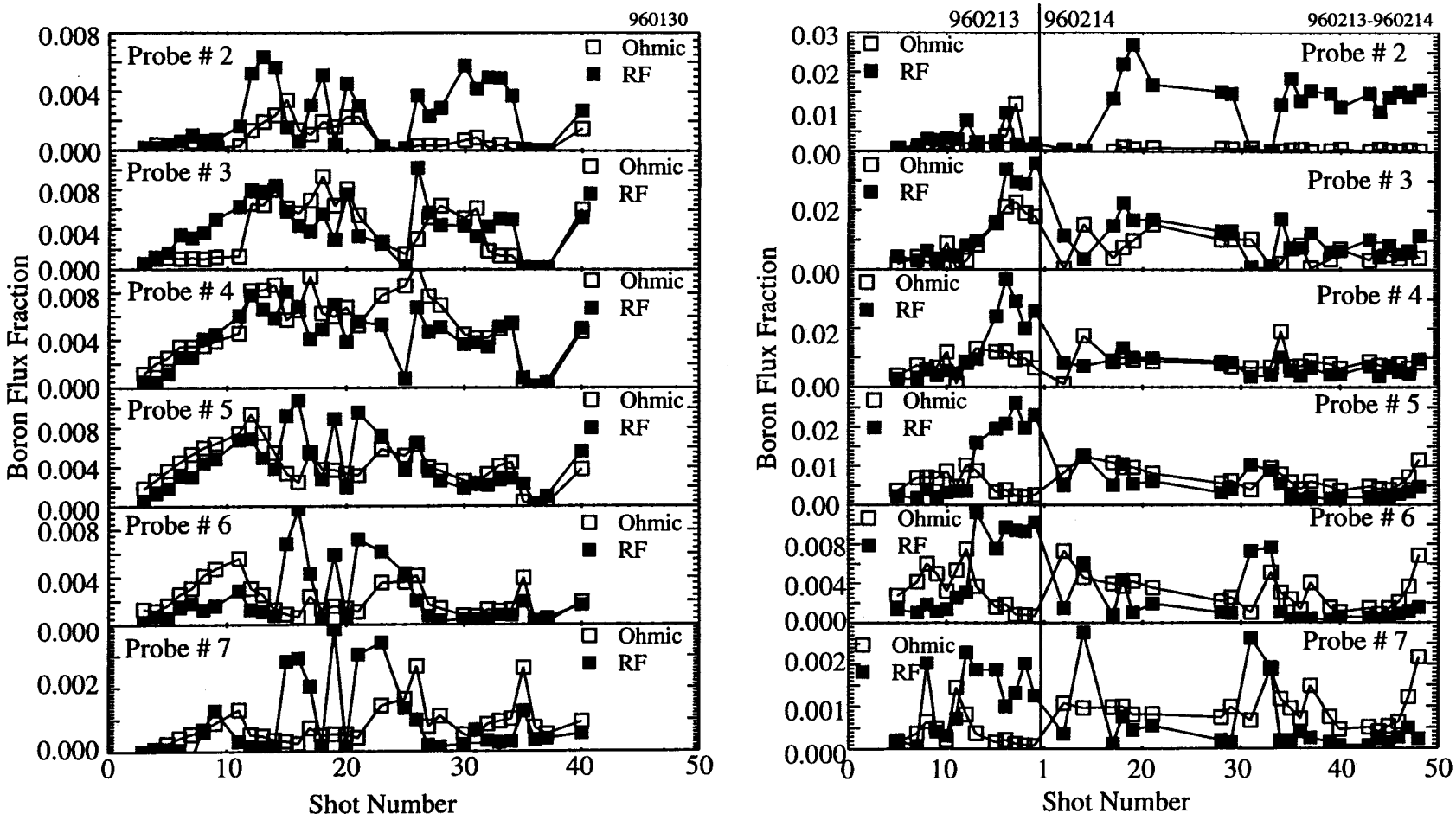

Fig. 5-19: Average values of the boron flux fraction for the ohmic and RF phases of plasma discharges from the 960130 run (left panel) and 960213-960214 runs (right panel).

verify that the boron flux fraction in the 960213-960214 runs was higher than the 960130 run, as it was required by the original model. It should be noted however that there were no obvious differences between the boronizations that preceded the shots analyzed in terms of the amount of boron deposited and the technique used. Finally, for most of the probes and the majority of shots, the ohmic and RF boron flux fractions do not differ significantly. The only exception is in the vicinity of probe # 2, where the RF values are systematically higher. Specifically for the 960214 run there are high even in absolute value, which explains the better molybdenum source rate match between model and spectroscopy during the RF phase of these discharges (Fig. 5.18).

5.5 Discussion of the Model

The physical sputtering model described in the previous sections, has provided satisfactory agreement with the spectroscopic results, signifying a fairly good understanding of the mechanism responsible for the generation of molybdenum at the outer divertor plates. However, there are some points that need further investigation that will be discussed in this section.

In the discussion regarding the yields for the various species used in this model (see Fig. 5-12), it was noted that boron sputtering of molybdenum was expected to play an important role and actually dominate for temperatures below 20 eV. Figure 5-20 shows the contribution of the various projectiles to the molybdenum source rate for two shots. Note that the shot in the top panel is the one analyzed in the previous section (Figs. 5-13 trough 5-16). In this discharge, the boron clearly dominates the molybdenum sputtering. This can be mainly attributed to the relatively low temperatures in the divertor during this shot (see Fig 5-16). In the discharge shown in the bottom panel, the contribution from the other species, especially deuterium, is bigger, becoming at certain times comparable to that of boron. At all times, the contribution of the promptly redeposited molybdenum ions is the smallest. These results are representative of the findings for all shots. Boron contributes the most to the sputtering while self-sputtering does not typically exceed 25 % of the total calculated source rate.

An important assumption in our model is the inclusion of only promptly redeposited

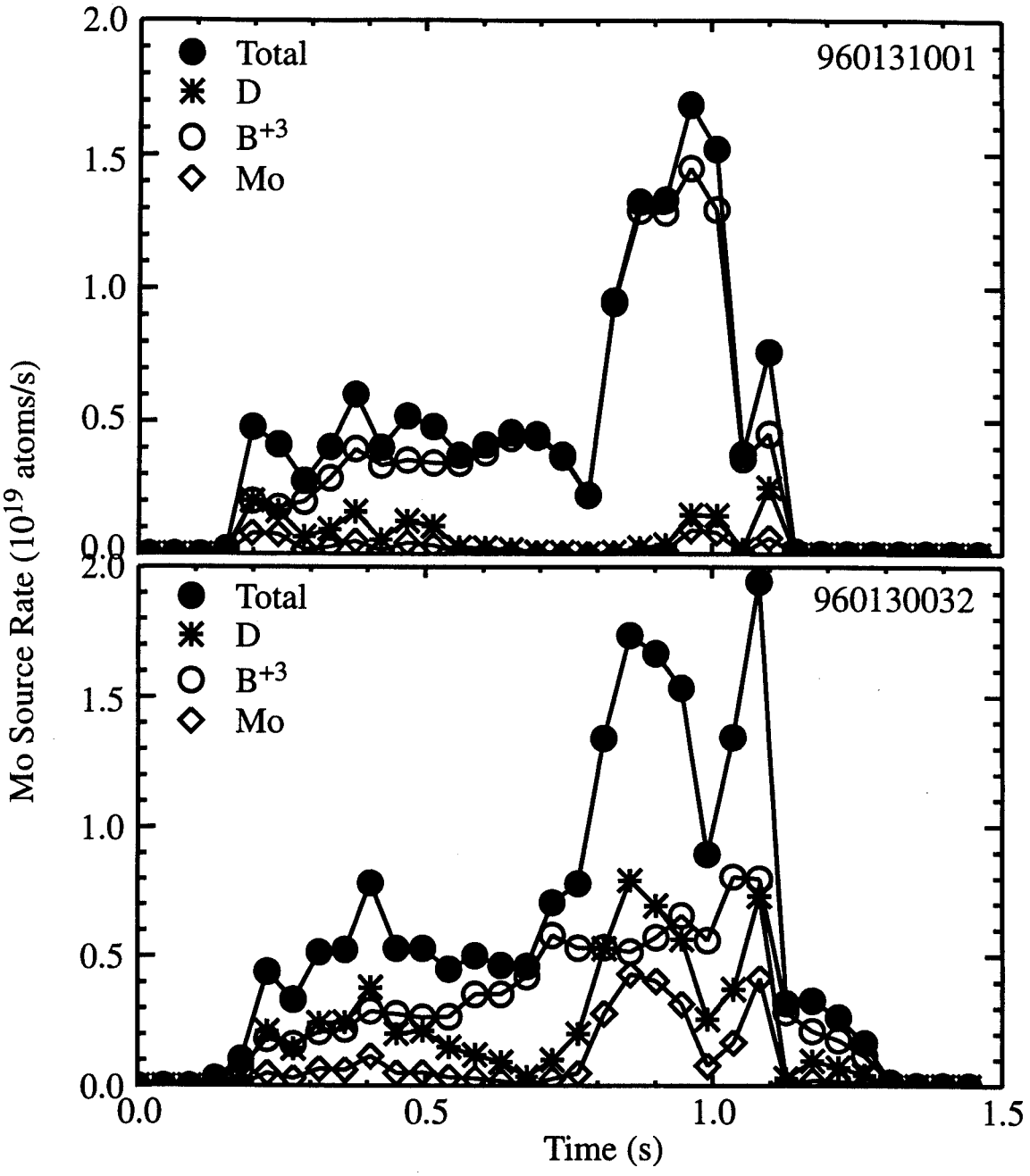

Fig. 5-20: Contribution of the various projectiles used in the model to the calculated molybdenum source rate. The data from two representative shots are given.

molybdenum ions in the self-sputtering calculation. Although the probability of redeposition frequently reaches values close to one for the conditions occurring in C-Mod plasmas, it was important to investigate the effect of the rest of the molybdenum ions. Two cases were considered. First, the extreme case in which all these ions are assumed to

be well collisionally coupled to the background plasma and return to the surface where they originated from. For the calculation of the molybdenum source rate, Eq. 5.21 was modified as follows:

$$\Gamma_{gross} = \Gamma_0 \frac{1}{1 - P_{pr,0}\, Y_{Mo} - (1 - P_{pr,0})\, Y'_{Mo}}. \tag{5.30}$$

In the above equation, Y'_{Mo} is the sputtering yield due to the non-promptly redeposited molybdenum ions. The energy of these ions was calculated from Eq. 5.27. However, for molybdenum ions collisionally coupled to the background plasma, their flow energy would be enormous, approximately 48 T_e. This approach lead to nonphysical results, with the calculated molybdenum source rate substantially higher than what found with spectroscopy. A more realistic case was then investigated. In this, Eq. 5.30 was again used for the calculation of the molybdenum source rate but now the non-promptly redeposited molybdenum ions are not considered collisionally coupled to the background plasma. This is consistent with the calculation (see Appendix D) that molybdenum ions are typically ionized at the sheath edge. With the sheath being collisionless it is probable that molybdenum ions do not have time to equilibrate with the deuterium plasma. However, we assumed that the charge of these ions was 3 and hence they gain an energy 9 T_e as a result of the acceleration inside the sheath. The result was that the contribution of these ions did not typically exceed 15 % of the total. Hence, neglecting them was a reasonable assumption especially because it is not easy to calculate, unless some sophisticated code was used, where on the target these ions would return.

The discrepancy between the measured and modeled molybdenum source rate results is a source of concern. Of course, even in the revised version of the model, there is a large uncertainty estimate on the boron flux to the target and in the parameters used in the calculation of the molybdenum yields from boron projectiles. As far as the underestimation of the molybdenum source rate that in many shots is observed during the RF phase, many mechanisms could be employed to explain it. One assumption that is called into question is that of toroidal symmetry. The probe and MoI spectroscopic measurements are made at two separate toroidal locations. It is possible that the level of toroidal asymmetry (unknown) changes upon transition to the RF phase of a discharge. However, we have no evidence that would support such a possibility.

Another possible explanation of the discrepancy between model and molybdenum source measurements is that the energy of sputtering ions is somehow enhanced during the RF phase of the discharge. This could occur due to either the emergence of a non-thermal electron population or an increase in T_i/T_e. The former increases the sheath potential even in the presence of very small (~1%) non-thermal populations [74]. The latter directly affects the energy of the ion and is, perhaps, more likely to be the cause of the discrepancy. While this requires further investigation, it is important to note that energetic ion particle tails of up to 4 keV, during RF heating, have been observed in the plasma edge of Alcator C-Mod [75].

5.6 Discharges which Contribute the most to Divertor Erosion

It is of great importance to identify the type of discharges that cause most of the observed erosion in the divertor surfaces. In particular, it is crucial to understand the effect of the various plasma parameters on the divertor erosion. If this is achieved, then in principle the plasma experiments can be designed in a way that erosion is minimized, or equivalently, the lifetime of the divertor surfaces is maximized. In chapter 3, the effect of a number of plasma parameters on the outer divertor molybdenum source rate has been investigated for Alcator C-Mod. However, spectroscopic information on the molybdenum sources is not always available due to the use of the Chromex spectrometer in a variety of experiments, which implies that the spectral range covered does not always include the molybdenum lines of interest. This prohibits us from having complete information for all type of discharges. On the other hand, based on the satisfactory agreement between model and spectroscopy, there is the option of using the model to obtain divertor erosion information for most of the shots during an experimental campaign. The erosion can always be calculated as long as divertor probe data, and information on local magnetic field orientation, are available, which is typically the case. For this reason, the outer divertor gross erosion was calculated for almost all shots of the 1995-1996 run campaign. Specifically, the molybdenum source rate was calculated for all shots with available probe data as a function of time and it was then integrated over the duration of each shot

to give the total gross erosion (in molybdenum atoms). It should be noted that this calculation, as well as the one described in the next section, had been performed prior to the revision of the sputtering model. Although there are differences between the results calculated in the two model versions, the main results should still be the same. Actually the old model may do an even better job in the specific calculations since for example it used an extra arbitrary factor of 2 to artificially correct the systematic underestimation of the results during the RF phase (for RF powers greater than 1.1 MW). Of course all results are subject to the problems mentioned regarding the performance of the model. However, since we are dealing with a big number (~1000) of shots, and the effect of boronization on the outer divertor is not long lasting, the model should still be able to reveal all the important parameters that influence the erosion levels.

A total of 944 shots were analyzed. The shots are separated into groups based on their plasma current. A shot is included in a specific group as long as its current falls within ± 50 kA of the nominal plasma current for the group. For example all shots with plasma currents ranging from 550 kA to 650 are considered as "600 kA" discharges. The majority of shots from the 1995-1996 campaign are included in one of the following four plasma current groups: 600 kA, 800 kA, 1000 kA, and 1100 kA.

Tables 5-2 through 5-4 summarize the most important findings with regard to the effect of the plasma current and the RF power on the divertor gross erosion. Table 5-2

Ip (kA)	Shots	Fraction of shots (%)	Total erosion below nose (Mo at.)	Erosion fraction(%)
600	83	8.8	2.81×10^{20}	4.2
800	404	42.7	1.83×10^{21}	27.3
1000	199	21.1	3.1×10^{21}	46.2
1100	78	8.3	1.32×10^{21}	19.7
All currents	944		6.70×10^{21}	

Table 5-2: Effect of plasma current on the calculated outer divertor gross erosion. The data include both ohmic and RF points.

gives the number of shots, and their fraction with respect to the total, analyzed in each of the major four plasma current groups, the total gross erosion for the shots of the group, and its fraction with respect to the total calculated erosion for all 944 shots. Both ohmic and RF data points are included in these data. Other parameters like the electron density could also vary widely. Despite that, it is evident that the erosion increases significantly with increasing plasma current. For a set of shots of constant density, higher plasma current would lead to higher temperature and thus to an increase in the erosion. In this case since a statistically large number of shots at various densities is available at each plasma current value, the effect of density is averaged out and the effect of the current dominates. To verify that the results shown in Table 5-2 are not somehow dominated by the RF power, the average gross erosion as a function of the plasma current for the ohmic phase of plasma discharges was calculated, and the results are presented in Table 5-3 and Fig. 5-21. As seen in the figure the erosion increases with plasma current, possibly in a linear way. Finally, Table 5-4 summarizes the effect of the RF power on the outer divertor erosion by giving the fraction of the time that the RF was on for each plasma current and the corresponding erosion fraction for the specific current. Clearly, for all currents, most of the outer divertor gross erosion occurs during the RF phase of plasma discharges.

The effect of the electron density on the gross erosion was also investigated. Although there is a general trend at the various plasma currents for the erosion to decrease with increasing density the spread in the data was too big to obtain any other useful conclusions.

Another way of looking at the data is to plot the total (for all 944 shots) gross erosion at the 10 outer divertor probes. This is done in Fig. 5-22 where the gross erosion and the erosion caused during RF heating is plotted versus the distance of the 10 probes from the midplane (probe 1 is the furthest away from the midplane, see Fig. 5-3). These two results are plotted in the top panel while in the bottom panel the RF erosion fraction is calculated by the ratio of the curves from the top panel. The erosion (in units of material thickness) for each shot was obtained by integrating the molybdenum influx over the duration of the shot and dividing by the molybdenum atom density

Average Ohmic Erosion (Mo atoms/shot)			
600 kA	**800 kA**	**1000 kA**	**1100 kA**
1.35×10^{18}	**2.70×10^{18}**	**5.74×10^{18}**	**7.74×10^{18}**

Table 5-3: Dependence of the average calculated outer divertor gross erosion on the plasma current for the ohmic phase of plasma discharges.

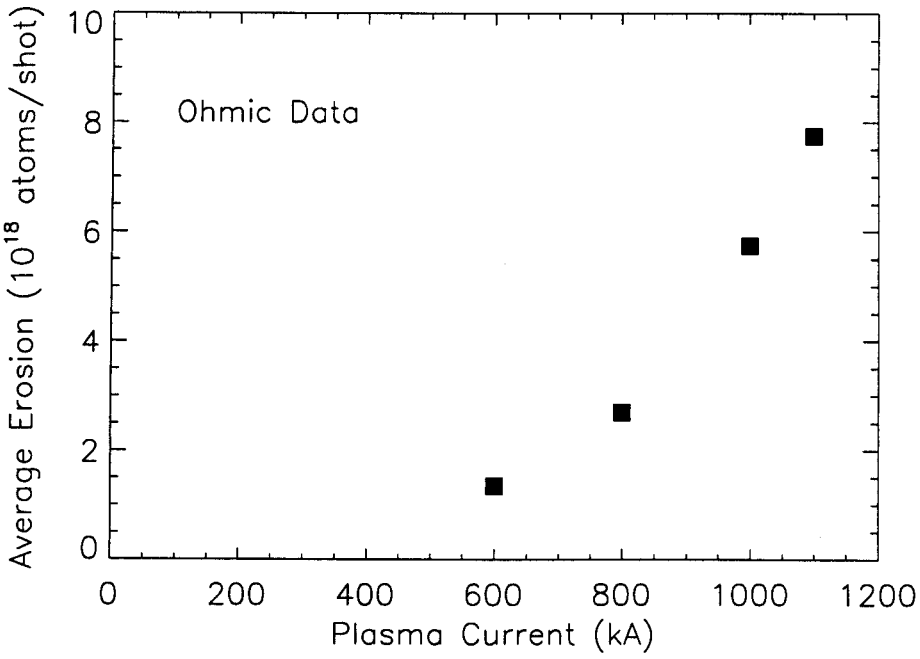

Fig. 5-21: Average calculated gross erosion vs. plasma current (from Table 5-3).

Ip (kA)	Time RF on (fraction of total, %)	Erosion during RF (fraction of total, %)
600	**27.1**	**60.1**
800	**18.7**	**40.3**
1000	**33.1**	**63.9**
1100	**29.4**	**54.2**
All currents	**22.2**	**55.6**

Table 5-4: Effect of RF power on the calculated outer divertor gross erosion.

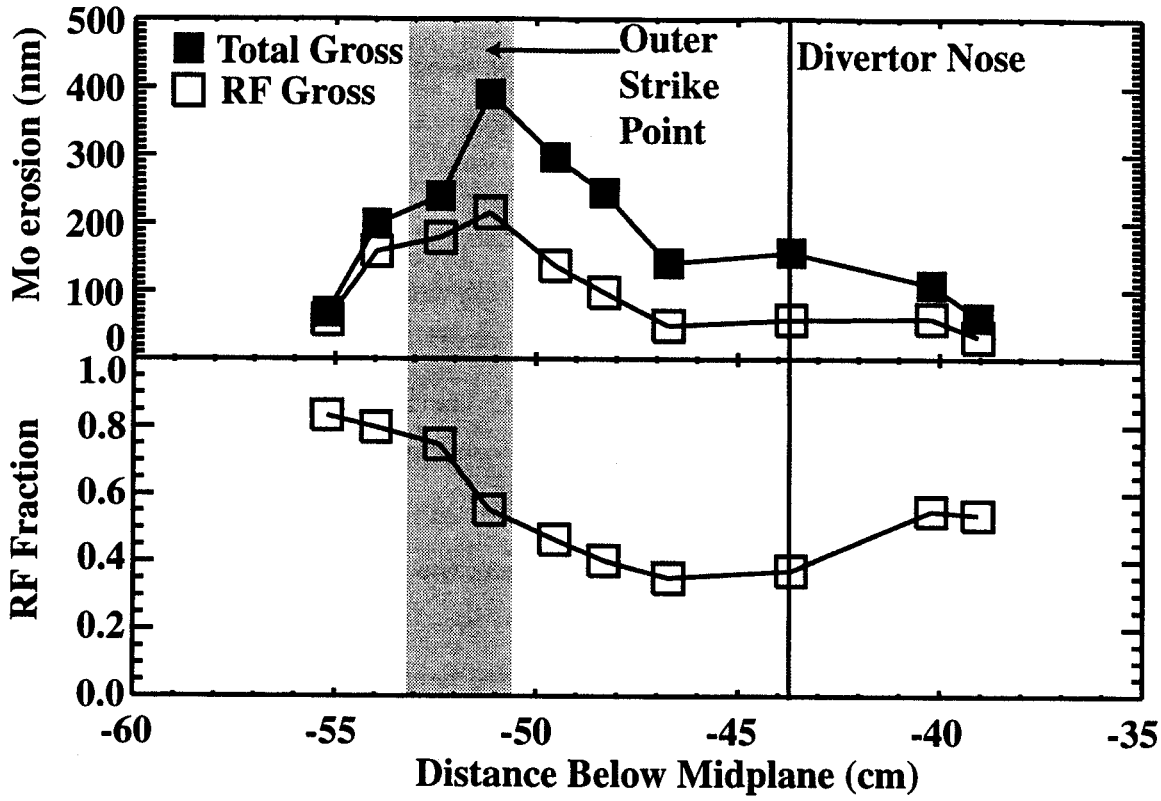

Fig. 5-22: Total gross erosion and gross erosion during RF heating as a function of the position on the outer divertor target (top panel). In the bottom panel, the RF erosion fraction at the same places.

$$n_{Mo} = \frac{\rho_{Mo}}{m_{Mo}} = \frac{10.22\,g/cm^3}{95.94 \times 1.66\times10^{-24}\,g} \approx 6.42\times10^{22}\ \text{atoms/cm}^3. \qquad (5.31)$$

As seen in Fig. 5-22, the gross erosion peaks in the vicinity of the outer strike point. In addition, the RF points dominate the erosion at the lower part of the plate. The peaking of the erosion during the RF phase in the area of the separatrix can be understood as follows: In most shots with sufficient RF power, the plasma would go into an H-mode confinement mode (with the main exception being shots at the beginning of a run campaign when the vessel is not well conditioned). In H-mode, the scrape-off-layer width decreases considerably and this implies that most of the interaction of the plasma with the target would occur in the vicinity of the separatrix.

5.7 Calculated vs. Measured Divertor Erosion

During the 1995-1996 experimental campaign the total molybdenum net erosion at various locations inside the C-Mod vessel was measured with the use of appropriately modified molybdenum tiles [45]. In these tiles, a layer of chromium was planted underneath the surface and used as a depth marker. The depth of the chromium layer beneath the surface was measured by Rutherford backscattering before and after the tiles were exposed to plasma discharges. A total of 21 such tiles were used in areas such as the inner wall, and the inner and outer lower divertor. The tiles were installed before the beginning of the run campaign and were exposed to 1090 tokamak plasmas during the period from November 1995 to March 1996. Examination of the tiles after the exposure showed significant net molybdenum erosion only near the outer divertor strikepoint area and much less, if any, everywhere else.

The outer divertor net erosion measurements have been compared with a campaign-integrated net erosion prediction, based on the model assumptions and probe measurements discussed in section 5.2. Specifically, Eq. 5.24 was used to calculate the net molybdenum influx for all 10 probes of the outer divertor target as a function of time and for all shots with available probe data. Data from 990 shots were used. The lack of data in the rest 100 shots is not a cause of concern. These are mainly short-period shots, many of them shortly after a vacuum break, that were not diverted at all. Figure 5-23 shows the probe-deduced campaign integrated gross and net erosion together with the net erosion as determined from the marker tiles as a function of the distance of each of the ten probes below the midplane (top panel). It also shows the contribution of the various projectiles used in the model to the total calculated gross erosion (bottom panel). As shown in the figure, there is generally a good qualitative agreement between the measured and calculated net erosions while quantitatively they differ, depending on the location, at most by a factor of about 3. From the bottom panel it is clear that the gross erosion is dominated by boron. It should be noted that the D contribution includes the enhancement of the calculated gross erosion by a factor of 2 during RF heating, that was mentioned in the previous section, since these data were also generated with the old version of the model.

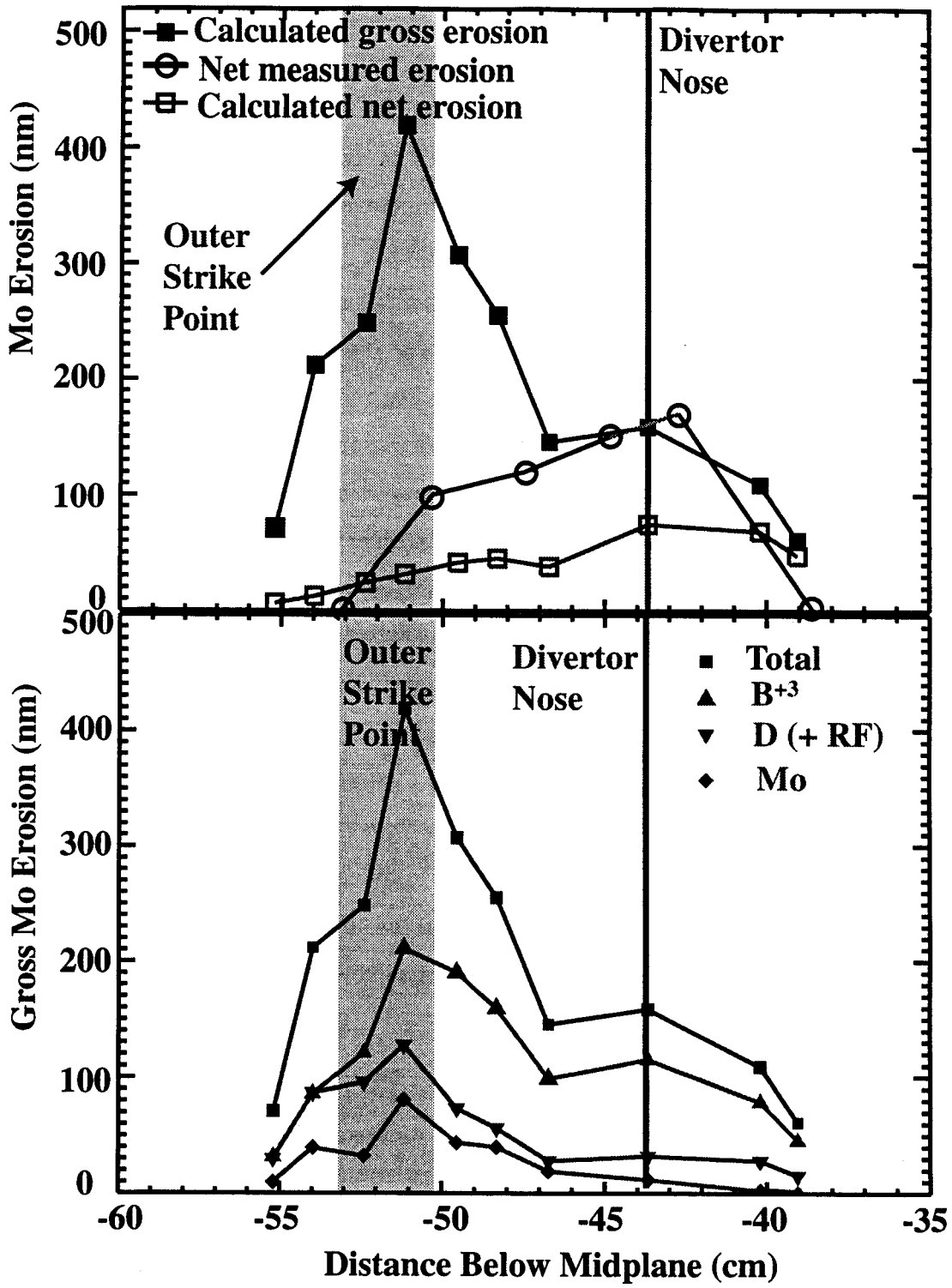

Fig. 5-23: Outer divertor campaign integrated gross and net calculated erosion and net measured erosion as a function of the distance of each of the ten probes below the midplane (top panel). Contribution of the various projectiles used in the model to the total calculated gross erosion (bottom panel).

What is striking, is the difference in the location of the peaks between the gross and the net erosion profiles. The gross erosion, as already seen, peaks in the vicinity of the separatrix while the net erosion away from it and actually in the area of the divertor nose. This result was expected since the molybdenum prompt redeposition is very strong close to the separatrix and much lower further away, where the mean free path for ionization is longer due to the lower values of density and temperature.

Looking at the net measured (or calculated) erosion results, useful information can be extracted for the usage of high-Z materials in the divertor region. With the peak molybdenum measured erosion being about 170 nm for a total exposure of about 1000 s, the average erosion is only 0.17 nm/s or 0.54 cm/exposure-year. This is not only very small in terms of absolute numbers but is also much lower than erosion rates (> 10 cm/exposure-year) measured for graphite tiles at the outer divertor region in the DIII-D tokamak [76]. This is consistent with the lower molybdenum sputtering yields [48]. In addition, one could make a very simplified, order of magnitude estimate of the net erosion expected in an ITER-like machine having high-Z divertor target plates. Assuming that the conditions in the vicinity of the divertor target in this future machine are not much different than the ones encountered in Alcator C-Mod then the peak net erosion for a single shot lasting 1000 s will be ~ 170 nm. Then for a campaign lasting a 1000 shots, the peak net erosion will be ~ 170 μm. These numbers are very small and hence encouraging. If they will be true in a future machine, then they imply that physical sputtering will not be a major source of concern for the integrity of the divertor.

Chapter 6

Conclusions

In this thesis a study of molybdenum sources and screening in Alcator C Mod has been presented. Specifically, the work has focused on the spectroscopic identification of all large molybdenum sources, on their dependence on plasma parameters, and their relative contributions to the core plasma molybdenum density. The effectiveness of boronization as a surface conditioning method which reduces the molybdenum source rates and core concentration has been also considered. A large fraction of this thesis was devoted to the understanding of the underlying mechanisms that cause the production of molybdenum at various surfaces, putting emphasis at the divertor. Overall, this work helps in characterizing the performance of molybdenum, a high Z material, as a tokamak first wall surface.

The primary diagnostic used in the experiment was a visible spectrometer that was capable of monitoring simultaneously emissions from 16 different locations around the tokamak. This allowed the comparison of the source rates from various surfaces under identical conditions. Unhindered operation of the diagnostic system in discharges characterized by high neutron rates ($> 10^{13}$ s^{-1}), required the use of shielding material (lead borated polyethylene) around it to minimize the noise caused in the spectra by the interaction of neutrons and gamma rays with the detector. For the conditions encountered in C-Mod until the completion of this work, the shielding used was adequate in reducing the noise to an acceptable level. However, with the anticipated extension of the C-Mod capabilities in the following years, which will lead to the generation of plasmas with

considerably higher neutron rates, relocation of the spectrometer outside the tokamak cell may have to be considered.

A number of surfaces have been monitored with the spectrometer. Only the inner wall near the midplane, the outer divertor, and the antenna protection tiles have been found to be significant sources of molybdenum. The outer limiters, which are 5 mm closer to the plasma than the antenna protection tiles, and the inner divertor target are not important molybdenum sources. The main experimental observations are summarized and discussed in the following paragraphs.

During inner-wall limited plasma operation, the inner wall is practically the only source of molybdenum. Strong correlations between the inner wall emissions and the core molybdenum density have been observed which have established that the inner wall is the source of the molybdenum that ends up in the core during limited discharges and the initial (limited) phase of all plasmas. Operating at high densities helps in reducing the molybdenum emissions from the inner wall for this type of plasmas. On the contrary, RF heating in limited plasmas results in a considerable increase of the emissions originating from the inner wall.

In diverted plasmas, emissions from all three (inner wall, outer divertor, antenna protection tiles) surfaces can be large depending on conditions. In terms of magnitude, the inner wall source level is much smaller compared to what was observed in limited plasmas. In dedicated experiments, in which the inner gap was changed in a controlled way, it was established that the source from the inner wall, which was found to decrease with increasing gap, does not correlate with the core molybdenum density. The same conclusion was reached from other experiments as well. The above results imply a very good screening of the molybdenum by the plasma at the inside of the tokamak. In this perspective, the inner wall is not an important source of molybdenum in diverted discharges at least for typical C-Mod experimental conditions. It is possible that there exists an intermediate case, between limited and typical diverted discharges, where, with sufficiently small - yet undetermined - inner gap, significant number of wall-emitted molybdenum atoms reach the core.

For ohmically heated diverted plasmas, the core molybdenum levels are very low and do not constitute a concern for tokamak operation. It was observed that during this phase

the divertor is particularly effective in screening impurities originating at its targets.

In RF-heated diverted plasmas, it is believed that the antenna protection tiles are the source of most of the molybdenum that penetrates in the core. Emissions emanating from there, have been found to correlate well with core molybdenum density levels in almost all cases. However, we can not exclude the outer divertor from being a contributor to the core molybdenum levels but there are indications that it is often not the dominant source. This result is significant since it is expected that the divertor target in the next generation fusion devices will be made primarily with a high-Z material.

Our observations regarding the screening of molybdenum during divertor operation are consistent with screening results obtained in Alcator C-Mod with nitrogen. In these, it was observed that nitrogen screening depended strongly on the poloidal position of injection, with the penetration being easiest when impurities were injected from the outer midplane and hardest when the gas was injected from the inner wall and the divertor.

In terms of the effect that plasma parameters have on the source levels during diverted plasma operation, the following observations have been made:

a) Emissions from the antenna protection tiles depend strongly on the RF power level and do not seem to be affected by the type of plasma confinement and possibly the outer gap.
b) Source rates from the outer divertor increase with increasing plasma current and RF power. High emission levels are related to the profiles of the electron temperature and ion flux to the target. ELM-free H-modes, unlike EDA H-modes, lead to a reduction of the source levels (for the inner wall as well) but are not desirable since they lead to accumulation of impurities in the main plasma. Operating at high densities reduces emissions which go to zero whenever the plasma detaches. However, although detachment is favorable regarding intrinsic impurity generation, it is not for seeded impurities which can penetrate more easily to the core [42]. It thus looks that, as far as the generation and screening of impurities at the divertor is concerned, the best scenario involves operation of tokamaks at the high density end of the high-recycling regime.

Understanding the molybdenum production mechanism is crucial if one wants to

minimize it. Physical sputtering seems to be the dominant mechanism responsible for the generation of molybdenum at the various surfaces. In the case of the antenna protection tiles, the emissions are consistent with an enhanced RF sheath rectification effect.

Special care has been devoted to the study of the molybdenum sputtering at the outer divertor. A simple physical sputtering model has been developed that calculates the molybdenum source at the divertor, providing satisfactory agreement with the spectroscopic results. The effect of deuterons, boron ions, and returning molybdenum incident on the target is included in the calculation. The deuteron flux to the target was calculated from Langmuir probe data while the boron flux was estimated from spectroscopic measurements of boron emissions. Boron flux levels were typically 0.5 to 1 % of the deuteron flux. It is found that the boron ions dominate the sputtering. It is also found that the probability of molybdenum being "promptly" redeposited (within a gyration after having been sputtered) can be as high as 80%. High probability of prompt redeposition is favorable in tokamaks because it reduces the net erosion. Specifically, it has been found that although the molybdenum gross erosion peaks close to the separatrix, the net erosion, which is not only significantly smaller but also rather small in absolute numbers, peaks further away in the target plate. The latter is also consistent with erosion measurements performed in C-Mod with appropriately modified molybdenum tiles. The molybdenum that is not promptly redeposited is ionized within the sheath or extremely close, making it likely that is quickly redeposited as well.

The study of boronization as a surface conditioning method which reduces the molybdenum source rates and core concentration has shown a varying effectiveness dependent on first wall surface location. The beneficial effects of boronization disappear rather fast for the outer divertor, last longer for the inner wall, with the antennas and plasma core benefiting the most. The strong correlation between antenna molybdenum source rate and core molybdenum level, in terms of both magnitude and time, supports the findings that the antennas are the surface of most interest, regarding molybdenum penetration to the plasma.

The results obtained in this thesis help us draw some conclusions regarding the suitability of using a high-Z material as a tokamak first wall surface, as far as a) production of intrinsic impurities and subsequent transport to the core and b) structural

integrity of the walls is concerned. Using a high-Z material for the antenna protection tiles is a source of concern especially because the tiles are located relatively close, compared to the divertor, to the main plasma and in a region of the tokamak where the screening of impurities is poor. On the other hand, the divertor findings are very encouraging. Not only is the molybdenum source level low compared to corresponding source rates from machines with low-Z divertor materials as a result of the lower sputtering yields, but the net erosion is even lower due to the favorable effect of prompt redeposition, which is much stronger for high-Z materials. Furthermore, based on our indications, a divertor configuration like the one in Alcator C-Mod is effective in screening intrinsic impurities.

Appendix A

Principle of Particle Flux Measurement

The calculation of the neutral molybdenum particle influx Γ in this thesis was based on Eq. 2.2: $\Gamma = 4\pi\, I\, (S/XB)$, where I is the measured intensity in units of photons per unit time, unit area, and unit solid angle. A derivation of this equation will be presented that is basically a reproduction of the derivation given in Ref. [29].

In the general case there are two methods that can be used for measuring particle influxes from surfaces: active laser-induced fluorescence (LIF) and passive spectroscopy. LIF has the advantage that no information on the temperature is needed. However, it is a rather complicated procedure since a tunable laser is required to excite the atoms in front of the surface, and two measurements are required for particle influx $\Gamma = n\ v$ measurement: one for the atomic density n and one for the streaming velocity v. On the contrary, passive spectroscopy is much simpler since only the absolute line intensities have to be measured. The passive method is also the only practical method for investigations of flux profiles from extended particle sources.

The passive spectroscopy method, which is what we have been using, is applicable in all cases where the neutrals are ionized close to the emanating surface but do not recombine into the neutral state within the plasma. For the derivation, coronal equilibrium is assumed [5]. In steady state, the continuity equation for the neutrals in the ground state n_g^0 can be written as

$$\frac{\partial n_g^0}{\partial t} = -\nabla\cdot\vec{\Gamma} - n_e\, n_g^0\, S = 0, \qquad \text{(A.1)}$$

where S is the neutral particle ionization rate. Integrating Eq. A.1 over the volume we have

$$\int \nabla \cdot \vec{\Gamma}\, dV = \int n_e\, n_g^0\, S\, dV\,. \tag{A.2}$$

Using Gauss's theorem leads to

$$\int_S \vec{\Gamma} \cdot d\vec{A} = \int n_e\, n_g^0\, S\, dV\,. \tag{A.3}$$

The volume is now specified as a box with area ΔA at the surface (see Fig. A-1). In practice, ΔA is the area viewed by the spectrometer. The length of the box in the direction normal to the surface, which is also the direction that the emissions are monitored, is chosen large in relation to the ionization length so that there is no outflux at the end surface. In addition, if the particle flux at the emanating surface is homogeneous over a scale length much larger than the ionization length, there will be no net particle flow through the side surfaces of the box either. Then, Eq. A.3 can be written

$$\Gamma = \frac{1}{\Delta A} \int n_e\, n_g^0\, S\, dV\,, \tag{A.4}$$

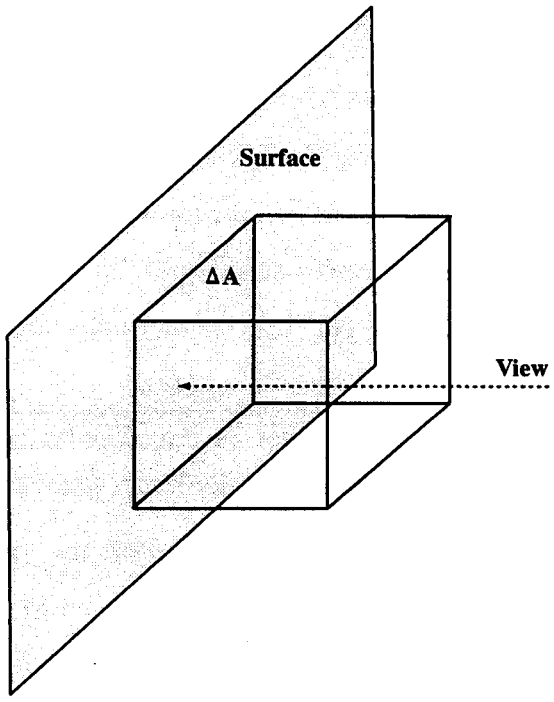

Fig. A-1: Sketch of the area monitored.

where Γ is the average particle influx averaged over the selected surface area ΔA.

The intensity I', in units of power per unit area, and unit solid angle, is given by

$$I' = \frac{1}{\Delta A} \int \varepsilon \, dV , \tag{A.5}$$

where ε is the emissivity integrated over the frequency range of a particular line:

$$\varepsilon = \frac{h\nu}{4\pi} A_{mn} \, n_m^0 . \tag{A.6}$$

In the above equation n_m^0 is the density of neutrals in level m, A_{mn} is the Einstein coefficient describing the probability for the spontaneous transition of an electron from an upper energy level m to a lower energy level n and $h\nu$ is the energy of the photon emitted. In coronal equilibrium, the density in state m, n_m^0, can be related to the number of neutrals in the ground state n_g^0 by the equation

$$n_m^0 \sum A_{mn} = n_e \, n_g^0 \, X , \tag{A.7}$$

where X is the excitation rate for transitions from the ground state.

Solving Eq. A.7 for n_m^0 and substituting in Eq. A.6, and inserting the result for the emissivity ε in Eq. A.5 we obtain

$$I' = \frac{h\nu}{4\pi} \frac{A_{mn}}{\sum A_{mn}} \frac{1}{\Delta A} \int n_e \, n_g^0 \, X \, dV . \tag{A.8}$$

The above equation can be rewritten as follows

$$I' = \frac{h\nu}{4\pi} \frac{A_{mn}}{\sum A_{mn}} \frac{1}{\Delta A} \int n_e \, n_g^0 \, S \, dV \; \frac{\int n_e \, n_g^0 \, X \, dV}{\int n_e \, n_g^0 \, S \, dV} . \tag{A.9}$$

Using Eq. A.4 we can write that

$$I' = \frac{h\nu}{4\pi} \frac{A_{mn}}{\sum A_{mn}} \frac{\overline{X}}{\overline{S}} \Gamma \tag{A.10}$$

where $\overline{X}$ and $\overline{S}$ are volume averages of the two rate coefficients.

Using the definition of the branching ratio $B = \frac{A_{mn}}{\sum A_{mn}}$ and $I = \frac{I'}{h\nu}$ we obtain the fundamental relation

$$\Gamma = 4\pi \frac{\overline{S}}{\overline{\overline{X}}\, B} \qquad \text{(A.11)}$$

Appendix B

Improvements to the Original Sputtering Model

The model described in Chapter 5 is an improved version of the model initially presented in Ref. [62]. The following improvements have been made:

a) In the previous model, the ratio β of the boron to the deuteron flux to the target, which is used in the calculation of the molybdenum sputtering, was not independently measured but was a fitting parameter inferred from the comparison of the calculated molybdenum source rates with the spectroscopic results for a number of shots. The boron flux was kept at a constant fraction of the deuteron flux for all views and all times. In the current model, the boron flux is calculated, with the assumptions discussed in Chapter 2, from the spectroscopically measured brightness of the 412.2 nm BII line, which is monitored simultaneously with the molybdenum triplet of interest (see section 2.4).

b) In the current model, the revised Bohdansky formula for the calculation of the yields is used (see Eqs. 5.3 through 5.7). The two formulae, original and revised, give, for all practical purposes, the same result for the molybdenum yield due to deuteron and boron projectiles. However, the old formula overestimated the molybdenum self-sputtering yield in the energy range of interest. The discrepancy between the two results can be calculated, for a given energy, by the ratio of Eq. 5.6 to Eq. 5.7. This number decreases from ~ 2, for energies in the self- sputtering threshold region (64

eV), to ~ 1.5 for energies in the upper limit (~ 250-300 eV) of the energy range of interest.

c) The parameters Q and E_{th} (Eq. 5.3) for boron sputtering of molybdenum are not among those tabulated in Ref. [48]. In the previous model they were estimated from the available molybdenum sputtering data for other projectiles (H, D, T, ^{4}He, and C), since these parameters are functions of the projectile and target masses and the surface binding energy. However the uncertainty on these two parameters and especially E_{th} was rather big due to the lack of adequate data points for projectiles with mass values close to the boron mass. In this version they are calculated from the analytical expressions given in section 5.1: Eq. 5.8 for Q and Eq. 5.9 for E_{th}. This change resulted in an increase of the molybdenum yield due to boron projectiles by a factor of two or higher depending on the energy of the projectile.

Appendix C

Thermal Energy Transported to a Surface by a Maxwellian Distribution

Assuming a Maxwellian distribution of particles inside a volume, the average energy is given by the relation [77]: $E = 3/2\, T$, where T, in units of energy, is the temperature characterizing the distribution. However, for a particle flux hitting a surface, this value is different: $E = 2\,T$. This result can be obtained as follows:

Assume a surface that is perpendicular to the x-direction. Then, the energy flux q to the surface can be calculated from [4]

$$q = \int_{-\infty}^{\infty}\int_{-\infty}^{\infty}\int_{0}^{\infty} \frac{1}{2} M u^2 u_x f(u) d^3u \tag{C.1}$$

where

$$f(u) = n\left(\frac{M}{2\pi T}\right)^{3/2} \exp\left[-u^2/u_{th}^2\right] \tag{C.2}$$

is the Maxwellian distribution, with $u_{th}^2 = \dfrac{2T}{M}$ the thermal velocity, M the mass, and n the particle density. From Eqs. C.1 and C.2 we then have

$$q = \int_{-\infty}^{\infty}\int_{-\infty}^{\infty}\int_{0}^{\infty} \frac{1}{2} M u^2 u_x n\left(\frac{M}{2\pi T}\right)^{3/2} \exp\left[-u^2/u_{th}^2\right] d^3u$$

$$= \int_{-\infty}^{\infty} du_y \int_{-\infty}^{\infty} du_z \int_{0}^{\infty} du_x \frac{1}{2} M (u_x^2 + u_y^2 + u_z^2)\, u_x\, n \left(\frac{M}{2\pi T}\right)^{3/2} \exp\left[-(u_x^2 + u_y^2 + u_z^2)/u_{th}^2\right]$$

$$\Rightarrow \quad q = \frac{1}{2} M n \left(\frac{M}{2\pi T}\right)^{3/2} \int_{-\infty}^{\infty} du_y \int_{-\infty}^{\infty} du_z \int_{0}^{\infty} du_x\, u_x^3 \exp\left[-(u_x^2 + u_y^2 + u_z^2)/u_{th}^2\right] +$$

$$2 \frac{1}{2} M n \left(\frac{M}{2\pi T}\right)^{3/2} \int_{-\infty}^{\infty} du_y \int_{-\infty}^{\infty} du_z \int_{0}^{\infty} du_x\, u_x u_y^2 \exp\left[-(u_x^2 + u_y^2 + u_z^2)/u_{th}^2\right], \qquad \text{(C.3)}$$

where in the second term of the right hand side of the above equation we have used the fact that the expression was symmetric in u_y and u_z. To proceed, we need to calculate a number of definite integrals. The calculation is straightforward, requiring in some of them integration by parts, and knowledge of the following

$$\int_{-\infty}^{\infty} \exp\left(-\frac{u_y^2}{u_{th}^2}\right) du_y = \pi^{1/2}\, u_{th}. \qquad \text{(C.4)}$$

The results of the calculations are given below:

$$\int_{0}^{\infty} u_x^3 \exp\left(-\frac{u_x^2}{u_{th}^2}\right) du_x = \frac{1}{2} u_{th}^4 \qquad \text{(C.5)}$$

$$\int_{-\infty}^{\infty} u_y^2 \exp\left(-\frac{u_y^2}{u_{th}^2}\right) du_y = \frac{1}{2} \pi^{1/2}\, u_{th}^3 \qquad \text{(C.6)}$$

$$\int_{0}^{\infty} u_x \exp\left(-\frac{u_x^2}{u_{th}^2}\right) du_x = \frac{1}{2} u_{th}^2 \qquad \text{(C.7)}$$

Substituting Eqs. C.4 through C.7 in Eq. C.3 we find

$$q = \frac{1}{2} M n \left(\frac{M}{2\pi T}\right)^{3/2} \left[\pi^{1/2} u_{th}\, \pi^{1/2} u_{th} \frac{1}{2} u_{th}^4 + 2\, \pi^{1/2} u_{th} \frac{1}{2} \pi^{1/2}\, u_{th}^3 \frac{1}{2} u_{th}^2\right]$$

$$= \frac{1}{2} M n \left(\frac{M}{2\pi T}\right)^{3/2} \left[\frac{1}{2} \pi\, u_{th}^6 + \frac{1}{2} \pi\, u_{th}^6\right]$$

$$= \frac{1}{2} M n \left(\frac{M}{2\pi T}\right)^{3/2} \pi\, u_{th}^6$$

$$= \frac{1}{2} M n \left(\frac{M}{2\pi T}\right)^{3/2} \pi \left(\frac{2T}{M}\right)^3$$

$$\Rightarrow \quad q = (2T)\frac{1}{4} n \left(\frac{8T}{\pi M}\right)^{1/2} \tag{C.8}$$

In the above equation the factor $\left(\frac{8T}{\pi M}\right)^{1/2}$ is the average speed $\bar{u}$ [77], and hence

$$\Gamma = \frac{1}{4} n \left(\frac{8T}{\pi M}\right)^{1/2} = \frac{1}{4} n \, \bar{u} \tag{C.9}$$

is the particle flux crossing the surface [77].

From Eqs. C.8 and C.9 we get that

$$q = 2T \; \Gamma. \tag{C.10}$$

With q being the energy flux to the surface and Γ the particle flux to the surface, 2 T is the average thermal energy transported to the surface.

Appendix D

Location of Ionization of Sputtered Molybdenum in the C-Mod Divertor

In the sputtering model described in Chapter 5, it was assumed that the sputtered molybdenum neutrals are ionized just outside the sheath, thus gaining the full sheath energy, 3 Z_{Mo} T_e, upon returning to the surface. For this to be true, the neutral molybdenum ionization length must be comparable or larger than the characteristic scale length of the sheath.

The molybdenum ionization length is calculated from

$$\lambda_{ion} = \frac{u_{at}}{S n_e} \sim (\frac{2 E_{at}}{M_{Mo}})^{1/2} \frac{1}{S n_e}, \qquad \text{(D.1)}$$

where n_e is the local electron density, S the neutral molybdenum ionization rate (see Fig. 5-4), M_{Mo} the molybdenum mass, and E_{at} the energy of the sputtered molybdenum atoms. In section 5.1 it was mentioned that the energy distribution of the sputtered atoms has a maximum at half the binding energy ($E_S/2$). We take E_{at} equal to this value, which for molybdenum is approximately 3.5 eV.

As already discussed in Chapter 5, in the case of an oblique magnetic field to the divertor surface, the sheath consists of two parts [54]: an electrostatic part, with a characteristic length of the order of 10 Debye lengths

$$\lambda_{es} \sim 10\, \lambda_D = 10\, (\frac{\varepsilon_0 T_e}{e^2 n_e})^{1/2}, \qquad \text{(D.2)}$$

and a magnetic part with dimension of the order of the background plasma ion gyroradius

$$\lambda_m = \frac{m_D u}{eB}\cos\theta \sim (\frac{2 m_D T_e}{e^2 B^2})^{1/2}\cos\theta\,. \qquad (D.3)$$

In the above equations, m_D is the deuterium mass, B the local magnetic field, and θ the inclination angle of the field lines with respect to the divertor target surface (see Fig 5-2). As θ decreases, the potential drop in the magnetic part of the sheath increases while in the electrostatic decreases, until $\theta \rightarrow 0$ where the whole potential drop occurs in the magnetic part of the sheath and the electrostatic part completely disappears. For the Alcator C-Mod outer divertor, θ is of the order of ~ 0.5° and, hence, $\cos\theta \sim 1$. Assuming a rather moderate value for the electron density $n_e = 5.\times10^{19}$ m^{-3}, and B ~ 5.7 T in the divertor region, the magnetic part of the sheath is 3.4 times bigger than the electrostatic part. For higher densities, the discrepancy becomes even larger (e.g. the magnetic part is 4.8 times bigger for $n_e = 1.\times10^{20}\,m^{-3}$). Hence, the neutral molybdenum ionization length should be compared to the deuterium gyroradius. For $n_e = 5.\times10^{19}$ m^{-3} and T_e = 25 eV, Eqs. D.1 and D.3 give λ_{ion} = 0.17 mm and λ_m = 0.18 mm respectively while for $n_e = 5.\times10^{20}$ m^{-3} and T_e = 10 eV the two numbers of interest become λ_{ion} = 0.035 mm and λ_m = 0.11 mm. In general, whenever there is a combination of very high densities and moderate temperatures, the ionization may occur inside the sheath ($\lambda_{ion} < \lambda_m$). However, in the second of the two examples given above, the ionization length becomes comparable, λ_{ion} = 0.10 mm, to the deuterium gyroradius if a 5 eV temperature, instead of 10 eV, is assumed. Figure D-1 shows the time histories of the two characteristic lengths as calculated based on the measured electron density and temperature values in the vicinity of probe 4 for the shot that has been analyzed in detail in Chapter 5. In this case, the molybdenum ionization occurs typically outside the sheath. It is, thus, seen that for a wide range of conditions, the assumption that the molybdenum neutrals are ionized at the sheath edge is reasonable. However, there are conditions in which the above assumption is not true and the molybdenum neutrals are ionized inside the sheath. In this case, their energy at the target is overestimated in the model. This does not have any significant consequences in terms of the results obtained in Chapter 5, since it has already been shown that the contribution of molybdenum self-sputtering in the total source rate is

small compared to the boron and deuterium contributions.

It should be noted that for the case of molybdenum atoms ionized inside the sheath, the energy gained in it could be calculated from

$$E_{Mo,sheath} = e\,V = e\int E\,dx\,. \tag{D.4}$$

In the above equation, E is the electric field calculated by [67]:

$$E = V_S\, e^{-(x/\lambda_m)} / \lambda_m \tag{D.5}$$

with $eV_S = 3\ Z_{Mo}\ T_e$ being the energy gained by a particle ionized at the sheath edge.

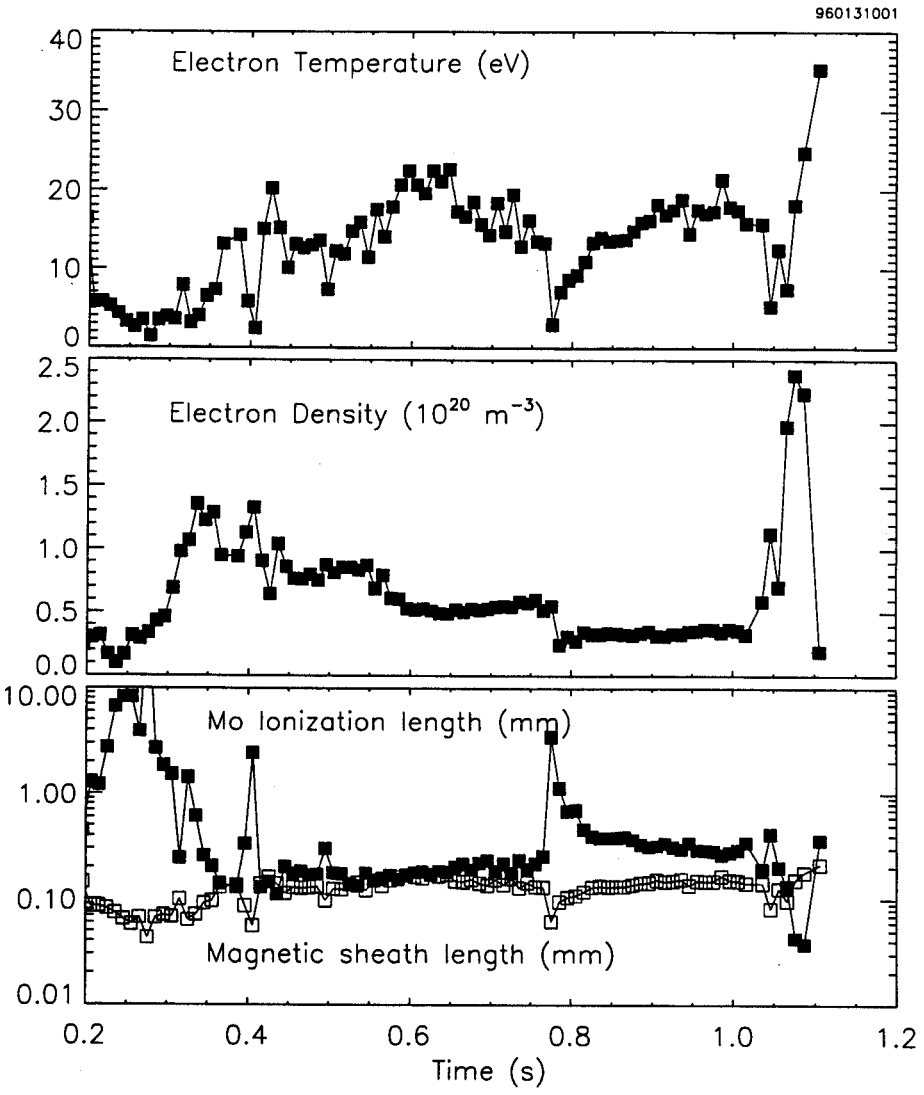

Fig. D-1: Time histories of electron temperature, electron density, and corresponding molybdenum ionization length and magnetic sheath length, as calculated from Eqs. D.1 and D.3. The electron data were measured with probe 4.

References

[1] C. S. Pitcher and P. C. Stangeby, "Experimental Divertor Physics", *Plasma Phys. Controlled Fusion* **39**, 779 (1997).

[2] G. M. McCracken and B. E. Stott, *Nucl. Fusion* **19**, 889 (1979).

[3] J. Wesson, "Tokamaks", Clarendon Press, Oxford, 1997.

[4] P. C. Stangeby, in "Physics of Plasma-Wall Interactions in Controlled Fusion" (D. E. Post, R. Behrisch, Eds), Plenum Press, New York, 41 (1986).

[5] I. H. Hutchinson, "Principles of Plasma Diagnostics", Cambridge University Press, 1987.

[6] P. C. Stangeby and G. M. McCracken, "Plasma Boundary Phenomena in Tokamaks", Nuclear Fusion, **30(7)**, 1225 (1990).

[7] W. Eckstein and V. Philipps, "Physical Processes of the Interaction of Fusion Plasmas with Solid", Academic Press, 1996.

[8] I. H. Hutchinson et al., *Phys. Plasmas* **1,** 1511 (1994).

[9] G. Federici et al., *J. Nucl. Mater.* **266-269**, 14 (1999).

[10] Chromex, 250IS Imaging Spectrograph Users Manual, Version 4.10, April 1993.

[11] Chromex, Grating Selection Parameters, Technical Report 3, September 1991.

[12] D. Lumma, "Investigation of a Diagnostic Tecnique for Measuring Electron Densities via Stark Broadening on the Alcator C-Mod Tokamak," thesis for the M.Sc. degree in Physics, Massachusetts Institute of Technology, 1996.

[13] J. L. Terry, private communication (1996).

[14] J. Briesmeister, "MCNP-A General Monte Carlo Code for Neutron and Photon Transport," LA-7396-m, Rev. 2, Los Alamos National Laboratory, Sep. 1986.

[15] C. Fiore, private communication (1996).

[16] B. Labombard, J. Goetz, C. Kurz et al., *Phys. Plasmas* **2**, 2242 (1995).

[17] J. H. Irby et al., *Rev. Sci. Instrum.* **59**, 1568 (1988).

[18] T. C. Hsu et al., Proc. 8th Joint Workshop on ECE and ECRH, IPP III/186, 409 (1993).

[19] J. E. Rice and E. S. Marmar, Rev. Sci. Instrum. **61**, 2753 (1990).

[20] D. Smith, private communication (1999).

[21] M. J. May, M. Finkenthal, S. P. Regan et al., *Nucl. Fusion* **37**, 881 (1997).

[22] M. A. Graf, "Impurity Injection Experiments on the Alcator C-Mod Tokamak'', thesis for the Ph.D. degree in Nuclear Engineering, Massachusetts Institute of Technology, 1995.

[23] K. Behringer, H. P. Summers, B. Denne, M. Forrest, and M. Stamp, *Plasma Phys. Control. Fusion* **31**, 2059 (1989).

[24] A. R. Field, C. Garćia-Rosales, G. Lieder, C. S. Pitcher, R. Radtke, *Nucl. Fusion* **36**, 119 (1996).

[25] G. Fussmann, J. V. Hofmann, G. Janeschitz, H. R. Yang, *Nucl. Fusion* **30**, 2319 (1990).

[26] A. Thoma, K. Asmussen, R. Dux et al., *Plasma Phys. Control. Fusion* **39**, 1487 (1997).

[27] J. Sugar and A. Musgrove, *J. Phys. Chem. Ref. Data* **17(1)**, 155 (1988).

[28] W. Whaling and J. W. Brault, *Physica Scripta* **38**, 707 (1988).

[29] G. Fussmann, J. V. Hofmann, G. Janeschitz, H. R. Yang, Sputtering Flux Measurements in the ASDEX Divertor, Rep IPP III/153, Max-Planck-Insitut fur Plasmaphysik, Garching (1989).

[30] N. R. Badnell, T. W. Gorczyca, M. S. Pindzola, and H. P. Summers, *J. of Physics B* **29**, 3683 (1996).

[31] G. M. McCracken, private communication (1999).

[32] Y. Takase et al., *Phys. Plasmas* **4**, 1647 (1997).

[33] M. Greenwald et al., *Nucl. Fusion* **37**, 793 (1997).

[34] I. H. Hutchinson et al., *Plasma Phys. Control. Fusion* **37**, 1389 (1995).

[35] R. J. Maqueda and G. A. Wurden, *Nucl. Fusion* **39**, 629 (1999).

[36] H. L. Manning, J. L. Terry, B. Lipschultz et al., *Nucl. Fusion* **26**, 1665 (1986).

[37] M. Bures, H. Brinkschulte, J. Jacquinot et al., *Plasma Phys. Control. Fusion* **30**, 149 (1988).

[38] F. W. Perkins, *Nucl. Fusion* **29**, 583 (1989).

[39] D. D' Ippolito, J. Myra, M. Bures, J. Jacquinot, *Plasma Phys. Control. Fusion* **33**, 607 (1991).

[40] R. Majeski, P. H. Probert, T. Tanaka et al., *Fusion Engineering and Design* **24**, 159 (1994).

[41] B. LaBombard, private communication (1999).

[42] G. M. McCracken, B. Lipschultz, B. LaBombard et al., *Phys. Plasmas* **4**, 1681 (1997).

[43] E.S. Marmar, *Bull. Am. Phys. Soc.* **41** (1996).

[44] J. Irby, private communication (1999).

[45] W. R. Wampler et al., J.Nucl. Mater. **266-269,** 217 (1999).

[46] J. Bohdansky, J. Roth, H. Bay, *J. Appl. Phys.* **51**, 2861 (1980) and **52**, 1610 (1981).

[47] J. Bohdansky, Data Compendium for Plasma-Surface Interactions, *Nucl. Fusion* Special Issue, IAEA, Vienna (1984).

[48] W. Eckstein, J. Bohdansky, and J. Roth, *Nucl. Fusion Suppl.* **1**, 51 (1991).

[49] L. H. Thomas, *Proc. Cambridge Philos. Soc* **23**, 542 (1927).

[50] E. Fermi, *Z. Phys.* **48**, 73 (1928).

[51] C. Garćia-Rosales, W. Eckstein, J. Roth, *J. Nucl. Mater.* **218**, 8 (1994).

[52] W. D. Wilson, L. G. Haggmark, J. P. Biersack, *Phys. Rev. B* **15**, 2458 (1977).

[53] P. Sigmund, Sputtering by Particle Bombardment I, Topics in Applied Physics, vol 47, Springer, Berlin, Heidelberg, 1981.

[54] R. Chodura, in Physics of Plasma-Wall Interactions in Controlled Fusion (D.E. Post,

R. Behrisch, Eds), Plenum Press, New York, 99 (1986).

[55] R. Chodura, *J. Nucl. Mater.* **111-112**, 420 (1982).

[56] M. W. Thompson, *Philos. Mag.* **18**, 377 (1968).

[57] C. S. Pitcher, G. M. McCracken, D. H. J. Goodall, *Nucl. Fusion* **26**, 1641 (1986).

[58] K. Krieger, J. Roth, A. Annen et al., *J. Nucl. Mater.* **241-243**, 684 (1997).

[59] B. Lipschultz, B. LaBombard, E. S. Marmar, M. M. Pickrell, J. Rice, *J. Nucl. Mater.* **128-129**, 555 (1984).

[60] V. Philipps, T. Tanabe, Y. Ueda et al., *Nucl. Fusion* **34**, 1417 (1994).

[61] D. Naujoks, K. Asmussen, M. Bessenrodt-Weberpals et al., *Nucl. Fusion* **36**, 671 (1996).

[62] D. A. Pappas, B. Lipschultz et al., J.Nucl. Mater. **266-269,** 635 (1999).

[63] L. L. Lao et al., *Nucl. Fusion* **25**, 1611 (1985).

[64] N. R. Badnell, private communication (1997).

[65] G. Fussmann et al., Plasma Physics and Controlled Nuclear Fusion Research, Vol. 2, IAEA, Vienna 143 (1995).

[66] D. Naujoks et al., Nucl. Fusion **33**, 581 (1993).

[67] D. Naujoks, Nucl. Fusion **37**, 1193 (1997).

[68] D. E. Post, R. V. Jensen, C. B. Tarter et al., Atomic Data and Nuclear Data Tables **20**, (1977).

[69] G. F. Matthews, R. A. Pitts, G. M. McCracken, and P. C. Stangeby, *Nucl. Fusion* **31**, 1495 (1991).

[70] R. T. Nachtrieb, "Ion Mass Spectrometry on the Alcator C-Mod Tokamak'', thesis for the Ph.D. degree in Nuclear Engineering, Massachusetts Institute of Technology, 2000.

[71] J. N. Brooks and D. N. Ruzic, *J. Nucl. Mater.* **176-177**, 278 (1980).

[72] J. P. Biersack and W. Eckstein, *Appl. Phys. A* **34**, 255 (1993).

[73] B. LaBombard, private communication (1998).

[74] P. C. Stangeby, *Plasma Phys. Control. Fusion* **37**, 1031 (1995).

[75] J. C. Rost, "Fast Ion Tails during Radio Frequency Heating on the Alcator C-Mod Tokamak," thesis for the Ph.D. degree in Physics, Massachusetts Institute of Technology, 1998.

[76] D. Whyte et al., J. Nucl Mater. **241-243**, 660 (1997).

[77] F. F. Chen, "Introduction to Plasma Physics and Controlled Fusion", Plenum Press, (1984).